SPATIAL VARIABILITY OF ACTUAL EVAPORATION IN A PRAIRIE LANDSCAPE

A Thesis Submitted to the College of

Graduate Studies and Research

In Partial Fulfillment of the Requirements

For the Degree of Doctor of Philosophy

In the Department of Geography and Planning

University of Saskatchewan

Saskatoon

By

Robert N. Armstrong

© Copyright Robert N. Armstrong, June/2011. All rights reserved.

PERMISSION TO USE

In presenting this thesis in partial fulfilment of the requirements for a Postgraduate degree from the University of Saskatchewan, I agree that the Libraries of this University may make it freely available for inspection. I further agree that permission for copying of this thesis in any manner, in whole or in part, for scholarly purposes may be granted by the professor or professors who supervised my thesis work or, in their absence, by the Head of the Department or the Dean of the College in which my thesis work was done. It is understood that any copying or publication or use of this thesis or parts thereof for financial gain shall not be allowed without my written permission. It is also understood that due recognition shall be given to me and to the University of Saskatchewan in any scholarly use which may be made of any material in my thesis.

Requests for permission to copy or to make other use of material in this thesis in whole or part should be addressed to:

Head of the Department of Geography and Planning
117 Science Place
University of Saskatchewan
Saskatoon, Saskatchewan
Canada
S7N 5C8

ABSTRACT

Land surface evaporation has considerable spatial variability that is not reflected in meteorological station data alone. Knowing the spatial variability of evaporation is important for describing drought, managing agricultural land, and is valuable for improving the parameterization of hydrological models and land surface schemes over large areas. General difficulties arise for obtaining reliable, spatially distributed evaporation estimates as a result of uncertainty in estimation techniques, scale issues and complexities regarding land surface and atmospheric interactions, and the spatial and temporal variability of key factors governing the evaporation process. Estimating evaporation is further complicated when soil moisture becomes a critical limitation, particularly during drought. An examination of the spatial variability of evaporation and its association with governing factors was conducted in Prairie landscapes using three modelling techniques. First, eddy covariance measurements and reference meteorological data were obtained at two Prairie locations to assess the accuracy of physically-based models for calculating point estimates of actual evaporation under non-limited soil moisture conditions and during drought. Second, estimates of actual evaporation were distributed at the field scale in order to examine the impacts of driving factors and their spatial associations on upscaled evaporation estimates. This required the assimilation of high resolution visible and thermal images which were used to derive estimates of surface albedo and surface emitted longwave radiation. These were combined along with surface reference observations to develop an index of the mid-day radiation in order to distribute a known value of mean daily net radiation over the field. Third, archived historical climate data were used as input for a continuous hydrological simulation to examine spatial and temporal variations in evaporation across the Prairie region of Western Canada during a drought and non-drought period.

Results of this research showed that the spatial variability of evaporation could be derived at the field scale by integrating remote sensing and surface reference climate data with a physically-based evaporation model. Surface temperature and soil moisture, and net radiation were found to be highly variable spatially at field scales whilst meteorological conditions tended to be less variable spatially but showed strong temporal

variability. At the field scale it was found that the variability in albedo and surface temperature were both important for characterizing differences in surface state conditions. Their combined influence was reflected in the resulting pattern of net radiation that governed the distribution of actual evaporation estimates obtained with the Granger and Gray evaporation model.

It was found that an areal estimate of evaporation obtained from the means of driving factors was similar to the areal average obtained from the distributed estimates. This was attributed to the offsetting interactions among the driving factors which effectively reduced the variability of the model estimates. In general, the physically-based models examined were found to provide reasonable estimates of actual evaporation when driven by observations at point-scales over multi-day and seasonal periods. This included periods when soil moisture was not a strong limitation and also under drought conditions. Variations in the spatial pattern of actual evaporation provided a useful indicator of drought across the Prairie region of Western Canada.

The results contribute to a better understanding of the effects of spatial associations of key factors on evaporation estimates in a Prairie landscape. The methodology developed for distributing net radiation from assimilated visible and thermal images could potentially be used in regional scale modelling applications for improving evaporation estimates using point scale estimation techniques. The modelling algorithms applied to derive point estimates of evaporation from surface reference data may be useful for operational purposes that require estimates of actual evaporation and for characterizing drought.

ACKNOWLEDGMENTS

I would like to extend my deepest gratitude to my colleagues, family and friends for their support which helped to make completion of this dissertation a reality. I am deeply indebted to my co-supervisors Dr. John Pomeroy and Dr. Lawrence Martz for providing support, guidance and their mentorship over the course of my academic journey; and for being the voices of reason when needed.

I am also very grateful to the members of my advisory committee, Dr. Raoul Granger, Dr. Bing Si, and Dr. Xulin Guo for their valuable insights, comments, and sharing with me their knowledge in the fields of evaporation science, soil science, and remote sensing. I would like to thank Dr. Brian Amiro, my external examiner, for his thoughtful insights and suggestions. I would also like to give thanks for financial support provided by the Department of Geography, the Drought Research Initiative (DRI), and the Canada Research Chairs.

I would also like to give a special thanks to several individuals at the Centre for Hydrology for their assistance over the years: Joni Onclin for her tireless efforts regarding office matters, Mike Solohub for his tutelage in the field, Tom Brown for his programming efforts of the Cold Regions Hydrological Model, and also Dr. Kevin Shook for always being available to assist with open source programming issues. I am also thankful for the time shared with my fellow students during this journey which included many conferences and social gatherings.

Finally, this would not have been possible without the love, understanding, patience, and support from my wife Monique and my mother and father, Cathy and Bob.

TABLE OF CONTENTS

LIST OF TABLES

LIST OF FIGURES

LIST OF ABBREVIATIONS

A-A Advection-Aridity model
AAFC Agriculture and Agri-food Canada
ASTER Advanced Spaceborne Thermal Emission and Reflection Radiometer
AVHRR Advanced Very High Resolution Radiometer
BG Brome grass
BOREAS Boreal Ecosystem-Atmosphere Study
BT Dalton-type bulk transfer model
C Cultivated
CLASS Canadian Land Surface Scheme
CRAE Complementary Relationship Areal Evaporation
CRHM Cold Regions Hydrological Model
DAI Data Access Integration
DN Digital Number
DRI Drought Research Initiative
F Fallowed
G-D Ganger and Gray model
FIFE First ISLSCP Field Experiment
ISLSCP International Satellite Land surface Climatology Project
MG Mixed grass
MODIS Moderate-resolution Imaging Spectroradiometer
PAMII Second Generation Prairie Agrometeorological Model
PFRA Prairie Farm Rehabilitation Administration
P–M Penman-Monteith model
RMSE Root mean squared error
SDNWA St. Denis National Wildlife Area
SIB Simple Biosphere model
TDR Time Domain Reflectometry
W Wetland
B Back radiation (to the sky)
β Bowen Ratio
C_p Specific heat of air
D Relative drying power of the air
E Evaporation
E_A Drying power of the air
E_L Moisture limited evaporation rate
E_R Evaporation ratio
G Relative evaporation (ratio of actual to potential)
I Incoming radiation
$K\downarrow$ Incoming solar radiation
$K\uparrow$ Reflected solar radiation
$L\downarrow$ Incoming longwave radiation
$L\uparrow$ Emitted longwave radiation
$L\uparrow_R$ Emitted longwave ratio
P Atmospheric pressure

R	Schmidt's Ratio (1915)
Q^*	Net radiation surplus
Q^*_d	Mean daily net radiation
Q^*_R	Net radiation ratio
Q_e	Latent heat flux
Q_g	Heat storage flux in a given medium (water / ground)
Q_h	Sensible heat flux
R_θ	Soil wetness ratio
T_a	Air temperature
T_s	Surface temperature
U_x, U_y, U_z	Orthogonal wind components
Z_{oR}	Roughness ratio
Q^*_{dref}	Reference mean daily net radiation
b	Pore size distribution index
d	Displacement height
e^*_a	Saturation vapour pressure at air temperature
e_a	*A*ctual vapour pressure or saturation vapour pressure at dew point temperature
e_s	Saturation vapour pressure at the temperature of the water surface
$f(u)$	Vapour transfer function related to wind speed
$_i$	Value at a given pixel
$_{iref}$	Reference value at a known pixel location
k	von Kármán constant
q	Specific humidity at air temperature
$qs(Ts)$	Saturated specific humidity at surface temperature
r_a	Aerodynamic resistance
r_c	Canopy resistance
r_{cmin}	Minimum unstressed canopy resistance
u	Wind speed
w	Vertical wind component
z	Reference height of wind speed
z_0	Aerodynamic roughness length
Δ	Slope of the saturation pressure curve
α	Priestly-Taylor coefficient; Surface albedo
γ	Psychometric constant
ε	Ratio of molecular weights of moist to dry air
θ	Soil moisture content
θmax	Maximum soil moisture content
λ	Latent heat of vaporization
ρ	Air density
ϕ	Porosity
ψ	Soil moisture tension
ψ_{ae}	Air entry tension

CHAPTER 1

INTRODUCTION

1.1 Background

In the natural environment, the process of evaporation involves the phase change of water from a liquid state into vapour. Evaporation can occur from free water surfaces, soil and vegetation (through stomata via transpiration), and even rock. As such, the term evaporation is used herein to describe the physical change from liquid to vapour and includes evaporation occurring from the soil and vegetation system, and free-water surfaces. Evaporation is one of the key factors governing the hydrological cycle and is a critical concern for many water resources and modelling applications. Consequently reliable estimates of 'actual' evaporation are needed for hydrology, meteorology, climatology, and water resources management problems (Sellers et al., 1997; Gowda et al., 2008). In general, these applications operate across a range of spatial scales and evaporation estimates are often needed at length scales in the order of a few metres (field scale) to hundreds of kilometres. However, evaporation is highly variable both spatially and temporally and obtaining accurate estimates, even at a 'point', can be a difficult challenge. Pomeroy et al. (2010) attribute the difficulties to issues such as differences and uncertainty in evaporation concepts, estimation methods and parameterization techniques; and complexities of soil-surface-atmosphere interactions.

In the Canadian Prairies, both water quantity and evaporation are of critical concern for agriculture practices and water resources management and planning. In recent years, emphasis has been placed on improving the understanding of hydrological and atmospheric processes associated with extreme events in Canada such as floods and droughts (Environment Canada, 2004). These are serious problems that can have major environmental and socio-economic impacts. Recently, the Canadian Prairie region which accounts for the largest portion of Canada's agriculture was strongly impacted by severe drought during 1999-2004. The economic consequences and questions related to water quantity, and land use and adaptation strategies provide strong motivation for better understanding the physical processes associated with severe drought across the Canadian Prairies (Pomeroy et al., 2010).

Given the importance of evaporation in water resource problems, the research presented in this thesis is interested in the spatial and temporal variability of evaporation across a range of scales during wet and dry periods. In the case of extended drought periods, seasonal evaporation can greatly exceed precipitation and subsequently dominate regional water balances. This has potential implications for future land management strategies in general. This raises a question as to the effects of spatial variations of key factors on estimates of evaporation. This, in turn, raises a further question as to whether spatial covariability may exist between key factors governing evaporation and whether such information may be used to improve our ability to obtain more reliable estimates for large scale applications.

Due to the importance of evaporation in managing water resources, the goal of this research is to improve upon the understanding of how spatial variations of factors governing evaporation impact the accuracy of its estimation, and to demonstrate the applicability of physically-based evaporation models within the Prairie landscape for water resource problems, particularly where drought is concerned. The problem is approached through a combination of physically-based modelling techniques that includes the application of evaporation models capable of providing direct estimates of actual evaporation, the assimilation of surface reference and remote sensing data, and long term continuous hydrological modelling that covers the drought period of 1999 - 2004.

1.1.1 Difficulties in Estimating Evaporation in Natural Landscapes

Reliably estimating evaporation on a consistent basis is by no means a trivial problem. The surface-atmosphere interactions governing the evaporation process are complex, particularly in the case of terrestrial landscapes. As a result, a large number of methods have been developed for its estimation and the issue of uncertainty remains a fundamental concern. The following discussion gives a brief introduction to sources of uncertainty in evaporation modelling. A more detailed overview of subjects pertinent to this thesis is reserved for a synthesis of the literature.

Theoretical Assumptions and Evaporation Concepts

Most evaporation estimation methods and measurement techniques have been developed under the assumption of steady state conditions. In other words, spatial and temporal variations in key

factors of the process are assumed to be negligible over the time step and spatial extent of the calculation. However, spatially variable topography, vegetation and available water are inherent in natural landscapes and violate the steady-state assumptions of most evaporation models. Perhaps more important is that the dependency of the evaporation process on both water and energy availability (i.e. surface state conditions) adds a level of complexity to the modelling process. This has resulted in various theoretical treatments of saturated and unsaturated surface conditions. Subsequently, a number of ambiguous evaporation concepts has appeared in the literature (e.g. potential, equilibrium, reference, and actual), and is a general source of confusion and uncertainty (Granger, 1989a).

Uncertainty in Estimation Methods

A great deal of the uncertainty in estimating evaporation can be attributed to the number of different theoretical approaches that have been proposed (Brutsaert, 1982). In truth, there is no universally accepted method of estimating evaporation, and the subject remains a contentious issue; particularly where evaporation from land surfaces is concerned. In general, the estimation of evaporation from land surfaces is approached differently than for free water surfaces. This is because the surface humidity gradient can be obtained directly over water when surface temperature data is available (Brutsaert, 1982); also considerations for soil and vegetation are not needed. In the case of land surfaces, however, the magnitude of evaporation largely depends on the surface state and soil moisture conditions (e.g. saturated vs. non-saturated), and the characteristics of the land cover. The non-saturated case is of general importance as regards land surfaces in the Canadian Prairies owing to the sub-humid climate conditions.

Another source of uncertainty is that the complexity of estimation methods varies considerably. Some methods are purely empirical and lack a theoretical basis, and are therefore not widely applicable given that parameters often require site specific calibrations. Others are physically-based and may or may not be computationally expensive. Physically-based evaporation models generally take the form of single-layer or multilayer canopy models, or may even be imbedded in the framework of predictive models. As Raupach and Finnigan (1988) have clearly stated, there is an inherent incompatibility between simplicity and realism. Unfortunately, this speaks to the general problem of how models are often perceived. Namely, that usefulness tends to be associated with simplicity of application, whereas correctness is potentially perceived

to be mired in the complexities of realism. Nevertheless, Raupach and Finnigan have concluded that both single and multilayer evaporation models can be accurate and are useful but are better suited for different applications.

The Spatial and Temporal Variability of Governing Factors

The heterogeneity of natural landscapes and variability of climate conditions presents a problem for accurately estimating evaporation on a consistent basis. The range of spatial scales over which reliable estimates are needed can vary widely depending on the application. In the terrestrial environment, three general scales can be identified (Brutsaert, 1982). These include estimates at a 'point' (metres to hundreds of metres), over field sized areas (kilometres) and across large regions (tens to hundreds of kilometres). Brutsaert (1998) has suggested the problem can be addressed via better treatments of land surface variability itself. A general problem is that landscape variability tends to increase with the length scale of interest (Blöschl and Sivapalan, 1995). As a result, important information may be lost during the application of scaling or averaging procedures, which in turn will have an impact on evaporation estimates and subsequent spatial patterns of evaporation. The challenge then is to obtain reasonably accurate estimates across the range of spatial scales by explicitly taking into consideration the pertinent natural variability of landscape features and surface state conditions.

Remote sensing is a useful tool for directly measuring spatial variations in land surface characteristics over large areas, which makes it attractive for a range of environmental applications. It is currently not possible to measure evaporation directly via satellite instruments (Engman and Gurney, 1991; Duguay and Pietroniro, 2005); although it is possible using an airborne eddy covariance system (Giola et al., 2004). However, spatial observations obtained via satellite instruments such as surface temperature can be assimilated directly into an evaporation model or used to derive key variables (e.g. surface albedo) needed for the parameterization of evaporation models (Granger and Bussières, 2005). A persistent and general limitation of optical remote sensing is the problem of atmospheric haze and clouds. Also, the relative complexity of algorithms needed for deriving variables from surface measurements can be a general limitation for practical applications.

1.2 Scope

The most practical means of approaching the aforementioned issues is through a combination of physically-based modelling techniques that includes an examination of stand alone evaporation models, the assimilation of remote sensing information and visualization using Geographical Information System (GIS) software, and long term continuous hydrological modelling. Such tools will allow for an examination of the reliability of point scale models to estimate evaporation in the Prairie landscape under varying surface conditions and various parameterization strategies. Physically-based evaporation models and bulk transfer equations can be parameterized via atmospheric and remote sensing observations obtained during field campaigns and from historical archives. The reliability of the models for obtaining accurate estimates is determined by comparing estimated values against evaporation measurements obtained using the eddy covariance technique. This is the most direct method of measuring evaporation at a 'point' and is well suited for validating model estimates. Also the spatial relationships between factors governing evaporation are used for distributing estimates of evaporation across the Prairie landscape.

1.3 Objectives

The research is conducted with the specific objectives:

- To determine the accuracy of a selection of physically-based models for estimating evaporation in prairie landscapes;

- To examine the spatial variability of estimated evaporation at the field scale resulting from the spatial associations between driving factors of evaporation and potential impacts of covariance on upscaled estimates of evaporation;

- To examine large scale spatial and temporal variations in evaporation across the Canada Prairies during a drought and a non-drought period.

1.4 Organization

Chapter 2 provides a review of evaporation theory resulting in the development of physically-based point scale evaporation estimation methods and the difficulties in reliably estimating evaporation at regional scales. Chapter 3 presents details on the study design and site characteristics. Chapter 4 discusses the eddy covariance technique for measuring evaporation and considerations regarding the parameterization of the models. The 1st objective is addressed in Chapter 5. Chapter 6 addresses the 2nd objective and Chapter 7 addresses the 3rd objective. Chapter 8 presents a summary of the conclusions and recommendations for future research.

CHAPTER 2

LITERATURE REVIEW

2.1 Introduction

Brutsaert (1982) gives an excellent and comprehensive overview of 'Evaporation into the Atmosphere' which presents the physical and empirical basis of developments in evaporation theory to that time. He notes that considerable variation in theoretical developments, model complexity, and differences in input requirements is a general source of uncertainty for estimating evaporation. His overview suggests that the uncertainty in model estimates may increase as models diverge further from the fundamental physics of the problem or the integrated physics become so complex that a model is difficult to apply for practical purposes. Therefore, choosing an appropriate model becomes an important consideration, particularly where operational applications may be concerned.

The choice of model more often depends on the specific input requirements and how readily these may be obtained as opposed to consideration for the appropriate use or correctness of any given model (Raupach and Finnigan, 1988). For example, analysis of evaporation trends has typically been conducted within the Canadian Prairie region using pan evaporation data and empirical estimates of gross evaporation from free water surfaces (Martin, 2002; Hesch and Burn, 2005; Burn and Hesch, 2007). However, there appears to have been no attempt at estimating actual terrestrial evaporation for operational purposes.

Reliably estimating evaporation from natural landscapes should begin from a sound physical basis. This promotes an overall understanding of the process, and allows for an examination of the realistic behaviour of the interactions within the natural system (Thom and Oliver, 1977). Yet, a certain level of empiricism is unavoidable due to the complexity of surface-atmosphere interactions governing the evaporation process itself; which is another source of uncertainty. There is large variability in topography, water and energy availability, soil and vegetation properties, and also climate conditions. These factors may generate considerable spatial variability in evaporation. Improving our ability to reliably estimate evaporation has wide ranging implications given potential changes in future water availability (Bremer et al. 2001).

For example, knowing the spatial variability of actual evaporation may improve our understanding of drought related processes in Prairie environments.

Given the sources of uncertainty, a synthesis of relevant literature begins from the physical basis considered for choosing appropriate models that provide realistic estimates of actual evaporation from the land surface. Interestingly, much of the progress toward terrestrial evaporation began from investigations of evaporation from water surfaces. A historical perspective highlights some noteworthy aspects that culminated in the fundamental advancements of the science by Dalton in 1802, and Bowen in 1926, and Penman's wisdom in combining these respective approaches in 1948. A discussion on the general difficulties associated with the complex soil-vegetation-atmosphere interactions and the variability of factors governing the evaporation process, and approaches to addressing these issues will follow.

2.2 Historical Developments in Evaporation Theory

As stated previously, evaporation is the process whereby water undergoes a phase change from a liquid (or solid, viz. sublimation) to vapour state and is transported to the atmosphere. Several conditions are necessary for the process of evaporation to occur,

1. There must be an available supply of water;
2. Sufficient energy is needed for the phase change from water to vapour;
3. A transport mechanism is needed to carry the vapour away.

There was little understanding beyond these general requirements from about 350 B.C. until 1800 A.D. (Brutsaert, 1982). For some two thousand years, philosophers held firmly to Aristotle's view of the sun as the only cause of evaporation. Experimentation was rare before the 17th century, and to openly refute the accepted views of the 'Ancients' on any subject literally meant risking one's life (Nace, 1947). In essence, the fundamental problem was incontrovertibly proving the cause and effect mechanisms of the evaporation process. In 1637, Descartes' 'Discourse on the Method'' represented a significant step toward this. Descartes emphasized the need for skeptiscm toward all past theories and knowledge, and outlined founding principles upon which scientific truth could be achieved. In the same year, he also theorized that evaporation was a result of the agitation and separation of water particles caused

by the sun's heat, and the rising of the vapours was the source of the winds (Brutsaert, 1982). Unfortunately, Descartes had no way of proving whether this was true.

By the late 17th century, the movements of air particles were found to be another cause of evaporation. In 1670, Pierre Perrault's use of a weighing apparatus elucidated the evaporation of frozen water in the winter, and he also observed evaporation from a vessel in an enclosed space in the absence of heat or cold (Nace, 1947). Perrault reasoned that the evaporation must be caused by the motion of the air particles which excited the water particles into separating (Nace, 1947). By 1695, however, Edmund Halley had likened the drying effects of wind to that of a solution of salt and water, whereby water particles were dissolved into the air in contact with them (Brutsaert, 1982). A debate ensued during the next 100 years over whether the cause of evaporation attributed to wind was due to the agitation and separation of the particles or the dissolution of water in the presence of air. The latter was supported most notably by Benjamin Franklin who reasoned that each air particle could only allow a finite number of water particles to adhere to it, and "when too much is added, it precipitates as rain" (Franklin, 1765, p. 183).

In 1802, a fundamental advance came from the experiments of John Dalton which resulted in the establishment of several general laws for the science. As such, he stated several factors that strongly controlled evaporation (Dalton, 1834, p. 125),

> "The following circumstances are found powerfully to promote evaporation ; namely, *heat*, *dry air*, and *decreased weight* or *pressure* of the atmosphere on the evaporating surface"

Specifically, he showed the change in saturation vapour pressure at a water surface was a function of surface temperature alone. He also showed evaporation occurred in a vacuum, proving that the presence of air was not a requirement. He further stated that for temperatures below 138 °F (58.9 °C) evaporation must also be proportional to the difference between the vapour pressures at the temperature of the water surface and the dewpoint temperature of the air (Henry, 1854). The rate was also enhanced by an unknown wind function related to wind speed. As such, the actual quantity evaporated from a water surface can be obtained from a general Dalton form of the equation (Penman, 1948; Brutsaert, 1982),

$$E = f(u)(e_s - e_a) \quad , \tag{2.1}$$

where e_s is the saturation vapour pressure at the temperature of the water surface, e_a is the saturation vapour pressure at the dew point temperature of the air (also equivalent to the actual vapour pressure), and *f(u)* is an unknown vapour transfer function of wind related to wind speed. In light of Dalton's fundamental advance, efforts focused on data collection and empirical investigations of the wind function (Penman, 1947).

In 1915, Schmidt provided the first estimates of evaporation for the ocean viz. the energy budget (Lewis, 1995). The general form of the energy equation can be written as,

$$Q^* = Q_e + Q_h + Q_g \quad , \tag{2.2}$$

where Q^* is net radiation surplus, Q_e is the latent heat flux, Q_h is the sensible heat flux, and he assumed that Q_g, the change in heat storage, was negligible on an annual basis. Schmidt further assumed the annual net radiation surplus was balanced by conduction and evaporation, and introduced the ratio of the sensible to latent heat fluxes,

$$R = \frac{Q_h}{Q_e} \quad , \tag{2.3}$$

and upon rearranging the terms, the evaporation rate, E can be determined as,

$$E = \frac{Q^*}{\lambda(1+R)} \quad , \tag{2.4}$$

where λ is the latent heat of vaporization. Angstrom (1920) then elucidated the inherent difficulties in obtaining reliable estimates of R. As such, the method was highly uncertain due to the complex interactions and mutual dependencies of radiation, temperature, evaporation, wind and convection. Shortly after, Bowen (1926) showed that Schmidt's ratio, R could be derived as a function of the gradients of temperature and humidity between the surface and atmosphere which can be given by (Penman 1948),

$$\beta = \frac{Q_h}{Q_e} = \frac{\gamma(T_s - T_a)}{(e_s - e_a)} \quad , \tag{2.5}$$

where β is the Bowen Ratio designated previously as R, γ is the psychometric constant, T_s and T_a are the respective temperatures of the surface and air. He also assumed the turbulent transport mechanism for both heat and vapour was essentially the same so the need for wind speed could be eliminated entirely.

In a further development, Cummings and Richardson (1927) showed that the net radiation balance over a shallow pan could be obtained from the difference between the incoming radiation, I and the energy radiated back to the sky, B. This can be found as the sum of the net shortwave and net longwave radiation components,

$$Q^* = I - B = K\downarrow - K\uparrow + L\downarrow - L\uparrow \quad , \tag{2.6}$$

where, $K\downarrow$ is the incoming solar radiation, $K\uparrow$ is the radiation reflected from the surface, $L\downarrow$ is the incoming longwave radiation, and $L\uparrow$ is the longwave radiation emitted from the surface. For adjacent surfaces exposed to the same external conditions (i.e. two pans), the sum of the incoming radiation terms is essentially equal. Therefore the variation in net radiation is controlled by the surface reflected and emitted energy to the atmosphere. For surfaces with different temperatures the emitted longwave radiation can be found according to Stefan's Law, whereby the energy emitted is proportional to the fourth power of the absolute surface temperature. The significance was that energy budgets of adjacent surfaces could be estimated based on differences in the reflected energy and surface temperatures if the energy budget was known for at least one of the surfaces (Penman, 1947).

More importantly, their research did two things; it showed the practical application of the Bowen Ratio for estimating evaporation over water (albeit from two pans of different sizes), and it addressed a growing concern over the uncertainty of relating estimates of pan evaporation to that of nearby lakes or regional estimates via the water balance. The relationship between pan and regional evaporation estimates is highly suspect because there is a negative correlation between pan evaporation and actual evaporation under the conditions of increasing aridity during periodic water shortages (Monteith, 1981).

2.3 Physically-Based Estimation Methods

2.3.1 Penman's Combination Evaporation Model

Penman (1948) provided a fundamental advance by combining the thermodynamic principles of the energy balance, which supplies the energy for the latent heat of vaporization, and Dalton's aerodynamic form of the transport mechanism needed to carry the vapour away. As such, Eq. 2.1, 2.4 and 2.5 were fundamental to Penman's developments. An analytical solution also required the introduction of a new term and a second thermodynamic 'constant'. The new term was the "drying power of the air", which was expressed in Dalton's form as $E_A = f(u)(e^*_a - e_a)$, where e^*_a is the saturation vapour pressure at air temperature. He also introduced the slope of the saturation pressure curve, Δ,

$$\Delta = \frac{e_s - e^*_a}{T_s - T_a} \quad , \tag{2.7}$$

which can be calculated at the temperature of the air,

$$\Delta = \frac{4098\left[0.6108\exp\left(\frac{17.27T_a}{T_a + 237.3}\right)\right]}{\left(T_a + 237.3\right)^2} \quad . \tag{2.8}$$

Eq. 2.8 describes the change in saturation pressure with temperature as first elucidated by Dalton. Combining the equations eliminated the need for surface temperature, which at the time was rarely available and difficult to measure. This resulted in Penman's evaporation equation for a saturated surface which only requires atmospheric data at one height,

$$E = \frac{\Delta\frac{Q^* - Q_g}{\lambda}}{\Delta + \gamma} + \frac{\gamma E_A}{\Delta + \gamma} \quad , \tag{2.9}$$

where E is in mm day^{-1}, Q^* and Q_g (W m^{-2}), λ (kJ kg^{-1}) is slightly temperature dependent to 60 °C (List, 1966) and calculated as 2501 – 2.361(T_a), Δ (kPa °C^{-1}), E_A (mm day^{-1}), and γ (kPa °C^{-1}) which relates pressure and temperature by,

$$\gamma = \frac{C_p P}{\varepsilon \lambda} \quad , \tag{2.10}$$

where C_p is the specific heat of air (1.005 kJ kg^{-1}), P is the atmospheric pressure (kPa), ε is the ratio of the molecular weights of moist to dry air. When analysed over a range of air temperatures, the evaporative flux contributions from the energy and aerodynamic terms, $\Delta/(\Delta+\gamma)$ and $\gamma/(\Delta+\gamma)$, represent weighting factors that sum to 1. As air temperature increases the energy supplied from the air becomes more important. The developments of the Penman model are significant in that they are physically-based in thermodynamic principles governing the evaporation process at a water surface (i.e. actual evaporation). As such, it was also found to agree well with evaporation over other saturated surfaces exposed to the same weather conditions (e.g. soil and grass).

In the same year, Thornthwaite (1948) introduced the term 'potential evapotranspiration' in his seminal paper on an approach to climate classification. In essence, he defined it in terms of a an oasis effect such that as the water supply increased the evaporation would increase to a maximum rate that only depended on climate conditions. In contrast to Penman's physically-based actual evaporation equation, however, Thornthwaite derived an empirical method that depends only on mean monthly temperature and an index of heat. In fairness, this was proposed for climate classifications rather than an analytical approach for estimating potential evaporation. It was also clear that the potential evaporation was an awkward quantity that could not be measured, unlike actual evaporation, because the conditions of an unlimited supply of water are seldom encountered in terrestrial landscapes.

Nevertheless, potential evaporation is generally defined as the quantity of evaporation that would occur from a natural surface under the conditions of an unlimited water supply (Brutsaert, 1982). Subsequently, Penman's model has become known as a potential evaporation model. But other definitions of potential evaporation also exist (Granger, 1989a). For instructive purposes it is pertinent to distinguish the Penman equation from another so called potential evaporation equation, namely the 'equilibrium' evaporation (Eichinger et al., 1996). This method assumes the humidity gradient disappears over a saturated surface and advection is assumed to be negligible, and drops the aerodynamic term from Eq. 2.9. However, this assumption has been shown to

produce considerable underestimates of evaporation in the order of 20 to 30% as indicated by Eichinger et al. (1996).

To further elucidate the point, Priestly and Taylor (1972) introduced a coefficient, α, to the equilibrium evaporation equation. α is a constant that is related to the evaporative fraction which is the "ratio of latent heat flux to the sum of latent and sensible heat fluxes" (Nichols and Cuenca, 1993). Values of α were calculated from available measurements and were found to be in the order of 1.26 on average. In other words, the vapour transfer mechanism plays an important role in promoting evaporation and cannot be neglected. Eichinger et al. (1996) cite a considerable body of research that have reported values similar to 1.26 under saturated conditions and attempted to provide an analytical solution for α. However, it has been found that α may vary substantially over shorter time periods (Hobbins et al., 2001); and is considerably higher in arid environments and considerably lower under the moisture limited conditions of non-saturated surfaces. As such, a rational physical explanation of the significance of α for saturated conditions has yet to be elucidated.

2.3.2 Actual Evaporation

Theoretical differences exist for the treatment of saturated and unsaturated surface conditions. In sub-humid to arid environments, like those encountered in the Canadian Prairies, actual evaporation is primarily governed by water supply. Estimates of actual evaporation are typically obtained from estimates of some potential evaporation as a function of water availability viz. surface and soil moisture accounting in hydrological models (e.g. Leavesley et al., 1983; Kite, 1995; Kouwen, 2001). Fluctuations in soil moisture are an important concern for hydrological applications in general due to the high spatial and temporal variability of soil moisture (Western et al., 2002).

In the terrestrial landscape, evaporation rates are also governed by the temporal and spatial variability of the net supply of available energy, forcing meteorology, and the complexities of surface-atmosphere feedbacks. Physically-based 'single layer' model approaches have been developed based on Penman's analytical developments. More theoretically based and very complex 'multilayer' model approaches have also been proposed. For example, a resistance-based network has been developed and applied to surfaces with sparse vegetation cover (Shuttleworth and Wallace, 1985). The increased complexity of this approach is attributable to

the combined interactions of the many resistances theorized to exist between the soil surface to the atmosphere. Such a model has not been considered here and is rarely warranted in the case of most Prairie landscapes where vegetation tends to be well established. A notable exception might be the sand dune landscapes found in Saskatchewan where vegetation is observed to be sparse and separated by extensive patches of bare ground.

2.3.2.1 Penman-Monteith

The Penman-Monteith (*P-M*) method (Monteith, 1965) is a 'single layer' approach that extends Penman's model to non-saturated surfaces by introducing the stomatal and aerodynamic resistances that control the transfer of water vapour to the atmosphere. These represent the diffusion path lengths for vegetation and the boundary layer respectively. The general form of the equation can be written as,

$$E = \frac{\Delta \frac{(Q^* - Q_g)}{\lambda} + \left(\rho C_p \frac{\left(e_a^* - e_a\right)}{r_a} \right)}{\Delta + \gamma \left(1 + \frac{r_c}{r_a} \right)} \quad , \tag{2.11}$$

where ρ is the air density (kg m^{-3}), and r_a and r_c are the aerodynamic and canopy resistances (m day^{-1}), and all other terms are the same as defined previously. The canopy resistance term exerts a major control on evaporative losses from plants. Jarvis (1976) found that several environmental factors correlate well with the operation of stomata and therefore evaporative losses from leaves. These factors include soil moisture, incoming solar radiation, humidity, and air temperature.

In essence, this form of the *P–M* equation is considered to be a 'big leaf' model generally applicable to a full canopy with limited exposure of bare soil between plants (Stannard, 1993). Interestingly, Monteith (1981; 1986) has used the inverted form of the equation as more of a diagnostic tool to examine variations in the stomatal or canopy resistance when the evaporation and meteorological forcing is known, as opposed to an evaporation estimation method when the surface resistance is assumed. A potential limitation of the *P-M* method is the added complexity of estimating the canopy resistance which has a dependency on plant available soil moisture, soil texture properties which regulate water transport through the soil, and potential effects of plant growth related to leaf area.

2.3.2.2 Granger and Gray

Granger and Gray (1989) developed another model that extends Penman's equation to the case of non-saturated surfaces. This model is representative of a surface feedback model, and in contrast to the resistance-based approaches, circumvents the need for detailed descriptions of land surface and vegetation characteristics. This is accomplished by introducing the relative evaporation which is the ratio of actual to potential evaporation. This method takes advantage of the inherent feedbacks that exist over range of surface state and atmospheric conditions as has been shown by Bouchet (1963) and Morton (1983); however an adequate physical description of the feedbacks is a general difficulty.

The general form of the Granger and Gray equation can be written as,

$$E = \frac{\Delta G \dfrac{(Q^* - Q_g)}{\lambda} + \gamma G E_A}{\Delta G + \gamma} \quad , \tag{2.12}$$

where G is the dimensionless relative evaporation which they show to be inversely related to the dimensionless relative drying power, D, of the atmosphere. G has been experimentally derived for a variety of environments and surfaces, specifically, the prairie, arctic, sub-alpine and boreal forest regions of western Canada. It can be estimated by (Granger, 1999),

$$G = \frac{1}{0.793 + 0.2e^{4.902D}} + 0.006D \quad . \tag{2.13}$$

D is assumed to be a function of the humidity deficit and available surface energy and is estimated by,

$$D = \frac{E_A}{E_A + \dfrac{(Q^* - Q_g)}{\lambda}} \quad . \tag{2.14}$$

In combination, the Granger and Gray model or *G-D* model (based on the relationship) takes into account the feedbacks between the surface and atmosphere which results in a non-linear decline in G with an increase in D. An advantage is that soil moisture status does not need to be known directly to calculate evaporation until the soil moisture status becomes a critical

limiting factor. An attractive feature of this method is that soil and vegetation specific factors used by the Jarvis algorithm to estimate canopy resistance are not required to obtain estimates of actual evaporation. However, the empirical nature of *G-D* and other relationships (e.g. wind function) have a long history dating back to Dalton's enlightenment of the science. Not surprisingly then, the lack of a purely physical description of the feedback relationships increases the uncertainty of such methods (Crago and Crowley, 2005; Lhomme and Guilioni, 2006).

2.3.2.3 Dalton-Type Bulk Transfer

A Dalton-type aerodynamic formula also appears in the literature that takes into consideration the diffusive path lengths of canopy and aerodynamic resistances (Monteith, 1981). As suggested by the name, this method is based on the general laws of evaporation stated by Dalton. That is, the method directly considers the humidity gradient between the surface and overlying atmosphere; and also variations in the density of the atmosphere over time. The equation can be written in the general form,

$$\lambda E = \frac{\lambda\rho(q_s(T_s) - q)}{r_a + r_c} \quad , \tag{2.15}$$

where q_s is the saturated specific humidity (kg kg^{-1}) obtained at the surface temperature (T_s), q is the specific humidity of the air (kg kg^{-1}).

Approaches such as this are often embedded in land surface schemes which are used to parameterize the lower boundary conditions of atmospheric and climate models for larger scale applications (Mahrt, 1996; Sellers et al., 1997a). Variations have found general application in predictive land surface models such as that used for the vegetation component in the Canadian Land Surface Scheme (CLASS) (Verseghy et al., 1993) and the Simple Biosphere (SIB) model (Sellers et al., 1986). An advantage of land surface schemes is their inherent capacity as predictive models attributed to the thermodynamic principles of heat and mass transfer on which they are based. The exactitude of such models inherently depends on the diagnosis of surface temperature from an iterative solution to closing the energy balance. From a theoretical standpoint, energy balance closure is not a problem in predictive models. In reality, however, even when the relevant terms are measured in natural landscapes, the difficulties in closing the

energy balance are well documented (Foken et al., 2006) which is partly attributed to scaling issues associated with measurements (Foken, 2008).

Another variation can be found in the second generation prairie agrometeorological (PAMII) model (Brimelow et al., 2010). PAMII has few input requirements, namely, daily precipitation and maximum and minimum air temperature, but also requires profiles of humidity, temperature, and wind speed within the planetary boundary layer. Such profiles can only be obtained from either sounding measurements or from climate model forecast output which can be considerably different from the observed atmospheric conditions. PAMII also employs a phenological model that uses the photoperiod, accumulated heat and planting date to determine specific growth stages for crops; specifically for wheat crops.

A general disadvantage for models such as those described previously is that they often rely on parameters which may require calibration which limit their use for general operational applications. However, the Dalton-type equation can also be applied independently to assess the model behaviour in natural landscapes when surface temperature observations are available.

2.4 Land Surface and Atmosphere Interactions

The variability of land surface and soil characteristics, physiological controls of vegetation, water and energy availability, and general climate conditions play a fundamental role in governing evaporation rates from terrestrial landscapes. This introduces a general difficulty, and is another source of uncertainty, for obtaining reliable estimates of evaporation. Therefore, it is important to quantify evaporation in a realistic and reliable manner to better understand the effects of variability. The differences in theoretical approaches among the models discussed previously provide several ways of treating land surface-atmosphere interactions. Strategies for parameterizing such models partly depend on the complexity of the interactions considered and methods available to obtain reliable values of the required inputs.

2.4.1 Land Surface Heterogeneity and Scaling Issues

A key concern is the inherent spatial variability associated with heterogeneous landscapes. This presents a major difficulty for scaling point estimates to areal estimates over larger regions (Shuttleworth, 1991). Methods of explicitly considering spatial variations in land surface

characteristics are needed which can be applied towards more reliable modelling. This is valuable towards improved understanding of the effects of spatial variability on evaporation. A critical issue is the spatial scale at which evaporation models are typically developed compared to the scales at which reliable estimates are needed. Operational applications tend to be larger scale problems which can extend over regions in the order of a few kilometres to hundreds of kilometres. A general problem exists in that nearly all approaches to estimating (or measuring) evaporation provide "point-scale" values, in the order of a few centimetres to kilometres depending on the 'footprint' scale of the inputs (Brutsaert, 1982).

Two models have been developed for obtaining 'true' regional scale estimates of evaporation; the Complementary Relationship Areal Evaporation (CRAE) model (Morton, 1983) and the Advection-Aridity model (Brutsaert and Stricker, 1979). Both are based explicitly on the complementary theory of Bouchet (1963). There have been mixed results reported for the CRAE model. Granger and Gray (1990a) found it to be poorly suited for short time periods (e.g. daily) whilst Hobbins et al. (2001) indicate it has performed well for monthly regional estimates when compared to long term regional water balances. The A-A model reportedly suffers from the need for frequent recalibration for it to be applied successfully (Hobbins et al., 2001). A general problem of Bouchet's relationship is that it assumes that there can be no sharp horizontal environmental moisture or energy gradients, which may be a large source of uncertainty in natural landscapes as the representative scale of the estimate increases.

Complex nested measurement approaches have been attempted which incorporate observations collected during intensive field experiments; e.g. FIFE (Sellers et al. 1992) and BOREAS (Sellers et al., 1997b) conducted under the International Satellite Land surface Climatology Project (ISLSCP). The nested approach is conducted using a multiscale measurement strategy to examine subgrid variability from individual plants up to the regional scale. Interactions between individual plants are related to the canopy; the 'mosaic' of canopies is related to the landscape; and interactions between the landscapes comprise the region. However, even under such a comprehensive approach, it was concluded that uncertainties in the measurements of sensible and latent heat fluxes in the order of 10% to 20% on a daily basis were apparent (Nie et al., 1992). Brutsaert (1998) attributes this uncertainty to the unpredictability of turbulent air flow and the natural variability exhibited by heterogeneous landscapes.

The importance of reliably estimating evaporation is well known for the purpose of coupled land surface and atmospheric modelling (Sellers et al., 1997a). Fluxes from respective land covers may be considerably different depending on the variability of the surface conditions (e.g. energy and moisture availability). Improved understanding of the spatial variability problem and methods of upscaling or aggregating evaporation estimates can be attributed to developments for numerical weather modelling and land surface parameterizations (Klaassen and Claussen, 1995). One approach has considered the turbulent transport issue by establishing a blending height at which the overlying air becomes well mixed (Wieringa, 1986). The second considers the surface variability directly and divides the landscape into a mosaic of homogeneous land covers. Areal estimates can then be determined from the weighted areas of individual cover types (Avissar and Pielke, 1989).

The latter offers a more realistic representation of the landscape for estimating fluxes compared to the past treatment of the landscape based on the dominant land cover. However, results from a recent data assimilation study conducted by Alavi et al. (2010) show that difficulties persist for accurately estimating evaporation using a land surface scheme such as CLASS which uses the mosaic approach indicated previously. They show large differences between the modelled and observed latent heat flux, approximately 10-100 W m^{-2}, during a pre-assimilation run (e.g. during the peak evaporation period). Subsequently, the assimilation of soil moisture data had the smallest effect on evaporation estimates during the same period but provided some improvement at the beginning and end of the season. Whether the general differences are due to an issue of scale or model parameterization is not clear.

A general limitation of dividing the landscape into homogenous tiles regardless of their respective spatial locations, is that spatial associations between adjacent cover types is not considered; nor are potential variations in soil moisture and soil characteristics for similar land cover types at different spatial locations. Brutsaert (1998) has previously indicated there is still a need for better treatment of land surface variability itself. Considerable importance continues to be placed on the need for spatially varying surface inputs at moderate to high spatial resolutions (Bisht et al., 2005). This can be attributed to the fact that information about surface heterogeneity and process interactions becomes smoothed or lost as a result of upscaling or aggregation procedures.

Part of the problem is the complex surface-atmosphere interactions and interdependences of energy and water availability, temperature, humidity and wind that affect the evaporation process. As such, there is a need for better understanding the spatial variability among factors driving evaporation. For example, Faria et al. (2000) have demonstrated the importance of spatial covariance as a factor in upscaling snow hydrological processes. Specifically, they examined the effects of covariability between ablation and snow water equivalent (SWE) on snow cover depletion. They showed that the covariability between melt rates and SWE enhance the depletion of snow covered area at the scale of forest stands. Consideration for the potential covariability among driving factors of evaporation may also be useful for upscaling evaporation estimates. However, addressing the problem first requires a better understanding of the spatial associations of driving factors affecting evaporation and how their spatial variability may bias evaporation estimates.

2.4.2 Surface Energy Availability

At any natural surface, the balance of net radiation, Q^* is typically partitioned into the three heat fluxes Q_e, Q_h and Q_g defined previously in Eq. 2.2. The importance of the available energy supply in governing evaporation rates has been well established to this point. In the case of the terrestrial landscapes covered by vegetation, 10% of the energy is typically attributed to Q_g during the day, although it can reasonably be ignored over daily periods or longer (Brutsaert, 1982). Factors such as clouds, differences in slope and aspect, surface roughness, albedo, leaf area, and soil moisture may have a considerable impact on energy availability as well.

The surface cover type is important in that available energy is proportioned differently according to the vegetation coverage and the availability of soil moisture. Vegetation is a major factor in that as much as 70% of the available energy may be used in the conversion of water to vapour (Segal et al., 1988). In contrast, available energy is increasingly partitioned into sensible heat under conditions of reduced water availability; i.e. surface temperature increases. Evaporative losses from soils largely depend on the surface wetness and vegetation cover. In the case of well established crops, much of the incoming solar radiation is intercepted by the vegetation thereby reducing evaporation from the soil surface (Shuttleworth and Gurney, 1990). In the case of an exposed soil, increased drying and potential development of a crust at the

surface creates a barrier to the flow of water vapour from deeper soil layers which also reduces soil evaporation.

These considerations demonstrate the difficulty of reliably estimating net radiation for environmental applications in general. This has resulted in the development of methods aimed specifically at providing distributed estimates of net radiation as discussed by Bisht et al. (2005). These approaches generally require the use of empirical techniques or complex radiative transfer models which are generally limited to providing larger scale estimates that produce overly smoothed or generalized data; i.e. this is a limitation for capturing spatial variations in net radiation. However, considering the combined effects of spatial variations in key surface variables driving the net radiation term, namely the surface reflected and emitted radiation may provide improvements for large scale estimates of evaporation.

2.4.3 Soil Moisture Availability

The issue of water availability is a major concern for agricultural and operational water management, in particular when extreme events occur such as drought. Historically, drought has been a common problem in the Prairie region of western Canada (Khandekar, 2004). The recent drought of 1999-2004, and particularly in 2001, had a major impact on agriculture, water resources, and the economy (Environment Canada, 2004). Soil moisture status becomes a critical limiting factor for estimating evaporation with the onset of prolonged dry periods and drought conditions. Estimating actual evaporation under these conditions requires the enforcement of hydrological continuity which complicates the modelling process and is an added source of uncertainty. During periods of reduced water availability and particularly under drought conditions, evaporation from the land surface may be greatly reduced but may also dominate the water balance.

From a hydrological modelling standpoint, soil moisture may be easier to characterize at a point than over large areas. Difficulties in accurately characterizing soil moisture patterns have been summarized by Western et al. (2002). A general problem is that soil moisture patterns are highly variable both spatially and temporally and often depend on the complexity of the landscape and soil texture. Subsequently, there is an inherent mismatch in spatial scales, namely, between soil moisture observations and the representative area over which they are needed. Further, near surface soil moisture is typically measured at a point using Time Domain

Reflectometry (TDR), or may be observed through remote sensing but the moisture status to rooting zone depths is largely unobserved. A dependency on soil moisture observations and various sampling strategies presents a problem for practical estimation of evaporation.

As a result, the spatial variation and characterization of soil moisture has received much attention in the past decade; particularly via statistical analysis techniques. Attempts at obtaining areal estimates from point scale values have been met with limited success. Grayson and Western (1998) have shown that time-stable moisture patterns may exist over limited areas within a catchment. These are partly controlled by topography, vegetation and soil characteristics and vary depending on the degree of wetting during precipitation events, and any lateral movement of near surface moisture. Yet, Teuling et al. (2006) have found that topographic wetness and leaf area indices which are useful hydrological indicators are poorly correlated to the mean spatial and temporal patterns of soil moisture.

Geostatistical techniques have also been applied to characterize spatial variations in soil moisture patterns. A standard statistical tool used for this purpose is the semivariogram which estimates the variance between successive points within a given area, as a function of the distance between them (Western et al., 1998a). The semivariogram can be used for identifying length scales over which hydrological characteristics may be considered similar. Western et al. (1998b), however, have shown that the seasonal structure of soil moisture can vary between wet and dry periods. Specifically, the correlation length (range) of soil moisture tends to be higher under dry conditions and lower under wet conditions and the respective ranges may also overlap. When they overlap, semivariograms are not able to distinguish between connected (wet) and unconnected (dry) patterns of soil moisture (Western et al., 1998a).

This is a major limitation which may be resolved only through more complex modelling functions (Western et al., 2001). Another limitation is that geostatistical techniques require a very large number of sampling points in relatively close proximity to obtain the true structure of a landscape. This makes geostatistical techniques better suited for site specific applications and also limits their transferability to other areas which may exhibit very different landscape characteristics.

2.4.3.1 Rooting Zone Depth

The availablity of soil moisture accessible by the root systems of plants has long been considered the main limiting factor affecting prairie grasses and crop yields (Weaver, 1925; Weaver, 1926; Weaver and Clements, 1938). From an ecohydrological perspective, knowledge of physiological characteristics of respective plant species is a key to estimating actual evaporation at a given location or region; this includes growth both above and below the ground surface. The magnitude to which evaporation is affected is generally dependent on physiological adaptations of the plant species to handle periods of water stress.

Extensive research on grasslands and crops and their rooting habits within the Great Plains by Weaver (1925; 1926) and Weaver and Clements (1938) indicate that short to mid height grasses typically root to depths of approximately 1 m to 1.5 m. Tall grass species can extend to depths of 2 to 3 m, and alfalfa (a legume) to greater than 4 m. The tendency for roots to be more concentrated in the upper layers or extend to greater soil depths often depends on initial moisture conditions. For example, Weaver and Clements (1938) found that under wetter conditions grasses and crops (including deeper rooting species) may root to realtively shallow depths since the availability of soil moisture is not a factor. Another consideration is that roots tend to die off under prolonged exposure to the reduced oxygen levels of saturated soil layers which can, in turn, adversely impact plant health. During drought conditions, they found that short to mid height grasses tend to invest more energy in increasing the area of their roots but extend their depth very little. Above ground the plant is typically dwarfed and may even go dormant, only to become revitalized when adequate moisture becomes available; whereas deeper rooting and tap rooted species can explore the soil to greater depths.

Plant roots and their distribution within the soil profile are also important with regard to the water storage potential of the soil (England, 1975). A review by Jackson et al. (1996) shows the largest fraction of roots for terrestrial plants and trees tend to be located in the upper layers of soil. They found that on a global average, 75% of the root profile is located in the top 40 cm of the soil. For grasses, 80% of the roots are within the top 20 cm to 75 cm of the soil but this also depends on plant species and biome. Therefore it is evident that plant root development and effective rooting depth are important factors when considering the soil moisture available to plants in the terrestrial environment. Unfortunately, measurements of soil moisture to the rooting depths of vegetation are either scarce or are unavailable within the Canadian Prairies.

2.4.4 Remote Sensing of Surface Properties

Remote sensing via ground, airborne and satellite-based instruments is a valuable tool for observing surface properties of hydrological or ecological importance. A major advantage of remote sensing is that spatial information can be measured directly and often over extensive areas. More importantly, a number of state variables (e.g. soil moisture, snow water equivalent, surface temperature) or even rainfall rates may be obtained over large areas (Engman and Gurney, 1991). Remote sensing techniques are based on measurements over the electromagnetic spectrum, and have become useful for estimating evaporation over large regions. Specifically, measurements at visible and thermal wavelengths can be used to observe continuous variations in landscape characteristics, and microwave wavelengths can provide observations of hydrologic state variables near the surface (Engman and Gurney, 1991).

Surface reflectance properties are obtainable over the visible to near-infrared wavelengths, 0.4 - 4 μm (Zoran and Stefan, 2006). Due to the influence of the atmospheric haze etc, corrections are typically needed to better interpret the surface reflectance values. Advanced methods of atmospheric correction tend to require detailed information about vertical profiles of water vapour and aerosol concentrations which may not be readily available. Alternatively, relatively more simple and accepted methods (e.g. Dark Object Subtraction) are available for reducing atmospheric influences (Liang, 2004). The portion of the spectrum from 4 to 14 μm contains the thermal wavelengths from which surface emitted longwave radiation may be obtained as a function of surface temperature. Various satellite based sensors covering portions of the visible and thermal wavelengths that are commonly used for this purpose include Landsat, AVHRR (Advanced Very High Resolution Radiometer), and MODIS (Moderate-resolution Imaging Spectroradiometer). Table 2.1 gives a general summary of the spectral range of measurements and their general applications.

Table 2.1: Summary of spectral range and applications; after Schultz and Engman (2000).

Wavelength	Application
Visible Light (450 – 700 nm)	Vegetation characteristics
Near and Middle Infrared (750 nm – 2.35 microns)	Surface inventory mapping (crops, water, ice, geology, etc.)
Far/Thermal Infrared (10 – 12.5 microns)	Temperature, moisture, vegetation class
Microwaves (1 mm – 24 cm)	Snow characteristics, water content (soil, vegetation), water boundaries

The vast array of remote sensing techniques (surface-based, aerial, and satellite) employ a variety of instruments that vary in spatial resolution, and frequency of observations made at the same location. A principle advantage of remote sensing based estimation methods is that spatial variations in key factors can be measured over large areas rather than at points alone. As such, evaporation estimates for daily periods may be obtained from spatially and temporally scaled parameters viz. assimilated remotely sensed images; typically one image per day and a set of surface and atmospheric data. This has resulted in the development of numerous remote sensing based methods for obtaining distributed evaporation estimates as discussed in reviews by Courault et al. (2005) and Gowda et al. (2008).

The first attempts at estimating evaporation from remote sensing data was done by calculating evaporation as a residual of the simplified energy balance as first introduced by Jackson et al. (1977). Subsequently, modifications to the method have been made by Seguin et al. (1989) and Bussières et al. (1997). The energy balance approach is of particular interest with respect to remote sensing given the response of surface targets to energy (Menenti, 2000). Resistance-based formulations have also been developed which consider plant controls on evaporation (Norman et al., 1995; Anderson et al., 1997; Boegh et al., 2002; Houborg and Soegaard, 2004; Anderson et al., 2007).

Purely empirical relationships have been used to correlate evaporation with derived surface variables; for example vegetation indices (Nagler et al., 2005). Several methods scale evaporation estimates based on the evaporative fraction, largely through solar radiation modelling as discussed by Colaizzi et al. (2006). The problem of estimating evaporation on a global scale via remote sensing information has also been addressed recently (Mu et al., 2007; Fisher et al., 2008). These global modelling studies have taken advantage of expert knowledge

and the wealth of data obtained via ecosystem observations collected through the eddy covariance based Ameriflux network which is part of the global Fluxnet network (Baldocchi et al., 2001).

A general limitation of most of these methods is that evaporation is estimated indirectly as a residual term of the energy balance or distributed largely on an empirical basis. Purely empirical methods lack a sound physical basis as well as transferability outside of the range of observations on which they are based. Estimates may also depend on the use of remote sensing images to estimate complex surface resistance terms needed for single and multilayer models. This can be problematic in that resistance terms also have high temporal and spatial variability. As a result, the relative increase in complexity can be an important limitation for the practical use of these models beyond areas where detailed surface measurements are available. A feedback method developed by Granger (2000) is capable of estimating evaporation directly from estimates of net radiation and the humidity deficit based on remotely sensed surface temperature observations but the regression equations may require recalibration on a site by site basis.

Many remote sensing approaches do share a commonality which is the physical principle on which such methods are founded. That is, the incorporation of distributed estimates of net radiation which governs surface energy and mass exchanges (Bisht et al., 2005). From an ecological perspective, landscape features and their associated land covers and biological attributes can exhibit spatial associations from which apparent patterns may be realized visually and analyzed statistically (e.g. Yates et al., 2006; Zhang and Guo, 2007). As such, similar information may prove valuable for evaporation modelling as regards the distribution of key parameters over the natural landscape. More specifically, observations at visible and thermal wavelengths can be used to derive surface reflected and emitted radiation components (back radiation to the sky) of the net radiation balance. These components are a function of two key variables, namely, surface albedo (α) and surface temperature (*Ts*).

2.4.4.1 Surface Albedo (*α*) and Surface Temperature (*Ts*)

The importance of surface albedo in surface-atmosphere energy exchanges and radiative transfer calculations in general, is well documented (Sellers et al., 1997a; Liang, 2000; Lucht et al., 2000; Roberts, 2001; Liang et al., 2003; Disney et al., 2004). Shortwave radiation reflected back to the atmosphere represents a large radiative loss which is unavailable for the process of evaporation.

Accurate determination of surface albedo from remote sensing data continues to be a considerable source of uncertainty (Yang et al., 2008). Variations in surface temperature also represent another important radiative loss and are used to determine differences in the amount of longwave radiation emitted from the surface based on the Stefan equation; which is a fundamental law of heat transfer calculations (Fishenden and Saunders, 1950).

2.4.5 The Role of GIS

The spatial data management, display and analysis capabilities of Geographic Information Systems (GIS) provide an important tool for incorporating the use of remotely sensed data (Mattikalli and Engman, 2000). This is particularly useful for the parameterizating of evaporation equations to distribute evaporation estimates over large areas. For example, available energy can be partitioned at the surface as a function of topography (e.g. elevation, slope and aspect etc), represented in a GIS by a Digital Elevation Model (DEM), and vegetation. The use of DEMs and maps showing distributions of land cover and important surface characteristics (e.g. albedo and roughness) could be used for examining the spatial variability of factors driving evaporation. GIS also offers the capability to perform large scale analysis quickly, thereby allowing for examination of relationships over a range of spatial scales (e.g. field to regional scales).

For example, Medina et al. (1998) used a combination of remote sensing information obtained over Spain and GIS to determine evaporation from crops and soil as the residual of the energy balance using the Surface Energy Balance Algorithm for Land (SEBAL). They found that the surface characteristics such as topography, soil and vegetation influenced the spatial variability of remotely sensed parameters used to determine evaporation. More recently, Diodato et al. (2010) examined the spatial and temporal changes of evaporation in a mountainous basin in southern Italy, using a water balance approach. For this purpose, they combined topographic and vegetation indices with the mapping and analysis capabilities of GIS to examine spatial and temporal trends of evaporation.

CHAPTER 3

STUDY DESIGN AND SITES

3.1 Overview of Study Design and Sites

The study is designed to address the three main objectives presented in Chapter 1 and considers some key issues discussed in the literature review. Specifically, the uncertainty in a selection of physically-based, point-scale evaporation models is examined during non-drought and drought conditions. Remotely sensed surface observations are assimilated into an evaporation model to examine the spatial variability of evaporation over a field sized area; a continuous hydrological modelling approach is applied to examine spatial and temporal variations in evaporation during a drought and non-drought period.

The Canadian Prairie region of Western Canada presents a natural laboratory for conducting this research. For example, drought is a major problem over the Canadian Prairies in general, and the impacts of the recent drought of 1999-2004 provided the impetus for the Drought Research Initiative (DRI) project to better understand the physical characteristics and processes contributing to drought in the Canadian Prairie landscape. The research conducted here contributes to the second objective of DRI which is to improve the understanding of physical processes influencing drought.

For research purposes the regional extent considered is limited to the Prairie ecozone specified by Marshall et al. (1996). The Prairie ecozone extends across the southern portions of all three Prairie Provinces and into the United States but the Canadian portion is only considered here. The Canadian portion of the Prairie ecozone extends over an area of approximately 435,000 km^2. Over half of this area (approximately 238,000 km^2) is bounded by a portion of the Palliser Triangle, a region characterized by semi-arid climate, centralized within the southern portions of Alberta and Saskatchewan, and extends south into the United States. The Palliser Triangle is named after Captain John Palliser who explored western Canada (British North America) from 1857-1860. The extents of the Prairie ecozone and the Palliser Triangle are shown in Figure 3.1.

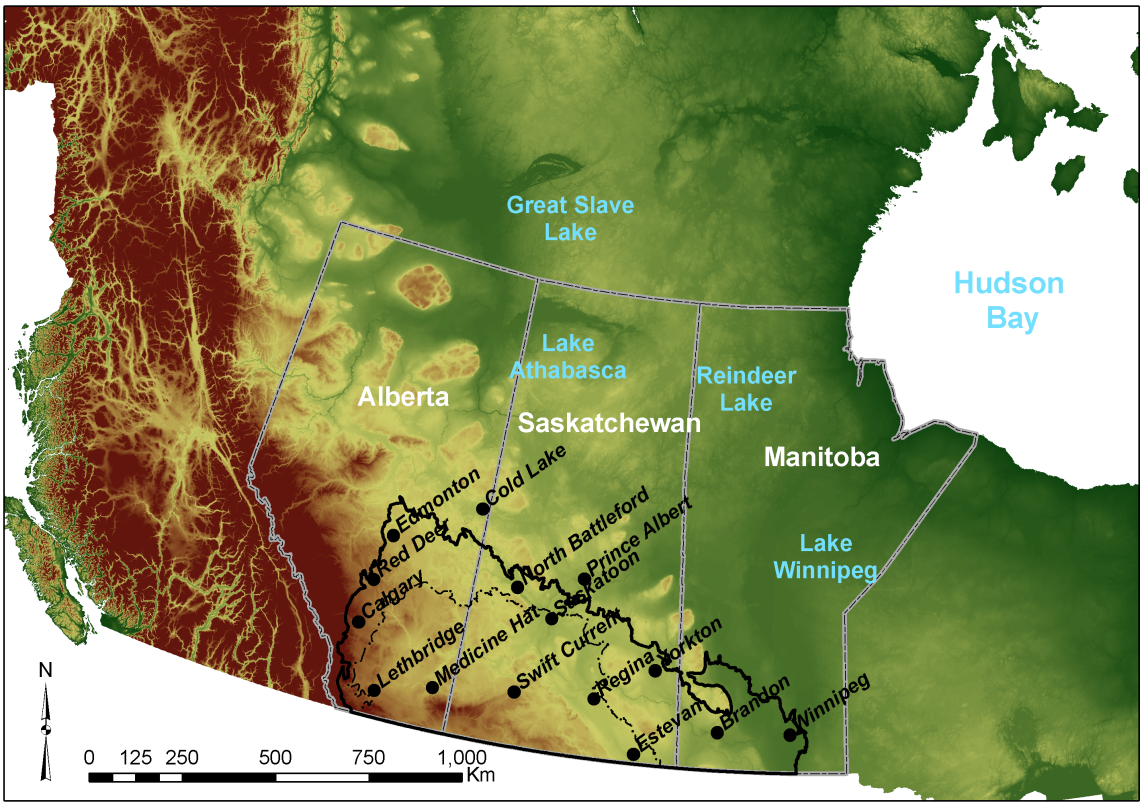

Figure 3.1: Map of Western Canada showing outlines of the Prairie ecozone (solid black line) and Palliser Triangle region (dashed black line) and locations of selected Environment Canada stations.

3.1.1 Palliser Triangle

This region has historical significance and is climatologically distinct compared to the mountain, coastal and northern regions of Canada, and warrants a brief discussion on its relevance to water resource problems. In 1863, Captain Palliser reported the region was too arid for agriculture purposes but indicated a belt of fertile land surrounded the Triangle extending to the west, north and east (Spry, 1959); despite this, settlements were established and cultivation across the region began.

Devastating droughts were experienced in the region during the early 1900's and more notably during the 1930's. Since then, the region has been more productive as a result of changes in agricultural practices, the establishment of major reservoirs, and technological advances. Nevertheless, the Palliser Triangle is typically the driest region of western Canada and periods of drought continue to impact the Prairie region as a whole (Khandekar, 2004). As such, there are

important differences between the climate conditions experienced within the Palliser Triangle area compared to the typical conditions observed outside the area. Maps of the 1971-2000 normal climate conditions for the growing season (May 1 – Sept 30) are provided in Figure 3.2. These maps were produced by interpolating (spline) the archived data of rainfall, air temperature, relative humidity (RH) and wind speed between the 15 Environment Canada stations indicated previously in Figure 3.1.

It is noted here that the horizontal distance between the stations is in the order of at least 100 km and greater, and represents a large scale generalization of the data between stations. The integrity of the station observations is maintained by using the spline interpolation method. With this in mind, Tobler's (1970) first law of geography may be invoked and more appropriately stated – in that the general climate conditions between adjacent stations are more similar than climate conditions between distant stations. This has relevance for mapping the observed large scale spatial patterns of the normal climate conditions over the region as a whole.

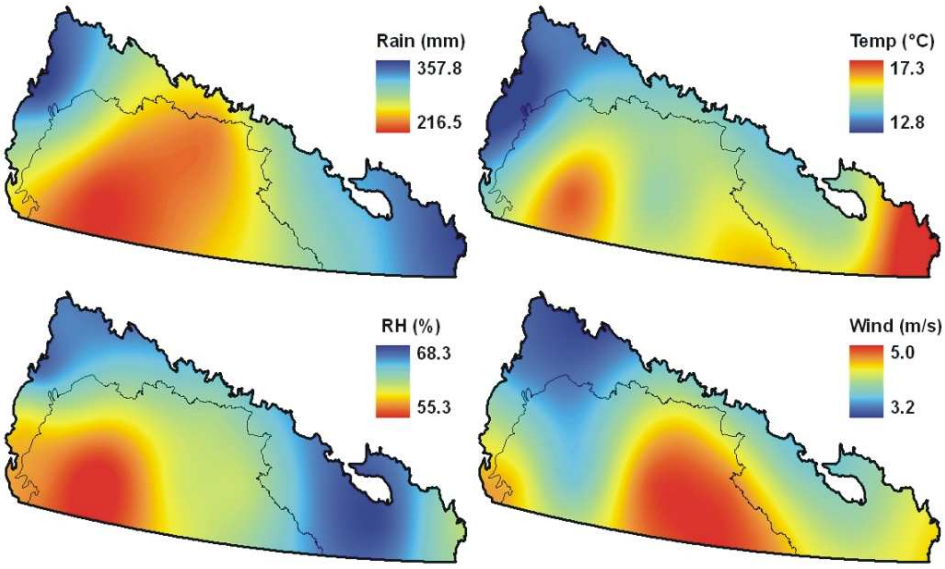

Figure 3.2: Maps showing the 1971-2000 normal climate conditions for the growing season (May 1 – Sept 30).

As shown in Figure 3.2, rainfall (mm) and RH (%) tends to be highest near the edges of the Prairie region and lowest in the southwestern portion of the Palliser Triangle in the area of Medicine Hat and Lethbridge. The pattern of air temperature shows a general trend, declining with both latitude and increasing elevation. Wind speeds, however, show a general increase from

the north to south and are highest in the south-eastern portion of the Palliser Triangle region in Saskatchewan around Swift Current, Regina and Estevan.

3.1.2 Local and Regional Scale Modelling

An examination of the variability of evaporation during drought and non-drought periods was undertaken within the Prairie region to improve the understanding of drought related processes and surface-atmosphere interactions at local and regional scales. For this purpose, a point scale evaporation algorithm was applied to characterize and better understand variations in evaporation at local and regional scales across the Prairie region. Long term archived climate observations available at several locations across the Prairies were used as forcing data for long term continuous model simulations presented in Chapter 7.

The accuracy of selected physically based models for estimating evaporation were examined at two "point" locations where surface and climate reference and eddy covariance observations of evaporation were either collected during a field study or obtained as archived data. The physically-based models selected were outlined previously in the literature review, namely the Penman-Monteith (*P-M*), Granger and Gray (designated *G-D* herein) and the Dalton-type bulk transfer (*BT*) models. In 2006, measurements of evaporation were collected at the St. Denis National Wildlife Area (SDNWA) during a field study for this research; these measurements were collected during a non-drought year. Archived climate data and measurements of evaporation for two drought years (2000 and 2001) at Lethbridge Alberta, collected as part of the AmeriFlux observation network, were provided by Larry Flannigan (University of Lethbridge); discussed in section 3.2.3. Results of the point scale studies at SDNWA and at Lethbridge are presented in Chapter 5.

In 2007 surface reference and remote sensing data collected at the SDNWA were used to examine the spatial variability of evaporation over a field sized area. In this case, one-time-of-day visible and thermal remote sensing images were assimilated into an evaporation model and a method of deriving distributed estimates of daily evaporation was developed. Model developments and results are presented in Chapter 6.

3.2 Study Sites

3.2.1 Environment Canada Stations

Archived data for the 15 Environment Canada stations (Figure 3.1) were used for continuous modelling simulations applied at each location for which the results are presented in Chapter 7. These stations were selected because they provide the most complete sets of long term observations in the Prairie region which can be used as model input data. Specifically, they have continuous observations of hourly temperature, humidity, wind speed, and daily observations of precipitation (snowfall and rainfall) over a period of 46 years (1960-2005) which were used to drive a hydrological model. The archived data were obtained through the Data Access Integration (DAI) system maintained by Environment Canada.

3.2.2 St. Denis National Wildlife Area (SDNWA)

The St. Denis National Wildlife Area (SDNWA) was chosen as a field study site for both its accessibility as a federally regulated research area and its representativeness of land uses and landscapes occurring over much of the Prairie region of Western Canada. Since its establishment in 1967, a wealth of agricultural, hydrological, and wildlife related research has been conducted at the SDNWA primarily by branches of Environment Canada located in Saskatoon, Saskatchewan (e.g. Canadian Wildlife Service and National Hydrology Research Centre) and various departments at the University of Saskatchewan (e.g. Soil Science, Biology, and Centre for Hydrology).

The SDNWA is located 40 km east (52°12′ N 106°5′ W) of Saskatoon, Saskatchewan, Canada. Elevations within the SDNWA range from approximately 540 m to 565 m (Figure 3.3) and up to 593 m outside the area to the north. The landscape is characterized by moderately rolling knob and kettle moraine surrounding many wetlands. Slopes are typically gentle (< 6%) although they can be as much as 20% or more leading down to large wetland areas. Soils are classified as Dark Brown Chernozem which are generally fine textured (silty loams) with parent materials consisting of clay-rich glacial tills (van der Kamp et al., 2003). Land cover varies from cultivated land to wetlands, grassland and woodland. Some wetlands are surrounded by grass and shrubs fringes and others by stands of trembling aspen.

3.2.2.1 Reference Sites

A field campaign was conducted at the SDNWA during the May – September growing period of 2006 and 2007. Possible locations for establishing eddy covariance measurement sites at the SDNWA are limited due to the complexity of the landscape and diversity of the land covers encountered. As such, the potential influence of large ponds and willow and aspen bluffs on turbulent flux measurements was taken into consideration. Micrometeorological and eddy covariance observations collected during the summer period of 2006 and 2007 were used for the purpose of model parameterization, development and validation.

Observations during 2006 were used to parameterize and evaluate the *P-M*, *G-D* and *BT* models to examine their accuracy in the prairie landscape over a mixed-grass surface which is presented in Chapter 5. Data were collected during the growing season period of May 19 – Sept 11. Observations during August 5, 2007 were used for developing a data assimilation method for distributing evaporation estimates over a field size area as discussed in Chapter 6. Eddy covariance measurements obtained at the same time allowed for comparisons of the accuracy of modeled results and validation of the models.

3.2.2.2 Upland Grass Site

For the 2006 field season, an upland area was selected for installing a micrometeorological station with a full suite of radiation balance and eddy covariance instruments. The data collected were subsequently used for model parameterization and validation purposes. The upland area is quite extensive and the terrain is relatively flat (slopes < 2%). The upland is surrounded by large ponds in lower valley areas indicated in Figure 3.3. The upland is characterized by small wetlands and a distinct contrast in vegetation types can be observed from the aerial view provided in Figure 3.4. Environment Canada leases the western portion of the upland to local farmers for agricultural purposes. In 2004 the eastern portion of the upland was seeded to a mixture of cool season grasses (Yates et al., 2006). In 2006 the most dominant species included several wheat grasses (*Agropyron elongatum*, *intermedium* and *trachycaulum*) and two forage crops, alfalfa (*Medicago sativa*) and sainfoin (*Onobrychis viciifolia*). Over the season some of the grasses grew to a maximum height of 1.2 m but on average were measured to be approximately 1 m tall.

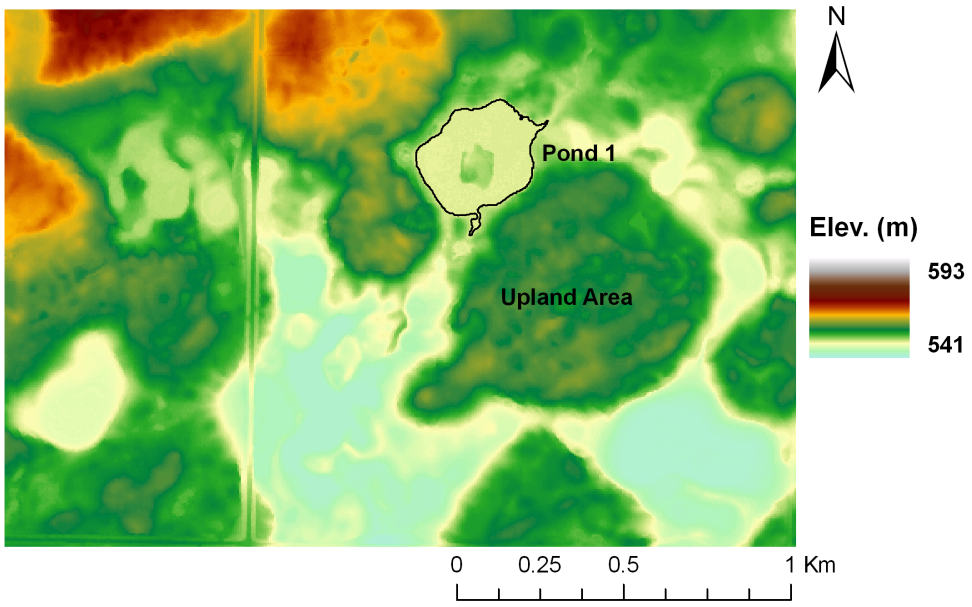

Figure 3.3: LIDAR DEM of SDNWA showing the locations of the upland area and pond 1 outlined.

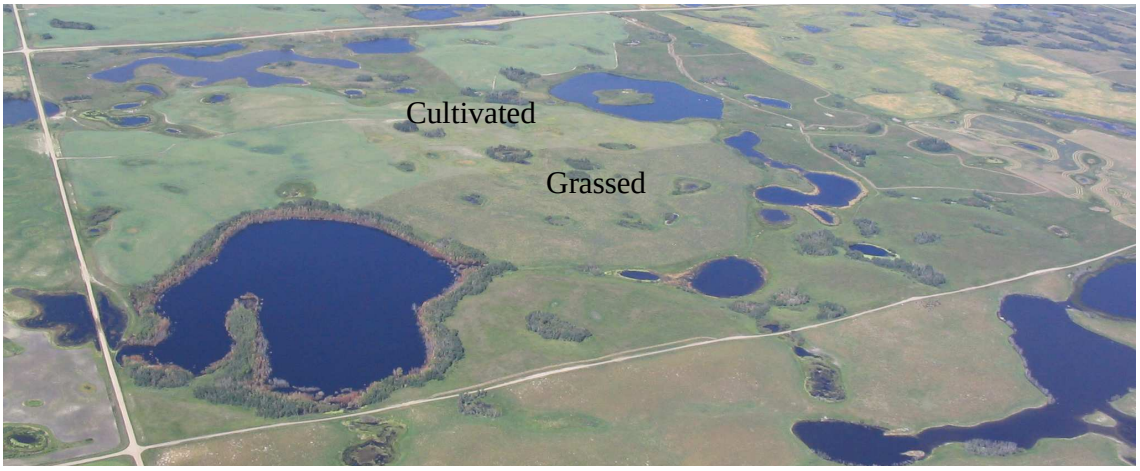

Figure 3.4: Photograph of SDNWA and area during August 5, 2007.

Instruments

A list of instruments installed during the measurement period and subsequently used for research purposes in Chapter 5 is provided below. The details of the instrument models and use (variable measured, and instrument height or depth in soil) is as follows:

- Kipp and Zonen CNR1 (incoming, ↓, and outgoing,↑, radiation fluxes, 1.35 m)

- Campbell Scientific CSAT3 (horizontal and vertical wind fluxes, and heat flux, 2.5 m)
- Campbell Scientific KH20 (atmospheric water vapour fluxes, 2.5 m)
- Exergen (IRTC) Infrared Thermocouple (surface temperature, 1.15 m)
- Campbell Scientific HMP45C212 (air temp. and RH, 2.15 m)
- Radiation and Energy Balance (REBS) HFT3 (ground heat flux, 10 cm)
- Campbell Scientific CS616 (volumetric water content, 30 cm probe vertical insertion)

A photo of the instrumentation is provided in Figure 3.5. Measurements were collected and stored using a Campbell Scientific 23x data logger. The sampling rate for eddy covariance measurements was 10 Hz (0.1 sec) and 0.2 Hz (5 sec) for all other instruments. Sampled data were recorded as averages at 15 minute intervals. The CNR1 and IRTC were installed approximately 10 m away from the main mast but were placed over similar vegetation with similar ground coverage as the grasses measured by the eddy covariance instruments.

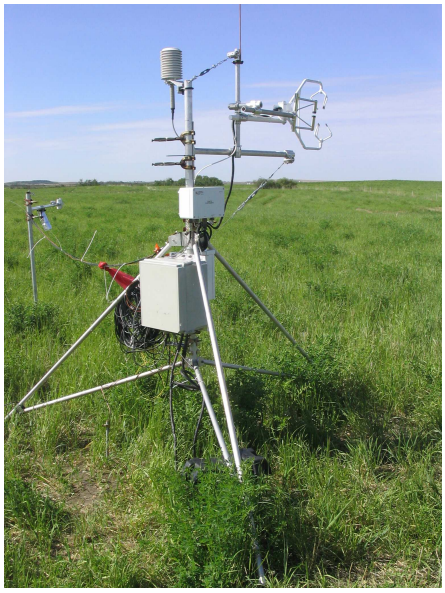

Figure 3.5: Photograph of fixed station at upland grass site (June 2006).

Site Characteristics

As shown in Figure 3.6, the station was placed so the unobstructed fetch was approximately 100-200 m in all directions. The CSAT3 sensor head was oriented in the X direction giving a fetch length of 135 m to the leading edge of the grass-cultivated boundary. The wetland/bluff at the

top of the image was not considered to be an obstacle because the tops of the trees were approximately level with the terrain on which the station was located. The difference in elevations between the sites is approximately 2.5 m.

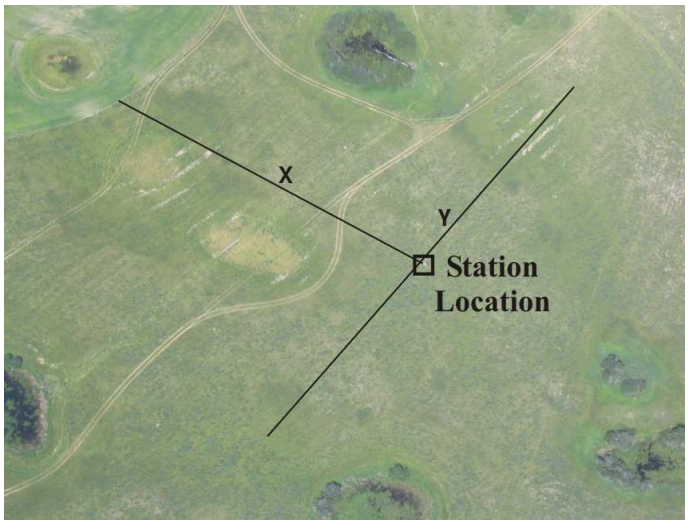

Figure 3.6: Photograph of station location and general fetch conditions.

Portable Eddy Covariance System

A portable eddy covariance (EC) system was also placed at fixed locations within the SDNWA for extended periods. To reduce the disturbance within the study area, placement of the portable system was limited to the edge of a bare soil shortly after cultivation in June and the edge of a growing crop starting in July. The purpose of these measurements was to examine variations in observed evaporation between different land surface types over the course of the growing season. Some general observations of differences between measured evaporation from the mast and the reference site are provided in Appendix A. The portable EC mast was equipped with the following instruments:

- Campbell Scientific CSAT3 (horizontal and vertical wind fluxes, and heat flux, 2.5 m)
- Campbell Scientific KH20 (atmospheric water vapour fluxes, 2.5 m)
- Exergen (IRTC) Infrared Thermocouple (surface temperature, 1.15 m)
- Campbell Scientific HMP45C212 (air temp. and RH, 2.15 m)

Transect Observations

Surface and climate data were also collected from a series of transects over the growing period in 2006. This was done using a portable mast constructed from a metal pipe that was fixed to a camera tripod as shown in Figure 3.7. The mast was fitted with a hand held Omegaette HH311 series data logger and temperature and humidity probe. The instrument is capable of measuring air temperature, relative humidity with a Vaisala probe and surface temperature with an Exergen (IRTC) Infrared Thermocouple. A portable TDR (Time Domain Reflectometry) system equipped with a 20 cm probe was also used during observation periods. Transects covered a variety of surface types and landscape features and ranged from 100 m to 200 m in length; observations were collected at points spaced 5 m apart. Between 60 and 90 minutes was typically needed to sample a single transect. Some general observations based on the transect measurements are provided in Appendix A.

Figure 3.7: Photograph of the portable mast used for collecting observations along transect points in 2006.

3.2.2.3 Pond 1 Sites

In 2007, focus shifted to the simultaneous measurement of water vapour fluxes occurring from a pond and land surface respectively. The largest pond at the SDNWA (pond 90) is surrounded by a stand of tall, dense aspen and was therefore unsuitable for land based eddy covariance measurements. Pond 1 (Figure 3.3 and 3.8) was better suited than others because it has a reasonable fetch length across an unobstructed portion of the pond. Pond 1 is also characterized by grass fringes where eddy covariance stations could be stabilized. The grasses around these sites are also tall growing to a maximum height of 1 m by late June. From the edges of the pond, two locations have relatively flat terrain with fetches of 50 - 75 m leading toward gentle slopes at first and then much steeper slopes. These sites are near opposite edges of pond 1 and allowed for simultaneous land and open water measurements depending on the wind direction. The direct distance between these stations is approximately 275 m.

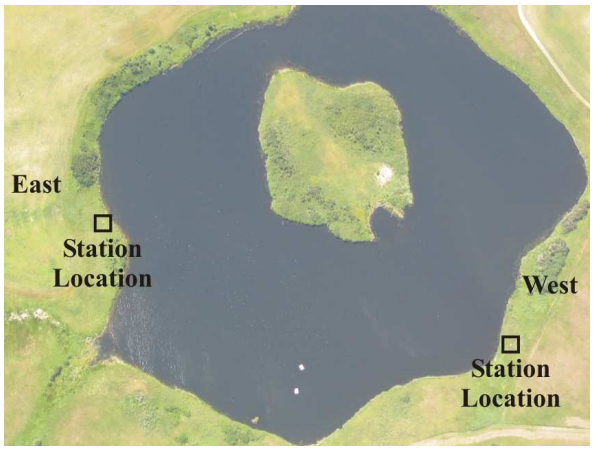

Figure 3.8: Photograph of pond 1 and location of eddy covariance stations (Aug, 2007).

Instruments

A list of instruments installed at both sites during the measurement period and subsequently used for research purposes in Chapter 6 is provided below. Where possible, the same instruments used in 2006 were also used for 2007 at the pond 1 sites. To ensure measurements were comparable between the sites, the same instrument models were installed at each station. Details on instrument models and use (variable measured, instrument height or soil depth) are as follows:

- Kipp and Zonen CNR1 (↑↓ radiation fluxes, 1.35 m)

- Campbell Scientific CSAT3 (horizontal and vertical wind fluxes, and heat flux, 2.5 m)
- Campbell Scientific KH20 (atmospheric water vapour fluxes, 2.5 m)
- Exergen (IRTC) Infrared Thermocouple (surface temperature, 1.15 m)
- Campbell Scientific HMP45C212 (air temp. and RH, 2.15 m)
- Radiation and Energy Balance (REBS) HFT3 (ground heat flux, 10 cm)

A photo of the instrumentation at both locations is provided in Figure 3.9. Measurements were collected and stored using Campbell Scientific 23x data loggers. The program used in 2006 was also used for the 2007 season and data were recorded as averages at 15 minute intervals. At the site on the eastern edge the CNR1 and IRTC were installed several metres away from the main mast. At the site on the western edge, the IRTC had to be mounted to the main mast while the CNR1 was installed several metres away. At both locations the CNR1 was placed well away from the pond edge so that the field of view was limited to the grassed surface alone.

Figure 3.9: Photographs of stations located at opposite edges of pond 1 (Aug, 2007). Left: East side, Right: West side.

3.2.3 Lethbridge AmeriFlux Short Mixed Grass Site

The Lethbridge AmeriFlux site was chosen because archived climate data were available for examining evaporation under drought conditions within the Prairie landscape. Fortunately, the archived data included measurements of evaporation for two major drought years during the focal years of the DRI project, 1999-2004. In 2000 and 2001, Lethbridge experienced a severe drought which significantly affected plant growth and evaporation rates during the growing

season (Flanagan et al., 2002; Flanagan and Johnson, 2005). This presented an opportunity to examine evaporation estimation methods and the effects of rooting zone depth under drought conditions as presented in Chapter 5.

The AmeriFlux grassland site is located in southwest Alberta at approximately 49°43′ N 112°56′ W (Richardson et al., 2006). Wever et al. (2002) and Flanagan et al. (2002) indicate the site is relatively flat with dark-brown chernozem soils that are clay loam to clay in texture. Vegetation is comprised of short to mid height grasses and forbs which include thickspike and western wheatgrass (*Agropyron dasystachyum* and *Agropyron smithii*), needlegrass (*Stipa comata*) and blue grama grass (*Bouteloua gracilis*).

The Lethbridge grassland site contributes observations to a much larger biospheric global monitoring network (FLUXNET). The object of the networks is to better understand water, energy, and carbon fluxes obtained using eddy covariance, remote sensing and in situ measurement techniques (Running et al., 1999). A comprehensive overview of FLUXNET objectives, monitoring sites and data availability has been provided by Baldocchi et al. (2001).

CHAPTER 4

EVAPORATION MEASUREMENT AND MODELLING CONSIDERATIONS

4.1 Eddy Covariance Method

Observations of actual evaporation obtained for this research are based on the eddy covariance technique. This is the most direct method of measuring turbulent fluxes of water vapour, heat, and momentum over natural surfaces (Brutsaert, 1982; Oke, 1992). The basic principle of eddy covariance is that the turbulent flux of a scalar quantity such as water vapour (also heat and CO_2) is obtainable from the covariance between the vertical wind component, w and the water vapour concentration, q (Munn, 1961),

$$E = \rho \overline{w'q'} \quad , \tag{4.1}$$

where ρ is the air density. The overbar denotes the mean values obtained over a sufficient time period to allow the passage of many eddies or parcels of air transporting heat and water vapour between the surface and atmosphere. The primes indicate the instantaneous fluctuations from the respective means. Swinbank (1951) was the first to provide a practical demonstration of the measurements and manual calculations needed for the eddy covariance method. Taylor and Dyer (1958) later improved upon the method by developing a prototype instrument to automatically carry out the needed measurements and analog mathematical operations.

The instrumentation requirements for eddy covariance measurements are critical to capturing the vertical wind component and scalar concentrations of rising and sinking air parcels (Lee et al., 2004a). The current state-of-the-art is such that eddy covariance instruments are capable of high frequency sampling (e.g. 10 Hz or 10 samples per second) which is required for measuring small eddies. Sensor placements and their respective orientation for measuring the wind components are also critical for obtaining unbiased measurements of the vertical flux component. As such, the data collected are potentially subject to a variety of errors that require consideration. In other words, quality control of the data is an essential step to ensuring the relative accuracy of the method. The literature does not outline a set series of steps for correcting

potential errors in flux data. In fact, depending on the general site conditions, reliability of the instrumentation and overall setup, some flux corrections may not be required (Lee et al., 2004a).

Foken et al. (2004) discuss various techniques employed for identifying errors (automated methods within the program and manual inspection) and approaches to assessing or correcting errors associated with electronics and instrumentation problems and setup. In general, biased flux estimates resulting from sensor orientation, and data spikes (or large changes in the amplitude of the measurement) due to instrument or electronic problems and meteorological conditions (e.g. water droplets on the transducer of a sonic anemometer) are two common sources of error encountered when applying the eddy covariance method. Foken et al. (2006) have also identified the problem of energy balance closure as a continued source of uncertainty as regards flux measurements in the eddy covariance method. The residual of the energy balance is often considered as a check against the relative quality or accuracy of eddy covariance fluxes, where a residual of 10 - 20% is considered to be acceptable.

To this point, a general consensus on the underlying cause of discrepancies in the energy balance is lacking. However, Foken et al. (2004) and Foken (2008) refer to measurement issues related to different sensors as well as their respective footprints, scale issues, and in other cases there have been no identified sources for the lack of closure. One aspect of the eddy covariance method that is certain is the need for applying a coordinate (or axis) rotation to the horizontal and vertical flux components to correct the data for sensor tilt errors. Lee et al. (2004b) identify the planar-fit method of Wilczak et al. (2001) as a generally accepted method used for this purpose. The basic principle of the method is that the instrument coordinates upon which the horizontal and vertical velocity measurements are made, are rotated into a set of planar-fit coordinates.

The steps for performing the axis rotation are provided in Lee et al. (2004b) and are restated here:

- The z-axis is fixed over a specified observation period;
- A tilted plane (or mean streamline plane) is defined based on a regression of the mean velocity components obtained in the instrument coordinates;
- The regression coefficients are used to determine the angles for the rotation from the instrument coordinates to the planar-fit coordinates;
- The data are transformed into the new system.

This procedure results in the z-axis being perpendicular to the mean streamline and the mean vertical velocity is equal to zero which eliminates measurement bias due to possible sensor tilt. Errors associated with axis tilt, however, tend to be more pronounced over sloped surfaces as result of levelling of the sensor head

4.1.1 Measurements at St. Denis

During the 2006 and 2007 field seasons at the SDNWA, a Campbell Scientific CSAT3 and Campbell Scientific KH20 sensor were used to measure the vertical wind speed component and humidity needed for calculating water vapour fluxes. The CSAT3 is a three dimensional sonic anemometer that measures horizontal and vertical wind speed fluctuations. The CSAT3 consists of a single anemometer head with a vertical measurement path length of 10 cm and horizontal path length of 5.8 cm. Wind speed fluctuations are obtained from three pairs of nonorthogonally oriented transducers which emit and receive an ultrasonic signal. These are transformed into the orthogonal wind components U_x, U_y, U_z in reference to the sensor head.

The KH20 is a krypton hygrometer that measures fluctuations in atmospheric water vapour density. The sensor consists of a krypton lamp that emits ultraviolet light at 123.58 nm and 116.49 nm of the electromagnetic spectrum respectively which is absorbed by water vapour. The water vapour density is obtained as a function of the absorption coefficient, the path length of the emitted light and the signal output of the sensor. Water vapour fluxes collected at the SDNWA were corrected for any tilt of the CSAT sensor head relative to the surface using the planar-fit axis rotation and correction algorithm of Wilczak et al. (2001) as discussed above. A Webb-Pearman-Leuning (WPL) (Webb et al., 1980) correction for density fluctuations due to temperature and water vapour was not applied as changes in the flux density were found to be negligible on a daily basis over the study period, and was a maximum of 4 W m^{-2} during the blooming period. Given that 28.57 W m^{-2} day^{-1} is required to evaporate 1 mm of water the associated error is a maximum of ± 0.14 mm.

4.2 Evaporation Modelling and Parameterization

An important component of this research is the modelling of actual evaporation from grasses during growing season snow free periods using physically-based algorithms. This may or may

not require the need for soil moisture accounting depending on the general climate conditions. Under relatively normal to wet conditions it is possible to obtain reasonable estimates of actual evaporation without imposing soil moisture limitations from deeper layers (Chapter 5). During periods of drought induced water stress, however, soil moisture status is a critical factor and requires an enforcement of hydrological continuity (Chapter 5). For remote sensing applications, the status of soil moisture at depth is a difficult problem that can be circumvented using the *G-D* feedback model which can moderate evaporation as a function of the drying power of the atmosphere and available energy supply (Chapter 6). In the case of continuous modelling over several years, cold season processes such as blowing snow redistribution, sublimation and infiltration into frozen soils impact spring soil moisture recharge and can be modelled along with the summer processes using a selection of process based algorithms (Chapter 7).

4.2.1 Cold Regions Hydrological Model Platform

The Cold Regions Hydrological Model (CRHM) platform contains a suite of physically-based algorithms describing important hydrological processes that are typical of cold region, northern environments (Pomeroy et al., 2007). CRHM is highly flexible allowing for the alteration of existing algorithms or addition of new ones to address specific modelling problems. This is an attractive feature not typically found in most hydrological models. Models are assembled in CRHM by linking a series of process specific algorithms. For example, moisture limited rates of actual evaporation may be obtained during the growing season by assembling a model that includes evaporation, infiltration, runoff generation, and soil moisture accounting. Extensive field investigations have been the basis for developments of specific algorithms. A comprehensive overview of the model has already been given by Pomeroy et al. (2007). As such, a few topics relevant to this thesis are briefly discussed here.

CRHM treats spatial arrangements of elements in a basin as hydrological response units (HRU). An HRU represents a single biophysical landscape unit with a distinct set of parameters, location in a flow network and driving meteorology. Energy and mass balances are applied to each HRU independently and the interaction between HRU units through water and energy exchanges is calculated at discrete time steps. A landscape unit that does not contribute surface or sub-surface runoff to a particular stream or river is also considered a valid HRU. This makes

the CRHM platform and assembled hydrological models relevant for use within the Canadian prairie region where large areas are non-contributing to stream flow. A variety of observations can be used as input data where available (e.g. solar or net radiation, climate data, soil moisture etc.). CRHM also offers empirical relationships and standard modelling techniques to supply the needed forcing data when observations are lacking.

For example, with the exception of field research studies, incoming solar radiation and net radiation, and soil moisture to the depth of the rooting zone are seldom measured in Canada. As a result, simple techniques are often needed to model surface energy and mass balances. The major component of the surface energy balance is incoming solar radiation. This can be determined from the extraterrestrial solar radiation and atmospheric transmittance which is estimated as a function of the daily range of air temperature and altitude (Annandale et al., 2001; Shook and Pomeroy, 2010). In turn, the surface balance of net radiation can be calculated from the estimated incoming solar radiation and an empirical relation between air temperature, vapour pressure and sunshine hours.

Evaporation can be computed with or without continuity. When continuity is enforced, evaporation is limited to that water available as interception, depressional storage, near-surface soil moisture or rooting zone soil moisture. For simplicity interception storage has not been considered. When soil moisture becomes severely limiting further restrictions are applied depending on the general soil texture (sand, loam and clay). The moisture limitations are simple functions based on the developments of Zahner (1967) and modifications by Leavesley et al. (1983). This approach requires that the soil wetness ratio, R_θ, be calculated. R_θ is the ratio of current soil moisture, θ, to maximum water holding capacity of the soil, θ_{max}.

The functions indicate that at certain fractions of available soil water step changes in actual evaporation occur. Under moist conditions soil moisture tension is low and moisture may be depleted at the rate, E or the direct estimate of the actual evaporation rate. For example, when R_θ is above 0.67 (67%) for a clay-loam soil the calculated actual evaporation, E_L, (e.g. Eq. 2.11 or 2.12) can meet the atmospheric demand,

$$E_L = E \quad , \tag{4.2}$$

where E_L is the moisture limited rate.

As the fraction of available soil water falls to between $0.67 > R_\theta > 0.33$ under drying conditions, moisture tension increases and soil water depletion becomes restricted. The effects of this moisture stress on E_L can be described as a linear function of the fraction of available water content and is calculated as,

$$E_L = R_\theta E \quad . \tag{4.3}$$

Finally, when the fraction of available soil water becomes critical under severely drying conditions (e.g. drought) and $0.33 > R_\theta$, soil moisture tension increases more rapidly. At this stage, soil water depletion becomes severely restricted and E_L is greatly reduced and is estimated as,

$$E_L = 0.5 R_\theta E \quad . \tag{4.4}$$

4.2.1.1 Evaporation Parameters

Vapour Transfer Function, *f(u)*

The *G-D* method requires an estimate of the vapour transfer function, *f(u)* to parameterize the drying power of the air; $f(u)(e^*_a - e_a)$. Thom and Oliver (1977) have shown that Penman type formulas need to consider the surface roughness which can lead to enhanced evaporation. CRHM employs an experimentally derived vapour transfer function which has reportedly worked well for a variety of surface types and general surface conditions encountered in western Canada (Granger and Pomeroy, 1997; Granger, 1999),

$$f(u) = 8.19 + 0.22 z_0 + (1.16 + 0.08 z_0) u \tag{4.5}$$

where z_0 = h/7.6 is the aerodynamic roughness length (cm), h is vegetation height (cm), and u is the wind speed (m s^{-1}).

Aerodynamic Resistance

Application of the *P-M* and *BT* equations to non-saturated surfaces requires consideration for the resistances of water vapour transfer to the atmosphere. Estimates of the aerodynamic resistance are obtained assuming a standard logarithmic wind profile formulation;

$$r_a = \frac{\left[\ln \frac{(z-d)}{z_0}\right]^2}{k^2 u} \tag{4.6}$$

where u is the wind speed at the reference height, z, d = 0.67h, is the displacement height of the vegetation (m), and k is the von Kármán constant (0.41).

Canopy Resistance

Introduction of the canopy resistance concept used for describing the diffusion path length of vegetation was due to the efforts of both Penman and Monteith (Lhomme, 1991). According to Bougeault (1991) there has been a general acceptance that the canopy resistance parameterization depends on several factors as described by Jarvis (1976). These factors are a minimum resistance, the amount of incoming solar radiation, water availability to plant roots, the atmospheric humidity deficit, and air temperature. Where estimates of evaporation were obtained using the Penman-Monteith and Dalton-type bulk transfer methods, estimates of the canopy resistance were derived using the general approach proposed by Jarvis (1976). The method treats canopy resistance as a series of multiplicative factors describing environmental stress effects on stomatal control,

$$r_c = r_{c\min} f_1 f_2 f_3 f_4 \tag{4.7}$$

where $r_{c\min}$ represents the minimum unstressed canopy resistance (s m^{-1}). There is no generally accepted approach to estimating the factors as they are typically derived from correlation and regression analysis, or on a more theoretical basis. Formulas for calculating the resistance term and contributing factors can be found in Bougeault (1991). For this research, the factors were estimated using equations based on the experimental relationships found in Verseghy et al. (1993). These relationships were chosen in part due to their ease of application, field observations could be provided for calculating the factors, and they require no additional parameters that may need to be calibrated. As another option, Verseghy (2008) has more recently provided an alternative formulation for the resistance and contributing factors which includes several parameters that need to be set depending on vegetation category.

The multiplicative factors used here describe stomatal control as a representative value of 1 for what may be considered optimal conditions for plant growth, and a value > 1 for less than optimal conditions. f_1 increases under conditions when light is limiting, and is a function of the incoming solar radiation, K↓ (W m^{-2}) required for photosynthesis,

$$f_1(K\downarrow) = \max(1.0, (500 / K\downarrow - 1.5)) \quad . \tag{4.8}$$

f_2 is a function of the vapour pressure deficit, $\Delta e = e^* - ea$, (mb) required to maintain water and nutrient uptake to the plant, which increases as the plants ability to transmit water from the soil rooting zone is exceeded,

$$f_2(\Delta e) = \max(1.0, (\Delta e / 5.0)) \quad . \tag{4.9}$$

f_3 is a function of soil moisture supply, specifically the soil moisture tension to the depth of the soil layer considered, ψ (m) which increases with decreasing soil moisture,

$$f_3(\psi) = \max(1.0, \psi / 40.0) \quad , \tag{4.10}$$

where ψ is derived using the Campbell power law function for specific soil texture classes based on the air entry tension ψ_{ae}, porosity ϕ, a pore size distribution index, b and soil moisture, θ (Campbell, 1974),

$$\psi = \psi_{ae}\left(\frac{\phi}{\theta}\right)^b \quad . \tag{4.11}$$

f_4 is a function of temperature with an operating range between 0 and 40 °C

$$f_4(T) = 1.0 \quad \text{if } t < 40\ °C \text{ and } > 0\ °C \tag{4.12}$$

OR

$$\text{if } T > 40\ °C \text{ or } < 0\ °C \quad \text{then } f_4(T) = 5000 / r_{cmin} \ ,$$

and indexes the range of temperatures at which transpiration may be considered to occur. The range of operating temperatures indicated above were not a factor in the current analysis since

the observed daytime air temperature rarely fell below 5 °C and seldom were above 30 °C during the observation period.

4.2.1.2 Plant Available Water Holding Capacity of Soils

The general soil module (Pomeroy et al., 2007) used in CRHM treats the soil column on a conceptual rather than physical basis. As such, only the field capacities of the recharge and soil column need to be set. This is advantageous for testing soil-vegetation interactions and diagnostic assessments of model behaviour. A potential limitation, however, is that known water holding characteristics for various soil textures are not considered. This has implications for evaporation modelling in that specifying unrealistic water holding capacities can result in excessive amounts of available water, or conversely, too little. Considering experimentally derived values may be useful for imposing physical limits on the water holding capacities of soils.

For the purpose of this research, the problem was approached from a plant growth perspective. That is, water holding capacities can be expressed based on the maximum water available for use by plants for a given soil texture. The general assumption is that the plants can only use a certain portion of the soil water depending on the rooting zone depth and soil characteristics. The soil moisture available to the plants is taken to be the difference between the maximum plant available water holding capacity and the permanent wilting point. This is consistent with the conceptual approach of the soil module used in CRHM. However, physical limits on the maximum holding capacity and wilting point can be imposed. For this purpose a look-up table was developed for specific soil textures from reported depths of available water per meter of soil given by the U. S. Department of Agriculture (1955) and Scherer et al. (1996). The maximum plant available water is then set by specifying the desired rooting zone depth and the soil texture. For example, for a clay-loam soil with a rooting zone depth of 1 m, the maximum capacity is taken to be 367 mm and wilting point is 150 mm; 167 mm of soil moisture is available for plant use.

Another possible treatment would be to approach it from a soil physics perspective. That is, pedotransfer functions or empirical relations have been developed to estimate the water retention soil properties from soil survey data. This includes the need for data such as bulk density, porosity and percent sand, silt and clay (if and where available). Basically, the purpose of a

pedotransfer function is to use the existing information to estimate parameters that are more difficult or time consuming to obtain. These functions are more commonly used for estimating saturated hydraulic conductivity but have also been developed for estimating field capacity and permanent wilting point (Wösten et al., 2001; Cemek et al., 2004; Parasuraman et al., 2007). A general limitation of this method is that the empirical pedotransfer relations are often only valid under conditions for which they are developed.

4.2.1.3 Soil Infiltration Capacity

Consideration was also given to the infiltration rates of soils in CRHM which is represented by the Green-Ampt equation (Green and Ampt, 1911). Specifically, a concern is that the saturated hydraulic conductivities, and in turn, the estimated infiltration rates for given soil textures are potentially low where actively growing vegetation might occur. The general assumption is that vegetation, litter and roots should effectively increase the infiltration capacities of typical prairie soils (e.g. agricultural and pasture land). A lack of consideration for the influence of vegetation on infiltration rates can lead to a large portion of rainfall forming runoff which typically is not the case in prairie environments. General exceptions to this are spring melt runoff over frozen soils as observed at the SDNWA, or excessive rainfall coupled with saturated soils (e.g. the summer of 2010).

The assumption on the potential effect of vegetation on infiltration is supported by results of field research conducted by Hutten and Gifford (1988). They found that the soil textural relationships of Green and Ampt used for estimating infiltration rates do not hold for agricultural and rangeland environments. Specifically, the field infiltration rates were as much as 1 - 4 cm higher than those estimated by the Green-Ampt equation. Hutten and Gifford (1988) have suggested that the infiltration rates need to be measured rather than estimated; however this is often not possible and typically even less practical given the spatial variability of soil properties.

In order to estimate realistic infiltration over agricultural landscapes infiltration capacities have been implemented which are based on field research for pastures, crops and forests as summarized in Ayers (1959). Based on this treatment, surface runoff events are limited to saturation overland flow and infiltration excess overland flow during intense rainfall events. This treatment is implemented during the snow-free periods.

4.2.1.4 Vegetation Growth and Ground Heat Flux Parameters

Vegetation characteristics are an important consideration for estimating evaporation over long periods of time. Specifically, plant growth can be simulated using a degree-day (heat unit) or biometeorological time scale approach to grow roots and signal changes in crucial growth stages (Robertson, 1968; Raddatz and Cummine, 2003). However, modelling the dynamics of rooting zone development and plant growth as a function of photoperiod and temperature, and moisture availability is a difficult challenge in itself and beyond the scope of the present research. Presently, CRHM does not employ a biophysical plant growth model. For this research a linear plant growth model was used to scale measured vegetation heights from the start of growth to a specified maximum value which is maintained until the end of the growing season. The start and the end of the growing season are specified as parameters and vegetation height is supplied as an observation based on field measurements over the season. A vegetation module was written and incorporated into CRHM to account for important factors when vegetation is not actively growing. For example, Granger (1991) and Miller (1994) have shown that the ground heat flux is not negligible during the early spring as a larger amount of energy goes into thawing the soil and can increase to 20% or higher. Evaporation is assumed to be limited to the recharge layer prior to the growth of vegetation and after a specified maturity date when the plants are shut down. The vegetation module is provided in Appendix B.

CHAPTER 5

POINT SCALE EVAPORATION ESTIMATES IN PRAIRIE LANDSCAPES

5.1 Introduction

The analysis presented in this chapter addresses the first research objective by evaluating the accuracy of the *P-M*, *G-D* and *BT* point scale evaporation estimation models for application in a Prairie landscape. Reasons for choosing these specific models were established earlier in a review of the literature on developments in evaporation theory. Namely, the models are physical based, provide direct estimates of "actual" evaporation which is needed for agriculture, water resources applications, and modeling hydrological and atmospheric processes, and they differ considerably in the theoretical treatment of land surface characteristics.

An examination was conducted using two modelling approaches; 1) the *P-M*, *G-D* and *BT* models were applied at the SDNWA during the 2006 field campaign, that is to say, they were not coupled directly to a hydrological model, and 2) the *P-M* and *G-D* models were linked to infiltration, runoff and soil moisture accounting algorithms within CRHM and their behaviour was evaluated using data from the Lethbridge AmeriFlux site during the 2000 and 2001 drought period. An analysis was performed through comparisons of the point-scale estimates of 'actual' evaporation against observations obtained using the eddy covariance method.

5.2 St. Denis National Wildlife Area

5.2.1 Measurements and General Conditions

The *P-M*, *G-D* and *BT* evaporation models were evaluated at the SDNWA over an observation period extending from May 19 – Sept 11 in 2006. An instrumented tripod mast continuously monitored eddy covariance fluxes and climate conditions at the upland reference site (described in Chapter 3) from May 19 through September 11, 2006. Modelled evaporation estimates were evaluated against observations collected at the mast. A fetch to height ratio of 1:100 was assumed such that the eddy covariance instruments were placed at a height of between 1 m to 1.5 m above the vegetation throughout the measurement period to remain within the boundary layer over the grassed surface. The leading edge of the reference grass site (bordered by cultivated land) was located approximately 150 m upwind in the direction of the CSAT sensor.

Continuous micrometeorological measurements collected at the reference site were used to parameterize the evaporation models. Specific observations required for this include: net radiation (Kipp and Zonen CNR1 net radiometer); ground heat flux (REBS soil heat flux plate); wind speed (CSAT3); temperature and humidity (Campbell Scientific Vaisala HMP45C series probe); volumetric soil moisture in the upper 30 cm of the soil profile (Campbell Scientific CS616 water content reflectometer), and surface temperature (Exergen IRTC infrared temperature sensor). Volumetric soil moisture within the upper 30 cm profile ranged from abundant (~ 45%) in spring to relatively dry (~ 20%) in early September.

Modelled evaporation estimates were derived from 15-min averages of the observations during the growing season period of 2006. The estimates were compared to observed values for several optimal data periods including 15 min, daily, multi-day and 68 total days of observations.

5.2.1.1 Observations During Study Period

Figure 5.1 shows measured daily averages of evaporation, net radiation, air temperature, surface temperature, wind speed, soil moisture, and relative humidity. Observed evaporation ranged from approximately 0.8 mm/day to 4.4 mm/day, peaking in late June – early July and then decreasing over the summer. The highest rates of evaporation typically occurred after precipitation events, primarily early in the season, and peaked during the summer blooming period. Following the peak evaporation period, there is a large decline in evaporation over the course of the season which coincides with a trend of declining soil moisture.

In general, other climate and surface variables that drive evaporation do not show similar trends; although a gradual decline in net radiation begins at the end of July. The daily surface temperature is shown to be lower during the peak evaporation period and higher in July under conditions of declining soil moisture. The surface temperature is also lower later in the season largely as a result of a seasonal reduction in solar radiation. As would be expected, the daily surface temperature tends to be lower immediately following wetting periods due to the increase in near surface water availability and increase in evaporation. Increases in surface temperature tended to occur during drying periods as near surface water availability and evaporation declined, and is generally higher immediately following the end of the peak evaporation period.

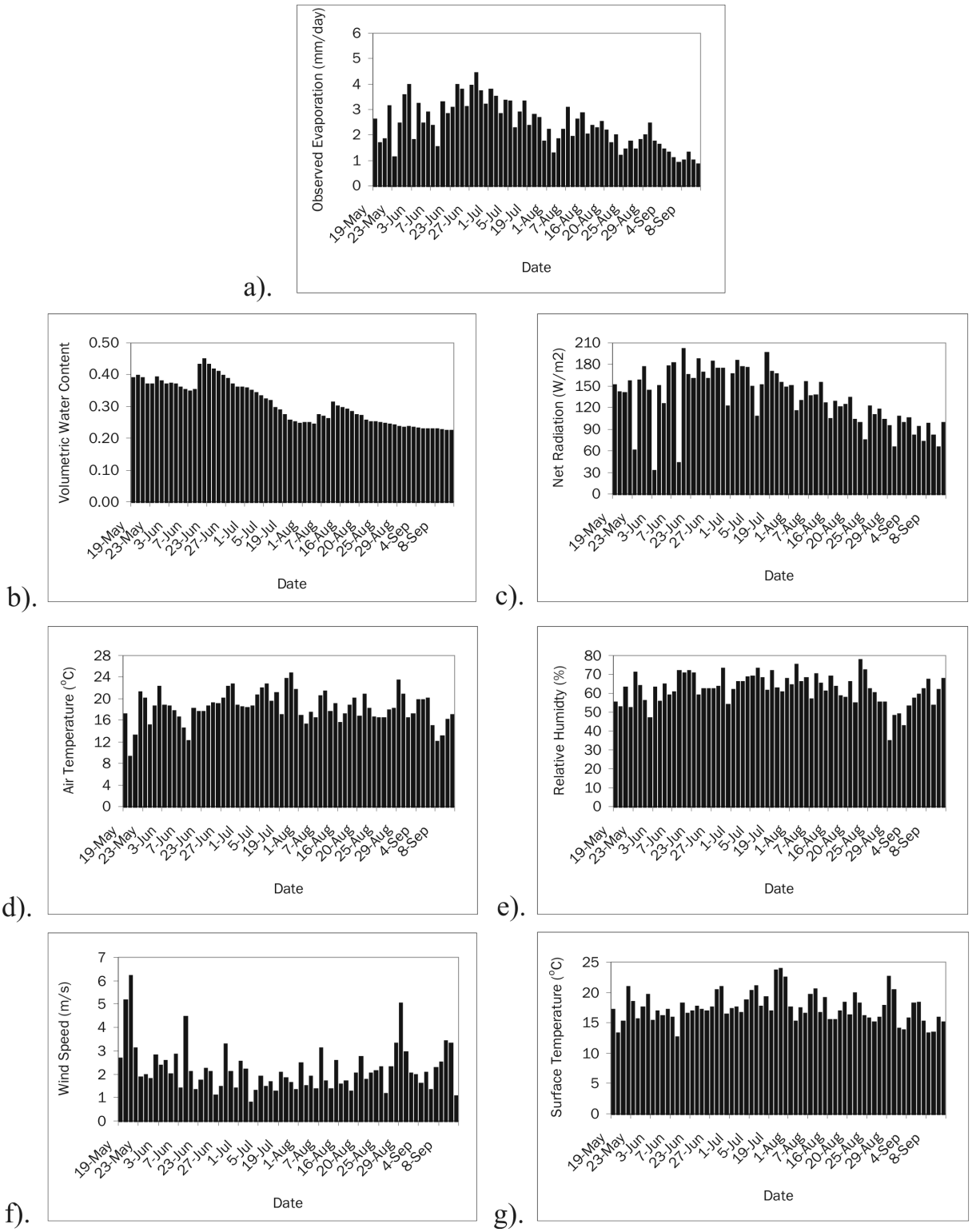

Figure 5.1: Measured daily averages for a) observed evaporation, b) volumetric water content, c) net radiation, d) air temperature, e) relative humidity, f) wind speed and, g) surface temperature.

5.2.2 Modelling Assumptions

It should be noted here that the evaporation models evaluated were driven directly by field observations and applied independently of a hydrological continuity approach. That is, no explicit modeling of the mass balance of soil moisture is considered to limit evaporation. The models were run under the measured atmospheric conditions, and observations of surface temperature and soil moisture. As a result, the only calibration required was for $r_{c\min}$, or the minimum resistance for plants not under moisture stress (Sherrat and Wheater, 1984), needed for the *P-M* and *BT* models. An advantage of the *G-D* model is that it does not require any calibration.

A manually calibrated value of 62 s m^{-1} was determined for $r_{c\min}$ to represent the unstressed conditions for the grassed surface. This is in the general range reported for grasses and crops 25 – 100 s m^{-1} (Verseghy et al., 1993). Sherrat and Wheater (1984) have indicated a value of between 40 – 50 s m^{-1} for a well watered pasture grass is reasonable. At the St. Denis site, very little bare soil was visible under the plant canopy near plant stems. As such the site did not warrant dividing evaporation between the soil and plants using a complex multilayer resistance network such as that of Shuttleworth and Wallace (1985).

Only those observations obtained during optimal data periods were considered for evaluating the model estimates. Optimal observation periods ranged from 2 days to 2 weeks. For these periods in which the CSAT and Krypton Hygrometer were working well and complete field measurements were available to drive the evaporation models. Data falling outside these criteria were not used in order to reduce some of the uncertainty in measured evaporation using the eddy covariance method (due to missing values and data spikes). Specifically, during periods of rain or high humidity resulting in the condensation of water droplets on the instruments, the signal of both the CSAT and hygrometer become corrupted. Therefore, results reported here are for periods when the instruments were dry and operational. In total, 68 days of "reliable" observations were collected over the period from May 19 through Sept 11, 2006.

Net Radiation Balance

For periods less than daily, the application of Penman-type models (*P-M* and *G-D*) becomes somewhat problematic. This is because evaporation models based on the energy balance

approach are only applicable under conditions when net radiation, Q^* is positive; whereas Q^* is predominantly negative during the night. This means the *P-M* and *G-D* models are not applicable during night time periods. Further, the largest portion of evaporative losses via transpiration during photosynthesis in C_3 and C_4 carbon fixing plants (e.g. cool season and warm season grasses) is generally restricted to daylight periods. Given these limitations, the estimation problem was simplified by restricting evaporation to those 15 min averaging periods when Q^* was positive; for periods where Q^* was negative evaporation was set to zero.

Canopy Resistance

In the case of the *BT* model, the surface humidity gradient and consideration for the aerodynamic and canopy resistances determines the evaporation. As a result, the *BT* aerodynamic approach can be used to estimate evaporation during the night time and can potentially identify periods of condensation when the humidity gradient is negative. To model this, however, requires an increase in complexity, such as a resistance network, where intercepted condensation and evaporated condensation would need to be accurately tracked. Therefore, the estimation problem was simplified by restricting evaporation to periods when Q^* was positive. For application of the *BT* model, this was controlled by setting the canopy resistance r_c to 5000 s m^{-1} during periods when Q^* was negative. As a result, there was no modelling of evaporation during night time periods.

Atmospheric Stability

Most evaporation models have been developed under the implicit assumption of neutral stability. Given the relatively strong surface winds observed during the daytime at St. Denis which is typical of prairie environments, the assumption of neutral stability is valid. Therefore, for the purpose of present comparisons neutral stability was assumed and no corrections for stable or unstable conditions were made.

5.2.3 Results and Discussion

The general agreement between the modelled and observed values was evaluated using the root mean squared error (RMSE)

$$\text{RMSE} = \sqrt{\frac{\sum (X_i - X_e)^2}{n}} \quad , \tag{5.1}$$

where X_i and X_e are the modelled and observed values and n is the sample size. The relative errors of each model were also assessed by considering the mean bias error (MBE) between the modelled and observed values,

$$\text{MBE} = \frac{\sum \frac{X_i}{X_e} - 1}{n} \quad . \tag{5.2}$$

5.2.3.1 Cumulative Estimates

For comparative purposes, $r_{c\min}$ for both the *P-M* and *BT* models should be equal in value for both models and not biased due to differences in the theoretical approaches. For this study it was found that a manually calibrated value of 62 s m^{-1} for $r_{c\min}$ resulted in minimal errors for both the *P-M* and *BT* methods for the 68 days of optimal data observations. Table 5.1 provides a comparison of the cumulative observed and modelled evaporation for all 68 days during optimal periods when the supply of net radiation was positive. The cumulative observed evaporation for these days was 152.8 mm in total or approximately 2.3 mm/day.

Table 5.1: Modelled vs observed total evaporation over 68 days of optimal observations for periods when the supply of net radiation was positive.

Evaporation Method	Cumulative Total (mm) over 68 Days
Measured	152.8
P-M	156.5
G-D	153.5
BT	153.5

Overall, the *P-M*, *G-D*, and *BT* model estimates represent the total evaporation very well and were nearly identical to the observed value. The difference between the observed value and the *G-D* and *BT* models for these days was less than 1 mm whilst the difference was less than 4 mm for the *P-M* model estimate. This means the MBE for the *P-M* model was within 2.5% of the observed value and the *G-D*, and *BT* models were within 0.5% of the observed value.

5.2.3.2 Multi-day Estimates

A comparison of modelled and observed evaporation for multi-day periods is shown in Figure 5.2. The modelled and observed values are expressed as the total amount of evaporation for optimal observation periods when the supply of net radiation is positive (i.e. excludes night time processes). The multi-day totals have been reported here for periods ranging from 2 to 14 consecutive days in duration. For the purpose of comparison the values have been expressed as a rate (mm/day) for each period. The one to one line, the r^2 values and root mean squared error (RMSE) are also indicated.

For several optimal periods the modelled evaporation estimates agreed reasonably well with the observed values. No single model consistently provided the best agreement to the observed values of evaporation. Overall, the *G-D* and *P-M* models provided the best results for the optimal periods when compared with the observed values; $r^2 = 0.77$ for the *G-D* model and $r^2 = 0.71$ for the *P-M* model. The RMSE values for all of the model estimates showed a range of approximately 0.3 mm/day. Overall, the *G-D* model had the smallest error (RMSE = 0.33 mm/day) and the *P-M* model also compared well to the observed totals for these periods (RMSE = 0.36 mm/day). The largest error was produced by the *BT* model estimates (RMSE = 0.65 mm/day). On average the MBE of *P-M* model estimates were 5% larger than observed values and the *G-D* and *BT* models were approximately 8% larger.

Table 5.2 provides a summary of the performance of each model for the ten multi-day periods by considering the absolute differences between the modelled and observed values. The *G-D* model provided the best agreement to within 1 mm or better of the observed evaporation five out of ten times (i.e. frequency of 50%) for the multi-day periods. These were comprised of two 2-day periods, one 3-day period, one 5-day period, and one 10-day period. Both the *P-M* and *BT* models estimated the evaporation to within 1 mm or better 30% of the time. All three multi-day periods were 2 days in length for the *P-M* model. For the *BT* model two were 2 days in

length and the other 3 days. The *P-M* and *BT* models also provided estimates to within 1.0 – 1.5 mm of the observed value 20% and 30% of the time respectively, and the *G-D* model achieved this one time (10%). The length of the multi-day periods also varied for each model in this case: *G-D* model (2-day period); *P-M* model (3-day and 9-day period); *BT* (2-day, 7-day, and 10-day period).

a).

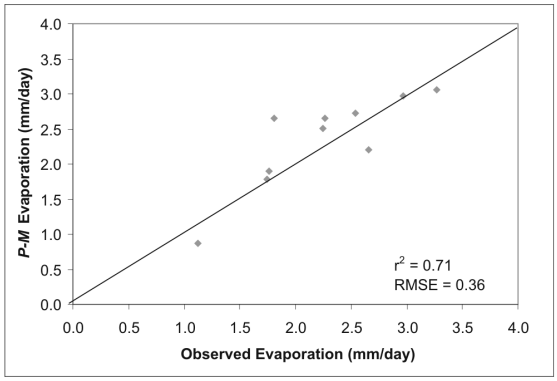

b).

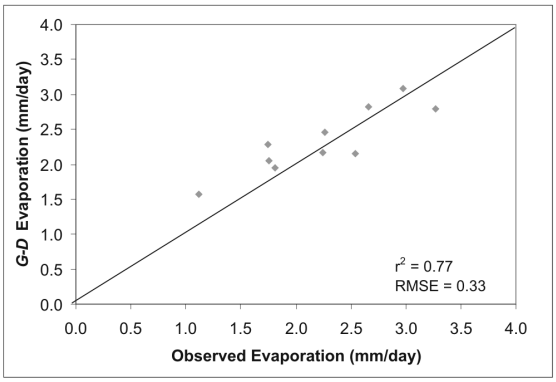

c).

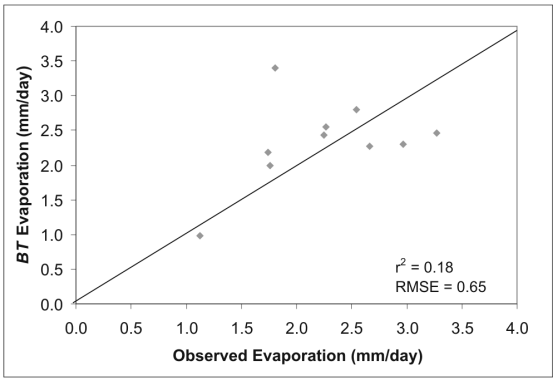

Figure 5.2: Modelled versus observed evaporation rates for the optimal periods of 2 days to 2 weeks in duration. a) *P–M*, b) *G–D*, c) *BT*. Solid line is one -to- one line.

Table 5.2: Frequency of model estimates for a range of differences from the observed value for the 10 multi-day periods.

Difference from Observed	Frequency of Model Estimate %		
	G-D	*P-M*	*BT*
< 1.0 mm	50	30	30
1.0 - 1.5 mm	10	20	30
1.5 - 3.0 mm	10	30	20
3.0 - 5.0 mm	20	20	0
> 5.0 mm	10	0	20

The models also produced some larger differences compared to the observed values. A difference of 1.5 – 3.0 mm occurred once out of the ten times (10%) for the *G-D* model, and 30% and 20% of the time respectively for the *P-M* and *BT* models. The *G-D* and *P-M* models both provided estimates with a difference of between 3.0 – 5.0 mm from the observed multi-day values on two occasions (20%). For the *G-D* model, this occurred for one 9-day and one 10-day period. For the *P-M* model this occurred for one 5-day period and one 15-day period. Only the *G-D* and *BT* models produced estimates with differences from the observed value that were larger than 5 mm. In the case of the *BT* model this occurred for one 5-day period, and also one 15-day period for both models. For the 15-day period extending from June 22 – July 6 all three models underestimated the observed evaporation of 49.1 mm; which considers those periods when the supply of net radiation is positive. The *P-M* model provided the best agreement at 46 mm and the *G-D* and *BT* models provided lower estimates of 42 mm and 37 mm respectively.

Overall, the results show that all three models were capable of providing reasonable estimates of evaporation for several of the optimal periods. Between 50% - 60% of the estimates were within 1.5 mm of the observed value for the multi-day periods. In general, the *G-D* and *P-M* methods tended to perform better than the *BT* method. For example, the *BT* model produced a large overestimate (7.9 mm) for the May 19 – 23 period and a larger underestimate (12.1 mm) for the June 22 – July 6 period. These large differences may be attributed in part to the flux gradient relationship derived from a small areal radiometric measurement of surface temperature. The plant and soil surface exposed for radiation transfer is not exactly the surface exposed to turbulent transfer. The relative differences may also be potentially reduced by considering stability corrections. Another consideration is the canopy resistance term. No measurements of LAI were available so leaf area was not considered in the calculation when estimating the canopy resistance term. Intuitively, accounting for reduced leaf area would produce a higher canopy resistance resulting in a further reduction of the modelled evaporation if leaf area was a factor during early growth periods. However, the exclusion of leaf area had less of an impact on the *P-M* model.

In general, the variability among the models may be attributed to several factors, 1) the atmospheric conditions over the optimal periods tend not to be steady state, 2) it is difficult to adequately account for energy storage at the surface, 3) the feedback mechanisms of the *G-D* method are subject to lag effects such that atmospheric changes tend to occur more slowly than

do conditions at the surface, 4) the surface temperature for the *BT* model is measured radiometrically over a small area and does not completely represent the surface involved in turbulent exchange with the atmosphere over the variable flux footprint of the eddy covariance measurements, 5) no assumptions have been made regarding plant phenology and health, and 6) no consideration has been given for the possible effects of spatial variability on driving factors contributing to the evaporative flux measured at the sensors.

5.2.3.3 Daily Estimates

Figure 5.3 compares the modelled and observed evaporation over the course of the daily optimal periods. These values were determined for each day by summing the interval evaporation for the periods when the supply of net radiation was positive. The one to one line, r^2 values and RMSE are also indicated in each graph. Again, the *P-M* and *G-D* models provided the best agreement to the observed values, although in this case, the r^2 was higher for the *P-M* model (0.66) compared to that for the *G-D* model (0.61). The RMSE values associated with each model were also similar. For the *P-M* model the RMSE = 0.52 mm/day and for the *G-D* model the RMSE = 0.54 mm/day. The *BT* model provided the poorest daily estimates; $r^2 = 0.22$ and RMSE = 0.9 mm/day.

The variability of estimates by a given model and between the models is evident from the scatter between the modelled and observed values. Despite these variations (Figure 5.3), the MBE of the model estimates were similar to those for the multi-day estimates. The MBE for the *G-D* model estimates remained at 8% larger than the observed values whilst there was a slight increase in MBE for the *P-M* and *BT* models to 6% and 9% respectively. In general, the daily estimates obtained from each of the models resulted in RMSE values that were larger compared to the estimates expressed as daily rates for the multi-day periods. This suggests that the variance of the model estimates increased as the time scale was shortened to a daily period. This would further indicate that while there might be a small increase in the variability among the daily estimates, the relative errors between the modelled and observed values tended to balance over the multi-day periods.

a).

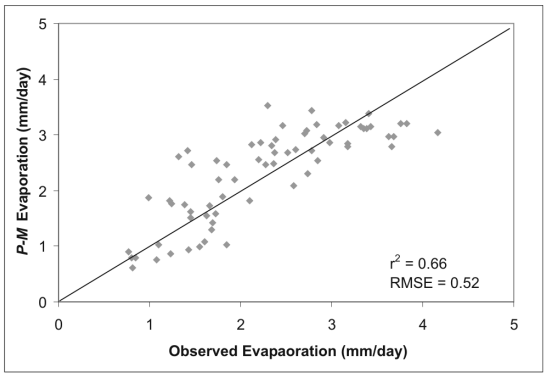

b).

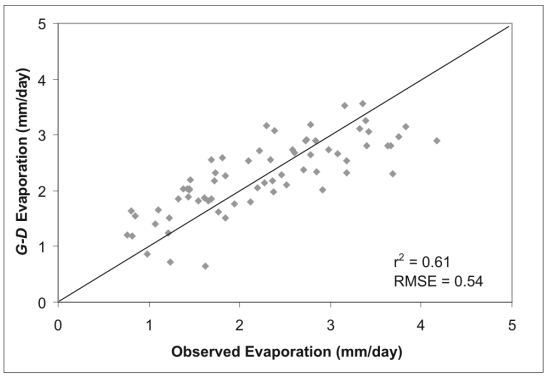

c).

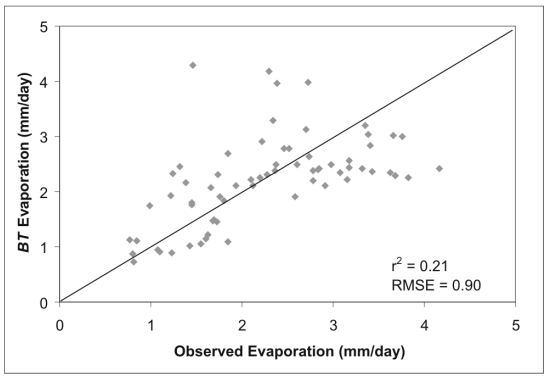

Figure 5.3: Modelled versus observed daily evaporation for the optimal periods. a) *P–M*, b) *G–D*, c) *BT*. Solid line is one -to- one line.

5.2.3.4 15 Minute Interval Estimates

In Figure 5.4, modelled and observed evaporation for the 15 minute average measurement periods are compared. The one to one line, r^2 values and RMSE are indicated in each graph. As was the case for the daily estimates, the statistics suggest the *P-M* and *G-D* models provided similar estimates and also performed better than the *BT* model in general. The *P-M* and *G-D* models showed similar r^2 values of 0.55 and 0.59 respectively. The RMSE for the *P-M* and *G-D* models is also nearly identical with values of 0.018 mm/15 min and 0.02 mm/15 min. The *BT* model did not perform as well compared to the observed values over the 15 min intervals as indicated by the much lower value of $r^2 = 0.3$ and larger RMSE = 0.026.

For this much shorter time period there was a large increase in the relative error of the models. The MBE was lowest for the *G-D* model estimates which were found to be an average of 14.6% larger than the observed values. The MBE for the *BT* model was found to be 19% higher

than the observed values and the P-M model produced the largest MBE which were an average of 28% higher than the observed values.

.

a).

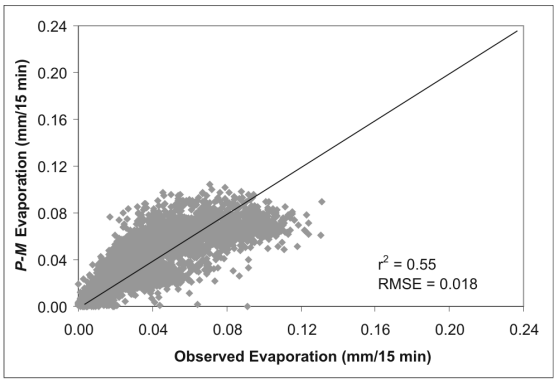

b).

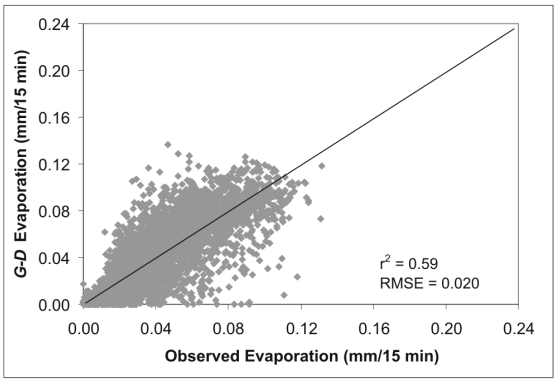

c).

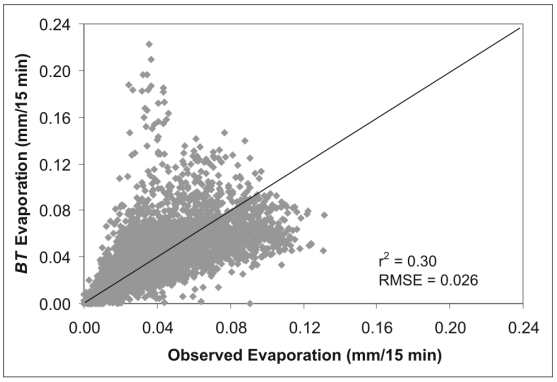

Figure 5.4: Modelled versus observed fifteen-minute-interval evaporation. a) *P–M*, b) *G–D*, c) *BT*. Solid line is one -to- one line.

The scatter of the data points around the one to one line for all three methods appears to be similar to that for the daily periods shown in Figure 5.3. Given the large scatter among the modelled vs. observed evaporation it is unlikely that corrections for stability alone would rectify the performance of the models at this short time scale but may potentially enhance the agreement between the model estimates and observed values.

5.2.3.5 Peak Period Estimates

Modelled results for the June 22 - July 6 period are of particular interest. As indicated previously, all of the models underestimate the observed evaporation which totalled 49.1 mm during this 15 day period (3.3 mm/day). These differences are of interest because the observed evaporation peaked during this period of the season. First, there are several notable reasons for

the peak evaporation to occur during June 22 - July 6, 1) as shown in Figure 5.1, water and energy availability do not appear to be strong limiting factors, 2) the mixed grasses, namely wheat grasses, alfalfa, and sainfoin, were fully developed and in full bloom (blooming began in early to mid June), 3) water use by the grasses during the blooming period can be assumed to be optimal to maintain maximum photosynthesis and thus plant activity/productivity; support for this can be found in the case of prairie grasses (Verma et al., 1992) and more so in the case of wheat crops (Raddatz and Cummine, 2003; Shen et al., 2002), and 4) the leaf area of plants can reasonably be expected to be near a maximum value for an extended period prior to the onset of blooming and through the blooming period.

Therefore, the possible physical basis behind the evaporation underestimation by the models warrants further consideration. Two potential factors are the general effects of plant phenology and the humidity deficit on evaporation estimates. In the case of the *P-M* and *BT* models plant phenology does not restrict transpiration during the peak evaporation period since there is a fully developed plant canopy. In the case of the *G-D* model the relative evaporation parameter limits evaporation as a function of the available energy and the humidity deficit. The humidity deficit itself is a reflection of the availability of surface water and water vapour transfer to the atmosphere and is one factor that is common to all three models. As shown in Figure 5.1, the mean daily relative humidity (RH) was relatively low (~ 60%) during the period of peak evaporation compared to that following the peak evaporation period. During the daytime, the RH was typically around 40% or less.

In the case of the *G-D* method, a higher humidity deficit and the abundant supply of available energy increases the drying power of the air, *D* which produces a lower value of relative evaporation, *G*, thereby reducing evaporation. In the case of the *P-M* method, increases in the humidity deficit beyond the optimal plant operating conditions would result in an increase in the canopy resistance. The overall effects of this increase in canopy resistance, however, may be offset by the balance of available energy. Unlike the *P-M* combination approach, the *BT* method directly considers the humidity gradient driven by measured surface temperature. Observations at the St. Denis upland site show that the evaporation generally follows diurnal variations in surface temperature. In general, r^2 values for surface temperature and evaporation were in the order of 0.85 to 0.90. Further, the observed surface temperature follows diurnal variations in net available energy. This presents a difficulty for using a radiometric measurement

of surface temperature at a point, whereas the energy balance is generally considered over a larger area. Assuming a height to area measurement ratio of 10:1 for a CNR1 net radiometer, the measurement footprint would be in the order of 5 m – 10 m. Also, due to the difference in theoretical approaches of the models, the canopy resistance term appears to have a larger influence on evaporation estimates for the *BT* method than it does for the *P-M* method.

For the majority of the peak evaporation periods, the daytime surface temperatures and mean daily surface temperature (typically around 16.5 – 17.5 °C) were generally lower than afterwards. As shown in Figure 5.1, the lower surface temperatures are likely explained by the ample soil moisture in the upper 30 cm soil profile leading to increased water losses from the plants via transpiration during this phenological stage. This may point to a potential disadvantage of applying the *BT* method to a vegetation canopy under these conditions. That is, based on Dalton's earlier findings, lower surface temperatures should result in lower rates of evaporation due to the reduced surface specific humidity (all other considerations being equal). In order to improve the *BT* estimate compared to the observed value under the condition of lower canopy temperatures, the value of r_{cmin} would also need to be lower to effectively increase the evaporation rate. This may help to explain why the *BT* method produced the largest underestimate compared to the observed value for the peak evaporation period.

For instructional purposes, a lower reference value of $r_{cmin} = 50$ s m^{-1} was specified for the *P-M* and *BT* models. The resulting estimate for the June 22 – July 6 period for the *P-M* model increased to 53.5 mm, which is very close to the observed value of 51 mm. The *BT* estimate increased to 44.8 mm compared to the previous estimate of 37 mm but was still 6.2 mm less than the observed value. When considered for the entire 68 days of optimal observations, however, using a value of 50 s m^{-1} resulted in a large evaporation overestimate of approximately 30 mm when compared to the observed, by both the *P-M* and *BT* methods. These results suggest that there is a problem in using a common canopy resistance term in these evaporation models. That is, the value of r_{cmin} lacks a common meaning given the different theoretical approaches of the *P-M* and *BT* models and so the calibration of r_{cmin} is a model specific problem.

For the *BT* method, the optimal value of r_{cmin} would need to be in the order of 40 s m^{-1} compared to 50 s m^{-1} for the *P-M* method, for the estimated evaporation to approach the observed value of 51 mm for the period. A second potential problem is a limitation inherent to the Jarvis (1976) multiplicative approach for deriving the canopy resistance term. Due to the

linear nature of the algorithm there is a potential for runaway increases in canopy resistance depending on the sensitivity of the equations used to derive the factors. This is of potential importance since plants typically increase their stomatal activity when it is needed most (i.e. during blooming), and likely in spite of the general atmospheric conditions if available water and energy are not limiting factors.

The use of a single reference value for $r_{c\min,}$ regardless of whether it is adjusted as a function of leaf area, assumes that optimal water use conditions apply for all plant phenological stages when water is not limiting. This precludes the potential for declining water use by plants when water availability is no longer crucial for maintaining overall plant health. For example, immediately following the peak evaporation period changes in leaf area are small but the plant may simply use less water. Adjusting the relative activity of stomata based on the timing of important life cycle events (i.e. blooming) would require the incorporation of a detailed plant growth model and tracking measured values of $r_{c\min}$ over the growing season. Nevertheless, changes in plant phenology or the timing of plant life cycle events has been widely identified as a potentially important focus for climate change research (Beaubien and Johnson, 1994; Chen et al., 2000; Myneni et al., 1997; Schwartz, 1999; Spano et al., 1999; Wolfe et al., 2005). Ultimately, the consideration of a plant growth model would be a more physically based approach to modelling the vegetation canopy but would also increase the complexity of point scale evaporation modelling and provide difficulties in dealing with complex landscapes comprised of several major plant species.

5.2.3.6 Comparison of Maximum Daily Value with Other Studies

Several previous studies have reported measured maximum daily rates of evaporation for various grassland regions (Baldocchi et al., 2004; Burba and Verma, 2005; Kelliher et al., 1993; Meyers, 2001; Verma et al., 1992; Wever et al., 2002). This includes grassland sites located in both Canada (Saskatchewan, Alberta) and the United States (Kansas, Oklahoma, and California). These studies have also used the eddy covariance method to obtained measurements of evaporative fluxes. Within the central Canadian Prairie region, cool season C_3 grasses tend to be the dominant plant species while warm season C_4 grasses dominate the central Great Plains region of the United States. Cool season C_3 grasses tend to reach their peak activity in the late spring to early summer period whereas the warm season C_4 grasses reach their peak activity

towards mid to late summer. The measured maximum daily evaporation rate for the mixed grass site at St. Denis was approximately 4.4 mm day^{-1}. This is comparable to the measured maximum daily rates reported for past studies (Table 5.3).

Table 5.3: Maximum daily evaporation rates (mm d^{-1}) for several previous grassland studies.

Source	Region	Dominant Vegetation Type	Water Availability during growing period	Maximum Evaporation rate (mm d^{-1})
Verma et al. (1992)	Kansas (U.S.A.)	warm season C_4 grasses	ample to dry	6.6
Kelliher et al. (1993)[1]	31 - 55° Latitude	various grass species	ample	4.8
Meyers (2001)	Oklahoma (U.S.A.)	warm season C_4 grasses	ample	4.0
			drought	2.5
Wever et al. (2002)	Alta (Can.)	cool season C_3 grasses	ample	4.5
			drought	3.0
Baldocchi et al. (2004)	California (U.S.A.)	annual grass	ample to dry	4.0
Burba and Verma (2005)	Oklahoma (U.S.A.)	warm season C_4 grasses	ample	5.0

[1] Review paper which examined grassland regions for both southern and northern hemispheres. Maximum evaporation rate is the average value for the six studies examined.

It is interesting to note the relative consistency reported for the maximum daily rates of evaporation for the various grassland regions, with the exception of the Kansas site. Some of the sites are characterized as tall grass sites (> 1 m tall) while others are short grass sites (< 0.50 m tall). Yet, the measured daily rates of evaporation for non-drought conditions are generally in the order of 4.5 mm on average regardless of the region studied and potential differences in biomass or leaf area. This is noteworthy since there are differences in the general climate conditions of the regions which have led to the divergence in plant species. This suggests that the peak evaporation rate for prairie grasses in general under well watered conditions would be close to 4.5 mm day^{-1}.

5.3 Drought Application: Lethbridge AmeriFlux Site

The modelling process becomes more complicated under conditions of drought, when extremely low soil moisture availability restricts evaporation from the soil and plants. Under such severe conditions, soil moisture accounting to the depth of the rooting zone is needed to exert a further control on actual evaporation. The objective in this case study is to present a modelling

application to examine the effect of rooting depth estimates on cumulative actual evaporation for a Canadian Prairie environment during severe drought.

The modelling was performed within the Cold Regions Hydrological Model (CRHM) platform (Pomeroy et al., 2007). Within CRHM two land surface hydrological models were assembled to estimate actual evaporation from a mixed short-grass prairie at Lethbridge, Alberta in the drought years of 2000 and 2001. In this case, the *P-M* and *G-D* models were coupled to the soil moisture balance to enforce limitations on the actual evaporation as soil moisture was depleted further throughout the soil column. For the purpose of examining the effects of rooting depth on cumulative evaporation several model runs were performed with each one having a different maximum soil column depth (maximum rooting depth). For each run the depth was incremented by 200 mm starting from a minimum depth of 800 mm. The upper limit was taken to be approximately 1400 mm. These depths are reasonable lower and upper limits to which the grasses at Lethbridge might be rooted based on 50 years of research conducted by Weaver (1968). In this case, the behaviour of the *P-M* and *G-D* models was evaluated with respect to the magnitude and shape of the cumulative evaporation curve. The *BT* model was not considered in this case because surface temperature measurements were unavailable.

5.3.1 Measurements and General Conditions

Near surface meteorological and ecological observations were obtained through the AmeriFlux network (data courtesy of Larry Flanagan at the University of Lethbridge, Alberta) and the Agriculture and Agri-Food Canada (AAFC) Lethbridge Research Centre (data courtesy of Hugh McLean and Sean McGinn). These were used as model input and for evaluating model performance. Precipitation in the form of rainfall represents the only input (irrigation and ground water were not factors), and runoff was neglected due to the lack of any heavy convective rainfall events during these drought years. This allows the water budget to be simplified to vertical components. As a result, only precipitation and evaporation were considered and the change in storage can be simply determined from the difference between them, $\Delta S = P - E$.

As shown in Figure 5.5 the measured total evaporation was much higher than precipitation for the period of May 1 – Sept 30 for both 2000 and 2001. In 2000 measured evaporation (188 mm) was approximately 1.6 times larger than the total precipitation of 113 mm and in 2001 measured evaporation (164 mm) was nearly 2.5 times larger than the precipitation of only 67 mm

recorded over the same period. These differences indicate rather large changes in soil moisture storage of approximately -75 mm and -100 mm respectively.

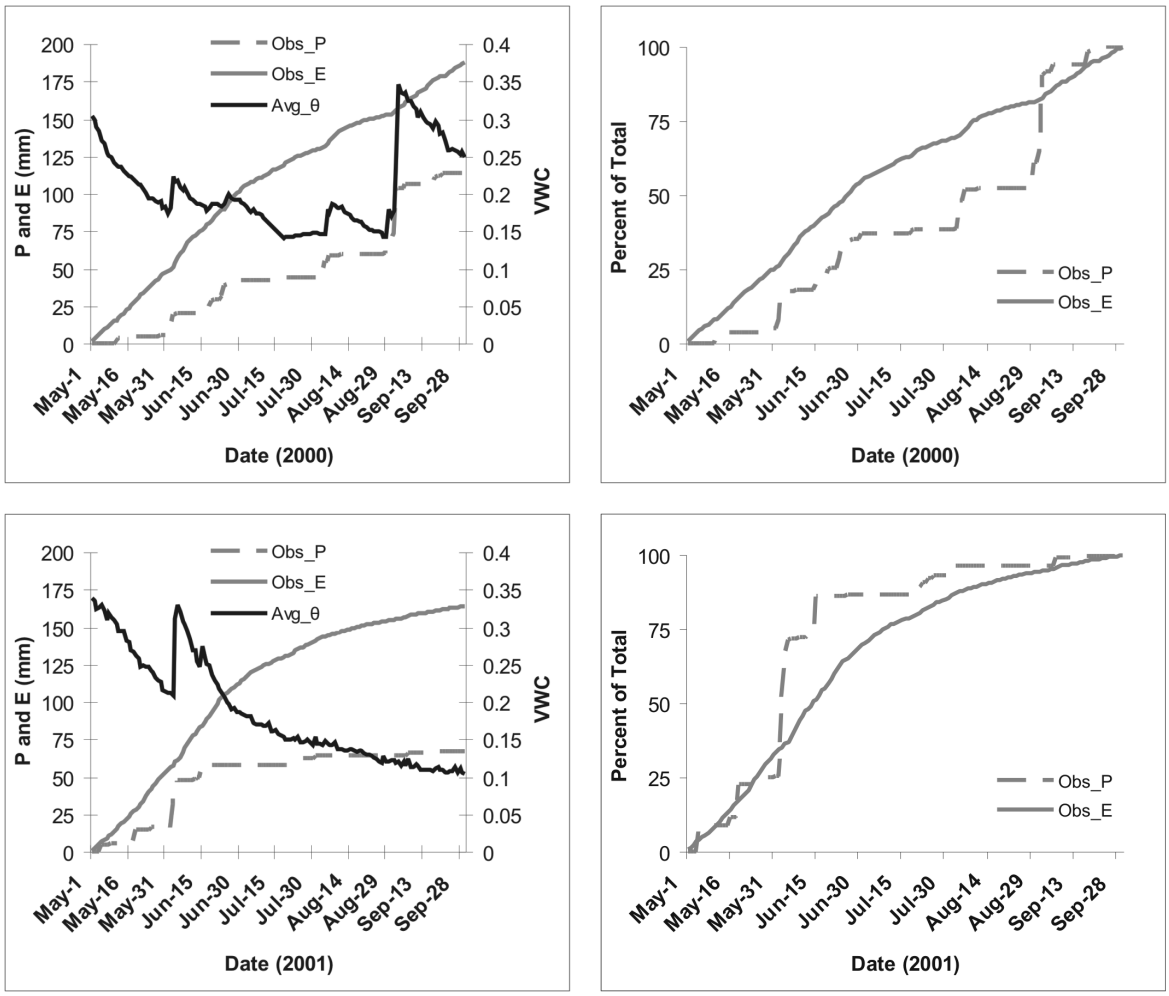

Figure 5.5: (Left): Cumulative measured evaporation (Obs_E) is more than twice the cumulative rainfall (Obs_P) over the period of May 19 – Sept 11, 2001, and begins to level off as volumetric soil water content falls below 0.2. (Right): Daily cumulative P and E as percentage of cumulative totals.

Figure 5.5 also shows a marked change in the slope of the cumulative evaporation over time in both years; this occurred in early July. By July 2 of 2000 the cumulative evaporation was 105 mm (1.67 mm per day on average) or 56% of the total cumulative evaporation. By comparison only 37% of the total cumulative precipitation had been received by this date (Figure 5.5). The daily average evaporation rate dropped abruptly thereafter to 0.91 mm/day for the remainder of the period. For 2001 the difference was even greater; by July 4 the cumulative evaporation was

119 mm (1.83 mm/day on average) or 72% of the total cumulative evaporation whilst 86% of the total rainfall had been received. Thereafter, the decline in the daily average evaporation (0.51 mm/day) was even larger than that in 2000.

Changes in observed evaporation tended to coincide with changes in soil moisture (Figure 5.6). Evaporation (mm/day) lagged slightly behind observed changes in volumetric soil moisture as clearly shown for 2001. For example, 27 mm of rain fell over a two day period in early June, increasing the volumetric soil moisture content from 0.21 to 0.31. This was followed by a peak period of evaporation through most of June. By early July both the volumetric soil water content (~ 0.18) and the evaporation rate (generally < 1 mm/day) had declined dramatically, signalling strong moisture limitations.

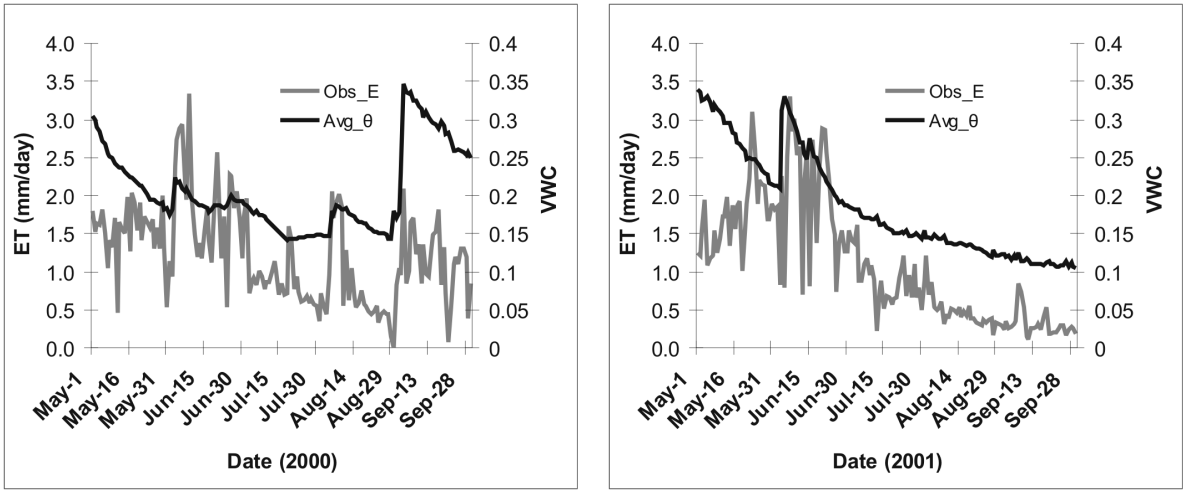

Figure 5.6: Eddy covariance measured evaporation and volumetric soil moisture over 15 cm profile depth at Lethbridge grassland site from May 1 – Sept 30 for 2000 and 2001.

5.3.2 Description of CRHM Modules and Modelling Assumptions

A general overview of CRHM and modelling considerations for estimating evaporation was previously given in Chapter 4. Figure 5.7 shows a flowchart of the modules assembled in CRHM for modelling evaporation at the Lethbridge site and the respective input variables. A brief description of modules is also provided below.

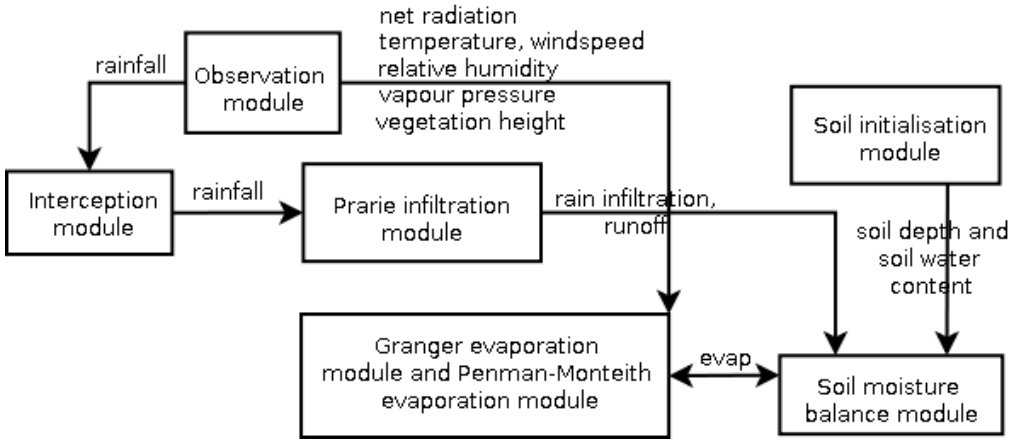

Figure 5.7: Flowchart of CRHM hydrological modules assembled for modelling evaporation at Lethbridge.

Observation module

The observation module reads the climatological data from the observation files into the HRU's which is then used as input to drive other modules; observations for this application include net radiation, temperature, wind speed, relative humidity, vapour pressure and interpolated vegetation heights.

Interception module

When implemented, determines the amount of precipitation (rain or snow) that is intercepted by the canopy and the amount that reaches the soil or snow surface.

Prairie infiltration module

Estimates the amount of infiltration into frozen and unfrozen soils and updates the water content in the soil moisture balance module. This application only requires infiltration into unfrozen soil which is determined using a look-up table of values determined from field research reported in Ayres (1959). The infiltration capacity of the soil (mm/hr) is set based on two parameters - the bulk soil texture of the soil profile and general condition of the ground cover. The general site conditions as described in Chapter 3 indicate the soils were clay-loam to clay in texture and the grassland was ungrazed. The parameter for bulk soil texture was set to a medium textured soil over fine textured clay till and the grass was assumed to be good pasture, for which the infiltration rate is 5.1 mm/hr according to Ayers (1959).

Evaporation module

This module estimates the amount of actual evaporation from a non-saturated surface during the snow-free period. The current application employed the *P-M* and *G-D* models which have been previously introduced in Chapter 2. Model parameters needed for estimating the canopy resistance were previously described in Chapter 4 (see Eq. 4.7 – 4.12). The *P-M* model requires the minimum and maximum LAI for tracking changes in LAI as a function of vegetation height which was done using Verseghy et al. (1993),

$$\mathrm{LAI} = H / H_{\max}(\mathrm{LAI}_{\min} + s(\mathrm{LAI}_{\max} - \mathrm{LAI}_{\min})) \quad , \tag{5.1}$$

where H and $H_{\max}$ are current vegetation and maximum vegetation heights, $\mathrm{LAI}_{\min}$ and $\mathrm{LAI}_{\max}$ are the minimum and maximum LAI values and s is a factor to account for seasonal changes which is assumed to be 1 (fully leafed) for grasses throughout the year. Calculation of the canopy resistance term also requires three parameters needed for calculating the soil moisture tension factor in Eq. 4.11; air entry tension, ψ_{ae}, porosity, ϕ, and pore size distribution index, b. Values for these were obtained from the look-up table corresponding to a clay-loam textured soil.

Soil initialization module

Parameters supplied in this module are used to determine the soil water available for plant use per metre of soil. These include the soil depth of the recharge layer and entire soil column, the volumetric water content, and soil texture. This information is used to set the initial soil moisture content and soil water holding properties (initial and maximum content of the recharge layer and entire soil column) in the soil moisture balance module. This is done using the method described previously in Chapter 4 (see 4.2.1.2 for example).

Soil moisture balance module

CRHM enforces continuity within a soil column which is divided into two soil layers (Figure 5.8). The upper layer is a recharge zone from which both soil evaporation and transpiration losses can occur. The lower layer represents the maximum extent of the rooting zone which supplies water for transpiration. The soil moisture content is given by θ and the total maximum soil moisture content is θ_{max}. Any rainfall infiltrating into the soil is supplied to the recharge

layer first, and once filled, percolates into the lower layer. Excess water from both soil layers contributes to the ground water and subsurface flows. In cases where the entire soil column is saturated or the rainfall intensity exceeds the infiltration capacity of the soil, the excess water is treated as overland flow and becomes surface runoff.

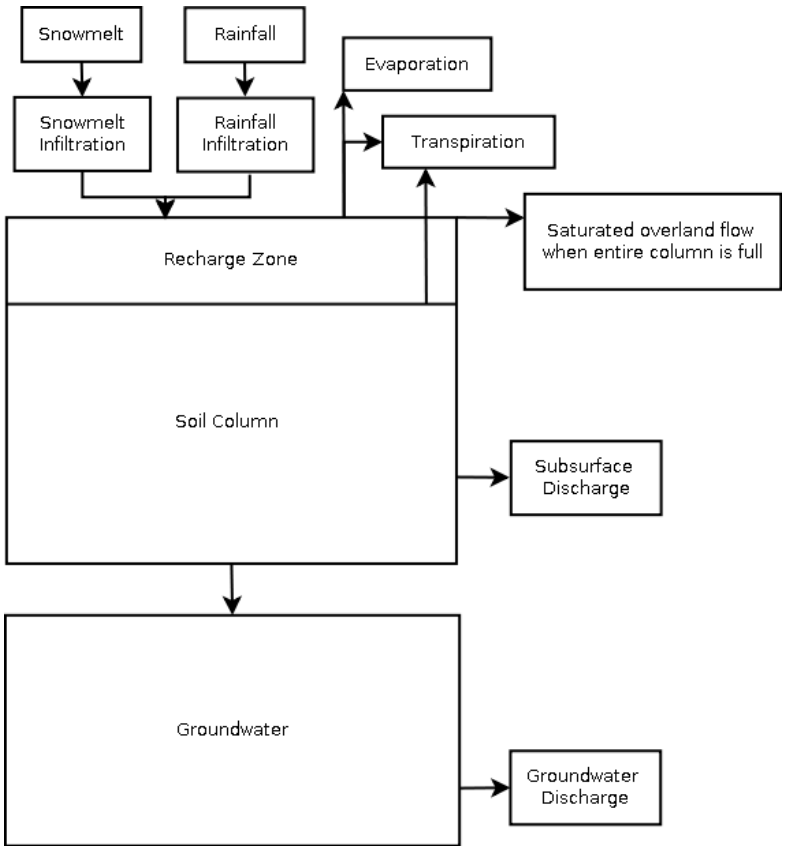

Figure 5.8: Flowchart of soil moisture balance module (*after Fang et al., 2010*).

Modelling Assumptions

The depth of the recharge layer from which both soil evaporation and transpiration can occur was set to 15 cm. This is also the profile depth of available soil moisture measurements at the site. The initial wetness (i.e. saturation) of the entire soil column for all model runs was set to 0.75 or 75% for simplicity since no soil moisture measurements are available to a depth of greater than 15 cm. This saturation value is considered reasonable for this application since the observations indicate the volumetric soil moisture of the upper 15 cm was fairly similar on May

1 (JD 121) for both 2000 and 2001 (0.31 and 0.34). For a clay-loam soil with a porosity of approximately 0.476 as obtained from the look-up table based on the U. S. Department of Agriculture (1955) and Scherer et al. (1996) this results in a soil saturation of 65% and 71% respectively. Given that volumetric soil moisture in this upper layer had peaked at 0.37 on JD 104 (2000) and 0.39 on JD 99 (2001), and was reducing slowly prior to JD 121 it is more than likely that the profile had a higher moisture content at depths below the upper shallow layer since surface layers dry more rapidly.

As discussed in section 5.2.2, Sherrat and Wheater (1984a) indicated a value of 50 s m^{-1} for $r_{c\min}$ is reasonable for an unstressed pasture grass. Therefore, this value was used for the *P-M* model runs. In the case of the *G-D* model there are no initial parameters to set and it is driven by meteorological forcing data. The Jarvis (1976) multiplicative approach was applied for calculating the canopy resistance, r_c. This was adjusted over the season as a function of leaf area taking into consideration observations of LAI. First, estimates of canopy height were derived based on the mid-growing season measurement reported in the ecological dataset for the Lethbridge AmeriFlux site (Courtesy of Larry Flanagan, University of Lethbridge). The mid-growing season value was assumed to be the maximum value of canopy height for the growing period. The progression of heights was assumed to be linear from the date of the measured minimum value of LAI (assumed to coincide with the minimum canopy height) to the date of the measured canopy height. LAI was then tracked continuously using Eq. 5.1 from the changes in canopy height using the approach in Verseghy et al. (1993),

$$r_c = r_{c\min}(\mathrm{LAI}_{\max} / \mathrm{LAI}) \quad . \tag{5.2}$$

5.3.3 Results and Discussion

5.3.3.1 Moisture Limited Evaporation During Drought

Figure 5.9 and Figure 5.10 show the results of the modelled cumulative evaporation for each rooting depth (800, 1000, 1200 and 1400 mm) from May 1 - Sept 30 for the 2000 and 2001 growing seasons. It is apparent that theoretical differences between the *P-M* and *G-D* models result in differences between the cumulative evaporation estimates at each depth. The cumulative evaporation for the *P-M* model was slightly higher than the *G-D* model, and the difference

between them increased slightly with rooting depth. Evaporation was underestimated with shallower rooting depths and overestimated at deeper rooting depths. In other words, this indicates the initial soil moisture is important when modelling evaporation over a single season in drought.

In 2000, the poorest agreement between modelled and observed cumulative evaporation was for the 0.8 m rooting depth. The *P-M* estimated cumulative total was 86% (-26 mm) of the observed total whilst the *G-D* was 79% (-39 mm) of the observed (Figure 5.9). The depth at which the best agreement occurred was different for the *P-M* and *G-D* models. In 2000, the total evaporation for the *P-M* model was nearly equal to the observed with a rooting depth of 1.2 metres. For the *G-D* model the best agreement (-3 mm) was for the 1.4 m rooting depth (Figure 5.9); whereas the *P-M* model overestimated the total evaporation at this depth by 7% (14 mm).

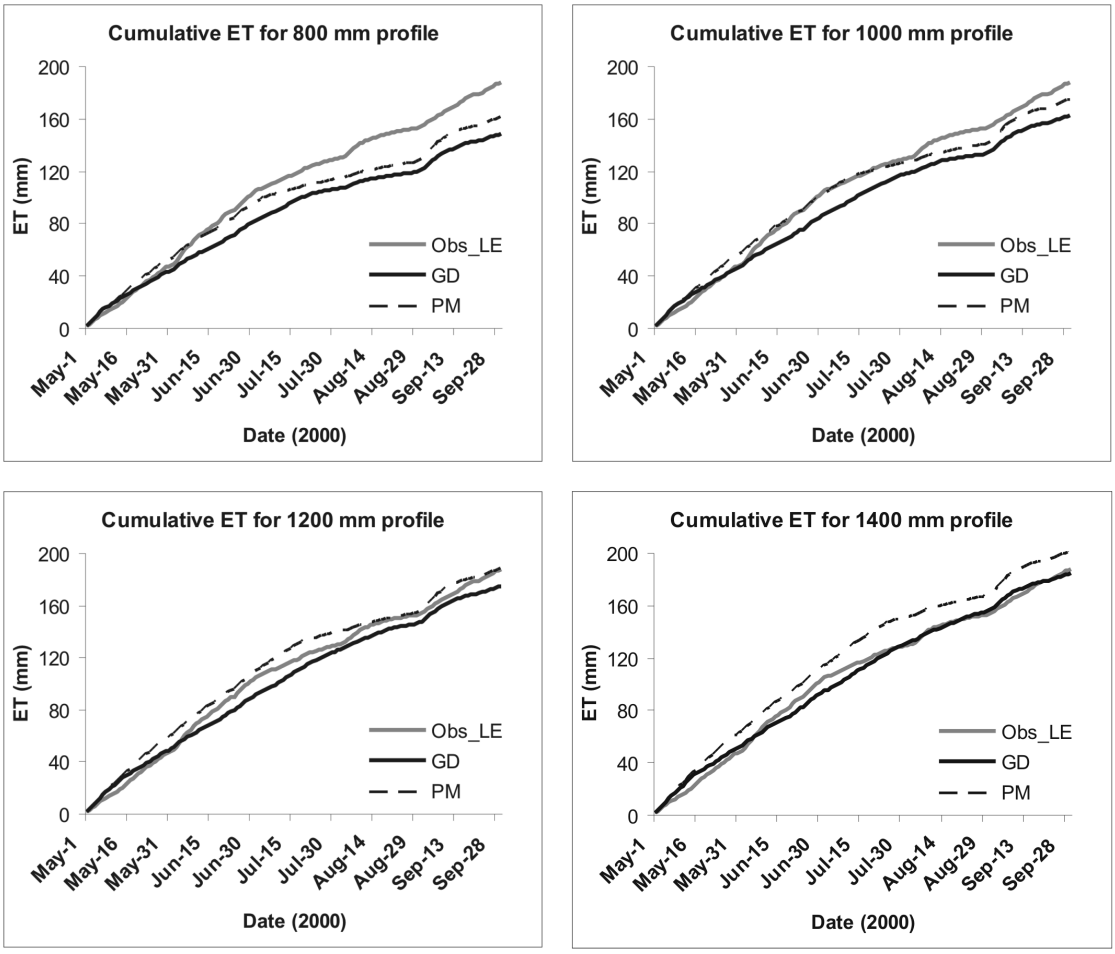

Figure 5.9: Model results for the 2000 drought period for soil profile depths of 800, 1000, 1200 and 1400 mm.

In 2001, the poorest agreement between modelled and observed cumulative evaporation was also for the 0.8 m rooting depth. The *P-M* cumulative total was 88.6% (-18.6 mm) of the observed total whilst the *G-D* was 83% (-27 mm) of the observed (Figure 5.10). The observed evaporation for 2001 presented a somewhat simpler case compared to that for the 2000 growing season where a sudden increase in evaporation occurred at the end of the season. In contrast, the evaporation in 2001 increased steadily from the beginning of May and then increased more slowly (began to level off) around the start of July.

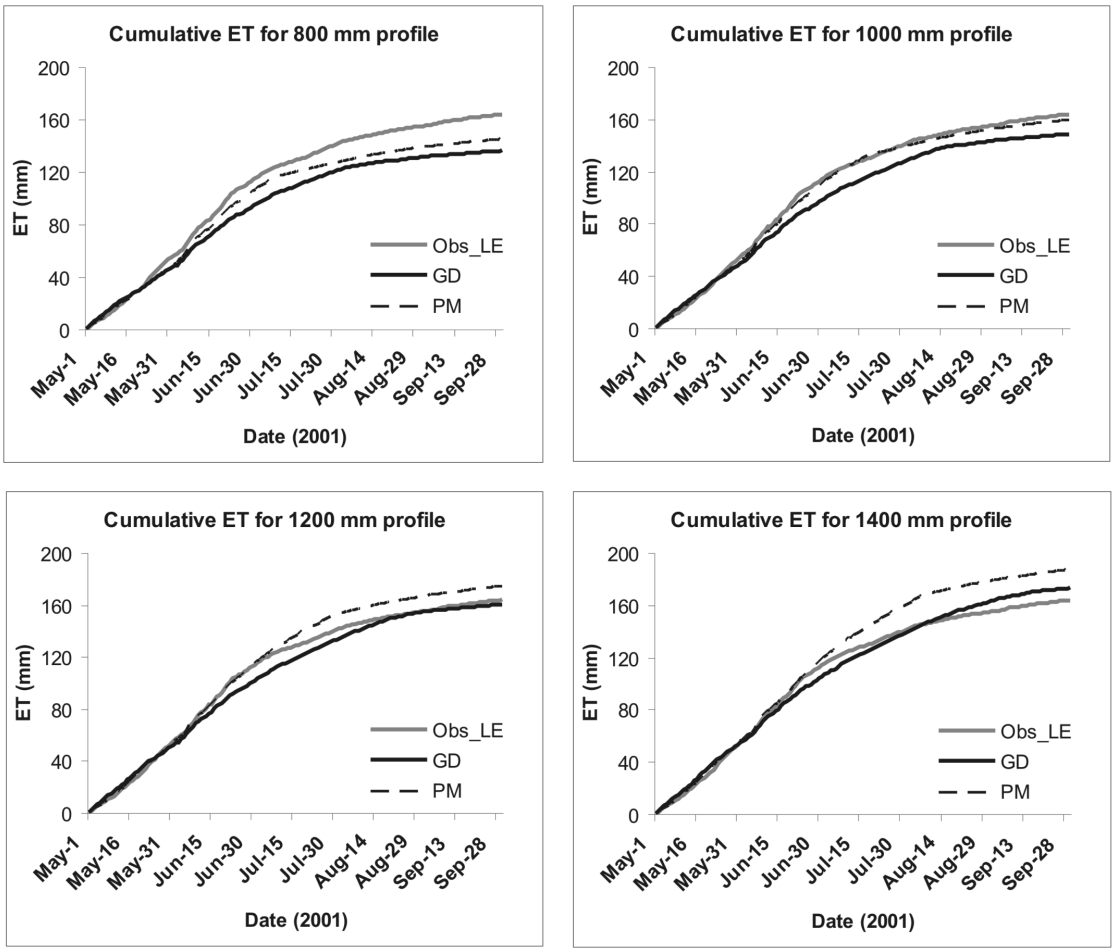

Figure 5.10: Model results for the 2001 drought period for soil profile depths of 800, 1000, 1200 and 1400 mm.

In this case, the cumulative evaporation with a rooting depth of 1 m for the *P-M* model agreed surprisingly well with observations over the season and only underestimated the observed total by 2.5% (-4 mm). The *G-D* model underestimated the observed evaporation by 10% (-15

mm) at this depth. The *G-D* model showed a considerable improvement compared to the observed total (-3 mm) at a rooting depth of 1.2 m, whilst the *P-M* method overestimated the total by 6% (10 mm). In general, reasonable agreement between the modelled and observed cumulative evaporation could be achieved with either the *P-M* or *G-D* models. In the case of the *P-M* model during drought for the grasses at Lethbridge, setting a rooting depth of 1 to 1.2 m provided the best results. This is in agreement with the rooting habits of these and similar grass species according to the extensive research of Weaver (1925; 1926) and Weaver and Clements (1938). In the case of the *G-D* model a depth of 1.2 m to 1.4 m provided the best agreement for the cumulative total.

The differences between the cumulative evaporation from the *P-M* and *G-D* models and apparent lack of a common optimal rooting depth can be attributed to the difference in theoretical approaches. In contrast to the *P-M* model the *G-D* model does not consider the physical characteristics of plants such as LAI which are very low in early spring and over the period in general. The reduced LAI produces an increase in the resistance early in the season for the *P-M* model which reduces evaporation estimates and subsequently can deplete the stored moisture less rapidly than does the *G-D* model. Also, later on the humidity deficit is generally high due to the drought conditions which results in an increase to the drying power term, and reduces the relative evaporation. As a result of the combined effects, the *G-D* model produces a lower estimate of seasonal evaporation when compared to that of the *P-M* model. For example, the results show the *G-D* tends to overestimate evaporation early in the season and underestimates evaporation during the period when vegetation is transpiring most rapidly.

As the rooting depth was increased for subsequent model runs, the available water content also increased which generally results in larger differences between the model totals. This can be attributed in part to the value of 50 s m^{-1} used for r_{cmin} in the *P-M* model runs. Under conditions of increased soil moisture, evaporation increases more appreciably relative to the evaporation that would occur if a larger minimum value were used (e.g. 62 s m^{-1}). In the case of the *G-D* model there is no provision to treat plant characteristics or phenology, so that the only adjustment that can be made to increase evaporation would be to either increase the initial moisture content or increase the rooting depth. It would appear based on the results, that overestimates of evaporation by the *G-D* model are more likely to occur early in the season when vegetation coverage is relatively low or during severe drying conditions.

Three recent studies are briefly discussed here and put into context of the current research. Brimelow et al. (2010) examined the application of PAMII (see literature review) for estimating evaporation in relation to drought. They validated daily evaporation estimates obtained with PAMII for the short-grass prairie (Lethbridge AmeriFlux site) and a barely field near Calgary, Alta for contrasting years during the drought period. At the grass site they obtained an RMSE of 0.64 mm/day for modelled estimates whereas the RMSE for estimates at the barely site were higher by comparison (1.19 mm/day). They also found that the minimum resistance required to model evaporation varied from year to year depending on the conditions. This supports the earlier discussion on limitations and difficulties of applying the resistance term. Further, Gervais et al. (2010) found that the resistance term needed to be modified in PAMII to more accurately model changes in the soil water content.

Zha et al. (2010) examined the interannual variation in eddy covariance measurements of evaporation during the drought period at the Lethbridge grassland site and also from three forested sites (aspen, pine, spruce) in the boreal forest region of Western Canada. They found considerable variation in the drought responses among the grass and aspen forest sites compared to the coniferous forest sites (pine and spruce). For example, the largest variation in annual evaporation occurred at the grassland and aspen sites whilst the largest reduction in evaporation occurred at the grass site under drought conditions. They also observed the annual variation was lowest at the coniferous sites which maintained a relative constant rate regardless of water stress. They attribute the varying responses during drought to physiological differences (e.g. phenological, structural, stomatal) among the vegetation types.

5.4 Summary and Conclusions

Two modelling approaches were used to examine the suitability of physically-based evaporation models for application under very different environmental conditions in distinct Prairie landscapes. The first approach examined the *P-M*, *G-D* and *BT* models at a tall mixed grass upland site during the 2006 field campaign at SDNWA without enforcing hydrological continuity. The second approach presented a demonstration of the effect of rooting zone depth on seasonal evaporation estimates for a short mixed grass prairie under drought conditions. In this case the *P-M* and *G-D* models were linked to infiltration, runoff, and soil moisture accounting algorithms within CRHM. Their ability to estimate cumulative evaporation was examined over

the growing season during the 2000 and 2001 drought periods. Modelled evaporation estimates were compared against eddy covariance observations obtained at the sites during the study periods.

SDNWA

In general, the *P-M*, *G-D* and *BT* models were shown to provide reasonable estimates of evaporation when compared with observations without the enforcement of continuity. There was good agreement between modelled and observed evaporation for a total of 68 days of observations. The models also provided good results for several multi-day periods ranging in length from 2 days to 2 weeks but no single model provided the best agreement consistently. The relative errors among the model estimates varied depending on the time scale of interest and tended to increase with a decline in the length of the observation period. As the frequency of the estimates increased to daily and 15 min intervals, it was found that there was a large amount of scatter among the estimates and observations but the errors are likely to cancel out over longer periods for hydrological applications in a prairie environment. Results suggest that the *G-D* model presents a useful alternative to methods that require estimation of a complex canopy resistance term when water is not strongly limiting and continuity is not enforced.

It is important to note that estimating evaporation over longer time periods (several days to weeks) may be appropriate for the purpose of long term water balance calculations. However, estimates of water vapour fluxes (also heat and momentum) at the surface are needed for much shorter time scales for modelling atmospheric processes. Estimates for shorter time periods are also needed for calculating antecedent soil water content conditions for runoff calculations in hydrological models. This has important implications for flood monitoring and management in that larger errors for daily and sub-daily periods may be unacceptable for specific uses, such as for numerical weather prediction models and hydrological runoff models.

Future improvements in resistance formulations might consider the limitation of using a single minimum reference value for the unstressed canopy resistance. This value may be potentially different following the period of peak evaporation where evaporation begins to decline but differences in leaf area are not large and soil moisture and available energy are not limiting factors (e.g. due to a reduction in stomatal activity after the reproduction stage of growth has been completed). In the case of the *BT* model the canopy resistance term has a considerable

influence on the rate of evaporation, as does changes in surface temperature. Nevertheless, a Dalton-type bulk transfer approach is attractive given its applicability for both land and water surfaces and it is also amenable to directly using observations of surface temperature. This has potential implications for studies concerning climate change or even characterizing severe drought which is a common occurrence in Prairie environments. Increased surface temperatures are likely to occur under conditions of reduced water availability resulting in feedbacks to the atmosphere. Future improvements to the *BT* model applied here might consider an improved resistance formulation that covers the complete range of plant-specific and phenological stages of growth.

Lethbridge Drought Application

The influence of rooting zone depth on actual evaporation estimates was examined for the drought of 2000 and 2001 at Lethbridge. Two hydrological models consisting of theoretically different evaporation models (*P-M* and *G-D*) were assembled using a suite of physically-based model algorithms provided within the CRHM platform. Under conditions when soil moisture is non-limiting the actual evaporation is calculated without restriction. Continuity is enforced to limit actual evaporation estimates as drying progresses and moisture reserves become depleted.

Both the *P-M* and *G-D* evaporation models were shown to provide reasonable agreement with the cumulative totals observed over the course of the growing period May 1 – Sept 31 for 2000 and 2001. The *P-M* model provided good agreement at specified rooting depths of 1 m and 1.2 m for 2000 and 2001 respectively. This is in agreement with research by Weaver (1968) in the case of the rooting habits of short, shallow rooting grasses and mid-height grasses such as wheatgrass under drought conditions. The *G-D* model was found to provide the best agreement at a rooting depth of 1.2 m in 2000 and 1.4 m in 2001.

In the case of the *G-D* model, the lack of a physical description of vegetation characteristics was problematic for early season estimates. This presents a general limitation for suggesting physically meaningful improvements to correct model errors. The results suggest that for the model simulation presented here, which explicitly considers soil moisture continuity, there would appear to be no benefit to choosing the *G-D* feedback model over the resistance-based model for estimating cumulative evaporation over the growing period. This is because soil moisture accounting is needed by both models to limit evaporation under drought conditions.

The potential effect of spatially varying driving factors has not been considered here. For example, accounting for spatial variations in surface temperature, soil moisture, turbulent transfer, or vegetation characteristics over the variable flux footprint may provide more reliable model estimates where model errors are apparent.

CHAPTER 6

DISTRIBUTED ESTIMATES OF EVAPORATION AT THE FIELD SCALE

6.1 Introduction

The analysis presented in this chapter addresses the second research objective by integrating the spatial patterns of key surface variables to obtain distributed estimates of actual evaporation over a field. Actual evaporation was modelled at the field scale using a combination of data assimilation and mapping using ArcGIS and IDRISI software. For this purpose, remotely sensed images were combined with surface and climate reference observations collected at St. Denis in 2007. Estimates of actual evaporation were obtained using the *G-D* model and the general equations are referred to in section 2.3.2.2 in Chapter 2, and Eq. 2.12 – 2.14, and Eq. 4.5.

The energy available for driving evaporation is a key factor in energy balance equations and Penman-type combination models. Available energy is the difference between net radiation, Q^* and the ground heat flux, Q_g. The net radiation at the surface dominates energy availability in terrestrial landscapes and can be expressed as

$$Q^* = K\downarrow(1-\alpha) + L\downarrow - L\uparrow \quad , \tag{6.1}$$

where $K\downarrow$ and $L\downarrow$ are the incoming shortwave and longwave radiation, α is the surface albedo or fraction of shortwave radiation reflected from the surface to the atmosphere, and $L\uparrow$ is the outgoing longwave radiation. Q^* has the potential to vary spatially depending on the surface conditions encountered. The spatial variation of $K\downarrow$ and $L\downarrow$ is negligible for surfaces exposed to the same atmospheric conditions. Spatial variations in α and $L\uparrow$, however, may be large depending on the surface cover (e.g. water, soil, vegetation) and general surface state conditions (wet vs dry). The variability of important surface properties is difficult to capture from point observations alone. Remote sensing imagery can provide valuable spatial information on α and $L\uparrow$ which can be used to distribute estimates of the net radiation needed for driving evaporation models.

A method was developed for distributing net radiation over the landscape which assimilates remotely sensed visible and thermal images and surface observations of incoming shortwave and longwave radiation. A case study is presented for August 5, 2007 at the SDNWA and distributed

estimates of the mean daily actual evaporation were derived using the *G-D* feedback model. The *G-D* model has been shown thus far to provide reasonable values of evaporation and is particularly useful where detailed soil moisture information is not available to parameterize a resistance type formula. There are four main objectives to this study:

1) To demonstrate an approach for distributing mean daily net radiation as a function of the one-time-of-day images and a reference value of mean daily net radiation and validate the estimates at two sites with available measurements. The sensitivity of the mid-day evaporation rate to changes in key surface variables obtained from the mid-day images was examined.
2) To obtain direct estimates of spatially distributed mean daily evaporation over the field sized area based on the distribution of the driving surface variables and reference station data.
3) To examine the distributions of evaporation and driving surface variables in order to evaluate the effects on upscaled estimates of evaporation. Differences between the point measurements and model estimates were compared, including against the areal estimate of the model.
4) To examine the spatial associations of driving variables and the implications for scaling are considered.

For the field scale study presented here, the thermal bands of Landsat, AVHRR and MODIS were too coarse. Alternatively, very high resolution aerial imagery (< 5 m), obtained from a hand held digital camera and a thermal radiometer were used for demonstration purposes.

6.2 Theory on Distributing Evaporation over a Field

The following section discusses the theoretical basis of an approach for distributing direct estimates of actual evaporation over larger areas. It may also be useful towards improving our understanding of spatial variations in evaporation in natural landscapes. An implicit assumption is that spatial variations of surface flux variables governing evaporation are close to their maximum around the time of solar noon. Colaizzi et al. (2006) indicate that such an assumption may be valid for a period of no more than approximately 2 hours from the actual time of solar

noon. As such, valuable information about spatial variations in driving surface variables may be obtained from remotely sensed images acquired near this time.

Furthermore, distributed estimates of mean daily evaporation were calculated over images containing the driving surface variables. Aerial images were obtained over the SDNWA from a hand-held digital camera (visible wavelengths) and thermal radiometer on Aug 5, 2007 concurrent with the Landsat 5 overpass at approximately mid-day (12 noon, Central Standard Time; 1800h UTC, Coordinated Universal Time). The sensitivity of evaporation to key variables derived at mid-day may be examined by considering the 'evaporation ratio', E_R. This is the ratio of evaporation, E_i to the reference evaporation, E_{iref} defined at a known location,

$$E_R = \frac{E_i}{E_{iref}} \quad . \tag{6.2}$$

Key variables derived from remote sensing information can be spatially distributed over the landscape and then normalized by reference values. The resulting ratio at each pixel can be used as an index to distribute a known value over the image. For instance, an albedo ratio, α_R, emitted longwave ratio, $L{\uparrow}_R$, and roughness ratio Z_{oR} can all be defined for pixels within an image from reference values,

$$\alpha_R = \frac{\alpha_i}{\alpha_{iref}} \tag{6.3}$$

$$L{\uparrow}_R = \frac{L{\uparrow}_i}{L{\uparrow}_{iref}} \tag{6.4}$$

$$Z_{oR} = \frac{Z_{oi}}{Z_{oiref}} \quad , \tag{6.5}$$

where, the subscripts "*i*' and "*iref*" represent the value at a given pixel, and the respective value at a reference location.

The ratios, α_R and $L{\uparrow}_R$ can be combined to obtain the mid-day net radiation ratio, Q^*_R which can be derived for pixels within an image from the common incoming short and longwave radiation fluxes over the image extent. This equation can be written as,

$$Q*_R = \frac{Q*_i}{Q*_{iref}} \quad . \tag{6.6}$$

6.2.1 Visible and Thermal Images

Remote sensing information of reflected shortwave and emitted longwave radiation can be used for calculating the net radiation balance. The wavelengths of interest approximately span the 0.4 to 14 μm portion of the electromagnetic spectrum (EM) (Liang, 2000). Unfortunately, remote sensing at these wavelengths may be affected by unfavourable atmospheric conditions, namely clouds and haze that can potentially limit the usefulness of remote sensing approaches to estimating evaporation. Nevertheless, remote sensing approaches remain attractive for modelling applications concerned with spatially varying surface properties. Surface albedo, α and surface temperature are key variables needed for the net radiation balance and can be obtained from visible and thermal images. Where higher resolution imagery is needed for a detailed study, and the influence of clouds reduced, images may be acquired from an aircraft using a digital camera and a hand-held thermal radiometer that cover the majority of the appropriate visible and thermal wavelengths.

Visible Imagery

High resolution images were obtained from the window of an aircraft (courtesy of Mitchinson Flying Service) at a height of approximately 1 km above ground level (AGL). The images were taken over the study site using a digital camera. Unfortunately, raw reflectance information was unavailable and alternative instrumentation for obtaining aerial imagery was not available at the time. The digital camera used was a Canon Powershot A70 and the technical specifications for the A70 are as follows: 3.2 megapixels with a maximum image resolution of 2048 x 1536 pixels, a CCD (charge-coupled device) imager, and a DIGIC (Digital Imaging Core) processor proprietary to Canon. The combination of CCD and DIGIC processing capabilities provide enhanced light sensitivity, reduces white saturation problems, and produces high-quality noise free images.

The light received at the CCD senor array spans the visible portion of the EM spectrum at 0.3 to 0.7 μm and includes a limited portion of near-infrared wavelengths. The full near-infrared portion of the EM spectrum was not measured but only a small portion is missed. The charge accumulated at each pixel location is converted to a voltage and transferred to the DIGIC for processing and conversion to a digital value, and finally compressed into a RGB colour format which spans 0.4 to 0.7 μm of the visible spectrum. The visible imagery contains valuable reflectance information that can be used for deriving the needed albedo estimates at a much higher spatial resolution (less than 1 m) than is achievable by current satellite instruments; which is generally greater than 30 m. An advantage of using a digital camera over satellite-based optical remote sensing is that the images are completely free of clouds due to the relatively low flight height. Conversion of the digital data to meaningful albedo values required the application of a scaling technique based on a known albedo value similar to that developed by Corripio (2004).

Thermal Imagery

High resolution images of surface temperature were obtained using a hand held Forward Looking Infrared (FLIR) radiometer; ThermaCAM P20. The detector of the P20 is comprised of a Focal Plane Array, uncooled microbolometer that provides measurements of emitted thermal radiation with a maximum image resolution of 320 x 240 pixels for a 24° by 18° field of view. It measures infrared radiation in the spectral range of 7.5 – 13 μm. This is a wider spectral range than measured by some satellites which operate at 10 – 12.5 μm (e.g. Landsat, MODIS, and AVHRR), but is similar to ASTER which operates at 8 – 12 μm. A number of environmental effects are needed to be compensated for in the internal radiometer software in order to derive surface temperature images; namely, surface emissivity, ambient air temperature and humidity, and an estimate of the distance between the target and the camera detector.

The surface emissivity was taken to be 0.98 which corresponds to a range of natural surface emissivities as reported by Brutsaert (1982). The remaining parameters were specified based on the average ambient conditions observed near the surface and the atmospheric conditions indicated by the plane's instrumentation at the flight height. The thermal radiometer provides a high level of spatial detail (< 5 m resolution) for images captured at a flight height of approximately 1 km AGL. This is a much greater spatial resolution than is achievable by satellite

radiometers which typically operate at a horizontal resolution of greater than 50 m; e.g. Landsat ETM, (60 m), ASTER (90 m), Landsat TM (120 m), MODIS (1 km), AVHRR (1 km), GOES (10 km). The spatial resolution of these radiometers is also much coarser than the resolution of the onboard optical sensors.

6.3 Measurement Sites for Model Parameterization and Validation

The arrangement of the eddy covariance/micrometeorological stations at the site was such that one station could serve as a reference site and the other a validation site for evaluating model estimates. A third micrometeorological station maintained by the National Water Research Institute (Environment Canada, Saskatoon) was also located several hundred metres away at an upland location. Figure 6.1 shows the locations of the three stations and relevant measurements for comparison with estimated values. Spectral reflectance measurements taken on Aug 21, 2007 during a field study at the mixed grass upland area were also available (data courtesy of Xulin Guo) for comparing the results of the estimated values. The measurements were obtained using methods described by Zhang and Guo (2007). Unfortunately, measurements were unattainable for Aug 5 but the reflectance data collected on Aug 21 is still useful for assessing the validity of estimated albedo values. This is reasonable as albedo values measured at both CNR1 sites were found to be relatively constant over this period. Spectral reflectance was sampled using an ASD FR Pro spectroradiometer (Analytical Spectral Devices, Inc. Boulder, Colorado) at intervals of 4.5 m (Figure 6.1). The measured wavelength range was 350–2500 nm with a spectral resolution of 1 nm. Measurements were collected at a height of 1 m above the canopy at nadir with a 25° field of view probe. Samples were taken between the times of 12 noon local time and solar noon. Reflectance was calibrated using a white spectralon reflectance panel (Labsphere Inc. North Sutton, New Hampshire) approximately every 10 min to account for variations in atmospheric conditions.

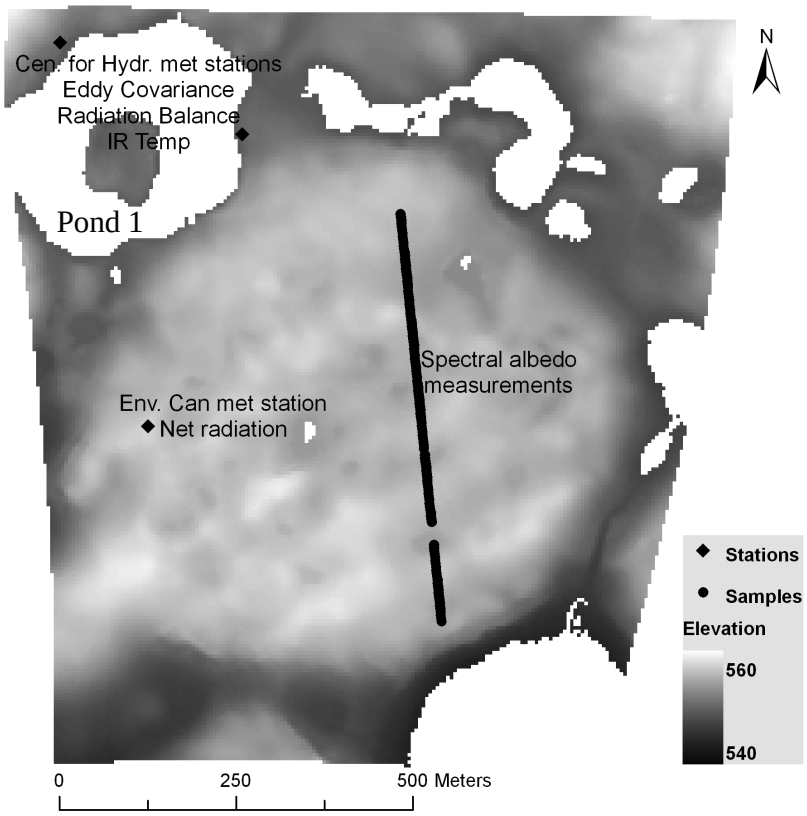

Figure 6.1: Land surface elevation map and locations of measurement sites for eddy covariance and micrometeorological observations, and sample points for spectral albedo along an existing transect with 4.5 m spacing.

6.3.1 General Conditions and Modelling Assumptions

Reference climate data needed for the model were obtained from concurrent observations taken at the site. These included measurements of the mid-day incoming shortwave and longwave radiation and also the mean daily air temperature, humidity, and wind speed. The mid-day incoming shortwave, $K\downarrow$ (835 W m^{-2}) and longwave, $L\downarrow$ (320 W m^{-2}) radiation needed for calculating distributed estimates of the mid-day net radiation were obtained from a CNR1 net radiometer located on the east side of pond 1 (Figure 6.1); the reference location. The potential impacts of spatial variations in the mean daily air temperature, the vapour deficit, and wind speed on evaporation estimates were taken into consideration.

Over the course of the day on Aug 5, 2007 the prevailing wind direction was approximately from the north-west (330°). Heat and humidity transported to the EC station on the west side of

pond 1 (Figure 6.1) was from the upwind grassed surface that dominated the area. At this station the mean daily temperature, vapour deficit and wind speed was 18.7 °C, 0.93 kPa and 1.9 m/s respectively. It should be noted here that sheltering effects may have influenced wind speed at this particular location due to the general rise in terrain toward the west and north-west of pond 1. On the east side of pond 1 heat and humidity was carried to the instruments from over the water surface. At this EC station the mean daily air temperature was 18.6 °C, the vapour deficit was 0.86 kPa, and the wind speed was 2.9 m/s. The small increase in humidity is likely due to the influence of the pond and the increase in wind speed can reasonably be attributed to a reduction in surface roughness. Atmospheric measurements were also obtained from an Environment Canada station (data courtesy of Chris Spence) located at the upland site indicated in Figure 6.1. Given the wind direction on this day, the station was downwind of a cultivated area. At this site the mean daily air temperature was 18.6 °C, the vapour deficit was 1.14 kPa, and the wind speed was 3.1 m/s.

In general then, the range of mean daily air temperature (0.1 °C), vapour deficit (0.2 kPa) and wind speed (1 m/s) that can reasonably be attributed to the grassed and cropped surfaces was relatively small. As such, further consideration was given to the sensitivity of the model to determine whether the small variations in humidity and wind speed could be important. For this purpose an examination was conducted on observations collected during the 2006 field season. During that study period, a portable eddy covariance mast was periodically placed over different surfaces in the area for comparisons against the fixed upland site (See Appendix A). Evaporation was estimated from the 15 minute observations at the fixed upland location using the *G-D* model. Measured values of the humidity deficit and wind speeds obtained during the same time from the portable EC mast were then substituted for those at the fixed site and the evaporation recalculated. The variation in evaporation estimates was small with an RMSE = 0.02 mm which suggested the *G-D* model was not sensitive to small differences in the humidity deficit and wind speed observed over the different land surfaces.

A wind flow model could have been applied to distribute wind speed over the area which would add to the complexity due to the scale at which the evaporation estimates are derived (5 m). In the case of the vapour deficit, an empirical feedback algorithm, such as that developed by Granger (2000), could have been applied to derive distributed estimates over the area. However, based on the field data collected in 2006 (See Appendix A), the variability of surface temperature

at 5 m resolution is likely to be much larger than the humidity deficit of the overlying atmosphere over the same spatial scale. Based on the sensitivity analysis and the previous considerations, it was decided that the climate conditions could reasonably be assumed constant over the extent of the image.

The aerodynamic terms, and also Δ and γ (discussed in Chapter 2, section 2.3.1) were subsequently calculated from observations of the mean daily temperature, humidity deficit and wind speed. A temperature of 18.6 °C was used for calculating mean daily values for the slope of the saturation pressure curve = 0.13 kPa $°C^{-1}$, and the latent heat needed for the conversion of water to vapour, λ = 2457 kJ. The psychometric constant, γ (Eq 2.10) was calculated based on λ and the elevation of the site above sea level, where the atmospheric pressure was taken to be 95 kPa. The humidity deficit measured on the west side of pond 1 was used at 0.93 kPa. Given that the site is largely unsheltered, a mean daily wind speed of 3 m/s was used. The ground heat flux term was not included in the daily calculation of available energy which was assumed to be driven by the net radiation. This was reasonable given that measured values of the ground heat flux at the two station locations basically balanced over the day. Specifically these were 2 W m^{-2} under a dense grass cover and site disturbance was small, and 10 W m^{-2} under a shorter grass that was more disturbed.

6.4 Distributing Net Radiation Balance Components

6.4.1 Reflected Shortwave Radiation – Albedo

Corripio (2004) developed a method of estimating snow albedo from film based terrestrial photographs. The underlying assumption of the method is that reflected radiances output from the camera can be directly related to surface albedo values. In other words, the camera interpreted surface reflectance information is dependent on solar incidence angle, surface reflectance and atmospheric properties, and view angle of the camera. Corripio (2004) has shown that it is possible to obtain albedo estimates over an image extent if, 1) surface albedo is known for a corresponding reference pixel in the image, and 2) the known albedo is linearly scaled over the landscape by the normalized reflectance derived at every pixel location. The normalized reflectance can be obtained from the ratio of the reflectance value of an individual pixel to the

reflectance at the corresponding reference pixel where albedo is known. This is consistent with the theory applied here for distributing the net radiation term.

The pixel reflectance can be normalized from a digital image where each pixel is characterized by a digital number (*DN*). Greyscale images are well suited for this purpose and an equation for distributing a known albedo as a function of relative surface reflectance can be written as

$$\alpha_i = \alpha_{iref} \frac{DN_i}{DN_{iref}} \quad , \tag{6.7}$$

where, α_i is the albedo estimate of an individual pixel and α_{ref} is a known albedo defined at a reference pixel. DN_i is the *DN* for an individual pixel and DN_{iref} is the *DN* value at the reference pixel where albedo is known. From Eq. 6.7 it becomes apparent that α_i will have the same value as α_{iref} when DN_i and DN_{iref} are equivalent.

In this study α_{iref} = 0.153 at mid-day was obtained from hemispherical measurements of incoming and outgoing shortwave radiation provided from a CNR1. The CNR1 provides a small area ("point") measurement of the broadband albedo (0.3 – 3.0 μm) based on the angular properties of the surface (Disney et al., 2004). The combination of linear scaling of Eq. 6.7 and the characteristics of the CNR1 helps to address two important considerations for estimating surface albedo from remotely sensed data. First, a linear function is typically necessary to perform a narrow-to-broadband albedo conversion (Liang, 2000; Liang, 2004). Second, the bidirectional reflectance properties of the surface need to be considered (Nicodemus et al., 1977; Lucht et al., 2000; Roberts, 2001).

In the present case, a direct measure of broadband albedo was provided by the CNR1 that is based on hemispherical sampling at the surface (i.e. bidirectional reflectance is inherent to the measurement). The measured value can then be scaled to each pixel as a function of the indexed surface reflectance using Eq. 6.7. In other words, the combined effects of directional and bidirectional reflectance properties of the surface, based on solar incidence angle and the radiance received at the camera viewing angle, are inherent in the narrow-to-broadband albedo scaling process.

To derive the estimates of albedo, the RGB colour aerial image was converted to an 8-bit grayscale image. The result is an image where each pixel had a reflectance value represented by

a digital number (*DN*) in the range of 0 – 255. This preserves the relative differences in reflectivity at the surface. As is the case with standard remote sensing imagery, less reflective surfaces are characterized by smaller *DN* values and more reflective surfaces by higher *DN* values. The visible image was then georeferenced to a 0.5 m resolution LiDAR digital elevation model (DEM) of the area surveyed in Aug, 2005 (Töyrä et al., 2006).

This was necessary as the image was acquired off-nadir. For this purpose, ArcGIS software was used, and in the interest of greater accuracy, 90 control points were identified in the image based on a ground survey conducted over the course of the study period in 2006 and 2007. A spline transformation was applied to rectify the image. The general advantage of applying the spline method is that the image coordinates are forced to pass through the projection coordinates at every control point which minimizes the residual error at the points. A general limitation is that the manual process is labour intensive and errors outside the control points are inevitable. The image was then resampled to a more practical resolution of 5 m to be comparable to the CNR1 footprint. Based on the assumption of a radiometer footprint being 10 times the instrument height above the canopy, gives a footprint in the range of between 5 to 10 m^2; which is typical of radiometer measurements (Vercauteren et al., 2009).

Since the intent was to use this apparent reflectance information in lieu of satellite based imagery, consideration was also given to potential atmospheric affects and inaccuracies where albedo values might be higher than would normally be expected (e.g. water bodies). For this purpose, a Dark Object Subtraction (DOS) method (Liang, 2004) was applied because the study area contains several wetland water bodies, some of which are a few meters deep. Song et al. (2001) and Liang (2004) indicate that it can reasonably be expected that these types of water bodies will have the lowest reflectance values (i.e. approximately 0).

Application of Eq. 6.7 produced an image of distributed albedo estimates and Table 6.1 shows the average and the range of a sample of albedo estimates for the various land covers. These values were obtained by averaging the estimate for every pixel falling along a line profile generated uisng ArcGIS. The resulting input image and the location of the reference and validation sites each equipped with a CNR1 are provided in Figure 6.2. An albedo estimate of 0.164 was obtained at the validation site on the west side of pond 1 and compares closely with the CNR1 measured value of 0.167. The agreement between the values is to be expected given that both the reference site located on the east side of pond 1 and the validation site located on

the opposite side of pond 1 are characterized by similar grasses. Low albedo values might also be attributed to tree shadows within the image but these appeared to impact only a very small portion of the data, and are mainly restricted to the tall aspen stand surrounding the pond located in the south east corner of the image.

Table 6.1: Estimated albedo mean and range for land cover types.

Landcover	Mean	Range
Wetland vegetation (W)	0.11	0.05 – 0.16
Brome grass (BG)	0.15	0.13 – 0.17
Mixed grass (MG)	0.17	0.15 – 0.19
Cultivated (C)	0.18	0.17 – 0.20
Fallowed (F)	0.20	0.17 – 0.23

The range of estimated albedo values is in the range of mean albedo values for deep water (0 – 0.05), grasses and crops (e.g. 0.15 – 0.25), forest (0.10 – 0.25), and gray soils (0.15-0.25) reported in Brutsaert (1982); 0.15 - 0.25. Relatively low values can reasonably be expected where vegetation was associated with increased water availability around wetlands and near bodies of water where the reflectance was assumed to be 0. Due to the specification of a spatial resolution of 5 m the general pattern of albedo estimates appeared to distinguish between cover types. For example, distinct boundaries emerged which marked the separation of albedo values for the mixed grasses (MG) and cropped area (C) from the sparser vegetation in the fallowed area (F), and the fringe vegetation of the wetlands (W) and the location of the surface water.

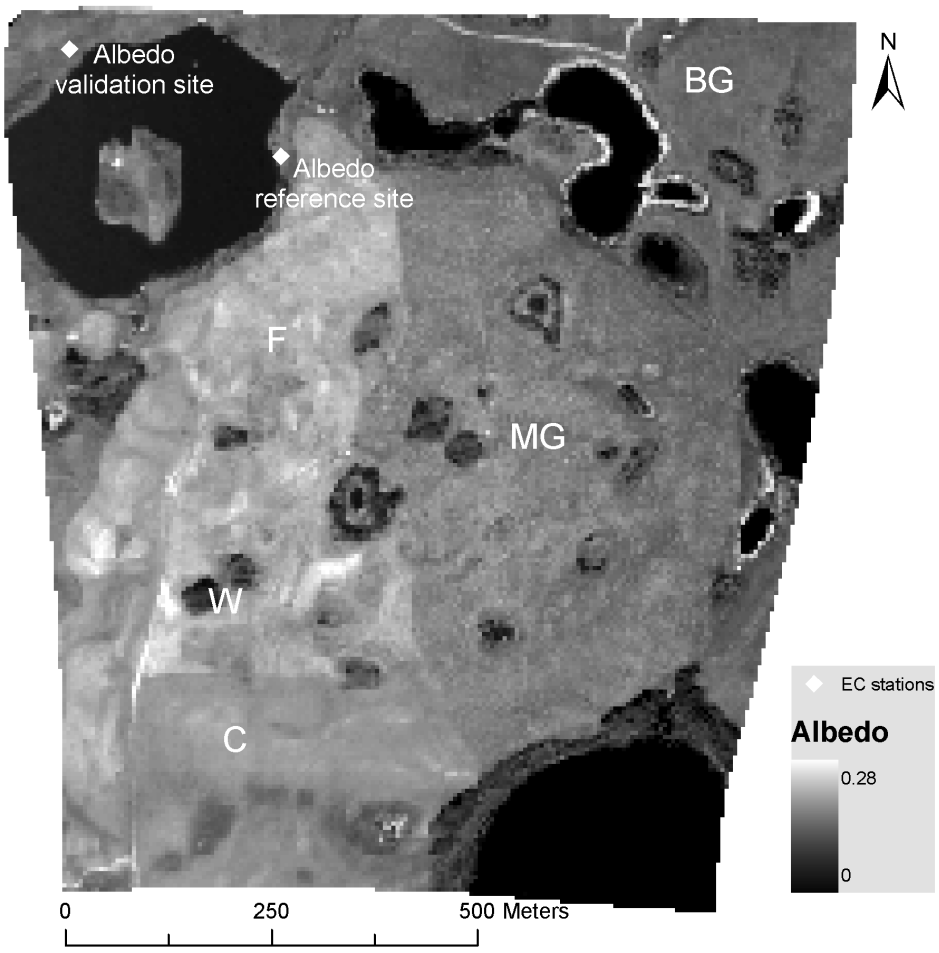

Figure 6.2: Albedo map (5 m resolution) derived from visible image taken at mid-day on August 5, 2007. Also shows location of reference and validation sites, letter codes indicate major land cover types: fallowed (F), mixed grass (MG), brome grass (BG), cultivated (C), and wetlands (W).

Albedo estimates for a series of pixels were compared against point values of albedo derived from the field measured reflectance which had been collected at a point spacing of 4.5 m. Disney et al. (2004) measured reflectance values at varying angles and found reflectance to be directionally invariant for winter wheat and therefore a Lambertian surface could be reasonably assumed. For simplicity, the mixed grasses were also assumed to behave as a Lambertian surface (i.e. scattering light equally in all directions). This allowed for the measured spectral reflectance to be treated analogous to Landsat imagery. As such, the measured reflectance data was separated into narrow wavebands corresponding to those measured by Landsat sensors 1, 3, 4, 5,

and 7. An empirically derived linear approximation for narrow-to-broadband albedo conversion, used for Landsat imagery (Liang, 2000), was then applied to the spectral reflectance data.

This allowed for a general comparison of estimated and field measured albedo values for the mixed grass area at approximately 100 sample points along the transect shown in Figure 6.1. In a few cases where two sample points fell within an image pixel (due to difference in point spacing) the average of the two values was taken. Overall, the Root Mean Square Error (RMSE) of the estimated and measured values was 3.5% or 0.035 for the non-dimensional albedo value. This was within the range of error 2% to 5% or 0.02 to 0.05 expected for the purpose of scientific research (Liang, 2004).

6.4.2 Emitted Longwave Radiation - Surface Temperature

The georeferencing procedure described earlier was used to georeference the longwave radiation map to the albedo map to in order to provide the best possible overlap between the visible and thermal images. The longwave radiation image was then coarsened (by averaging) to 5 m resolution to match the scale of the albedo map. The map of emitted longwave radiation, $L\uparrow$ provided in Figure 6.3 showed a large range of values 380 W m^{-2} - 480 W m^{-2}. The lowest values were associated with the bodies of water which are shown for instructional purposes but these were masked out in order to restrict evaporation estimation to the land surface. Again, the extent of tree shadows within the image was relatively small and appeared to be restricted to the north side of the tall aspen stand surrounding the pond located in the south east corner of the image.

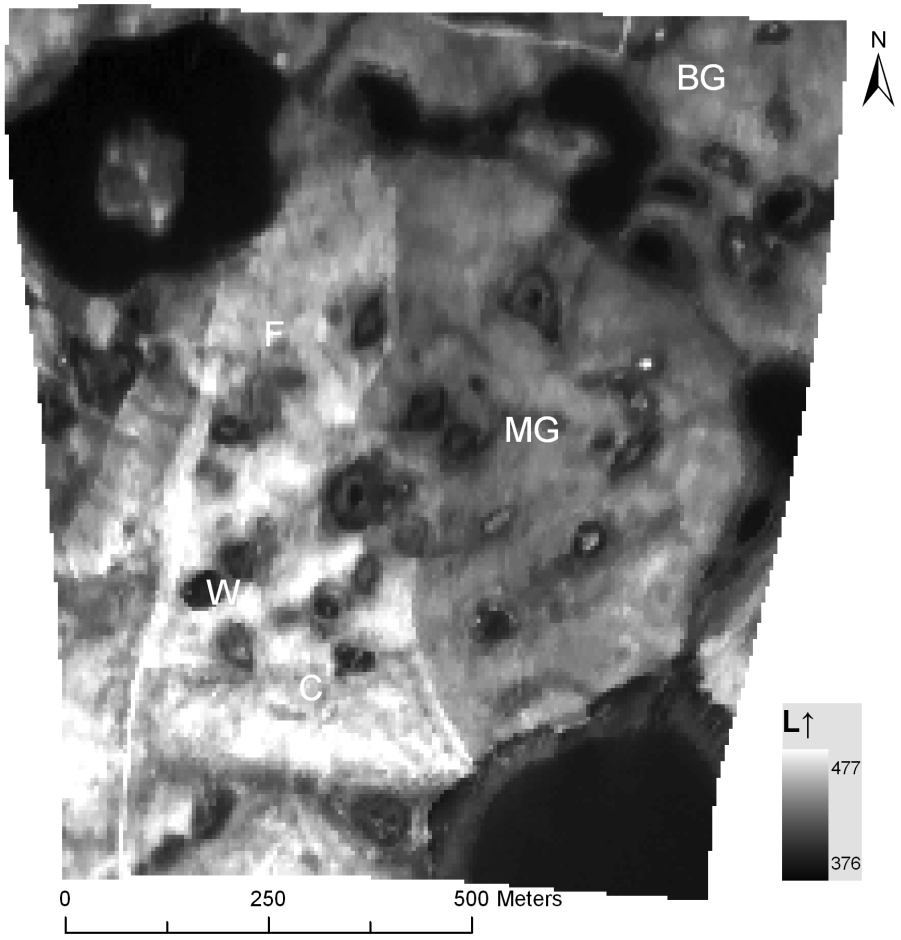

Figure 6.3: Surface emitted longwave radiation (W m^{-2}) map (5 m resolution) derived from thermal image taken at mid-day on August 5, 2007. Letter codes indicate major land cover types: fallowed (F), mixed grass (MG), brome grass (BG), cultivated (C), and wetlands (W).

A comparison was made between observations from the P20 thermal radiometer and measurements obtained at the reference and validation sites each equipped with a narrow-beam Exergen infrared thermocouple (IRTC) radiometer, and the emitted longwave radiation provided by the CNR1. The IRTCs were pointed at the respective vegetation surfaces and a control point collected during the field study was assumed to correspond to the location of a P20 radiometer pixel. The P20 measurements compared relatively well with the IRTC values, where the differences were less than -2 K (≈ -12 W m^{-2}). The P20 values deviated further from the CNR1 values by approximately -5 K (≈ -30 W m^{-2}). These larger differences may be attributed to, 1) the absorption properties of water vapour in the atmosphere which may reduce the signal at the P20 radiometer, and 2) general ambiguity between the footprint measurement scales of the respective

instruments, 3) possible influence of dust and dome heating of the downward facing pyrgeometer and elevated surface temperature resulting from site disturbance during routine maintenance. When considered against the entire balance of net radiation near mid-day, the difference in longwave radiation represents a relatively small error.

6.5 Distributing Aerodynamic Surface Roughness Height

Detailed descriptions of vegetation and surface characteristics are commonly needed for estimating evaporation which partly depends on the theoretical basis of the model. In the present case, only the surface roughness is required to calculate the vapour transfer function. Surface roughness is a key parameter in aerodynamic calculations of evaporation and is often derived as a function of the average height of surface elements (Brutsaert, 1982). The general assumption is that rougher surfaces enhance turbulence resulting in higher evaporation rates. It is possible to obtain roughness heights from LiDAR data. However, the data used to develop the DEM of SDNWA was collected in August of 2005. This was found to be problematic in that the spatial distribution and density of the major cover types, namely crops and grasses, was not the same in 2005 compared to 2007.

To maintain consistency, consideration was given to associating reflectance properties of the 8-bit grayscale visible image (used to index albedo) with generalized roughness classes. The approach used was similar to that commonly applied for the classification of vegetation from remote sensing imagery. That is, differences in the surface reflectance properties were the basis for identifying relatively homogeneous groups of data. It was previously indicated that the pattern of albedo appeared to be associated with differences in both cover type and water availability. The visible image also contained useful information about relative differences in texture among the respective cover types.

Given the level of detail (5 m resolution), a supervised classification that required training sites was not considered practical. Therefore, an unsupervised classification was performed based on the statistical properties of the reflectance data. This allowed the image to be initially segmented into grouped areas of similarity. This was accomplished using the IDRISI Kilimanjaro GIS software ‘surface analysis’ tool. The segmentation was performed by applying a standard deviation filter to the reflectance data. The process requires that data contain values between 0 and 255, which was already the case for the 8-bit image used to index albedo. The

standard deviation for each pixel in the image was derived by applying a moving filter consisting of a 3 x 3 grid and assigning the resulting value to the central target cell. Each standard deviation gets sorted from low to high and a bin range defined on either side of the pixel value by a specified threshold; this set the class width for pixels having similar standard deviations. Pixel values falling within the same bin range were then assigned the same class. Where a pixel value fell outside the range but the class boundaries overlapped, the mid-point is determined and a new class created.

Thirteen groups of reflectance values were produced from the initial segmentation of the image. The spatial associations of the grouped data were then evaluated against the visible imagery to determine if they could be combined further (i.e. associated with more generalized roughness classes). It was assumed that roughness classes could be assigned taking into consideration relative differences in topography, land use, vegetation structure, and apparent textures of the surface elements in the image. Subsequently, the thirteen initial groups were reduced to three groups of reflectance values.

The assignment of roughness heights, Z_o to the three groups was then addressed. Z_o is commonly taken to be 10% of the mean vegetation height, although it may be slightly different in the case of treed landscapes (Brutsaert, 1982). The fallowed, cropped and grassed areas were characterized by vegetation with heights generally between 30 cm and 80 cm, and 80 cm – 110 cm respectively. The fallowed and cropped surfaces were taken to be less rough and more uniform in the upland area compared to the denser, taller mixture of grasses assumed to represent a small step change in roughness. Therefore roughness values equal to 5 cm and 10 cm were assigned to the fallowed/cropped and grassed areas respectively; which was roughly 10% of the observed heights.

According to Brutsaert (1982), roughness values of between 20 cm and 40 cm are commonly specified for vegetation heights in the order of 1 m - 2 m and 8 m - 10 m respectively. In the case of trees, shrubs and tall, dense grasses surrounding many of the wetlands and areas in the northeast portion of the image, heights and the apparent roughness tended to be more variable; in the order of 1 m to 10 m depending on species and location. Regardless of actual height, these surface elements were fairly dense, tall and often more rigid than vegetation in surrounding areas. These surfaces were assumed to enhance turbulence and represented a larger

step change in surface roughness compared to the 5 cm and 10 cm classes. Therefore, a height of 40 cm was assigned to the roughest class.

Figure 6.4 shows the resulting distribution of the three roughness classes 5 cm, 10 cm, and 40 cm. assumed to be associated with grouped reflectance data and general differences in cover type. The resulting segmentation of the image into three general classes is analogous to approaches that divide the landscape into different land cover types. On a proportional basis the 5 cm, 10 cm, and 40 cm roughness classes represent 29.5%, 48.4% and 22.1% of the area.

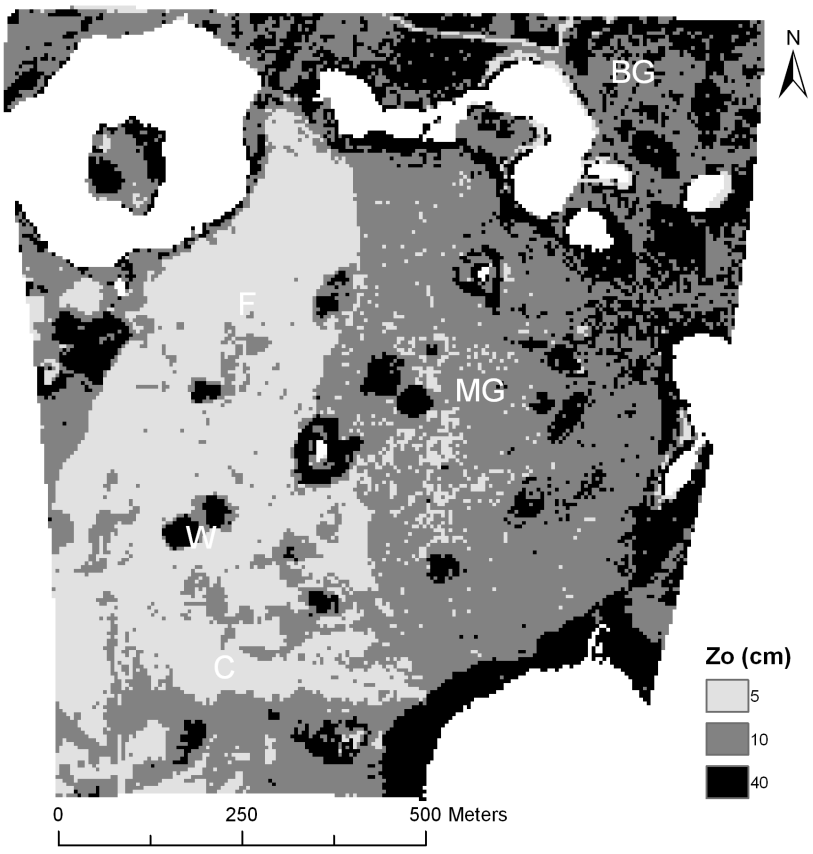

Figure 6.4: Classification map of aerodynamic surface roughness heights derived from visible image taken at mid-day on August 5, 2007, and values found in Brutsaert (1982). Letter codes indicate major land cover types: fallowed (F), mixed grass (MG), brome grass (BG), cultivated (C), and wetlands (W).

6.6 Temporal Transfer Function

The radiation ratio, Q^*_R calculated at mid-day for each pixel (Eq. 6.6) can be used as a temporal transfer function to distributed estimates of mean daily net radiation. This was done using the same procedure applied for distributing albedo. In the case for net radiation, however, the measured value of mean daily net radiation obtained at the corresponding reference pixel was distributed over the entire image. Net radiation is very dynamic over the course of a day, in contrast to the roughness height which is not a dynamic parameter on a sub-daily basis. Therefore, it was assumed that a linear relationship existed between the mid-day net radiation (near solar noon) and the mean daily net radiation. In order to upscale the mid-day radiation ratio from a temporal "point" to a mean daily value it was necessary to determine whether a stable proportionality existed between Q^* observed at mid-day and mean daily net radiation, Q^*_d.

For this purpose, data at three Canadian prairie locations of approximately similar latitude (49° – 52.2°) were examined for the period extending from May 1 – Sept 1. The data include two field seasons of observations at the St. Denis research site and archived observations at two short grass prairie locations; 5 years (1999 - 2004) at the Lethbridge AmeriFlux site, and two years (1999 - 2000) at Kernen Farm located at Saskatoon, Sask. As indicated in Figure 6.5, the assumption of proportionality appears to be reasonably valid. Overall, the relationship between mid-day and daily net radiation was shown to be of moderate strength and was also fairly consistent at each location; r^2 between 0.54 - 0.6. It is also noteworthy that the relationship appears to be better suited for periods when the mid-day net radiation is greater than 400 W m^{-2}. The larger scatter in the data below 400 W m^{-2}, suggests that the proportionality is most strong when the atmospheric conditions are less variable.

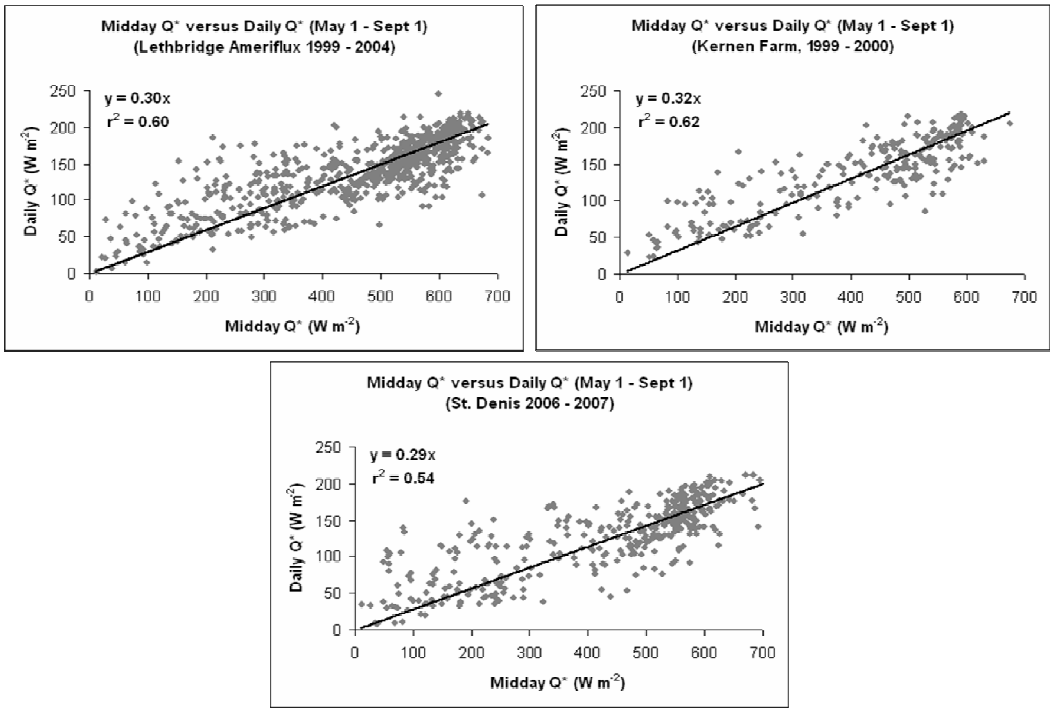

Figure 6.5: Relationship between mid-day and daily net radiation for various years at two Canadian Prairie sites and one Parkland site for the period May 1 through September 1.

The observed similarities in the data at each location suggest the assumption may be valid for any given location. This would eliminate the need for establishing empirical relationships from field data as long as a reference value of mean daily net radiation could be obtained. The assumption of proportionality is important because it allows for the mean daily net radiation, Q^*_d to be distributed from a known value at the corresponding reference location, Q^*_{dref}, as a function of the radiation ratio Q^*_R, obtained at mid-day. This equation can be written as,

$$Q^*_d = Q^*_{dref}\ Q^*_R \quad . \tag{6.8}$$

The resulting map of the mean daily net radiation is shown in Figure 6.6. In the present case, the corresponding reference pixel location of the daily Q^* was assigned the value of 155 W m^{-2} obtained from CNR1 measurements at the reference site on the east side of pond 1. Figure 6.6 also shows a comparison of the estimated and measured Q^* at two locations. One site was equipped with a Kipp and Zonen CNR1 and the other was equipped with a Kipp and Zonen NR

Lite maintained by Environment Canada. At the CNR1 site the estimated value was slightly higher by approximately +6 W m^{-2} (4 % error), and somewhat lower at the location of the NR Lite by -11 W m^{-2} (7 % error). This is well within the measurement error associated with such instruments.

These results are encouraging given the developments and validation involved a single day. It has been shown that a mid-day radiation ratio parameterized in part from remote sensing data may be used for obtaining distributed estimates of mean daily net radiation, from a single known reference value, over a field sized area exposed to similar conditions.

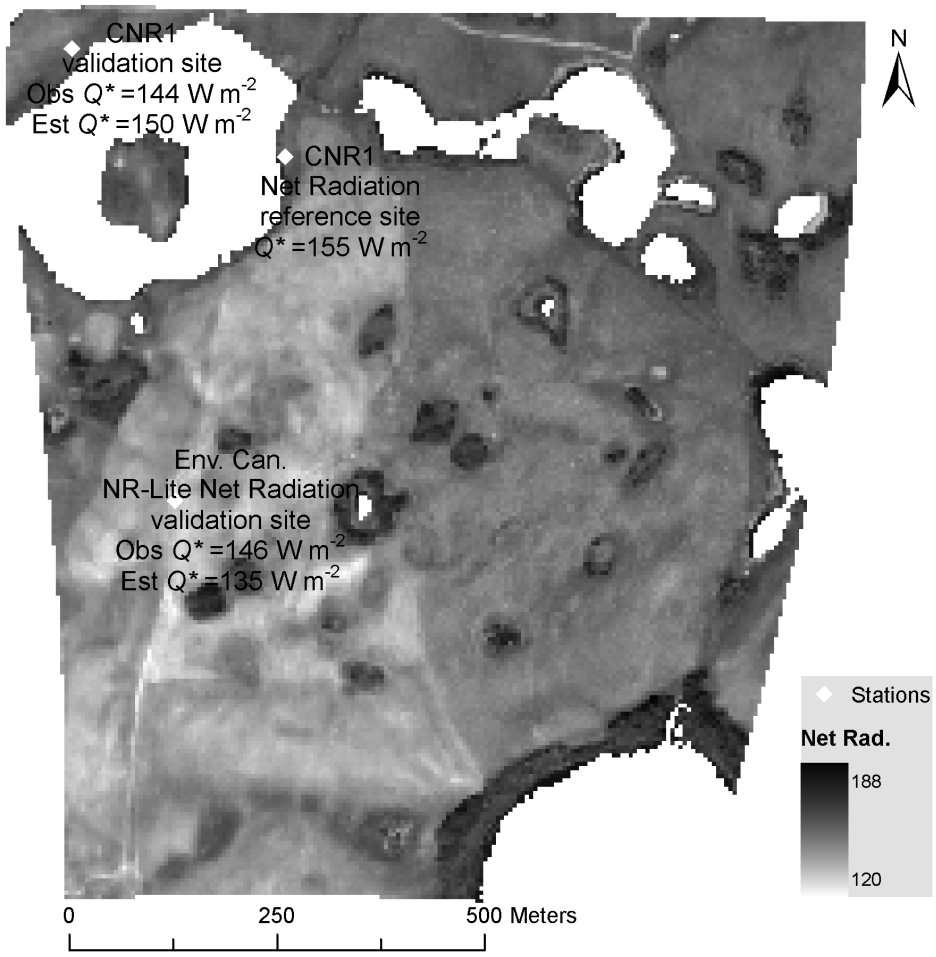

Figure 6.6: Map of mean daily net radiation derived from the index of mid-day net radiation and a known value of mean daily net radiation = 155 W m^{-2} obtained at the reference site. Also shows locations of two validation sites for comparing measured and estimated values of mean daily net radiation.

6.7 Sensitivity of the Mid-Day Evaporation Ratio

The sensitivity of the mid-day evaporation ratio, E_R can be examined by considering changes in α_R, $L\uparrow_R$, and Z_{oR} derived from the mid-day images. Figure 6.7 provides information on the general physical interactions of evaporation estimated by the model, and provides potentially useful information about the direction and magnitude of key relationships. Only the actual range of values observed from the images were considered in the sensitivity analysis of E_R so that the importance of variation within the range is clearly shown. Given the dependency of relative evaporation, *G* on the drying power of the air and the available energy, *G* was not allowed to remain constant for the sensitivity analysis.

In other words, *G* was assumed to vary with relative changes in available energy or surface roughness. Expectedly, E_R is shown to be inversely related to both α_R and $L\uparrow_R$. The reduction in either albedo or surface temperature resulted in an increase in the net radiation available for driving evaporation. This results in a reduction of the relative drying power, *D*, which in turn increases *G* (all other considerations being equal) and therefore, evaporation increases as well. The reverse holds for land surfaces where albedo and surface temperatures are higher which results in a reduction in evaporation.

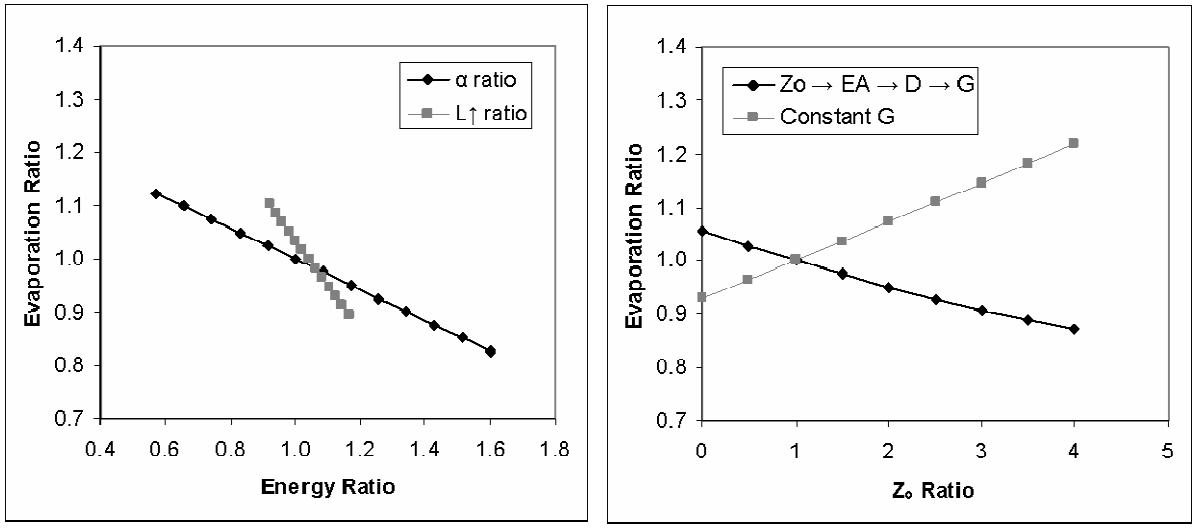

Figure 6.7: Sensitivity of evaporation to key inputs at mid-day. The measured range of inputs is shown to demonstrate potential variation in this case study.

For the case of Z_{oR}, the net radiation and climate variables were fixed at the mid-day values and G was allowed to vary with changes in Z_o. An increase in Z_o produced an increase in the wind function and therefore the drying power of the air, $E_{A;}$ when the humidity deficit was assumed constant; this produced an increase in D, and G decreased. Given this series of interactions, E_R was shown to be inversely related to Z_{oR}, which is contrary to what might be expected in nature. As indicated in Figure 6.7, if G was held constant and the increase in Z_o was assumed to only influence E_A, an increase in surface roughness enhanced turbulence and evaporation would increase.

More noteworthy is the relative magnitude of changes in E_R to the relative changes in the key variables, particularly in the case of the energy ratios. In Figure 6.7 the range of α_R is much larger than $L{\uparrow}_R$ but the slope of the relationship to E_R is less steep (-0.29 vs -0.84). A relative increase in $L{\uparrow}_R$ of only 16% resulted in a 10% reduction in E_R. By comparison, an increase in α_R of 34% was required to produce a similar 10% reduction in E_R. By comparison, the evaporation ratio appeared to be less sensitive to a change in roughness, however, the sensitivity increased when the interactions between roughness and the relative drying power were ignored and G was held constant.

The sensitivity analysis suggests that the longwave exchange between the surface and atmosphere is as important to estimating evaporation as the influence of shortwave radiative losses via albedo. Net longwave exchange can provide crucial information on the availability of water not just at the soil surface but also to the root systems of plants. This is generally observable when lower surface temperatures coincide with areas where higher water availability might be expected (ponds and depressions) or active vegetation can access stored soil moisture.

6.8 Distributed Estimates of Mean Daily Actual Evaporation

Distributed estimates of the mean daily relative drying power, D were derived using Eq. 2.14. The drying power term, E_A was calculated as a function of the roughness classes and mean wind speed (3 m s^{-1}) and humidity deficit (0.93 kPa), and the distributed mean daily net radiation. The relative evaporation, G was then calculated using Eq. 2.13. Figure 6.8 shows the distributed estimates of mean daily evaporation obtained by the *G-D* model using Eq. 2.12. The resulting pattern of evaporation follows the pattern of net radiation (Figure 6.7) which is driven by the combined influence of the spatial patterns of albedo and surface temperature.

Figure 6.8 shows the range of evaporation estimates was 1.2 mm. The minimum evaporation was estimated to be 2.2 mm/day and maximum was 3.4 mm/day. A visual assessment indicated lower rates of mean daily evaporation appeared to be associated with the fallowed/cropped area characterized by the 5 cm roughness height. In general, this area was characterized by the grouped albedo values having the highest range. The highest evaporation rates appeared to be associated with the 40 cm roughness height characterized by grouped albedo values with the lowest range associated with wetland areas where water stress is less likely to be a factor.

The prevailing wind direction for the day was from a north-northwest direction. A measured daily value of evaporation could be obtained at the eddy covariance station on the west side of pond 1. The observed evaporation corresponds to the upwind grassed surface to the west and north of the EC station. This general area was characterized by tall, dense brome grasses and was relatively homogenous compared to the mix of grasses comprising the upland site. Figure 6.8 shows the location of the measurements. The measured cumulative evaporation total was 2.2 mm for the entire 24 hour period, and 2.1 mm during the daytime period for which net radiation was positive. In other words, evaporation was negligible from the upwind grass surface during the night.

The observed value was used for validating a *G-D* model estimate obtained from the available grid cells for a small area upwind of the EC station. The areal estimate was derived by delineating a 2000 m^2 rectangle that extended over 10 columns by 8 rows of grid cells to the north and west of the EC station location. The estimates provided by the *G-D* model where then extracted to obtain the mean daily evaporation from the corresponding area. The range of values was relatively small (2.6 mm/day – 2.9 mm/day) and produced an areal estimate = 2.7 mm/day. This is 0.5 mm higher than the observed value but the difference is generally within the error of estimates shown in Chapter 5. For example, similar accuracy or better was obtained for daily and multi-day periods using the *G-D* model to estimate evaporation from the upland grass area during the 2006 field season. Nevertheless, the result is encouraging as it showed the applicability of the *G-D* method for estimating evaporation without the need for soil moisture data.

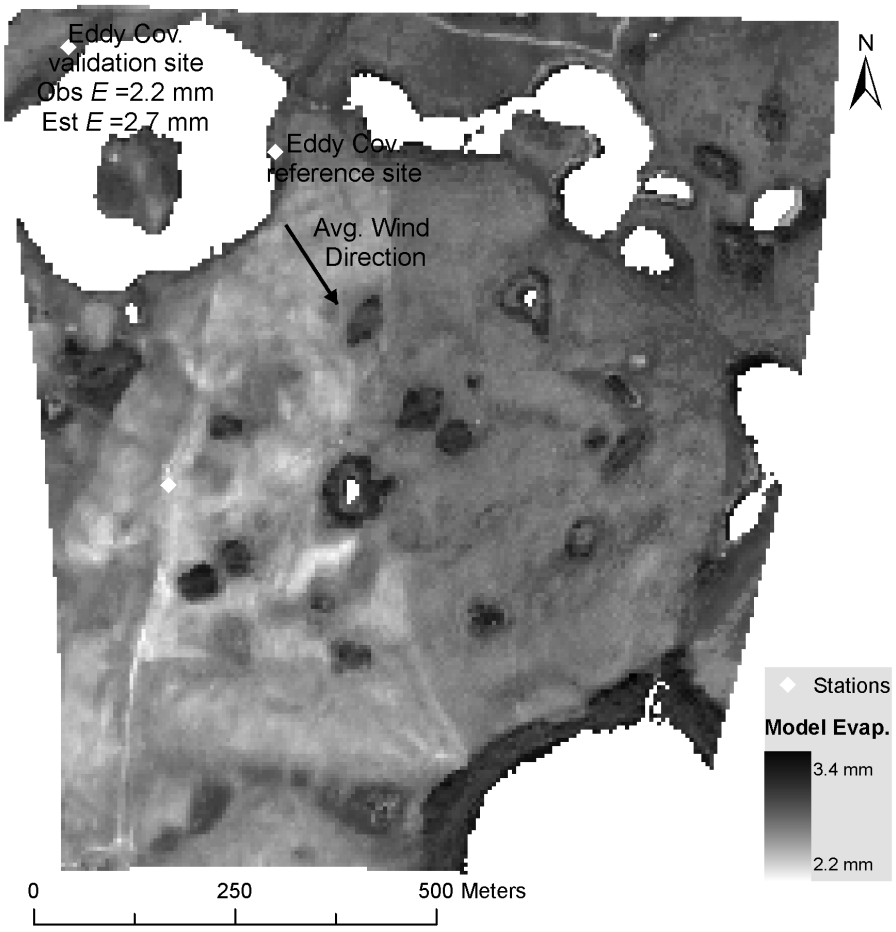

Figure 6.8: Map of estimated mean daily evaporation. Also shown is the approximate wind direction for the day.

The small areal estimate (2.7 mm/day) is only 0.2 mm less than the observed value of 2.9 mm/day obtained at the east side of pond 1. There is greater difficulty in determining the main source of the turbulent flux of vapour at the station on the east side of pond 1. For example, when the plants were shut down between midnight and 6 am on Aug 5, 2007, the prevailing winds were from directly over the pond; just north (285°) of due west (270°). During this period the total measured cumulative evaporation, which can reasonably expected to be from the water surface, was 2.2 mm. Interestingly, this is equal to the evaporation measured from the grassed area during the day on the west side of pond 1. More importantly it is a substantial amount for the 6 hour period during the night. In comparison, the cumulative evaporation totalled 2.9 mm at the station during the daytime when net radiation was positive and the distance to the opposite

edge was shorter given the prevailing wind direction. So, whether the contribution to the EC station on the east side of pond 1 was mainly from the grassed edge is unclear.

6.9 Distribution of Evaporation and Driving Surface Variables

6.9.1 Areal Distributions

A further examination was conducted with respect to the areal evaporation estimated by the model and the distribution of the estimates and driving surface variables. The value of using a physically-based distributed modelling approach is that it may be possible to obtain a realistic distribution of estimated mean daily evaporation. In the present case, spatial patterns of the observed surface properties, namely, albedo, surface temperature, and also the generalized pattern of surface roughness were used to drive estimates of evaporation over the area. The 'R' software environment was used for an analysis of the distribution of evaporation and driving surface variables. R is comprised of a programming language that has been used for statistical computing in the geosciences (e.g. Grunsky, 2002).

The boxplot was chosen for graphically displaying the statistical properties of the data. Boxplots provide a useful summary of an underlying distribution and the display does not depend on a class interval which is a general limitation of frequency distributions. The general structure of the boxplots used herein summarizes the data based on seven measures. The upper and lower limits of the box represent the 75^{th} and 25^{th} percentiles (i.e. the interquartile range), and the median and mean values are indicated within the box by a solid line and a point respectively. The minimum and maximum values within 1.5 times the interquartile range are represented by the ends of the whiskers connected to the box. Outliers beyond the whiskers are shown as open points. The skew (sk), standard deviation and coefficient of variation are also indicated in Figure 6.9. The cv is the dimensionless ratio of the standard deviation to the mean and is a useful descriptor because it allows for the variability among different data sets to be compared, even if they have very different means or have different units.

The roughness height classes represent discrete data and so are excluded from the present discussion. These classes were conveniently associated with three general groups of albedo values or continuous data and will be discussed later. The sensitivity analysis presented earlier showed the importance of both mid-day albedo and surface temperature for determining

evaporation. For an increase in either of these variables there is a decline in evaporation due to a reduction in available energy. The mid-day indexes of albedo and surface temperature were used to scale the mean daily net radiation over the field and boxplots summarizing the respective data are shown in Figure 6.9. Interestingly, there are some notable differences in the structure of these boxplots. For example, the distributions of albedo and surface temperatures were skewed in opposite directions. The albedo data showed a skew to the left (-0.83) and this was twice as large as the right skew (0.36) indicated for surface temperature. The influence of the interquartile range appeared to be greater for albedo, which resulted in outliers on both sides of the distribution; a larger portion of these were below 0.10. The location of the mean and median value was slightly different in both cases due to the shape of the distributions. The coefficient of variation (cv) indicated the variability of the data was smaller for the surface temperature data (14%) than for albedo (19%).

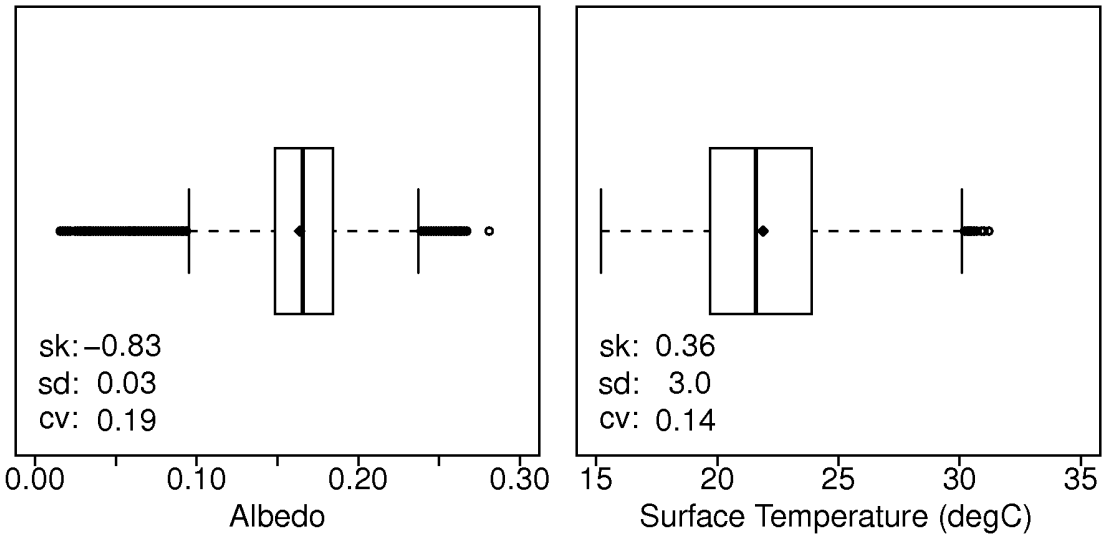

Figure 6.9: Distributions of albedo and surface temperature.

The boxplots shown in Figure 6.10 provide information on the distributions of mean daily net radiation and mean daily evaporation shown previously (Figures 6.6 and 6.8). For the purpose of comparison the net radiation is expressed in equivalent units of evaporation (mm/day). The distributions of net radiation and evaporation appeared to be very different when compared on similar scales. The width of the distribution for net radiation was twice as large as that for evaporation. The minimum and maximum values were 4.2 mm/day and 6.6 mm/day for

net radiation, and 2.2 mm/day and 3.4 mm/day for evaporation. As a result, the standard deviation was also twice as large for net radiation (0.34 mm/day) than for evaporation (0.18 mm/day). There were also some similarities between the distributions. For example, both indicated a positive skew, 0.34 for net radiation and 0.28 for evaporation. The mean and median values overlapped in both cases and were 5.2 mm/day for net radiation and 2.8 mm/day for evaporation. Also, the variation within the distributions appeared to be relatively small and the same in both cases (cv ≈ 0.066 or 6.6%). Interestingly, the variation in mean daily net radiation was reduced considerably compared to the variability in albedo and surface temperature used for distributing the mid-day net radiation.

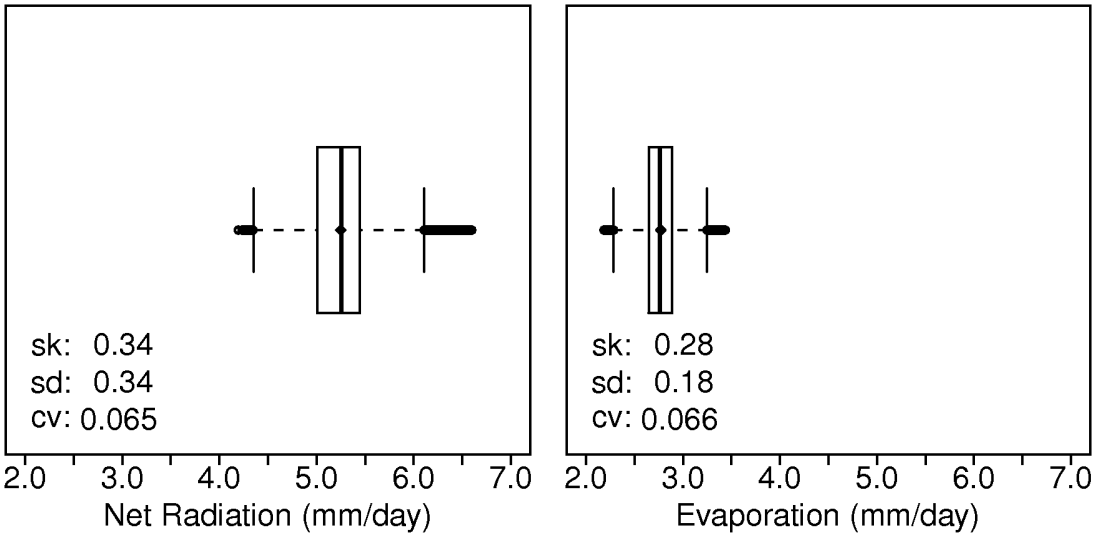

Figure 6.10: Distributions of mean daily net radiation expressed in equivalent units of depth and mean daily evaporation.

The relative evaporation, *G*, is also partly governed by turbulent transport driven by surface roughness and also the available energy driven by net radiation. A boxplot of *G* and a scatterplot of its association with net radiation are shown in Figure 6.11. These graphs show some points of interest. The noticeable break in the distribution of estimates of *G* would indicate there were two distinct distributions. This can be partly attributed to the step changes in roughness height (5 cm, 10 cm and 40 cm) and assuming the wind speed and the humidity deficit were constant. This is also supported by the three distinct positive linear relationships indicated between *G* and net

radiation; two are close in proximity compared to the third. The wide range in net radiation values among the three distributions would suggest there were general differences in the surface state conditions within the three classes of roughness (i.e. the conditions were not uniform within a given class). The pronounced shift in the distributions among the different roughness classes provides evidence of a negative response between the means of *G* and net radiation.

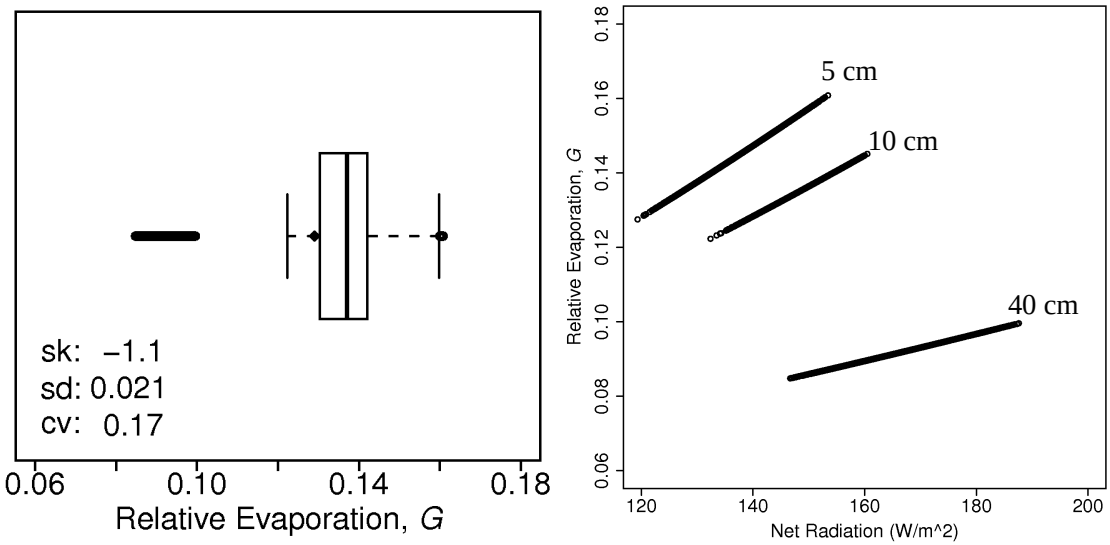

Figure 6.11: Distribution for *G* and relationship between *G* and net radiation among the roughness classes.

6.9.2 Distributions Within Roughness Classes

The distributions were then examined among the 5 cm, 10 cm, and 40 cm roughness classes. The distributions of albedo and surface temperature for each roughness height are provided in Figure 6.12. The respective boxplots indicated considerable differences in the shape of the distributions among the roughness heights and also between the variables. The distributions of albedo are particularly striking due to the segmentation of the visible image (used to index albedo) into three groups of continuous albedo values that were assumed to correspond in general with discrete categories of roughness.

The resulting distributions of albedo for the 5 cm and 40 cm roughness heights showed considerable skew in opposite directions. The skew was to the right (1.4) for the 5 cm roughness and to the left (-1.6) for the 40 cm roughness. By comparison, the distribution for the 10 cm roughness was close to symmetrical (skew = 0.04) and much more narrow, and so the variability

in reflected radiation was much lower within the 10 cm roughness class. The segmentation procedure also resulted in a general shift in the interquartile ranges and means (which were similar to median values) for the grouped albedo data with increasing roughness and there was no overlap between them.

In contrast, the distributions of surface temperature showed considerable overlap between the roughness classes. The overlap between the interquartile ranges for each class was relatively small but there was a shift in the interquartile ranges and means with increasing roughness, similar to that exhibited for albedo. The distribution was narrower for the 40 cm roughness height compared to the others. The data showed a general skew for each roughness class that apparently transited from left to right with increasing roughness; -0.32, 0.42, and 0.62 respectively. Such behaviour in the mean surface temperature is reasonable when taking into consideration there would be an increase in evaporative cooling with the increase in energy availability.

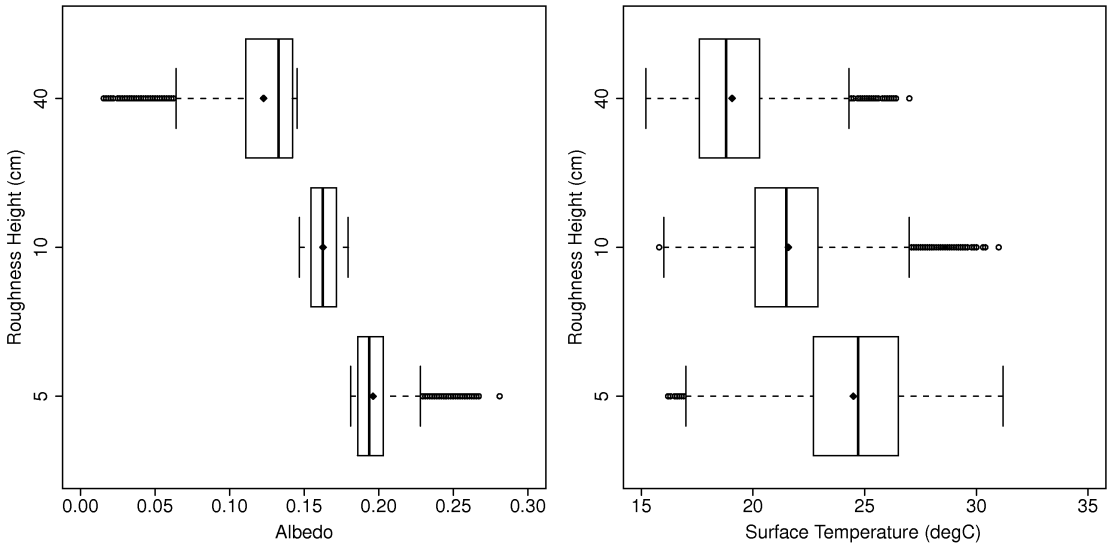

Figure 6.12: Distribution of albedo and surface temperature within each roughness class.

Figure 6.13 shows boxplots of net radiation and evaporation for each class which revealed several noteworthy points. The data were summarized based on their specific range of values in order to better describe their similarities and differences. A visual assessment of the respective distributions indicated that the evaporation estimates showed similar characteristics to that of the

net radiation. This includes visual similarities between the relative locations of the interquartile ranges, means and median values, skew, and outliers. The respective distributions also show similar overlap among the roughness classes. There was a small reduction in the coefficient of variation among the data (cv = 2.8% - 4.2%) compared to that indicated previously for the entire areal distributions of net radiation and evaporation shown in Figure 6.10 (cv = 6.6%).

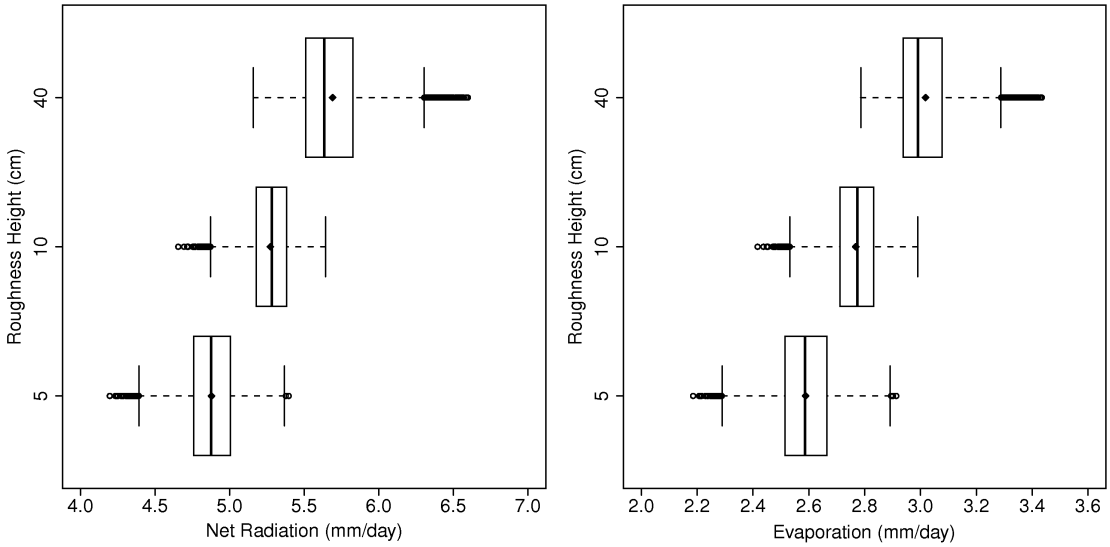

Figure 6.13: Distribution of evaporation and net radiation within each roughness class.

In general, the shifts in the means of net radiation, albedo, and surface temperature with roughness class appeared to be relatively linear. In contrast, the resulting shifts in the mean values of *G* appeared to be non-linear (Figure 6.14). In this case, the mean value of *G* declined with a step change in surface roughness due to an increase in drying power of the air and increased energy availability. The shift in the mean of *G* was much smaller from the 5 cm to the 10 cm roughness class, 0.146 to 0.136, compared to that for the 10 cm to 40 cm roughness class which declined from 0.136 to 0.09. With the energy increase associated with the roughness classes, the subsequent shift in mean net radiation would appear to be counteracted by the decline in the mean of *G*.

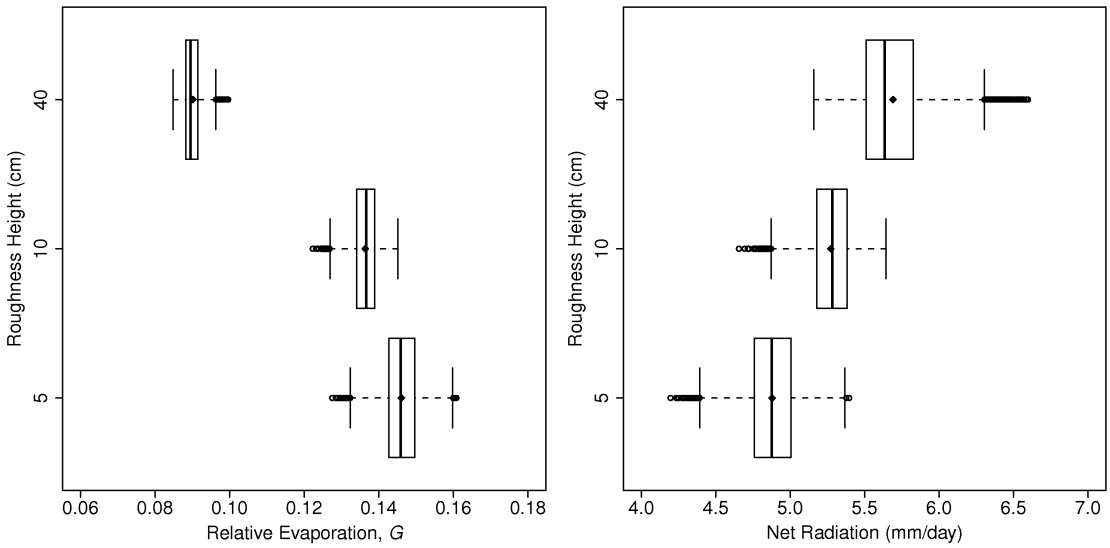

Figure 6.14: Non-linear decline in mean relative evaporation and linear increase in mean net radiation with increasing roughness height.

6.9.3 Spatial Associations and Scaling Implications

It was indicated previously that the areal estimate provided by the model was 2.8 mm/day. The relative contributions of evaporation to the areal estimate (E_{Areal}) can be determined by multiplying the fraction of the total area covered by each roughness height to the corresponding estimate of mean daily evaporation. The mean daily evaporation rate was found to be similar for the 5 cm and 10 cm roughness heights (2.6 mm/day and 2.77 mm/day respectively) and 3.02 mm/day for the 40 cm roughness height. The areal estimate for the entire image was calculated based on the respective proportions of the roughness classes (section 6.5),

$$E_{areal} = (0.295 * 2.6) + (0.484 * 2.77) + (0.221 * 3.02) = 2.77 \text{ mm/day} \quad . \qquad (6.9)$$

The resulting areal estimate of 2.8 mm/day is approximately 0.6 mm larger than the EC observed value of 2.2 mm/day obtained from the grassed location on the west side of pond 1. It is also approximately 0.1 mm larger than the estimate of 2.7 mm/day obtained from the 2000 m^2 grassed area upwind of the EC station that was discussed previously. Further, the E_{areal} estimate provided by the model for the field is 0.3 mm larger than a *G-D* point estimate of 2.5 mm/day obtained from climate reference data measured at the EC station; namely net radiation, air

temperature, humidity, wind speed, and also roughness height. Essentially, the point measurements and point estimates correspond to evaporation from the grassed surface which dominates the area as a whole.

In general, the differences are not surprising given that calculations and areas of influence for each are different. The EC method determines evaporation based on the statistical properties of the turbulent fluxes of water vapour from the upwind surface. As such, the EC method does not require information about the general state conditions of the surface. In contrast, estimates provided by the *G-D* model are governed by the available energy and requires an estimate of the general roughness conditions, and uses the drying power of the air to reflect the availability of water for evaporation in order to estimate the turbulent flux component. In this case, the observations and point estimate are also influenced depending on the footprint scales of the instruments. For example, the respective footprints of the EC measurements and air temperature and humidity might be in the order of 100 m to 200 m based on the measurement heights. In contrast, the CNR1 has a footprint of 5 m to 10 m. As a result of the uncertainties and differences in footprints that vary depending on the general atmospheric conditions, the absolute errors influencing the observations and model estimates are difficult to determine.

Nevertheless, differences in evaporation estimates can be evaluated further by considering the impacts of the means of driving variables to parameterize the model, and also the potential impact of spatial associations of driving variables, on upscaled estimates of evaporation. The various parameters of the *G-D* model were given previously in Eq. 2.12. The equation is rewritten here in a general form given by Granger and Gray (1989)

$$E = \frac{\Delta G Q^*}{(\Delta G + \gamma)} + \frac{\gamma G E_A}{(\Delta G + \gamma)} \quad . \tag{6.10}$$

Eq. 6.10 can be used to distinguish between the respective contributions of the energy and aerodynamic terms to evaporation. Table 6.2 shows the differences in evaporation estimates as calculated by parameterizing the model with mean values of the driving factors. This includes the mean values of the parameters within each roughness class and the mean values corresponding to the entire area. Under the assumption of constant air temperature, Δ and γ remained fixed for the calculation of evaporation. The differences in the distributions of grouped

albedo values, associated with the respective roughness classes, were reflected in the linear increase in the mean daily net radiation, Q*. The differences in drying power of the air, E_A, with roughness height were also clearly shown. As a result, there was negligible increase in the relative drying power, *D*, for the 5 cm and 10 cm roughness classes and a 12% increase in *D* for the 40 cm roughness class. Expectedly, there was a negative response in the mean of *G* with the increase in *D*.

Table 6.2: Areal evaporation estimates within each roughness class from *G-D* model and for entire area based on mean values. *E*_energy, *E*_aero are the contributions from the energy and aerodynamic components and *E*_total is the combined total. The mean value of the distributed estimates is given by "Expected" and the difference between the total and expected is given by "Diff".

Zo	Δ	G	Q*	γ	E_A	D	*E*_energy	*E*_aero	*E*_total	Expected	Diff
cm	kPa		mm/day	kPa	mm/day		mm/day	mm/day	mm/day	mm/day	mm
5	0.134	0.132	4.88	0.063	12.99	0.73	1.07	1.34	2.40	2.59	-0.18
10	0.134	0.124	5.27	0.063	15.13	0.74	1.10	1.48	2.58	2.77	-0.19
40	0.134	0.085	5.69	0.063	27.97	0.83	0.87	2.01	2.88	3.02	-0.14
E_{areal}	0.134	0.113	5.28	0.063	18.70	0.77	1.03	1.71	2.73	2.77	-0.03

Calculating evaporation (via Eq 6.10) from the means shown in Table 6.2 provided some useful information. In general, the evaporative contribution by the energy term, *E*_energy (left term of Eq 6.10) was shown to be smaller than the aerodynamic term, *E*_aero (right term of Eq 6.10) or the turbulent flux component of the model. The difference among the estimates attributed to the energy term was only 0.2 mm/day but was almost 0.7 mm/day for the turbulent flux which was shown to increase with the roughness height. As a result, the combined totals of evaporation, *E*_total tended to increase with roughness height.

For this case, results suggested a potential bias in evaporation estimates due to the enhancement of the turbulent flux with increasing roughness. However, the difference among the combined totals of evaporation, *E*_total was only 0.5 mm/day. This can be attributed to the observed inverse relationship between the means of *G* and Q* and *G* and E_A, which is clearly indicated in Table 6.2. In other words, potentially larger increases in evaporation that might be expected to occur with increased energy availability and enhanced turbulence were counteracted by the accompanied decline in the mean relative evaporation with roughness class.

Table 6.2 also shows how the resulting evaporation estimates derived from the mean values of *G*, Q*, and E_A compared to the expected values provided by the model for each roughness

class. The “Expected” values were derived as the weighted average of all the distributed estimates in each class shown previously in Eq. 6.9. Results showed that the estimates derived from the mean values of the driving factors underestimated the expected evaporation in each case; although the differences were generally small (< 0.2 mm). If the evaporation estimate was upscaled further, that is, the mean areal values of the driving factors over all the roughness classes were considered (i.e. from Table 6.2) an estimate of 2.73 mm/day was obtained. In other words, the difference in evaporation estimates was relatively small when the representative averages for the individual roughness classes were used to parameterize the model and also when the average over the entire field was considered. In this case, the complex interactions of the driving factors within the *G-D* model counteracted each other and resulted in evaporation estimates that tended toward the mean.

The spatial association of driving factors was also examined to determine whether evaporation estimates might be influenced by any existing covariance between driving factors. For this purpose, correlations among the variables over the entire field area were considered and the Pearson correlation coefficient, r was determined. The Pearson method is useful in that the coefficient r represents the ratio of the covariance between two variables normalized by the product of their standard deviations

$$r = \frac{\sum \frac{\left(Xi - \overline{X}\right)\left(Yi - \overline{Y}\right)}{n}}{\sqrt{\frac{\sum \left(Xi - \overline{X}\right)^2}{n}}\sqrt{\frac{\sum \left(Yi - \overline{Y}\right)^2}{n}}} \quad , \tag{6.11}$$

where Xi and Yi are the respective values of the variables, the overbar denotes the mean values and *n* is the number of values. In other words, a relatively strong correlation between two variables might indicate the possibility of a covariance that could influence upscaled estimates of evaporation. Due to the segmentation of the visible image into grouped albedo values, the positive relationship between the shifting means of energy availability with roughness class was already noted in Figure 6.12. However, given the roughness classes represent discrete data further evaluation in relation to other driving factors would be less meaningful. So the association among the energy terms is briefly examined here.

The correlations shown in Table 6.3 are all significant due to the large number of grid cells comprising the field area (32,750) so the strength of the relationships must be considered more carefully. Ts and albedo showed a moderate positive correlation over the field area which indicates they were found to vary together in some instances and their combined influence was important for Q*. Namely, the available energy might be greatly reduced or increased where they varied together compared to where only one might have changed and the other remained relatively constant. However, Ts and albedo are not explicitly multiplied in the calculation of Q* and so their covariance is not considered further.

The positive correlations between *G* and Ts and *G* and Albedo are counterintuitive and were a direct result of the shift in mean values between the roughness heights. When considered specifically within the roughness classes the correlations between the respective continuous variables (*G* and Ts and Albedo) were all negative and ranged from moderate (-0.65) to strong (-0.95). In other words, the relative evaporation tended to decline with increases in surface temperature and albedo, which would be expected given the implication of reduced water availability and possibly reduced plant activity.

Table 6.3: Correlations, r, among driving factors of evaporation for the field area.

	Ts	Albedo	Q*	G
Albedo	0.67			
Q*	-0.88	-0.94		
G	0.45	0.73	-0.67	
E	-0.89	-0.93	0.99	-0.68

The apparent negative relationship between *G* and Q* was also a function of the general shift in the distributions and corresponding mean values among the roughness classes. The three distinct relationships between these two variables were shown previously in Figure 6.11. Consequently, the strong correlation between them (Table 6.3) indicates the pattern of evaporation within each roughness class was governed by the available energy. So where the surface state conditions resulted in the reduction of available energy there was a reduction in the evaporation within that roughness class; the opposite was true then for a subsequent increase in available energy. This behaviour might be expected where the effects of evaporative cooling increases or decreases in relation to the availability of water. For example, where stored soil

moisture might be higher or more accessible to plants compared to areas where stored moisture might be lower or less accessible.

The possibility of a covariance between *G* and Q* can be considered because they are multiplied together as shown in Eq. 6.10. This is also true for G and E_A, except that E_A could only take on three values as a function of the general roughness classes and assumed uniformity of the climate conditions. In both cases, however, the covariance would be expected to be negative due to the apparent negative association among the mean values. The calculation of covariance is dependent on the units of the variables and so must be meaningful. *G* is dimensionless (ratio of actual to potential evaporation) and the units of Q* were expressed in equivalent depths of evaporation (mm/day) so the covariance between G and Q* would be in mm/day as well.

Calculation of the covariance term is shown in Eq. 6.11 and from this equation it is also apparent that the covariance can also be estimated by rearranging the terms and multiplying the correlation coefficient in Table 6.3 by the product of the standard deviations of the Q* and *G* given in Figures 6.10 and 6.11; 0.34 mm/day and 0.021 respectively. Multiplied in series this resulted in a covariance of approximately -0.0046 mm/day; (r = -0.67)*0.34 mm/day*0.02. In other words, the general increase in available energy was counteracted by the general reduction in *G* and the result was no covariance which means that further influence on upscaled estimates of evaporation would not be expected. Due to the limitations of the climate data and discrete classes of roughness, this study is not able to comment further on the possible covariability between driving climate factors and the turbulent flux component in relation to the *G-D* model.

6.10 Summary and Conclusions

The analysis presented here has shown that distributed mean daily evaporation estimates may be obtained for a field-sized area (1 km^2) using an evaporation ratio approach. This involved the development of a method to distribute a known value of mean daily net radiation over the field by indexing the mid-day net radiation ratio from remotely sensed visible and thermal images. Bisht et al. (2005) have indicated that daily values of net radiation are more useful for estimating evaporation compared to instantaneous values obtained at mid-day. In the present case, spatial variations in the mid-day net radiation were used to scale a known value of mean daily net radiation over the land surface. The estimated daily net radiation was found to be within 4 % - 7

% of the CNR1 and NR-Lite radiation measurements obtained at two available validation sites as indicated in Figure 6.6.

Some general differences were observed between the point measurements obtained by the EC method and point estimates obtained by the *G-D* model. A small areal (2000 m^2) evaporation estimate = 2.7 mm/day was obtained from a 10 x 8 grid of cells located within the station footprint which was 0.5 mm higher than the EC observation. Another *G-D* model estimate of 2.5 mm/day was obtained based on the point measurements over the footprint of the station (i.e. including the CNR1 footprint) which was 0.3 mm higher than the EC observation. Whether the differences were a result of the uncertainty in the measurements or due to model errors were not clear. It is possible that a portion of the difference may be attributable to an overestimation of the daily net radiation or an overestimation attributed to the interactions within the drying power term.

The pattern of mean daily evaporation was inversely related to the pattern of mid-day albedo and surface temperature and directly related to the mean daily net radiation driving the process. A moderate positive correlation was found between albedo and surface temperature on Aug 5, 2007 that governed the pattern of net radiation. As such, evaporation tended to be lower where surface temperatures and albedo was higher and evaporation was larger where surface temperatures and albedo were lower. This suggests that variations in mid-day visible and thermal observations over an area may be useful as indicators of surface state conditions and therefore spatial variations in evaporation over the course of the day.

An examination of the distributions of driving factors and their means showed they varied between the general roughness classes. This was partly attributed to differences in energy availability based on the segmentation of the visible image into grouped reflectance values, or three distinct distributions of albedo. In this case, they conveniently corresponded to general differences in the distribution of the roughness characteristics of the surface covers. The mean values obtained from the respective distributions were used to parameterize the *G-D* model to evaluate the potential effects on upscaled estimates of evaporation. The use of mean values for the driving factors within each roughness class resulted in a general underestimation, albeit small (< 0.2 mm/day) of the expected evaporation estimate. There were only small differences in the evaporation estimates for the field when the areal values of the driving factors were used to parameterize the *G-D* model.

The potential for large increases in evaporation due to increases in energy availability and the turbulent flux component was counteracted by the inclusion of the relative evaporation term. This provided a general stability in the evaporation estimates which tended toward the mean value as a result of the general spatial associations. Whereas the moderate positive relationship between albedo and Ts influenced the pattern of net radiation, they are not explicitly considered in the determination of a covariance that might influence upscaled estimates of evaporation. In the case of relative evaporation and net radiation the covariance was considered, and was found to be a very small negative value due to the offsetting relationship between them. Due to the limitations of the climate data over the field sized area, the results are unable to provide information on any possible covariances that might be associated with variations in the driving climate factors.

In summary, crucial driving variables of evaporation were obtained directly from remotely sensed visible and thermal images. Specifically, the surface albedo and surface emitted longwave radiation components were obtained for estimating the net radiation which is a major driver of the evaporation process. The aerodynamic surface roughness was also obtained based on the statistical properties of the visible image and a manual reclassification into generalized roughness heights. These are all key variables for calculating evaporation using methods based on the energy balance or a combination model such as applied here. The model approach applied here may be useful for obtaining reasonable estimates of the mean daily evaporation from a complex environment. The *G-D* model itself may also be a potentially valuable tool for assessing the physical behaviour of more complex parameterizations and surface schemes used for predictive purposes, or help to characterize relative differences in evaporation where there is a lack of soil moisture information. The theoretical development used to distribute the net radiation tem might also be useful toward improving regional scale estimates of evaporation using remote sensing assimilation techniques.

CHAPTER 7

VARIABILITY OF EVAPORATION ACROSS THE CANADIAN PRAIRIE REGION DURING A DROUGHT AND NON-DROUGHT PERIOD

7.1 Introduction

The analysis presented in this chapter addresses the third research objective by examining the spatial and temporal variability of evaporation over the Prairie region of Western Canada. In this case, the extent of the region presents a challenge for capturing spatial variations in land surface-atmosphere interactions. Whereas temperature and humidity changes may be relatively small over field sized areas, their variability increases greatly over larger areas. As such, a critical consideration is the availability of surface and climate data over the region.

Initially, a grid-based modelling approach was considered that combined moderate scale modeled NARR reanalysis output, MODIS visible and thermal images, land cover classes from AVHRR, a 1 km DEM, and the 2001 census of agricultural regions. Specifically, the gridded North American Regional Reanalysis (NARR) dataset contains the meteorological forcing data needed to parameterize the incoming radiation components. MODIS 1 km gridded surface albedo and surface temperature data are available on a daily basis and can be used to obtain the sub-grid variations in the surface radiation balance. Aerodynamic roughness heights can be obtained from 1 km gridded AVHRR land cover classes. Unfortunately, some fundamental limitations were encountered, and as an alternative, a hydrological approach was taken. A few of the more important limitations are briefly discussed.

Two issues were identified regarding data quality and availability. First, the MODIS surface temperature data are severely limited by the extent of cloud cover. Unlike albedo which is temporally invariant over relatively long periods, the surface temperature is highly variable and is not well suited for gap filling techniques over large regions. As such, very few days were found to be suitable for examining spatial variations in evaporation over the region. The second problem is the suitability of the NARR data for hydrological application in Canada. NARR is a follow-up to the NCEP-NCAR Global Reanalysis and includes several improvements (Mesinger et al., 2006). NARR provides a moderately high resolution gridded land surface and atmospheric dataset (32 km vs 180 km) that covers North America. The dataset spans a fairly long period

beginning in 1979 and is continually being updated in near real time. The advantage of assimilating NARR outputs is the use of continuous gridded data sets that cover the entire Prairie region. The grid resolution of 32 km is also practical for large scale modelling applications.

However, there are concerns over the reliability of NARR outputs which suggest the data are not reliable enough for large scale hydrological modelling applications over Canada. Specifically, precipitation, temperature, humidity and wind speed are important variables needed for long term hydrological simulations. Precipitation is a primary concern over Canada due to the relatively small number of observation stations (Mesinger et al., 2006). Bukovsky and Karoly (2007) indicate that over Canada a 1° rain gauge analysis is used versus 1/8° over the U.S. They also note that modelling anomalies occur as a result of blending the data across the U.S.-Canada border which impact rainfall distributions.

As an independent check, a regression analysis was carried out for three major prairie cities (Edmonton, Saskatoon, and Winnipeg) between daily NARR outputs and Environment Canada observations for May 1 through August 31 from 1979 - 2005. The variables relevant to evaporation modelling were examined, namely, precipitation, temperature, humidity and wind speed. Results indicated that the air temperature (2 m height) field was the most consistent and reliable at each location with an r^2 = 0.90 and slope = 0.92. The relationships for relative humidity at 2 m height and wind speed at 10 m height were very poor by comparison; RH (r^2 = 0.5-0.6) and wind speed (r^2 = 0.48-0.57). The precipitation posed the greatest concern as there was no relationship between the NARR and Environment Canada data; r^2 = 0.0-0.04. As a result, application of purely grid-based approach was considered to be unreliable for estimating evaporation over the Prairie region.

7.2 Modelling Approach and Parameterization

In lieu of a purely gridded analysis, a long term continuous hydrological modelling approach was applied at point locations where good archived observations are available. The Environment Canada data introduced in Chapter 3 provides the meteorological forcing data needed to operationalize a prairie hydrological model within CRHM. In contrast to the drought modelling performed in Chapter 5, both winter and summer processes relevant to Prairie hydrology were considered for this application. A flowchart of the assembled hydrological model is given in Figure 7.1. The modules applied include blowing snow transport, sublimation, spring melt,

infiltration into frozen and unfrozen soils, and soil moisture accounting. Several of the modules used for the summer processes have been described previously in Chapter 5; namely, the observation, interception, prairie infiltration, evaporation, soil initialization and soil moisture balance modules. A brief description of other modules relevant to winter processes and radiation modelling are provided below.

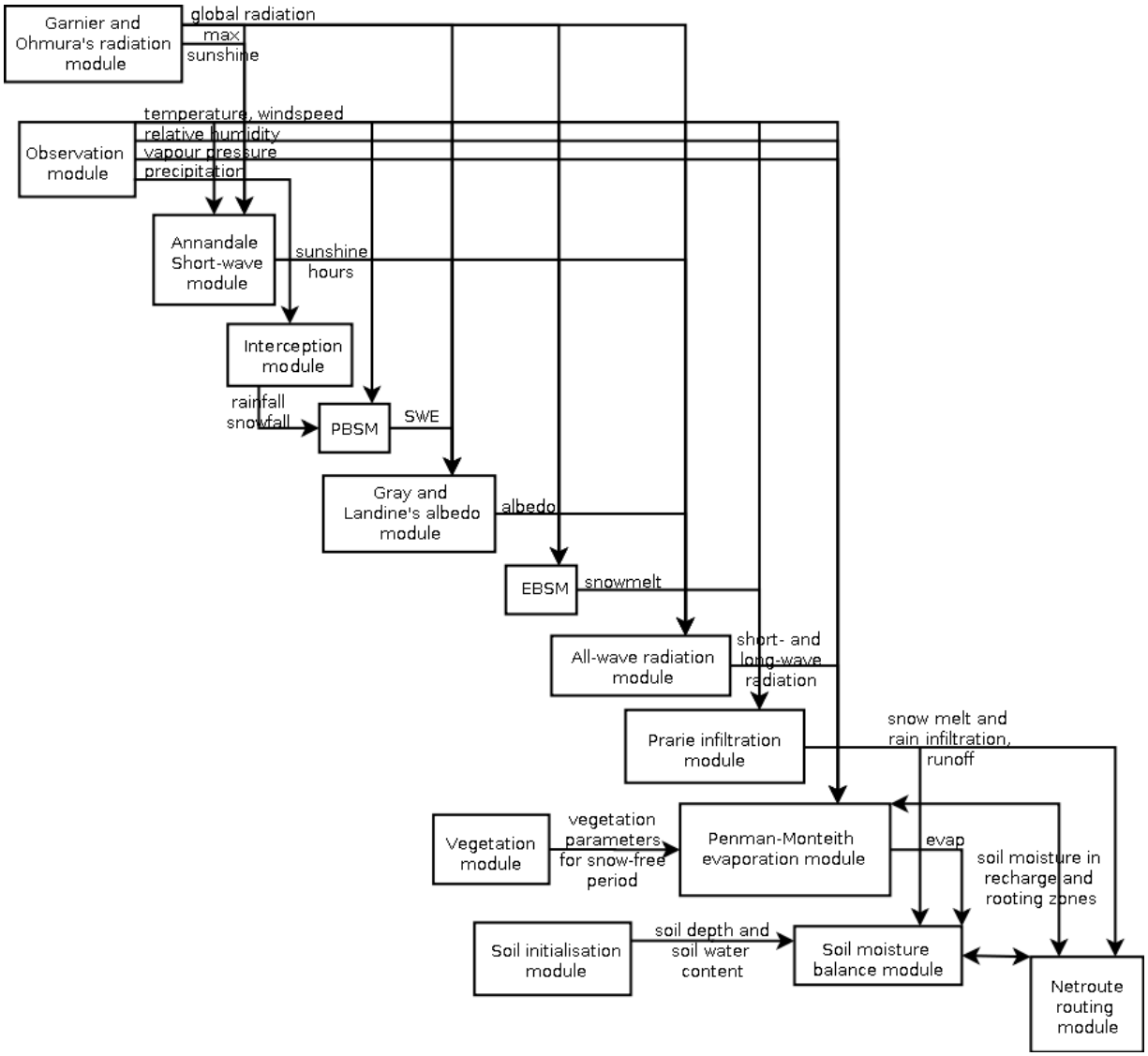

Figure 7.1: Flowchart of CRHM hydrological modules assembled for modelling evaporation at climate stations across the Prairie region.

Garnier and Ohmura radiation module

This module applies an expression proposed by Garnier and Ohmura (1970) to calculate the theoretical direct-beam incoming shortwave radiation. The diffuse shortwave radiation and maximum sunshine hours are also calculated. This information is supplied as input to the Annandale shortwave module, albedo module, energy-budget snowmelt module, and net all-wave radiation module. Parameters to be set in this module are latitude, elevation, ground slope, and azimuth direction of the surface.

Annandale shortwave module

Radiation is a problem since measurements are rarely provided at climate stations in Canada. This module uses an expression proposed by Annandale et al. (2001) to estimate the atmospheric transmittance as a function of the range of daily air temperatures and the elevation. The incoming shortwave radiation is then calculated from the theoretical direct-beam incoming shortwave radiation and the atmospheric transmittance. The actual sunshine hours are also calculated in this module and supplied as input to the net all-wave radiation module.

Prairie blowing snow module (PBSM)

A detailed description of PBSM has previously been given by Pomeroy et al. (2007). This module handles the transport and redistribution of snow between HRUs, and sublimation during the winter period. The transport and sublimation of blowing snow is calculated as a function of wind speed, air temperature and relative humidity. Snow is transported between HRUs depending on the roughness heights of the vegetation elements (i.e. from lower to higher) but no snow can be transported to an HRU with the lowest roughness. The snow water equivalent (SWE) determined from the accumulated snow is supplied to the albedo module.

Gray and Landine albedo module

The purpose of this module is to estimate the decline in snow albedo over the winter period and into the melt period. Inputs to this module include air temperature, net radiation, snowfall and SWE. The calculations track the decay of snow albedo based on depletion curves over three distinct periods (premelt, melt and post melt) developed by Gray and Landine (1987). This module also estimates the start date of melt which is supplied to the EBSM module.

Energy-Budget Snowmelt Model (EBSM)

A detailed description of EBSM has previously been given by Pomeroy et al. (2007). The purpose of this module is to calculate the daily melt for locations within the Canadian Prairies. This is done using the algorithm developed by Gray and Landine (1988). EBSM estimates the energy requirements for melting a volume of snow cover. The energy terms included in the determination of snow melt are: the net radiation balance which is calculated over the melt period as a linear function of daily net shortwave radiation; turbulent fluxes of sensible and latent heat calculated based on empirical expressions derived from detailed profile measurements; ground heat flux; energy supplied from rainfall estimated empirically as a function of the mean temperature; and change in the internal energy of the snow pack.

All-wave radiation module

This purpose of this module is to estimate the surface balance of net radiation using the expression proposed by Brunt (1932). The expressions for the net shortwave and longwave components consider the ratio of actual sunshine hours to the maximum sunshine hours. The net longwave radiation component is calculated as a function of the atmospheric temperature and humidity using the equation of Granger and Gray (1990b). The calculated net radiation is then supplied for estimating the evaporation.

Prairie infiltration module

This module handles the infiltration into both frozen and unfrozen soils and updates the water content in the soil moisture balance module. A description for infiltration into the unfrozen soils was given previously in Chapter 5. A detailed description of the infiltration into frozen soils has previously been given by Pomeroy et al. (2007). Infiltration into frozen soils is divided into three general categories; restricted, limited and unlimited. The limited category is used for all runs and infiltration is then determined as a function of the available water content. If the water refreezes after a melt event then the infiltration switches to the restricted category and no water is allowed to infiltrate (i.e. any new melt goes directly into runoff).

Netroute routing module

This module handles the routing of surface runoff, subsurface runoff and HRU routing using a lag and route method to move water between HRUs.

Evaporation module

A lack of soil moisture observations required the soil moisture balance to be simulated for all model runs. In this case, the soil moisture information needed to parameterize the canopy resistance term was supplied by the moisture balance. As a result, there was no apparent advantage in applying the *G-D* model to estimate evaporation. Therefore the *P-M* model was applied for estimating evaporation during the snow free periods.

7.2.1 Hourly and Daily Archived Climate Data

The virtual basin concept was applied at each climate station location. Only those stations for which continuous data sets could be assembled were considered for modelling. Specific climate variables needed include hourly observations of air temperature, relative humidity and wind speed, and daily observations of snowfall and rainfall. The archived data were processed in two steps. First, stations across the Prairie region were checked manually to determine whether they had complete records over the entire 1961 - 2005 period. In some cases data gaps existed which is inevitable due to instrument malfunctions or when stations were decommissioned. The second step was to combine station data into continuous time series and where needed, fill data gaps with a nearby station. This was done using a program to read in the station files to be combined, align the overlapping time series, and replace any missing values. Where more than one alternate station was available the average value was used. A data filter was also applied during model runs to ensure the upper and lower limits of the data were within an acceptable range normally observed in the natural environment; this was done to account for any potential measurement anomalies in the data.

7.2.2 Soil Types

General differences in soil types occur throughout the region. Some soil textures have larger water holding capacities than others which regulates the amount of soil water accessible to vegetation. Therefore, the bulk soil type was considered at each station location based on an analysis of the landscape polygons of Canada v3.1.1 (Soil Landscapes of Canada Working Group, 2007). This is a digital database of compiled soil survey maps at a scale of 1:1 million. The database includes a variety of soil information typically down to a 1 m profile depth which is comprised of 3-5 soil layers and two or more soil components. The bulk soil type was determined at each climate station based on the associated landscape polygon. This was done by obtaining a weighted average of the percent sand, silt, and clay over the entire profile depth for each soil component in the polygon. The representative percentages were then traced in a standard soil texture triangle to obtain the bulk soil type (e.g. loam, clay, clay-loam etc.)

7.2.3 Vegetation Growth and Leaf Area

The continuous modelling approach applied also requires that changes in vegetation height be tracked over the growing season. For this purpose, vegetation heights and the leaf area for an ideal crop and tall grass were estimated annually using the simple linear growth model described in Chapter 5. The leaf area varied between the minimum and maximum leaf area as a linear function of vegetation height. The progression of crop and grass growth considered the timing of important phenological stages and relative heights according to observations obtained at the SDNWA in 2006. For HRU 1, crop growth is taken to start in early June and crop harvesting occurs in mid September (typical life cycle of a cereal crop). Stubble (20 cm height) is left for blowing snow capture. Cultivation is taken to occur every other year with a fallow or crop-free period in between. For HRU 2, growth of the alfalfa is taken to start in early May and active vegetation is shut down at the end of September. The tall perennial grass is assumed to be harvested for the seed (as opposed to a forage or hay crop) to a stubble height of 20 cm for snow capture and new growth begins the following spring.

7.2.4 Initial Conditions and Assumptions

The model was run over a continuous period of 46 years (1960-2005) which allows hydrological continuity to be established over a long period; i.e. the initial starting conditions become less significant. The length of record also includes a normal period of 30 years which may be used as standard for comparisons with specific years of interest; the years 1971-2000 have been chosen to represent the normal period. For modelling purposes a virtual prairie basin concept was applied that consisted of three hydrological response units (HRUs). The conceptual model of the virtual basin is given in Figure 7.2. Model runs were started on Jan 1 1960 which coincides with a major drought period in the Canadian Prairie region from 1957 - 1962. According to the PFRA, "A Brief History" (AAFC), 1961 was "One of the driest years on record across most of the Prairies". This allowed for a standardization of the fall soil moisture conditions at each location which was taken to be 50% of available water holding capacity of a given soil type.

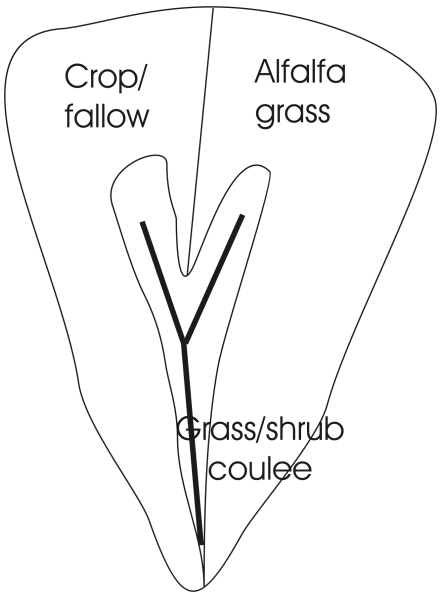

Figure 7.2: Diagram of conceptualized virtual basin with 3 HRUs.

The first HRU was treated as a standard cereal crop/fallow landscape unit which alternates between fallow and crop/stubble. In the winter, snow is allowed to be transported from this HRU to the others. The second HRU is treated as an alfalfa perennial tall grassed surface which grows each year and is the focus of the evaporation analysis. The alfalfa is assumed to be used for seed production and not as a forage crop which would require haying just prior to the blooming

period. Any runoff generated from these HRUs is routed to a grassed/shrub coulee (third HRU) which simply routes runoff out of the basin. These HRUs are assumed to be relatively flat which eliminates the need to account for differences in slope and aspect for radiation calculations. It is assumed that there is no lateral transport of surface moisture between HRU 1 and 2 and any runoff is routed directly to the outlet of HRU 3. Constant rooting depths were set for the HRUs based on the extensive research by Weaver (1926). A constant rooting depth of 1.5 m is assumed for the crop/fallow HRU which is typical of the fibrous root system of a wheat or barely crop. This can vary widely depending on the environmental conditions. Alfalfa, however, has a tap root that penetrates straight down typically to a few metres depth and even greater during drought to access deeper moisture. For this continuous modelling study, the rooting depth of the alfalfa is taken to be 3 m.

7.3 Results and Discussion

Given the immense volume of output produced by the 46 year model simulations at each station, the 'R' software environment was employed to automate the statistical and graphical analysis of the data. R is comprised of a programming language and has been applied for statistical computing in the geosciences (e.g. Grunsky, 2002), and many other physical and social sciences as well. Customizable boxplots and cumulative probability distributions were produced in R and are usfule for examining variations between several datasets at once.

Boxplots are useful for graphically describing the data and provide some general information on the underlying shape of the distribution of the data. The plots used for this analysis describe the data using seven statistics. The upper and lower limits of the box represent the 75^{th} and 25^{th} percentiles of the data (i.e. the interquartile range), and the median and mean values are indicated within the box by a solid line and a point respectively. The minimum and maximum values within 1.5 times the interquartile range are represented by whiskers connected to the box. More "extreme" values or outliers beyond the whiskers are shown as open points. The cumulative probability distribution provides information on the likelihood that a portion of the data values are smaller than another value. A two-sample Kolmogorov–Smirnov (K-S) test can also be applied to determine if there is a significant difference between two distributions. The K-S test is non-parametric and makes no assumptions about the underlying distribution of the data (i.e. no assumptions about normality).

7.3.1 Interannual Variability of Growing Season Evaporation

A graphical summary of the interannual variability of evaporation at several stations located in sub-humid zones outside the Palliser Triangle is provided in Figure 7.3. Evaporation totals are estimated for the alfafa grassed surface over the growing season (May 1 – Sept 30) for the 30 year normal period (1971 - 2000). The data for each location have been labelled and colour coded for clarity.

The range of seasonal evaporation totals at these locations was estimated to be approximately between 280 - 410 mm. These lower and upper limits occur at Winnipeg but the majority of the estimated totals at all locations lie between 340 - 400 mm as indicated by the respective whiskers. In general, the boxplots and cumulative distributions for these locations appear to be similar in shape and are relatively narrow. This indicates the variability of estimated growing season evaporation was not large for these locations. There were no high outliers but a few lower extreme totals ranging from 280 - 340 mm are noted at Brandon, Calgary, Winnipeg and Yorkton. At these locations the mean totals also lies below the median value and the lower whiskers tend to be wider than the upper whisker. As a result, the boxplots at these locations appear to be skewed toward the lower end (i.e. negatively skewed). In contrast, the spread of the estimates at Edmonton and Red Deer produced boxplots which were more symmetrical.

Figure 7.3 also shows evidence of variability in the estimated totals between several stations. This is indicated by the staggered appearance of the respective boxplots and differences in the locations of both the mean and median values; and also shifts in the cumulative distributions. At Brandon, Winnipeg and Yorkton the influence of the extreme values produced a separation between the mean and median values of the boxplots. The range in mean values was approximately 13 mm which is relatively small. Based on the means, the lowest estimated growing season totals occured at Edmonton and Yorkton. This may be partly attributed to a combination of lighter soils and the local climate conditions; e.g. cooler temperatures and lighter winds discussed as previously in Chapter 3. The highest totals tended to occur at Brandon and Winnipeg in the warmer region of southern Manitoba, but also occurred at Calgary. Overall, the results suggest that average annual precipitation at these locations is sufficient to maintain adequate soil moisture stores for the grasses.

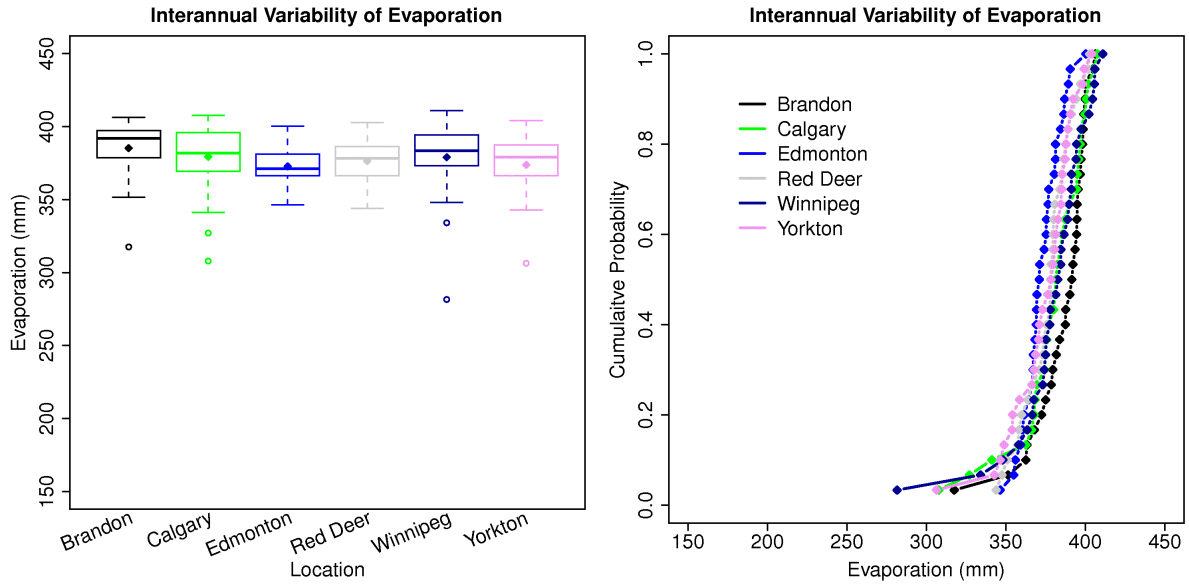

Figure 7.3: Boxplot and cumulative probability distribution graphs showing the interannual variability of growing season evaporation among stations in the sub-humid zone outside the Palliser Triangle.

A Shapiro-Wilk test for normality was performed in R to assess the departure of the estimated totals, over the normal period, from a normal distribution. According to Royston (1995) the Shapiro-Wilk test is well established and the W statistic represents a measure of the straightness of a quantile-quantile plot of the data. The null hypothesis states the data are distributed normally; this hypothesis was tested at a significance level of $P = 0.05$. When the calculated P – value is < 0.05 the null hypothesis is rejected. Results of the normality test presented in Table 7.1 show that only Edmonton and Red Deer fail to reject the null hypothesis of normality. Therefore, estimated totals for the other locations are considered to show a significant departure from a normal distribution.

Table 7.1: Shapiro-Wilk test of normality at $P = 0.05$ significance level.

Location	Shapiro-Wilk W	$P = 0.05$; P - value	H_0
Brandon	0.82	0.0002	Reject
Calgary	0.86	0.0015	Reject
Edmonton	0.99	0.99	Fail to Reject
Red Deer	0.97	0.47	Fail to Reject
Winnipeg	0.83	0.002	Reject
Yorkton	0.91	0.016	Reject

The variability was much larger, however, for those stations located within the Palliser Triangle region, and also at North Battleford (Figure 7.4). The range in estimated totals of evaporation for these locations was greatest at Lethbridge; 180 – 425 mm. For all locations the boxplots and cumulative distributions were much broader than those for locations outside the Palliser region. The interquartile ranges tended to be very large and there were considerable differences in the mean values, as well as the median values, among the locations. The upper limits of the evaporation totals were in the order of approximately 385 – 400 mm, and 425 mm at Lethbridge. The lower limits of evaporation among the locations were much more variable; 180 - 280 mm. The lowest estimated evaporation of 180 mm occurred at Estevan and is an apparent outlier.

Based on the mean values the lowest evaporation tended to occur at Medicine Hat and the highest totals tended to occur at Estevan. These results appear to be reasonable given that Medicine Hat is located within the driest region of the Prairies and Estevan is located in the southeast corner of the Palliser Triangle where rainfall is generally higher compared to that in the central and western regions. The large variability among the distributions indicates the average annual precipitation at these locations is often insufficient to maintain adequate soil moisture levels for the grasses. Differences between the mean and median values at several locations and the general lack of symmetry among the plots suggest the distributions may depart from normality. Results of the Shapiro-Wilk test are provided in Table 7.2 and shows the estimated totals for only Estevan and Swift Current may depart significantly from the normal distribution.

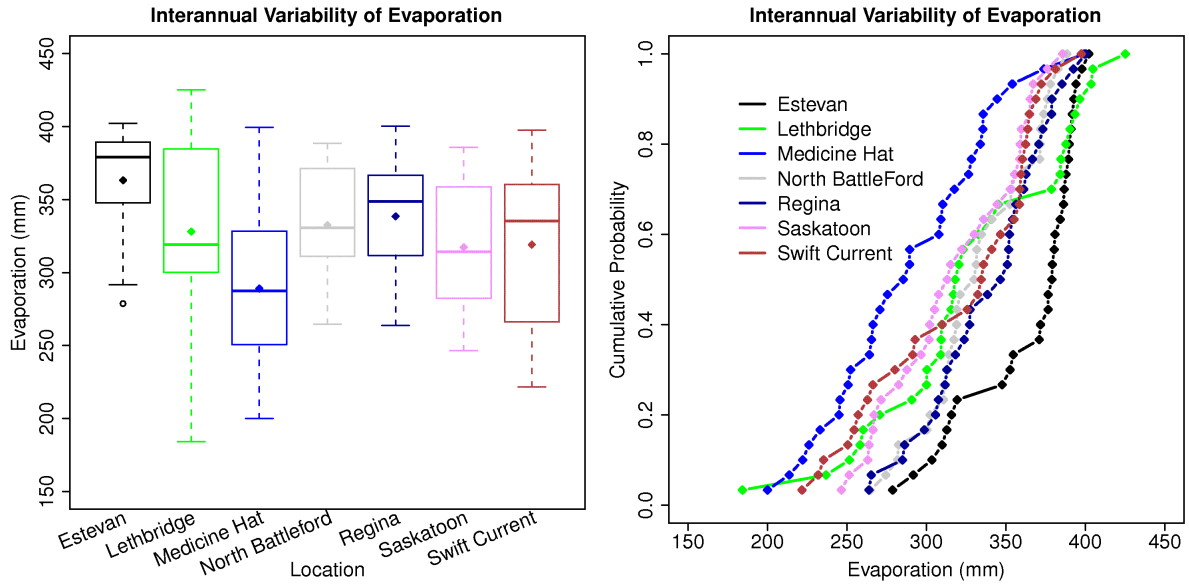

Figure 7.4: Boxplot and cumulative probability distribution graphs showing the interannual variability of growing season evaporation among stations within the Palliser Triangle and North Battleford.

Table 7.2: Shapiro-Wilk test of normality at $P = 0.05$ significance level.

Location	Shapiro-Wilk W	$P = 0.05$; P - value	H_0
Estevan	0.82	0.0002	Reject
Lethbridge	0.95	0.27	Fail to Reject
Medicine Hat	0.98	0.86	Fail to Reject
North Battleford	0.96	0.24	Fail to Reject
Regina	0.97	0.43	Fail to Reject
Saskatoon	0.94	0.11	Fail to Reject
Swift Current	0.91	0.014	Reject

7.3.2 Interannual Variability of Growing Season Daily Evaporation

7.3.2.1 Outside the Palliser Triangle

Figures 7.5 - 7.8 summarize the interannual variability of growing season daily evaporation during the drought period from 1999 – 2005 for Edmonton, Calgary, Yorkton and Winnipeg. The growing season daily evaporation for the normal period (1971 - 2000) is also shown and was used as a reference for performing a two-sample K-S test (0.05 significance level) with the distributions for each of the years during the drought period. All values of daily evaporation were

used to generate the cumulative distribution for the normal period. Results of the K-S test indicated there were significant differences between some of the distributions over the drought period compared to the normal period (denoted by an asterisk), and that the years varied depending on the location. The peak evaporation rates during the growing season for the alfalfa grass covered surface (and fully leafed) at these locations was in the order of approximately between 4 to 4.5 mm/day which is reasonable for a grass-type surface. A few higher estimates (out of almost 4900 values) of approximately between 5 mm/day and 8 mm/day (depending on the location) can be attributed to evaporation from bare soil under saturated conditions. This occurred in the early spring between Julian Days 121 – 126 when the surface resistance was zero under saturated conditions and vegetation was not yet active.

The interannual variability among the distributions was large due to the impact of drought compared to wetter years. During severe drought conditions there was a shift in the distributions toward lower values of evaporation which also resulted in a large shift in the median value. In drought years the value of the 25th percentile and the median were lower compared to non-drought years. In the case of the cumulative distributions, between 40% and 60% of the daily estimates were less than 2 mm/day under severe drought compared to 60% of the estimates which were less than 3 mm/day during the normal period at these locations.

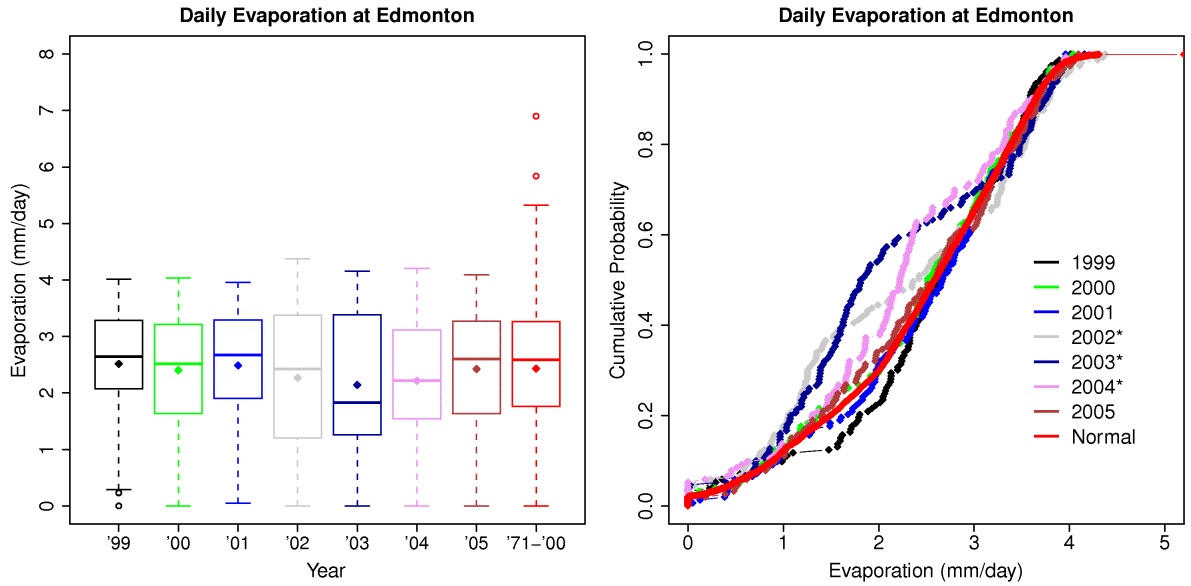

Figure 7.5: Boxplot and cumulative probability distribution graphs showing the interannual variability of growing season daily evaporation at Edmonton.

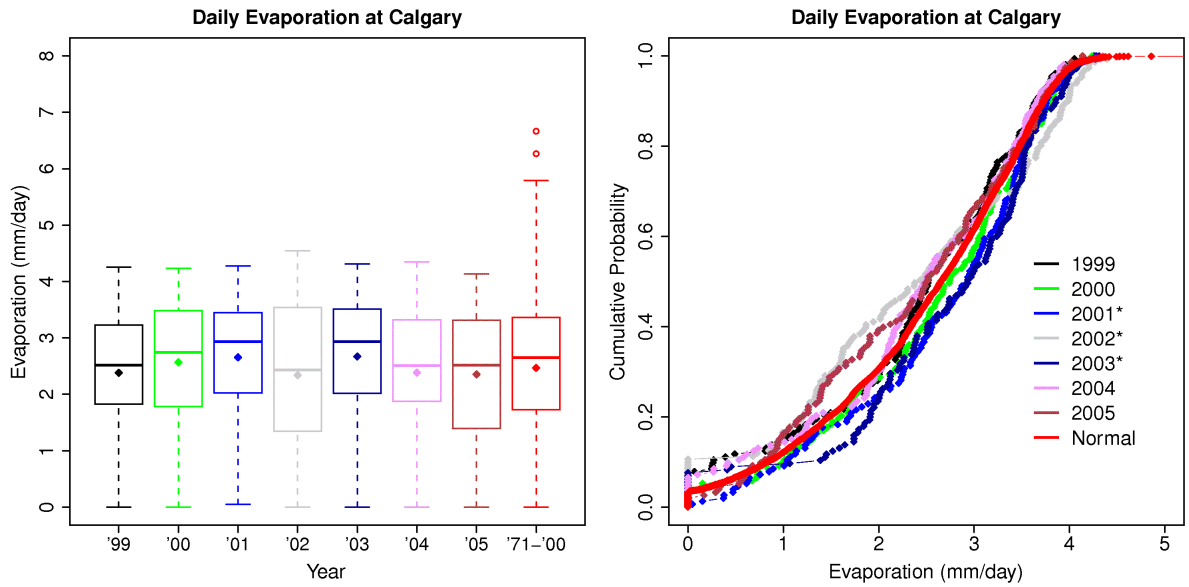

Figure 7.6: Boxplot and cumulative probability distribution graphs showing the interannual variability of growing season daily evaporation at Calgary.

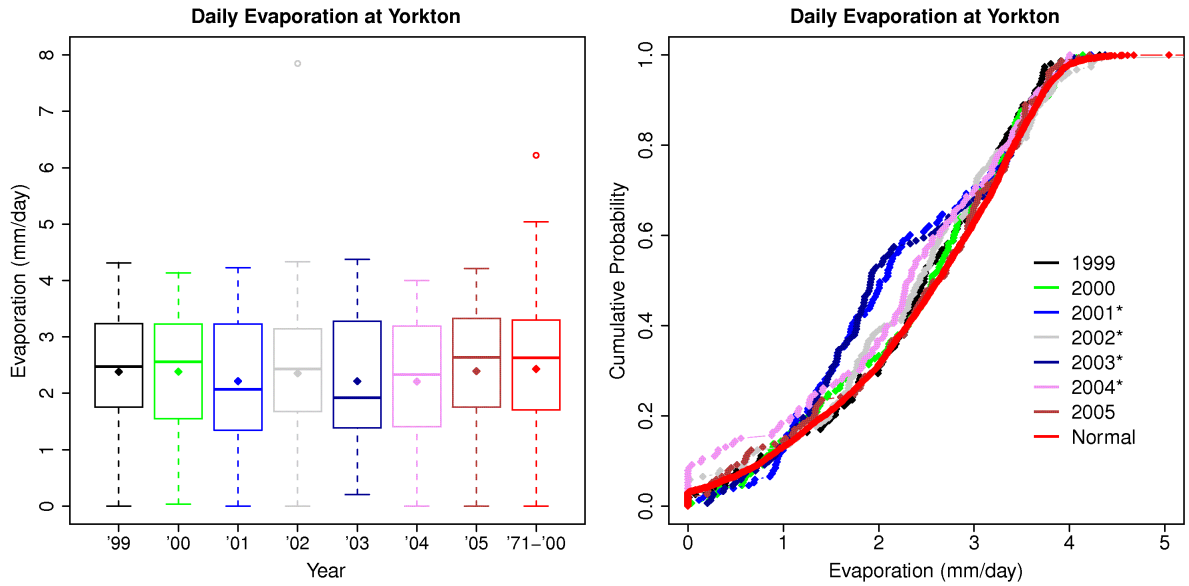

Figure 7.7: Boxplot and cumulative probability distribution graphs showing the interannual variability of growing season daily evaporation at Yorkton.

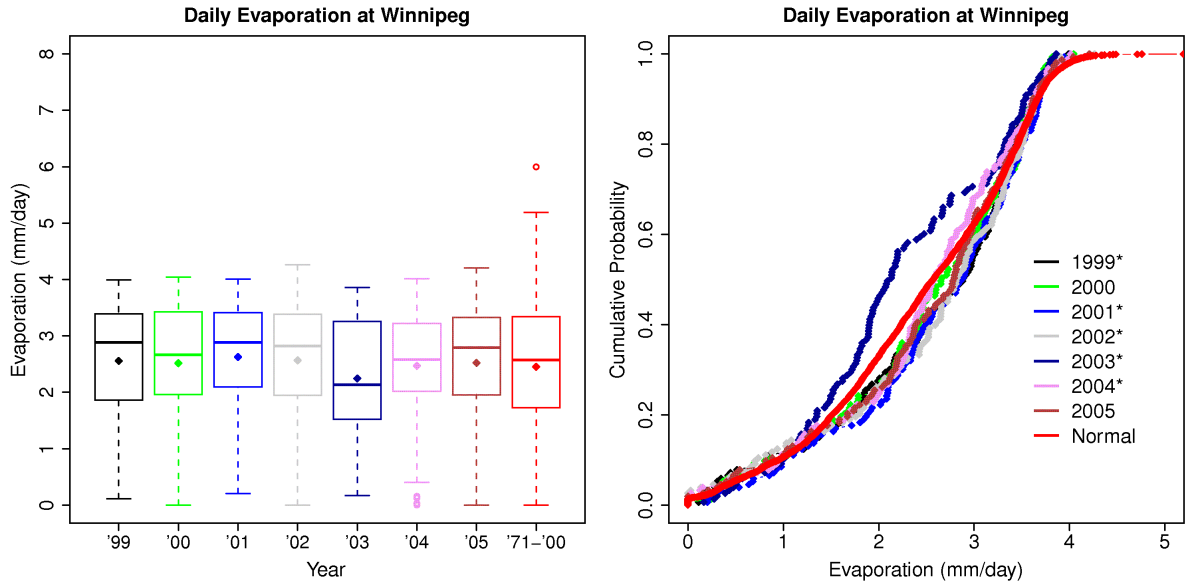

Figure 7.8: Boxplot and cumulative probability distribution graphs showing the interannual variability of growing season daily evaporation at Winnipeg.

7.3.2.2 Within the Palliser Triangle

Figures 7.9 - 7.12 summarize the interannual variaiblity of growing season daily evaporation during the drought period from 1999 – 2005 for Lethbridge, North Battleford, Saskatoon and Regina. Results of the K-S test also showed that significant differences between the distributions for the drought years and the normal period varied. In the case of Saskatoon, seasonal estimates of evaporation for all years during the drought period were found to be significantly different from the normal period. The year to year variability during the drought period was larger at these locations compared to those locations outside the Palliser Triangle, particularly in the cases of Lethbridge and Saskatoon (Figure 7.9 and 7.11). The largest range in the upper limits occurred at Lethbridge, which were in the order of approximately 3 mm/day during the drought year of 2000 to greater than 5 mm/day during the much wetter year in 2002.

In comparison to evaporation estimates for the normal period, there were large shifts in the distributions to lower values during the drought years and toward higher values during wetter years. The model behaviour appears to be physically meaningful based on the extreme swings in drought and non-drought conditions noted at Lethbridge which agree with observed variations in environmental conditions and evaporation for the AmeriFlux site. The interannual variability

among the distributions appeared to be very large over the seven year period due to the dramatic and rapid shifts between drought and wet conditions.

The value of the 25th percentile and the median values of the boxplots for Lethbridge, North Battleford and Saskatoon (Figures 7.9 – 7.11) were generally lower in drought years than in non-drought years. In the case of the cumulative distributions, between approximately 40% and 60% of the daily values were again less than 2 mm/day under severe drought compared to the normal values. In general, the large shifts in the distributions of evaporation would indicate that drought and non-drought conditions can be readily identified at a given location.

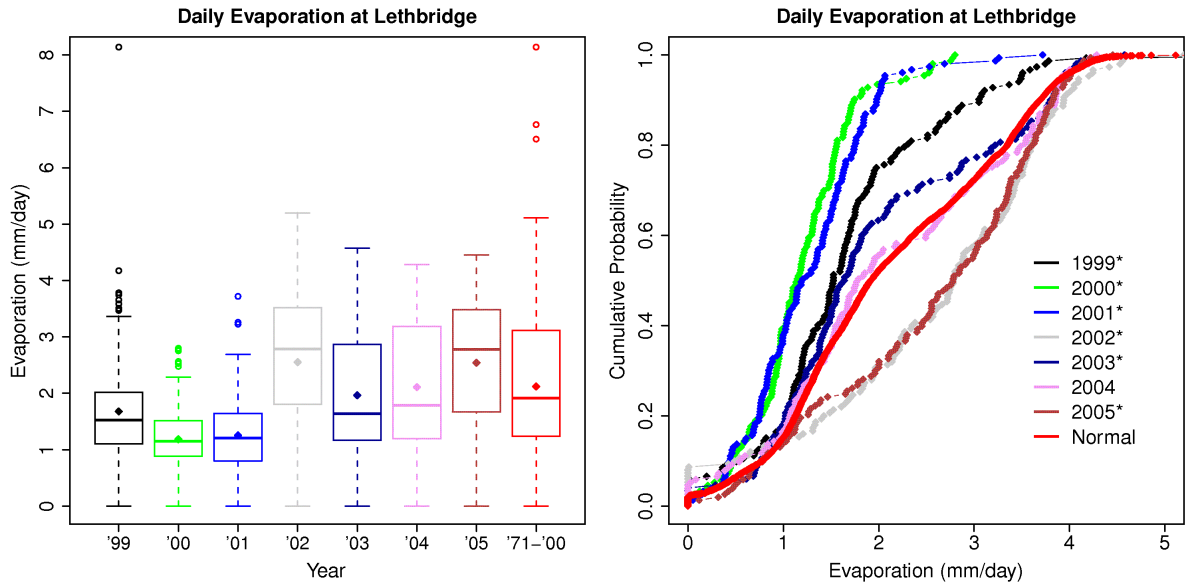

Figure 7.9: Boxplot and cumulative probability distribution graphs showing the interannual variability of growing season daily evaporation at Lethbridge.

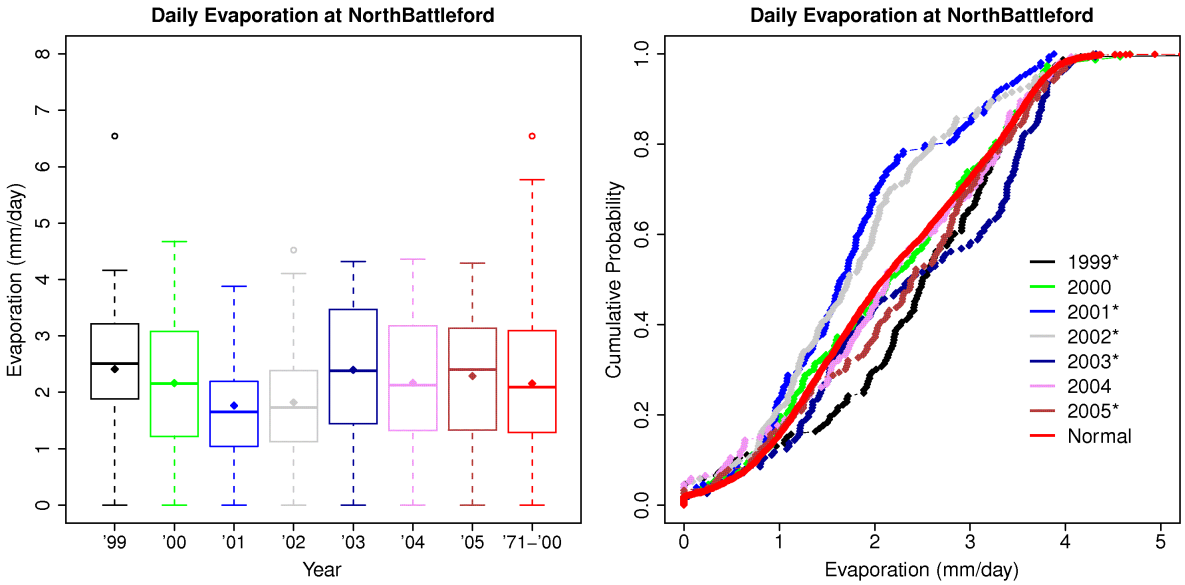

Figure 7.10: Boxplot and cumulative probability distribution graphs showing the interannual variability of growing season daily evaporation at North Battleford.

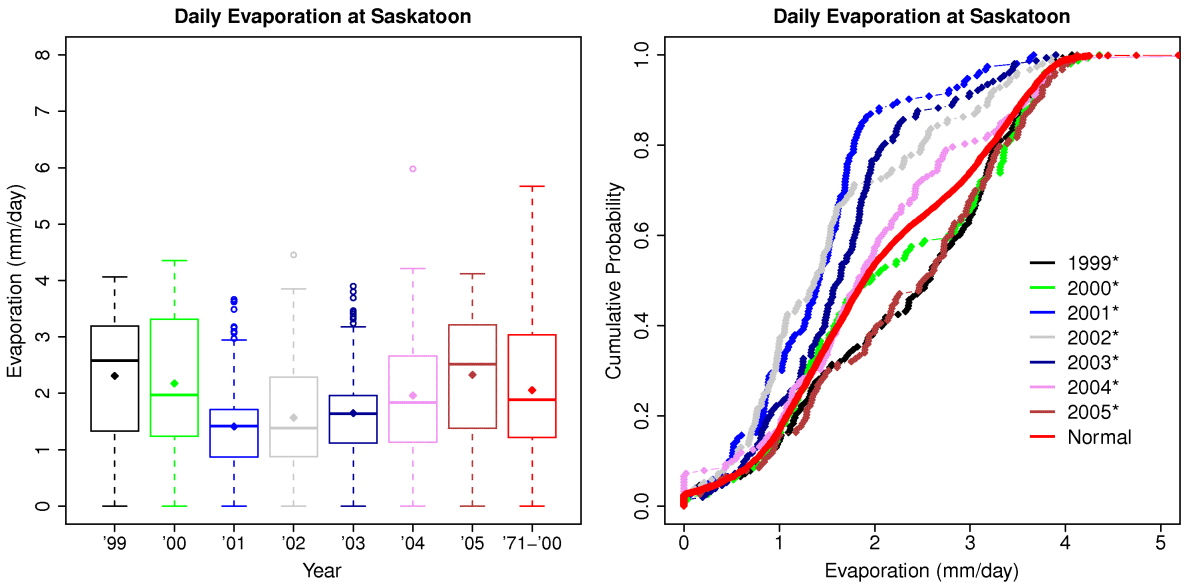

Figure 7.11: Boxplot and cumulative probability distribution graphs showing the interannual variability of growing season daily evaporation at Saskatoon.

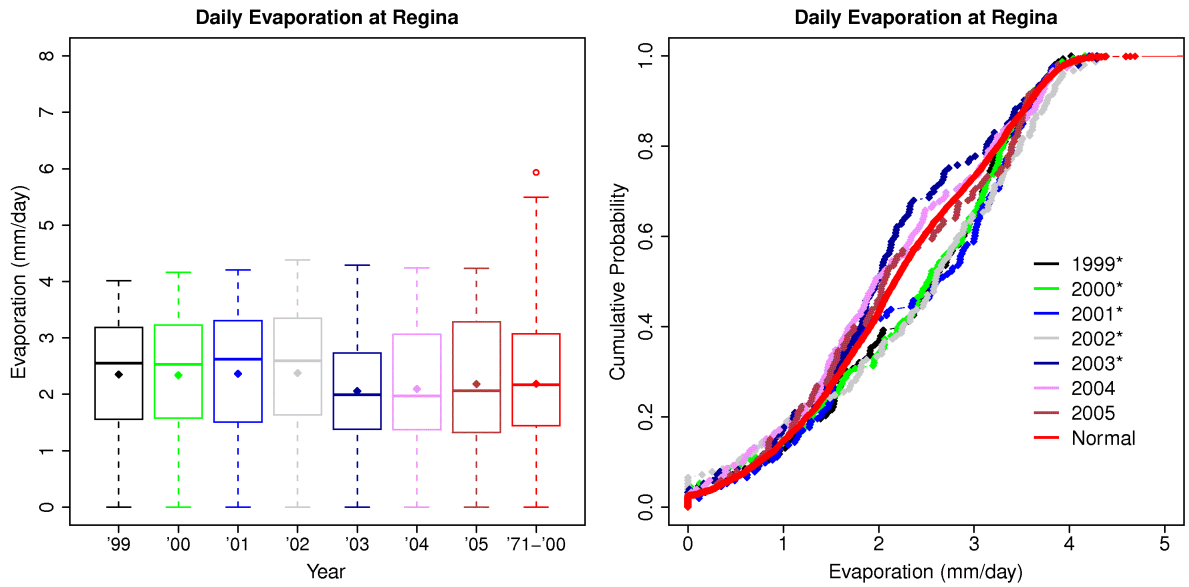

Figure 7.12: Boxplot and cumulative probability distribution graphs showing the interannual variability of growing season daily evaporation at Regina.

7.3.3 Variability of Growing Season Evaporation and Driving Factors

This section presents results for the anlysis of growing season estimates of evaporation among all 15 stations for the drought years 1999 - 2005. It is noted here that due to the limitations in the number of stations considered and the large distance that exists between them, there is insufficent information for conducting an analysis on scale related issues. However, the results were useful for describing the general variability of evaporation driven by climate factors and soil moisture differences among the stations, and also changes in the general sturcture of the drought.

A graphical summary of the growing season total evaporation among the stations is provided in Figure 7.13 using boxplots and the cumulative distribution. The measures provided by the boxplots indicate there were notable differences in evaporation estimates among the stations from year to year during the drought period. For example, there was large variation in the interquartile range of evaporation among the years. In the driest year (2001) the interquartile range was approximately 130 mm but for the wettest year (2005) was only 17 mm. The locations of the mean and median values also fluctuated for several years. This appears to be partly a result of the spread between estimates and general shifts in the distribution of the estimates during drier

and wetter years; keeping in mind that the limited number of data points is also a contributing factor. In some years (e.g. 1999 - 2002) the median value appeared to be a better descriptor of the structure of the data due to the larger influence of lower estimates and outliers on the mean.

Variations in the upper limit of the evaporation estimates between years tended to be smaller than compared to the lower limit. There was a general increase in the variability among evaporation estimates as the drought progressed from 1999 - 2001. In 1999, the variability between estimates was relatively small and increased for 2000. In both years, however, two extreme lower estimates were obtained at Medicine Hat and Lethbridge. These outliers provide a good indication of the increasing drought conditions within the southwestern portion of the Palliser Triangle. The largest variability in the estimates occurred in 2001 and was characterized by the lowest and highest evaporation totals and a large difference in the mean and median values. From 2002 – 2005 there was a decrease in the variability of the estimates as there was a progression toward wetter conditions. In the case of the cumulative distributions, 40% of the values tended to be less than approximately 350 mm in any given year. Results of the K-S test indicated that the distribution for 2001 was the only year for which there was a significant difference compared to the normal period (denoted by an asterisk).

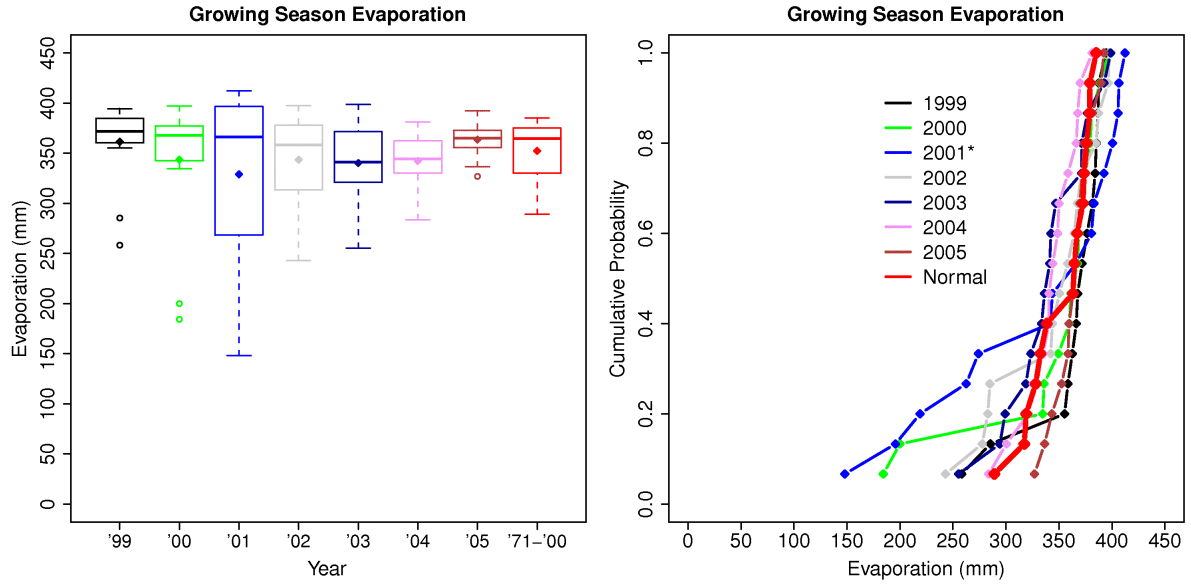

Figure 7.13: Boxplot and cumulative probability distribution graphs showing the regional variation of growing season evaporation among the 15 climate stations.

Figures 7.14 – 7.17 show the growing season total rainfall, soil water content on May 1, mean air temperature and vapour pressure deficit to be much more variable relative to the normal distributions than was the case for the evaporation estimates. The rainfall values among the locations for 1999, 2001, 2003 and 2005 were found to be significantly different compared to the normal period (Figure 7.14). Rainfall in both 2001 and 2003 tended to be low compared to the normal rainfall across the region whilst the range of rainfall among the stations was relatively large. Rainfall was relatively high at many locations in 1999 with a few locations indicating lower than normal values, and was generally the highest in 2005. In these cases, there was a large shift in the values relative to the normal values.

The soil water content (SWC) to the depth of the rooting zone on May 1 was considered because it is a useful indicator of the initial state conditions prior to vegetation being active. As shown in Figure 7.15, SWC among the locations on this date tended to intersect the normal values at the lower (less than 300 mm) and higher ends (greater than 350 mm) with some overlap in the middle range. Interestingly, SWC on May 1 for 2004 started off much lower than the normal SWC but was subsequently offset by above normal rainfall at several locations. Only the 2002 and 2004 values were found to be significantly different from the normal values.

The values of mean air temperature among the locations tended to show distinct shifts from the normal values (Figure 7.16). There were significant differences in the 1999, 2001, 2003 and 2004 values compared to the normal values. In 2001 and 2003 temperatures were much higher than normal. Temperatures were generally at their lowest among the locations in 2004. Figure 7.17 shows that shifts in the values of the mean vapour deficit (VPD) follow the values of air temperature closely from year to year; as is to be expected. In this case, all years but 2002 were found to be significantly different from the normal values. The mean VPD among the locations was much higher in 2001 and 2003 corresponding to the higher temperatures and lower rainfall whilst the VPD was the lowest during the wetter years of 2004 and 2005.

Values of mean wind speed among the stations (Figure 7.18) remained similar over the drought period and failed to show any significant differences from the normal values. The range of mean wind speeds over the growing season was shown to be in the order of 3 m s^{-1} to 5.5 m s^{-1}, and the mean and median values tended to increase slightly from 1999 - 2002.

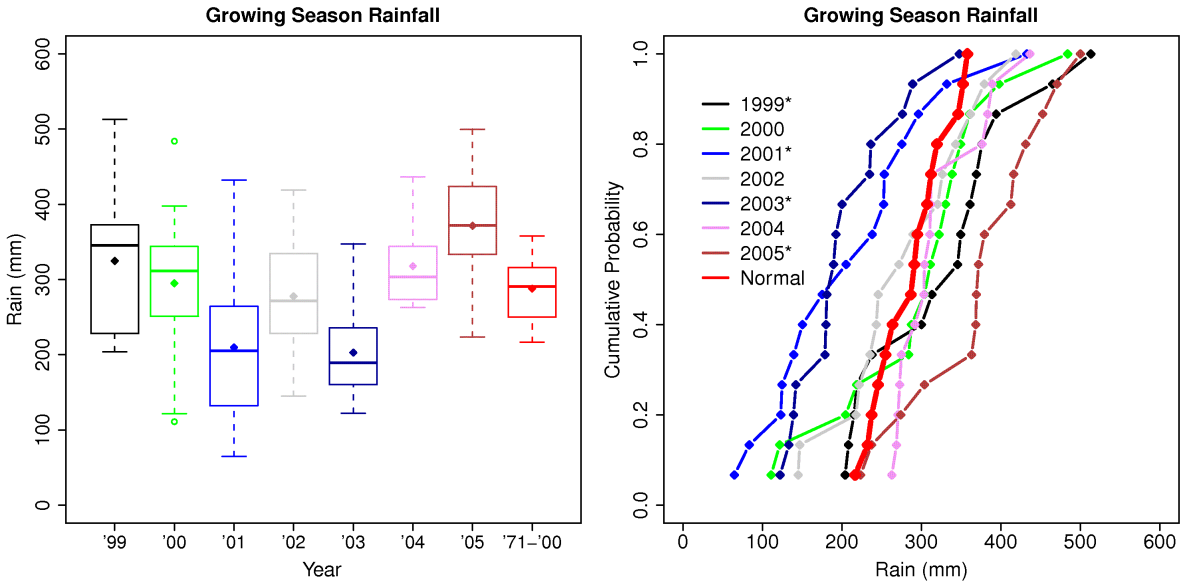

Figure 7.14: Boxplot and cumulative probability distribution graphs showing the regional variation of growing season rainfall among the 15 climate stations.

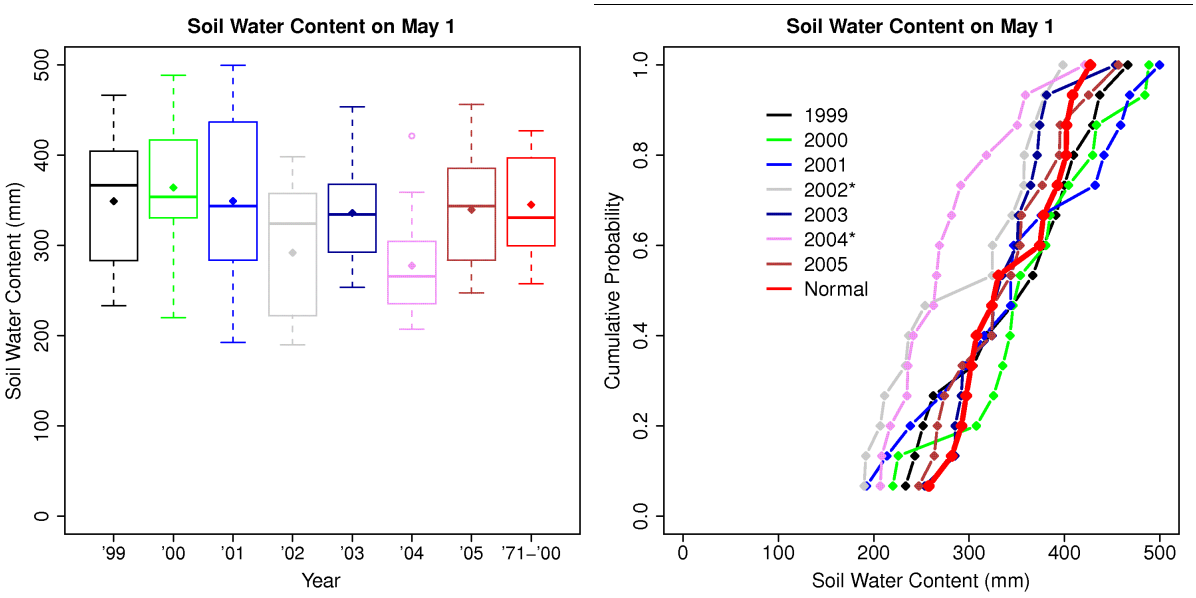

Figure 7.15: Boxplot and cumulative probability distribution graphs showing the regional variation of modelled soil water content on May 1 among the 15 climate stations.

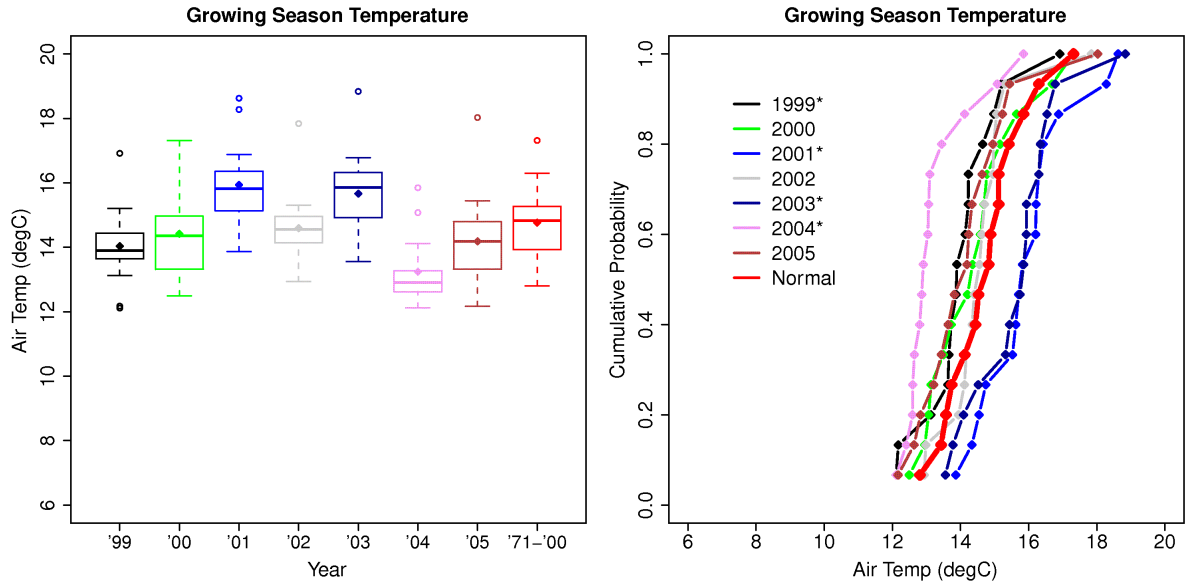

Figure 7.16: Boxplot and cumulative probability distribution graphs showing the regional variation of growing season mean air temperature among the 15 climate stations.

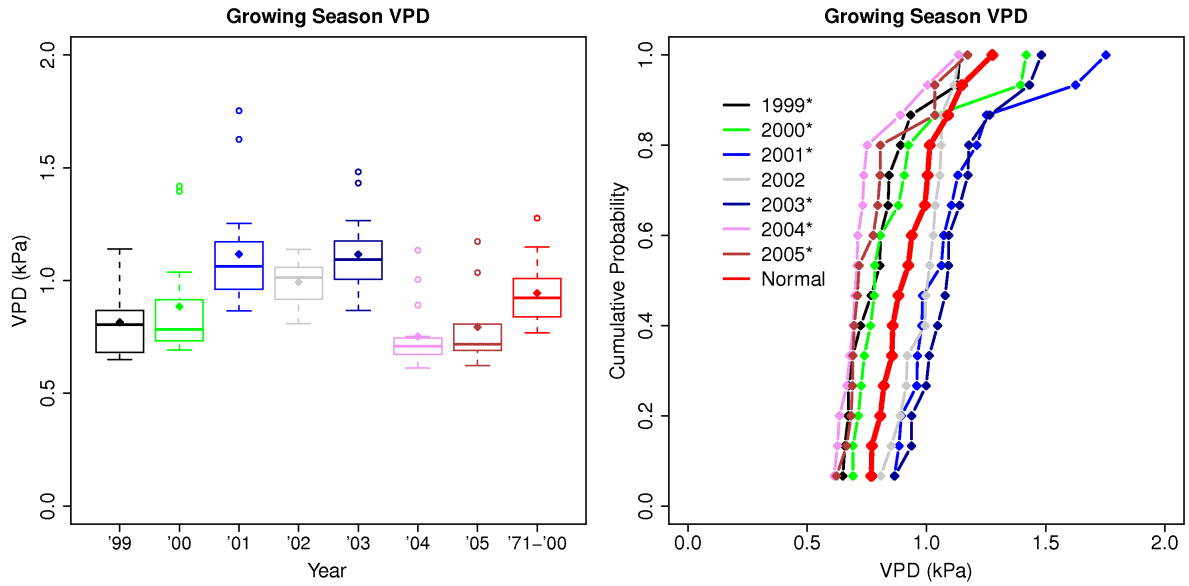

Figure 7.17: Boxplot and cumulative probability distribution graphs showing the regional variation of growing season mean vapour pressure deficit among the 15 climate stations.

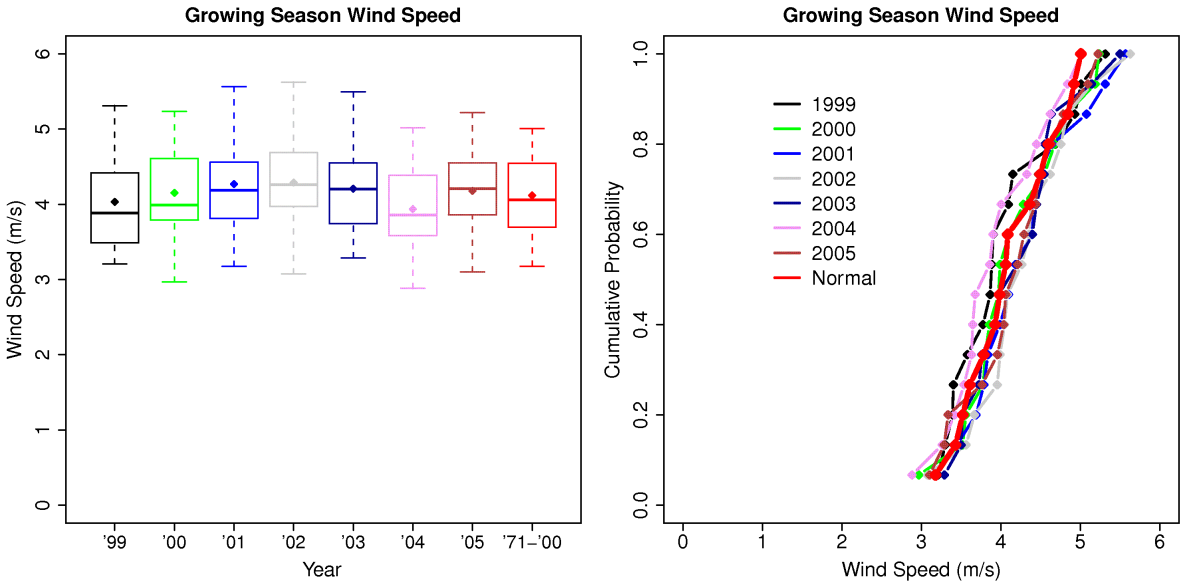

Figure 7.18: Boxplot and cumulative probability distribution graphs showing the regional variation of growing season mean wind speed among the 15 climate stations.

7.3.4 Changes in the Structure of Drought

7.3.4.1 Evaporation and Exceedance Fraction Analysis

Useful information on the year to year changes in the structure of the drought was obtained by generating maps of the general spatial pattern of evaporation. Maps showing changes in the spatial pattern of evaporation and exceedance fractions of evaporation relative to the normal period are presented in Figures 7.19 - 7.24. The evaporation maps were produced by applying a spline interpolation to the growing season totals for the 15 stations. The spline technique was applied for the following reasons, 1) according to Hutchinson and Gessler (1994) it provides results that are as good as kriging but does not require the determination of the semivariance between points, which partly depends on the spacing, 2) spline techniques have been developed specifically for use with climate data (Hutchinson, 1995), and 3) it applies a piecewise polynomial to produce a smoothed surface that passes through every data point while minimizing the curvature between the respective points.

A series of steps was needed to produce the exceedance fraction maps. First, the empirical cumulative distribution function was calculated at each location from the growing season totals corresponding to the normal period; values are ranked and associated with the probability of

being less than the next highest value. The exceedance fraction was then determined at each location for a specific year based on the culmulative distribution function for all the values over the normal period. The spline interpolation was then applied to the data at each location to produce a generalized map of the exceedance fractions. Station locations are indicated on the maps as a reference.

Terrestrial estimates of actual evaporation are typically not considered as primary descriptors of drought in Canada but may be useful where long term records exist for driving a hydrological model. In general, the spatial pattern of evaporation for the region as a whole does not appear to be stable over time. Figures 7.19 - 7.21 show the resulting pattern of drought as it shifted from the southwest to the north for the years 2000 – 2002. Figures 7.22 and 7.23 then show a shift towards the east in 2003 and 2004. In the 2005, the range of evaporation was greatly reduced as a result of the wetter conditions across the region (Figure 7.24).

The respective exceedance fraction maps provide further information by characterizing evaporation compared to what might normally be expected. Essentially, the exceedance fraction of evaporation could be used as an indicator at season's end of how the seasonal evaporation compared to previous years. A large moisture deficit might result when growing season rainfall is less than normal and evaporation is supplemented largely from stored soil moisture. This may be useful information in predicting soil moisture when combined with the knowledge of precipitation from the fall, winter (including snowpack), and early spring.

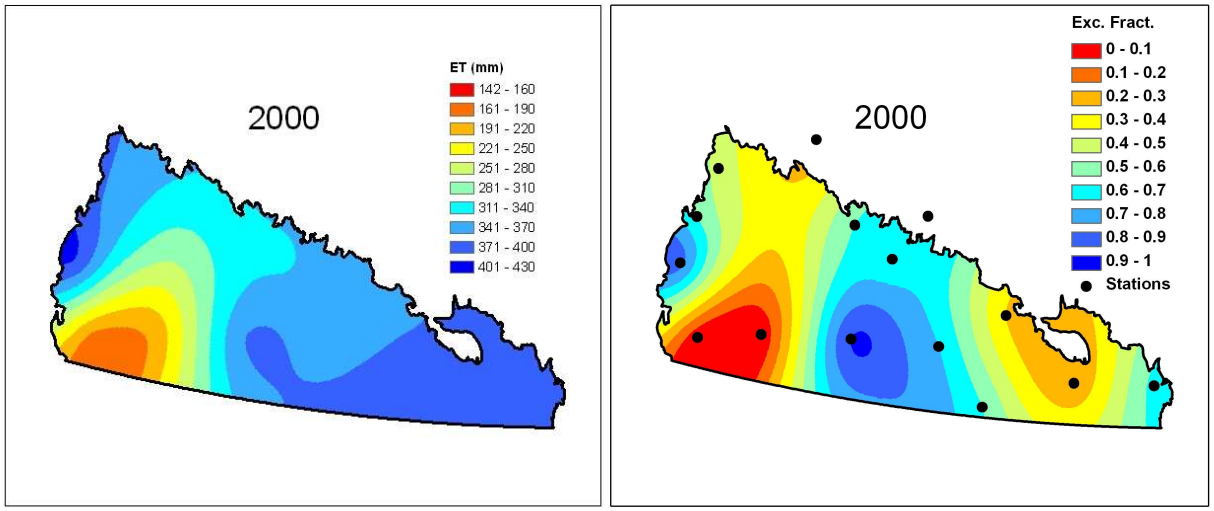

Figure 7.19: Growing season evaporation and exceedance fraction maps for 2000.

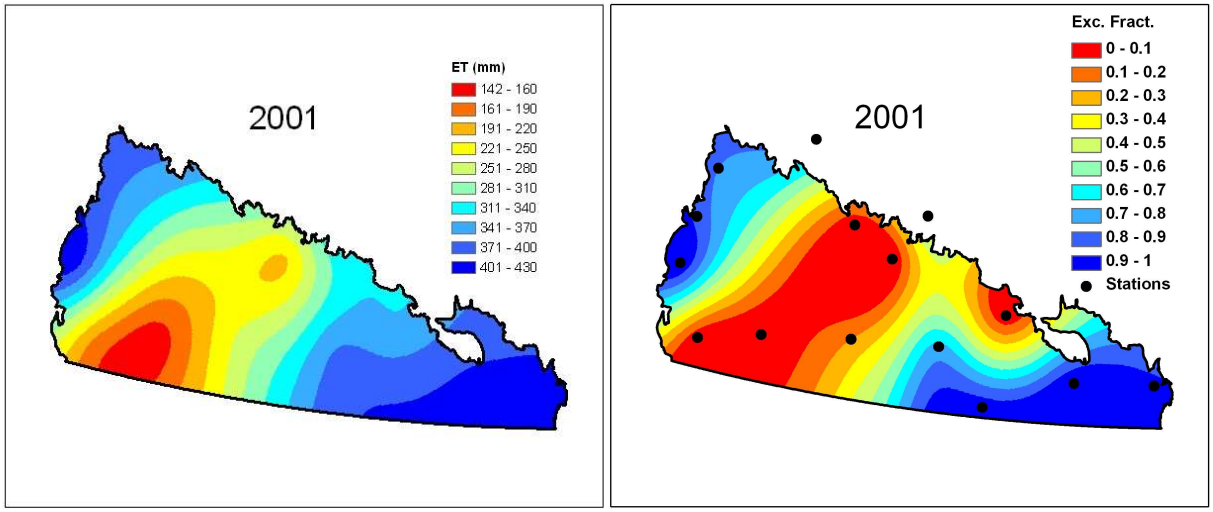

Figure 7.20: Growing season evaporation and exceedance fraction maps for 2001.

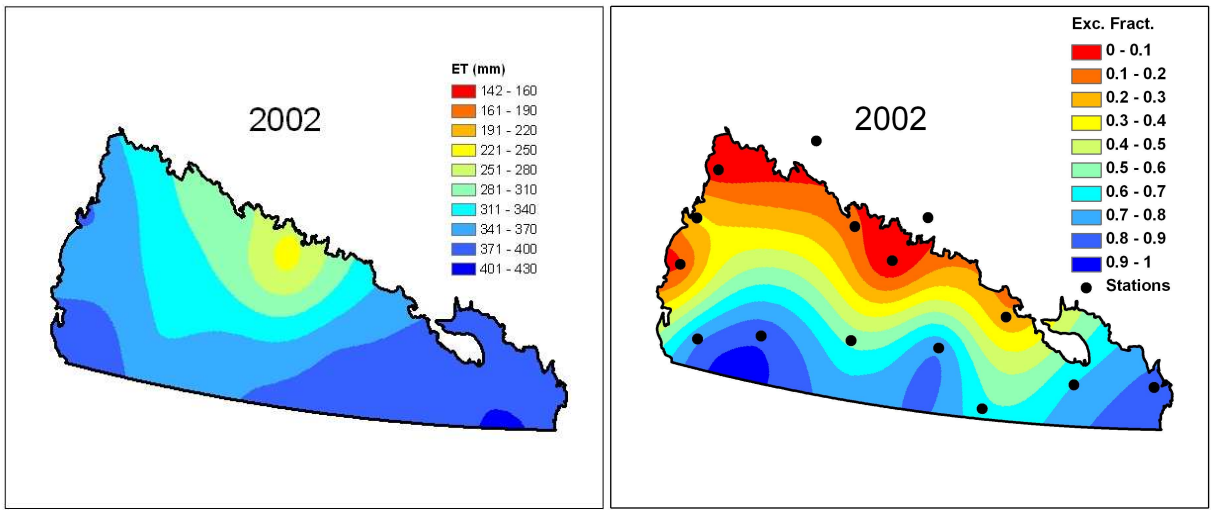

Figure 7.21: Growing season evaporation and exceedance fraction maps for 2002.

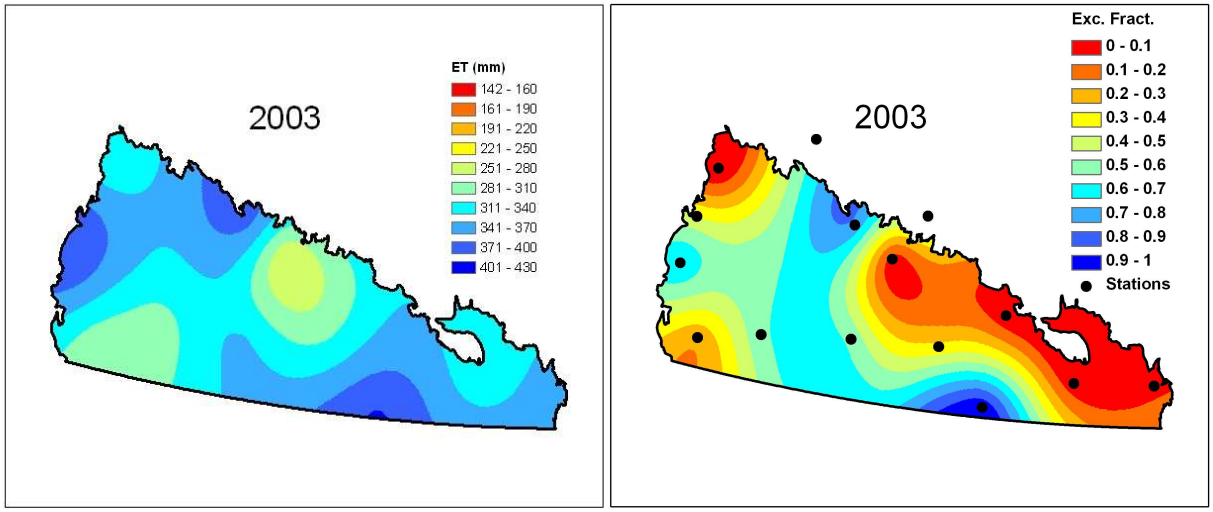

Figure 7.22: Growing season evaporation and exceedance fraction maps for 2003.

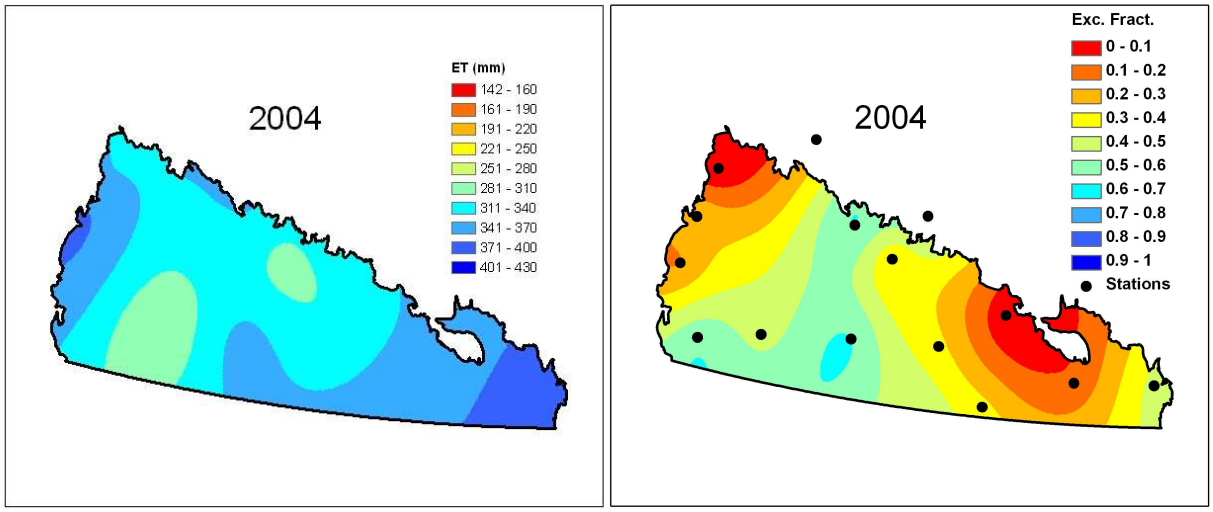

Figure 7.23: Growing season evaporation and exceedance fraction maps for 2004.

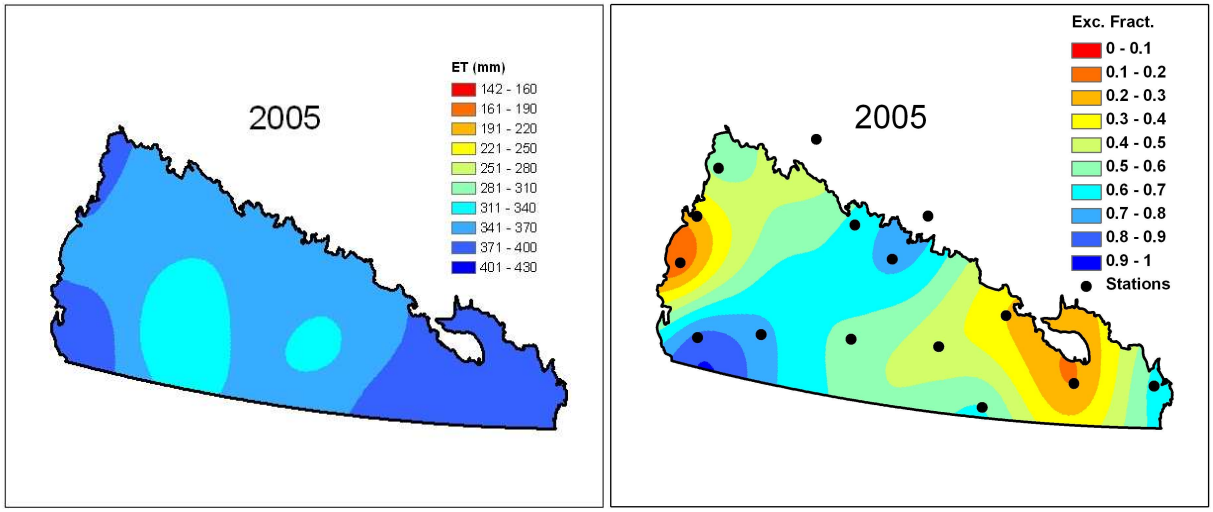

Figure 7.24: Growing season evaporation and exceedance fraction maps for 2005.

7.3.4.2 General Variability of Evaporation During the Drought Period

The general variability of the evaporation estimates among the stations was examined over the drought period by considering changes in the coefficient of variation, cv. As was indicated previously in Chapter 6 and as observed in Appendix A (see discussion on transect profiles), the cv can provide useful information on relative variations of data within a distribution when the means might be different. Figure 7.25 shows how the variability changed from year to year during the drought period. The results showed a relatively linear increase in variability as the drought progressed from 1999 to 2001 and a sharp reduction from 2002 through 2005 as the conditions became more uniform. By way of comparison, similar variability was found during a previous period (1987 – 1989) when a major drought is known to have occurred in 1988. For these years the variation (cv) among the stations was 0.10 for 1987, 0.20 for 1988 and 0.11 for 1989.

It would be difficult to compare the variability in evaporation estimates exhibited over the Prairie region to that for the case study presented in Chapter 6 due to the differences in magnitude of the estimates. However, it would appear the large scale variability of estimates during the drought period is larger in general than that shown for the distributed estimates obtained at SDNWA at the field scale during the case study. In other words, it would appear to be reasonable to obtain as many point estimates as possible for deriving the variability of evaporation at much large scales. This would suggest the variability between respective point

locations should not be ignored where regional scale estimates are needed and valuable information might therefore be missing between climate stations. Such information could also be valuable for further examining the possibility of covariance between factors driving evaporation.

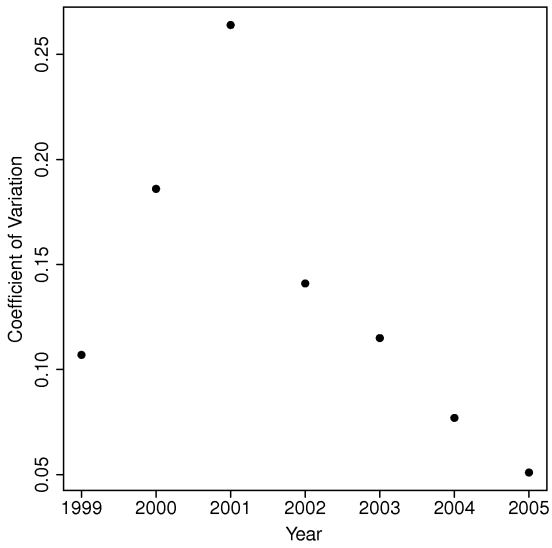

Figure 7.25: General variability of evaporation among the stations from 1999 - 2005.

7.4 Summary and Conclusions

The general spatial and temporal variability of evaporation and driving factors was examined at 15 stations across the Prairie region where complete sets of long term meteorological forcing data could be obtained. A hydrological model was assembled within the CRHM platform by linking the *P-M* evaporation model with a series of physically-based algorithms describing processes relevant to Prairie hydrology. For the winter period, these included blowing snow transport, sublimation and infiltration into frozen soils, and for the summer period, infiltration, runoff and soil moisture accounting. Due to a lack of observations, net radiation was modelled using radiation estimation algorithms available within CRHM. The hydrological model was allowed to run continuously over a 46 year period extending from Jan 1, 1960 – Dec 31, 2005 and evaporation was calculated from a grassed surface over the growing season period assumed to extend from May 1 to Sept 30.

An analysis consisting of summarized model output by means of boxplots and cumulative distributions examined the interannual variability of growing season total and daily evaporation,

and the general variability of seasonal evaporation estimates at several stations located within the Prairie region of Western Canada. Overall, the results showed that evaporation is both temporally dynamic and spatially variable as a result of the complex interactions between the surface state and atmospheric conditions. Results of model simulations at sites located within sub-humid zones suggest that growing season evaporation is generally balanced by average annual precipitation and interannual variations in evaporation tended to be relatively low compared to locations within the Palliser region. The shape of the cumulative distributions tended to be similar among the locations over the normal period. However, there were notable shifts in distributions between several of the locations which may be attributed partly to differences in the water holding capacities of the bulk soils and also the general climate conditions. The distributions were also relatively narrow which would indicate that the variability at a given location was reduced when moisture was not a strong limiting factor. Under severe drought conditions, however, the distribution of daily evaporation tended to show a strong departure, in both magnitude and shape, from the normal values and also the respective distributions in non-drought years. In other words the variability of the estimates tended to increase with more pronounced changes in soil moisture during drying periods at locations that typically had adequate soil moisture.

By comparison, within the Palliser region where annual precipitation was more variable, there were larger differences in evaporation estimates. In general, the distributions at a given site tended to shift from year to year depending on relative differences in soil moisture due to variations in spring melt and growing season rainfall. As a result there was greater difficulty in recharging large soil moisture deficits without receiving higher than normal precipitation prior to the start to of the next growing season. Distributions of daily evaporation at Lethbridge and Saskatoon tended to show less variability under conditions of severe soil moisture limitations during drought and also during periods when soil moisture was not as limited (e.g. Lethbridge in 2002 and 2005; Saskatoon in 1999 and 2005).

The combination of evaporation and exceedance probability maps provided some useful information on the general changes in the structure of drought. Specifically, the resulting pattern of evaporation was not consistent during the period and might show further differences if more detailed information were available between the stations. The exeedance fraction maps provided information on the relative differences in evaporation compared to the normal values obtained at

each location. Such maps may also provide useful supplemental data for describing drought conditions in preparation for the next growing season.

CHAPTER 8

CONCLUDING SUMMARY

A combination of physically-based modelling techniques was applied to examine the spatial variability of evaporation in the Prairie landscape of Western Canada. This included the application of point scale evaporation models, the assimilation of remotely sensed visible and thermal imagery and visualization using Geographical Information System (GIS) software, and archived historical climate data for long term continuous hydrological modelling. Where available, reference surface data were used to parameterize the models.

The accuracy of point scale evaporation models for obtaining direct estimates of actual evaporation under conditions when soil moisture was not a strong limiting factor and during drought were assessed against eddy covariance measurements. Net radiation is a key variable needed for estimating evaporation using energy balance approaches and Penman-type evaporation models. A method for distributing mean daily net radiation across a field sized area was developed based on remotely sensed mid-day images of surface albedo and surface temperature. The distributed estimates of net radiation and surface reference climate data were integrated with the Granger and Gray model to directly obtain distributed estimates of actual evaporation over a field area. Variations in the distribution of evaporation and driving factors were examined. A comparison was made of measurements obtained by the EC method and model estimates for points and also several areal estimates provided by the model. A hydrological model assembled in the Cold Regions Hydrological Model (CRHM) platform was applied at several locations within the Prairie region using archived historical climate data to examine spatial and temporal variations of evaporation over the Prairie region of Western Canada during a drought and non-drought period.

The *P-M*, *G-D* and *BT* point scale models were applied to a complex mix of tall grasses at the St. Denis National Wildlife Area (SDNWA) in 2006 under conditions where soil moisture was not a strong limitation. The models were driven by climate and surface reference observations and found to provide reasonable estimates of actual evaporation for multi-day periods and for the season. No single model was capable of consistently providing the best estimates of evaporation over multiday periods. The modelled estimates were found to be less accurate when considered over daily periods, which was indicated by an increase in the variance

of the estimates. Field data were also collected over the course of the study period during 2006 along several transects ranging from 100 m to 200 m in length with a point spacing of 5 m. In general the data showed that soil moisture and surface temperature were much more variable spatially than air temperature and atmospheric water vapour which tended to vary temporally as measurements were conducted. At relatively small length scales, larger observed differences in surface state conditions (i.e. moisture and surface temperature) were not reflected in the overlying atmosphere at a measurement height (2 m). This might be a result of general roughness conditions and winds observed at the site allowing the boundary layer over the surface to become well mixed (i.e. blended). This would suggest there are differences in the spatial scales of land surface-atmosphere interactions driving evaporation. Therefore, it may be possible to use spatially averaged values of climate variables for relatively short length scales depending on the sensitivity of the model. However, spatial variations in water and energy availability may require more detailed consideration.

The behaviour of the Penman-Monteith *(P-M),* and Granger and Gray *(G-D)* models was examined at the Lethbridge AmeriFlux site under drought conditions in 2000 and 2001 for estimating evaporation over a mix of short grasses and varying rooting zone depths. The models were parameterized based on observations of soil and vegetation characteristics and historical accounts of rooting habits of the species in other prairie environments. In general, the behaviour of the models was good compared to the seasonal variations in the observed cumulative estimates over the two periods. Variations in the model estimates were apparent which may be attributed to theoretical differences in the models. Historical observations of rooting habits for the short grasses during drought were considered in the parameterization of the model. Rooting zone depth was subsequently found to influence the magnitude of seasonal evaporation estimates under drought conditions.

For the range of relatively shallow rooting depths examined (0.8 m to 1.4 m), adjusting the depth appeared to have a minor effect on the shape of the simulated evaporation curves over the growing season which compared reasonably well with the observed curves. Better agreement between the simulated and observed cumulative evaporation could be achieved when the rooting zone depth was in the order of 1 m to 1.2 m for the *P-M* model and 1.2 m to 1.4 m for the *G-D* model. The results showed the general importance of adequately characterizing available soil moisture during drought and the rooting depth appeared to be a critical factor at least in the case

of shallower rooting grasses. Based on the results of the two studies, the point scale models appeared to behave in a realistic manner, and reasonable estimates of evaporation could be achieved over the growing season periods under conditions when soil moisture was not a strong limitation at the SDNWA in 2006 and under drought conditions at Lethbridge in 2000 and 2001.

Net radiation is a crucial factor for estimating evaporation from the land surface. A method of distributing net radiation over a field was developed at the SDNWA for a case study on August 5, 2007. The pattern of net radiation was driven by variations in albedo and surface temperature obtained from one-time-of-day remotely sensed visible and thermal images and surface reference data. An adequate spatial representation of soil moisture variability across the field was not possible for estimating evaporation but this was circumvented by deriving estimates of actual evaporation using the *G-D* model. Air temperature, the vapour deficit and wind speed were assumed to be constant over the field based on consideration of the observations and a sensitivity test of the model. The incoming shortwave and longwave radiation components were also assumed to be constant based on the available observations. The spatial patterns of surface albedo and surface temperature were used as an index for distributing the mean daily net radiation over the field. This required the derivation of the mid-day radiation ratio which is the ratio of net radiation at any given point to a reference value obtained at a known location, and a known value of the daily net radiation at the reference location. Surface temperature was found to be as important as surface albedo for distributing estimates of net radiation over different surfaces covers which included grasses, a fallowed/cultivated area, and tall trees and shrubs around wetlands. Generalized surface roughness heights were obtained by segmenting the visible image into groups of similar reflectance properties. The grouped data were found to conveniently correspond with the general characteristics of the surface cover types and general differences in surface state conditions.

Results of a validation at two available measurement sites showed the error between the model estimates and measured net radiation to be + 4% and - 7% respectively. This suggested that net radiation could be distributed over the field from a known value of the daily mean net radiation based on the indexed mid-day radiation ratio. Actual evaporation was then estimated directly over the field from the distributed estimates of net radiation and surface reference climate data. A comparison of measured values obtained from the EC method and model estimates was made which included point values and areal estimates. An areal estimate was

obtained for the brome grass surface from the distributed estimates provided by the *G-D* model for a 10 x 8 grid of cells (equivalent to 2000 m^2). The distributed model estimates were assumed to be within the footprint of the EC measurements of evaporation. The average of the distributed estimates surface was 2.7 mm/day and was within 0.5 mm of the EC observation of 2.2 mm/day. A *G-D* point estimate derived from station meteorological measurements alone was found to be 2.5 mm/day. The general variation in model estimates and measured values was generally small and partly reflect the differences in calculation methods. The differences also reflect the general uncertainty arising from possible errors in the measurements and theoretical considerations and assumptions of the model calculations.

An examination of the distributions of evaporation and driving factors was conducted to evaluate the effects of spatial associations on evaporation estimates and the potential implications for uspcaling evaporation estimates. When considered over the entire image, the distributed estimates obtained with the *G-D* model produced an areal average of approximately 2.8 mm/day. An equivalent areal estimate was also obtained by summing the weighted estimates of mean evaporation for the general roughness classes which effectively sub-divided the field into three general areas. Mean values of the driving factors, namely net radiation, relative evaporation and the turbulent flux component for each of the roughness classes were also used to parameterize the *G-D* model. It was found this resulted in a relatively small consistent underestimation (-0.2 to -0.14 mm/day) of the expected weighted average values of evaporation. Further, when the mean values of the driving factors for the entire area were used to drive the model, the areal estimate was found to be 2.73 mm/day. In other words, relatively similar evaporation estimates were achieved whether the variations in the distributed estimates of evaporation were considered over the field or the model was parameterized at varying scales from the mean values of the driving factors.

The general insensitivity of the model to the various parameterizations can be attributed to the offsetting interactions of the model parameters. In general, a negative relationship was shown between the mean values of *G* and the available energy Q* and the turbulent flux component, E_A among the roughness classes. The result was that potentially large estimates in evaporation resulting from increases in energy availability and enhanced turbulence were counteracted by a reduction in the mean of *G*. Also, where the turbulent component showed a general increase in evaporation there was a general decline in evaporation from the energy component; particularly

in the case of the largest roughness class. The variation in the energy component appeared to be much smaller than for the turbulent component likely due to the empirical nature of the wind function.

The spatial associations of driving factors were further considered to evaluate the possibility of a covariance that might influence upscaled estimates of evaporation. Expectedly, correlations between the energy components and evaporation were fairly strong and the general responses were consistent with expectations as a result of variations in surface state conditions. The general shifts in the distributions among the roughness classes meant spatial associations needed to be considered carefully. Surface albedo and surface temperature showed a moderate positive correlation, and so the influence on net radiation was larger when they varied together. This is one way in which the interactions of the radiative components can effectively influence evaporation estimates. However, they are not multiplied together and do not explicitly represent a covariance. The covariance between *G* and net radiation was a very small negative value (i.e. essentially zero). The complex interactions within the *G-D* model effectively limited any potential increases in evaporation estimates which might not be the case if another model had been applied. An assessment of possible covariance was restricted to the energy terms due to the small ranges in the mean daily driving climate data and the insensitivity of the model. A detailed evaluation over a larger area with larger variability in climate conditions might provide further insight.

Archived historical climate observations obtained for several point locations across the Prairie region were used to drive a physically-based hydrological model assembled within CRHM. Evaporation from a tall alfalfa type grass surface was modelled at each location over a 46 year period spanning 1960 - 2005 which included a recent major drought period (1999 – 2004). Overall, the simulations provided a reasonable representation of the drought and non-drought periods given the knowledge of the general conditions across the Prairie region during the period of record. Results of the simulations showed the interannual variability of seasonal evaporation was larger for stations located within the Palliser Triangle region compared to those generally located outside the region. Cumulative totals depended largely on the influence of spring moisture conditions and growing season rainfall. The distributions of daily growing season evaporation varied between successive years and large shifts in the distributions where observed when drought or wetter conditions were experienced. A general limitation of the

analysis was that more detailed surface and climate information was missing between the widely spaced stations. However, the maps were instructional as regards the changing structure of drought in general. Such information might be useful for operational purposes given that spatially varying estimates of actual evaporation are not often considered in the context of characterizing drought conditions.

The main findings of this research are:

1. Physically-based point scale evaporation models driven by surface reference observations provided reasonable estimates of evaporation over multi-day periods and over the season. The estimates for daily and sub-daily periods were less reliable and given the general scatter in the estimates it is unlikely that stability corrections alone would correct potential model errors. The observed variation in model estimates may be partly attributed to the theoretical differences of the models. It was interesting to note the consistent underestimation of evaporation by the models during the reproductive stage of plant growth. When this occurred, the *P-M* model estimate was in better agreement to the observed value than either the *G-D* or *BT* models. This might be due to the consideration for both the energy available to the vegetation and physiological controls inferred with the inclusion of the resistance term within the *P-M* model. In contrast, the *G-D* model relies on a generalization of the surface-atmospheric feedbacks at the representative scale of the measurements. The *BT* model might be limited by the small footprint of the point scale measurement of surface temperature and other influences on stomatal controls not accounted for in the model. More importantly, there was no evidence of systematic differences between evaporation estimates and observed values. This would suggest that any potential improvements to the reliability of the models applied here are unlikely to be achieved through simple linear corrections and an improved physical representation is likely needed to increase model precision at shorter time scales.

2. At the SDNWA, the surface state conditions were generally found to be more spatially variable than the overlying atmospheric conditions. As a result, the impact of the atmospheric differences on estimating evaporation at the reference site was small. In contrast, net radiation is a major factor driving evaporation and is a key indicator of surface state conditions which can reasonably be attributed to near surface water

availability to vegetation, and general differences in vegetation health and surface cover. It was shown that the mean daily net radiation can be distributed over a landscape from a known value by deriving an index of the mid-day net radiation from one-time-of-day visible and thermal images and surface reference data. Variations in surface temperature and albedo were important factors controlling the distribution of net radiation over the field scale. Through the assimilation of remote sensing data the *G-D* feedback model provided a reasonable estimate of the distributed daily actual evaporation where detailed soil moisture information was unavailable. The interactions among the energy and turbulent flux components of the *G-D* model where shown to be offsetting due to a negative relationship with the relative evaporation. In this case, the covariance between the relative evaporation and net radiation was negative but essentially zero. As a result, upscaled evaporation estimates tended to be similar despite the potential for there to be much larger differences associated with an increase in the turbulent flux component of the model.

3. The surface driving factors of evaporation were shown to be highly variable at the field scale and evaporation was shown to vary both spatially and temporally across the Prairie region of Western Canada. However, the large variability exhibited by the surface variables at the field scale suggests valuable information is missing between the widely spaced stations used for the long term hydrological modelling. The variability of evaporation was larger for stations located within the boundary of the Palliser Triangle region and smaller for those outside the general boundary, characterized by sub-humid climate conditions. Large shifts in the distributions of daily evaporation toward lower values, and reduced variability, tended to occur at all locations in years impacted by drought. A similar response toward higher values was noted for locations within the Palliser region when conditions were much wetter compared to the normal. Growing season rainfall and available water content was more variable across the region compared to differences in temperature and the humidity deficit; although there were large shifts in the respective distributions between years. Maps of evaporation and exeedance fractions were instructional as indicators of drought. The structure of the drought changed from year to year and so the there was no consistent pattern to the evaporation estimates.

8.1 Recommendations for Future Study

The field case study conducted in 2007 was unable to provide distributed observations of the driving climate factors, although these were much less variable than the driving surface factors. Where a detailed set of atmospheric and surface observations is obtainable over a small region comprised of numerous fields it might be possible to further examine the potential impacts of covariance among the driving energy and climate factors on evaporation estimates. Further insight might be gained from using a model with a different theoretical approach. A grid based approach over a larger area presents the most practical means of further examining the variability of evaporation and governing factors across a range of spatial scales. However, a detailed examination for a dense set of points might also be useful.

LIST OF REFERENCES

Alavi, N., Berg, A. A., Warland, J. S., Parkin, G., Verseghy, D. and Bartlett, P. 2010. Evaluating the impact of assimilating soil moisture variability data on latent heat flux estimation in a land surface model. *Canadian Water Resources Journal*, **35**, 157-172.

Ångström, A. 1920. Application of heat radiation measurements to the problems of evaporation from lakes and the heat convection at their surfaces. *Geografiska Annaler*, **2**, 237-252.

Anderson, M. C., Kustas, W. P. and Norman, J. M. 2007. Upscaling flux observations from local to continental scales using thermal remote sensing. *Agronomy Journal*, **99**, 240-254.

Anderson, M., C, Norman, J. M., Diak, G. R., Kustas, W. P. and Mecikalski, J. R. 1997. A two-source time-integrated model for estimating surface fluxes using thermal infrared remote sensing. *Remote Sensing of Environment*, **60**, 195-216.

Annandale, J. G., Jovanovic, N. Z., Benadé, N. and Allen, R. G. 2001. Software for missing data analysis of Penman-Monteith reference evapotranspiration. *Irrigation Science*, **21**, 57-67.

Avissar, R. and Pielke, R. A. 1989. A parameterization of heterogeneous land-surface for atmospheric numerical models and its impact on regional meteorology. *Monthly Weather Review*, **117**, 2,113-2,136.

Ayers, H. D. 1959. Influence of soil profile and vegetation characteristics on net rainfall supply to runoff. *Proceedings of Hydrology Symposium No. 1: Spillway Design Floods*. NRCC, Ottawa, pp. 198-205.

Bailey, W. G. and Davies, J. A. 1981. The effect of uncertainty in aerodynamic resistance on evaporation from the combination model. *Boundary-Layer Meteorology*, **20**, 187-199.

Baldocchi, D. D., Hicks, B. B. and Meyers, T. P. 1988. Measuring biosphere-atmosphere exchanges of biologically related gases with micrometeorological methods. *Ecology*, **69**, 1,331-1,340.

Baldocchi, D., Falge, E., Gu, L., Olson, R., Hollinger, D., Running, S., Anthoni, P., Bernhofer, C., Davis, K., Evans, J., Fuentes, R., Goldstein, A., Katul, G., Law, B., Lee, X., Malhi, Y., Meyers, T., Munger, W., Oechel, W., Paw U., Pilegaard, K., Schmid, H. P.,. Valentini, R., Verma, S., Vesala, T., Wilson, T. and Wofsy, S. 2001. FLUXNET: A new tool to study the temporal and spatial variability of ecosystem-scale carbon dioxide, water vapor, and energy flux densities. *Bulletin of the American Meteorological Society*, **82**, 2,415-2,433.

Baldocchi, D. D., Xu, L. and Kiang, N. Y. 2004. How plant functional-type, weather, seasonal drought, and soil physical properties alter water and energy fluxes of an oak-grass savanna and an annual grassland. *Agricultural and Forest Meteorology*, **123**, 13-39.

Beaubien, E. G. and Johnson, D. L. 1994. Flowering plant phenology and weather in Alberta, Canada. *International Journal of Biometeorology*, **38**, 23-27.

Bisht, G., Venturini, V., Jiang, L. and Islam, S. 2005. Estimation of the net radiation using MODIS (moderate resolution imaging spectroradiometer) data for clear sky days, *Remote Sensing of Environment*, **97**, 52-67.

Blöschl, G. and Sivapalan, M. 1995. Scale issues in hydrological modelling: a review. *Hydrological Processes*, **9**, 251-290.

Boegh, E., Soegaard, H. and Thomsen, A. 2002. Evaluating evapotranspiration rates and surface conditions using Landsat TM to estimate atmospheric resistance and surface resistance. *Remote Sensing of Environment*, **79**, 329-343.

Bonsal, B, Koshida, G., O'Brien, T. and Wheaton, E. 2004. Droughts. In: Threats to Water Availability in Canada. Environment Canada, National Water Research Institute, Burlington, Ontario. NWRI Scientific Assessment Report Series No. 3 and ASCD Science Assessment Series No. 1, 128 p.

Bouchet, R. J. 1963. Evapotranspiration r´eelle et potentielle: Signification climatique. *General Assembly,* Berkeley, *International Association of Scientific Hydrology*, **62**, 134-142.

Bougeault, P. 1991. Parameterization of land-surface processes for mesoscale atmospheric models. In Land surface evaporation: Measurement and parameterization. (Eds) T.J. Schmugge and J.C. André, Springer, pp. 55-92.

Bouma, J. 1989. Using soil survey data for quantitative land evaluation. *Advances in Soil Science*, **9**, 177-213.

Bowen, I. S. 1926. The ratio of heat losses by conduction and by evaporation from any water surface. *Physical Review*, **27**, 779-787.

Brimelow, J. C., Hanesiak, J. M., Raddatz, R. L. and Hayashi, M. 2010. Validation of ET estimates from the Canadian prairie agrometeorological model for contrasting vegetation types and growing seasons. *Canadian Journal of Water Resources Research*, **35**, 209–230.

Brunt, D. 1932. Notes on the radiation in the atmosphere. *Quarterly Journal of the Royal Meteorological Society*, **58**, 389-420.

Brutsaert, W. 1982. Evaporation into the Atmosphere. D. Reidel, Hingham, MA, 299 p.

Brutsaert, W. 1998. Land-surface water vapor and sensible heat flux: Spatial variability, homogeneity, and measurement scales. *Water Resources Research*, **34**, 2,433-2,442.

Brutsaert, W. and Stricker, H. 1979. An advection aridity approach to estimate actual regional evapotranspiration. *Water Resources Research*, **15**, 443-450.

Bukovsky, M. S. and Karoly, D. J. 2007. A brief evaluation of precipitation from the North American Regional Reanalysis. *Journal of Hydrometeorology*, **8**, 837-846.

Burba, G. G. and Verma, S. B. 2005. Seasonal and interannual variability in evapotranspiration of native tallgrass prairie and cultivated wheat ecosystems. *Agricultural and Forest Meteorology*, **135**, 190-201.

Burn, D. H. and Hesch, N. M. 2007. Trends in evaporation for the Canadian Prairies. *Journal of Hydrology*, **336**, 61-73.

Bussières, N., Granger, R. J. and Strong, G. S. 1997. Estimates of regional evapotranspiration using Goes-7 satellite data: Saskatchewan case study, July 1991. *Canadian Journal of Remote Sensing*, **23**, 3-14.

Carey, S. K., Barbour, S. L. and Hendry, M. J. 2005. Evaporation from a waste-rock surface, Key Lake, Saskatchewan. *Canadian Geotechnical Journal*, **42**, 1,189-1,199.

Cemek, B., Meral, R., Apan, M. and Merdun, H. 2004. Pedotransfer functions for the estimation of the field capacity and permanent wilting point. *Pakistan Journal of Biological Sciences*, **7**, 535-541.

Chen, X., Tan, Z., Schwartz, M. D. and Xu, C. 2000. Determining the growing season of land vegetation on the basis of plant phenology and satellite data in Northern China. *International Journal of Biometeorology*, **44**, 97-101.

Colaizzi, P. D., Evett, S. R., Howell, T. A. and Tolk, J. A. 2006. Comparison of five models to scale daily evapotranspiration from one-time-of-day measurements. *American Society of Agricultural and Biological Engineers*, **49**, 1,409-1,417.

Corripio, J. G. 2004. Snow surface albedo estimation using terrestrial photography. *International Journal of Remote Sensing*, **25**, 5,705-5,729.

Courault, D., Seguin, B. and Olioso, A. 2005. Review on estimation of evapotranspiration from remote sensing data: From empirical to numerical modelling approaches. *Irrigation and Drainage Systems*, **19**, 223-249.

Crago, R. and Crowley, R. 2005. Complementary relationships for near instantaneous evaporation. *Journal of Hydrology*, **300**, 199-211.

Cummings, N. W. and Richardson, B. 1927. Evaporation from lakes. *Physical Review*, **30**, 527-534.

Dalton, J. 1834. Meteorological Observations and Essays, 2nd ed. Manchester: Harrison and Crosfield, 284 p.

de Bruin H. A. R. 1978. A simple model for shallow lake evaporation. *Journal of Applied* M*eteorology*, **17**, 1,132-1,134.

Diodato, N., Ceccarelli, M. and Bellocchi, G. 2010. GIS-aided evaluation of evapotranspiration at multiple spatial and temporal climate patterns using geoindicators. *Ecological Indicators*, **10**, 1,009-1,016.

Disney, M., Lewis, P., Thackray, G., Quaife, T. and Barnsley, M. 2004. Comparison of MODIS broadband albedo over an agricultural site with ground measurements and values derived from Earth observation data at a range of spatial scales. *International Journal of Remote Sensing*, **25**, 5,297-5,317.

Duguay, C. R. and Pietroniro, A. 2005. Remote Sensing in Northern Hydrology: Measuring Environmental Change. Geophysical Monograph 163, American Geophysical Union, Washington , DC, 160 p.

England, C. B. 1975. Root depth as a sensitive parameter in a deterministic hydrologic model. *Water Resources Bulletin*, **11**, 1046-1051.

Engman, E. T. and Chauhan, N. 1995. Status of microwave soil moisture measurements with remote sensing. *Remote Sensing of Environment*, **51**, 189-198.

Engman, E. T. and Gurney, R. J. 1991. Remote sensing in hydrology. Chapman and Hall, London, 223 p.

Environment Canada. 2004. Threats to Water Availability in Canada. Environment Canada, National Water Research Institute, Burlington, Ontario. NWRI Scientific Assessment Report Series No. 3 and ASCD Science Assessment Series No. 1, 128 p.

Fang, X., Pomeroy, J. W., Westbrook, C. J., Guo, X., Minke, A. G. and Brown, T. 2010. Prediction of snowmelt derived streamflow in a wetland dominated prairie basin. *Hydrology and Earth System Sciences*, **14**, 991-1,006.

Eichinger, W. E., Parlange, M. B. and Stricker, H. 1996. On the concept of equilibrium evaporation and the value of the Priestley-Taylor coefficient. *Water Resources Research*, **32**, 161-164.

Faria, D. A., Pomeroy, J. W. and Essery, R. L. H. 2000. Effect of covariance between ablation and snow water equivalent on depletion of snow-covered area in a forest. *Hydrological Processes*, **14**, 2,683-2,695.

Finocchiaro, M. A. 2001. Science, religion, and the historiography of the Galileo Affair: On the undesirability of oversimplication. *Osiris*, **16**, 114-132.

Fishenden, M. and Saunders, O. A. 1950. An Introduction to Heat Transfer. Oxford University Press, London, 205 p.

Fisher, J. B., Tu, K. P. and Baldocchi, D. D. 2008. Global estimates of the land-atmosphere water flux based on monthly AVHRR and ISLSCP-II data, validated at 16 FLUXNET sites. *Remote Sensing of Environment*, **112**, 901-919.

Flanagan, L. B., Wever, L. A. and Carson, P. J. 2002. Seasonal and interannual variation in carbon dioxide exchange and carbon balance in a northern temperate grassland. *Global Change Biology*, **8**, 599-615.

Flanagan, L. B. and Johnson, B. G. 2005. Interacting effects of temperature, soil moisture and plant biomass production on ecosystem respiration in a northern temperate grassland. *Agricultural and Forest Meteorology*, **130**, 237-253.

Foken, T. 2008.The energy balance closure problem: an overview. *Ecological Applications*, **18**, 1,351-1,367.

Foken, T., Göckede, M., Mauder, M., Mahrt, L., Amiro, B., and Munger, W. 2004. Post-Field Data Quality Control. In Handbook of Micrometeorology: A Guide for Surface Flux Measurement and Analysis, (Eds.) Lee, X., Massman, W. J. and Law, B. Kluwer, Dordrecht, p. 181-208.

Foken, T., Wimmer, F., Mauder, M., Thomas, C. and Liebethal, C. 2006. Some aspects of the energy balance closure problem. *Atmospheric Chemistry and Physics*, **6**, 4,395-4,402.

Franklin, B. 1765. Physical and meteorological observations, conjectures, and suppositions. *Philosophical Transactions*, **55**, 182-192.

Garnier, B. J. and Ohmura, A. 1970. The evaluation of surface variations in solar radiation income. *Solar Energy*, **13**, 21-34.

Gervais, M. D., Bullock, P. R., Mkhabela, M., Finlay, G. J. and Raddatz, R. 2010. Improvements to the accuracy of modelled soil water content from the second generation Prairie agrometeorological model. *Canadian Journal of Soil Science*, **90**, 527-542.

Gioli, B., Miglietta, F., De Martino, B., Hutjes, R. W. A., Dolman, A. J., Lindroth, A., Schumacher, M., Sanz, M. J., Manca, G., Peressotti, A. and Dumas, E. 2004. Comparison between tower and aircraft-based eddy covariance fluxes in five European regions. *Agricultural and Forest Meteorology*, **127**, 1-16.

Gowda, P. H., Chavez, J. L., Colaizzi, P. D., Evett, S. R., Howell, T. A. and Tolk, J. A. 2008. ET mapping for agricultural water management: Present status and Challenges. *Irrigation Science*, **26**, 223-237.

Granger, R. J. 1989a. An examination of the concept of potential evaporation. *Journal of Hydrology*, **111**, 9-19.

Granger, R. J. 1989b. A complementary relationship approach for evaporation from nonsaturated surfaces. *Journal of Hydrology*, **111**, 31-38.

Granger, R. J. 1991. Evaporation from natural nonsaturated surfaces. Ph.D. Thesis, Department of Agricultural Engineering, University of Saskatchewan, 141 p.

Granger, R. J. 1999. Partitioning of energy during the snow-free season and the Wolf Creek Research Basin. In Wolf Creek Research Basin: hydrology, ecology, environment. Environment, Canada, Saskatoon, Sask, pp. 33-44.

Granger, R. J. 2000. Satellite-derived estimates of evapotranspiration in the Gediz Basin. *Journal of Hydrology*, **229**, 70-76.

Granger, R. J. and Bussières, N. 2005. Evaporation/Evapotranspiration estimates with remote sensing. In Remote Sensing in Northern Hydrology: Measuring Environmental Change, (Eds.) Duguay, C. and Pietroniro, A. Geophysical Monograph 163, American Geophysical Union, Washington , DC, 160 p.

Granger, R. J. and Gray, D. M. 1989. Evaporation from natural nonsaturated surfaces. *Journal of Hydrology*, **111**, 21-29.

Granger, R. J. and Gray, D. M. 1990a. Examination of Morton's CRAE model for estimating daily evaporation from field-sized areas. *Journal of Hydrology,* **120**, 309-325.

Granger, R. J. and Gray, D. M. 1990b. A net radiation model for calculating daily snowmelt in open environments. *Nordic Hydrology,* **21**, 217-234.

Granger, R. J. and Pomeroy, J. W. 1997. Sustainability of the western Canadian boreal forest under changing hydrological conditions - 2- summer energy and water use. In, Sustainability of Water Resources under Increasing Uncertainty, (Eds) Rosjberg, D., Boutayeb, N., Gustard, A., Kundzewicz, Z. and Rasmussen, P, IAHS Publ No. 240. IAHS Press, Wallingford, UK, pp. 243-250.

Gray, D. M. and Landine, P. G. 1987. Albedo model for shallow prairie snowcovers. *Canadian Journal of Earth Sciences,* **24**, 1,760-1,768.

Gray, D. M. and Landine, P. G. 1988. An energy-budget snowmelt model for the Canadian prairies. *Canadian Journal of Earth Sciences,* **25**, 1,292-1,303.

Grayson, R. B. and Western, A. W. 1998. Towards area1 estimation of soil water content from point measurements: time and space stability of mean response. *Journal of Hydrology*, **207**, 68-82.

Green, W. H. and Ampt, G. 1911. Studies of soil physics, part I – the flow of air and water through soils. *Journal of Agricultural Science*, **4**, 1-24.

Grunsky, E. C. 2002. R: a data analysis and statistical programming environment– an emerging tool for the geosciences. *Computers & Geosciences*, **28**, 1,219-1,222.

Halley, E. 1691. An account of the circulation of the watry vapours of the sea, and of the cause of springs. *Philosophical Transactions of the Royal Society of London*, **16**, 468-473.

Haque, A. 2003. Estimating actual areal evapotranspiration from potential evapotranspiration using physical models based on complementary relationships and meteorological data. *Bulletin of Engineering Geology and the Environment*, **62**, 57-63.

Henry, W. C. 1854. Memoirs of the Life and Scientific Researches of John Dalton. London, Cavendish Society, 264 p.

Hesch, N. M. and Burn, D. H. 2005. Analysis of Trends in Evaporation – Phase 1. A report submitted to: Agriculture and Agri-Food Canada Prairie Farm Rehabilitation Administration, May 2005, 127 p.

Hobbins, M. T., Ramirez, J. A., Brown, T. C., and Claessens, L. M. 2001. The complementary relationship in estimation of regional evapotranspiration: The Complementary Relationship Areal Evapotranspiration and Advection-Aridity models. *Water Resources Research*, **37**, 1,367-1,387.

Houborg, R. M. and Soegaard, H. 2004. Regional simulation of ecosystem CO2 and water vapor exchange for agricultural land using NOAA AVHRR and Terra MODIS satellite data. Application to Zealand, Denmark.. *Remote Sensing of Environment*, **93**, 150-167.

Hutchinson, M. F. 1995. Interpolation of mean rainfall using thin plate smoothing splines. *International Journal of Geographical Information Systems*, **9**, 385-403.

Hutchinson, M. F. and Gessler, P. T. 1994. Splines - more then just a smooth interpolator. *Geodema*, **62**, 45-67.

Hutten, N. C. and Gifford, G. F. 1988. Using the Green and Ampt infiltration equation on native and plowed rangeland soils. *Journal of Range Management*, **41**, 159-162.

Jackson, R. D., Reginato, R. J. and Idso, S. B. 1977. Wheat canopy temperature: a practical tool for evaluating water requirements. *Water Resources Research*, **13**, 651-656.

Jarvis, P. G. 1976. The interpretation of the variations in leaf water potential and stomatal conductance found in canopies in the field. *Philosophical Transactions of the Royal Society of London Series B-Biological Sciences, A Discussion on Water Relations of Plants*, **273**, 593-610.

Kaimal, J. C. and Finnigan, J. J. 1994. Atmospheric Boundary Layer Flows: Their Structure and Measurement, Oxford University Press, New York. 289 p.

Kelliher, F. M., Leuning, R. and Schulze, E. D. 1993. Evaporation and canopy characteristics of coniferous forests and grasslands – Review. *Oecologia*, **95**, 153-163.

Khandekar, M. L. 2004. Canadian Prairie Drought: A Climatological Assessment. *Report prepared for Alberta Environment*, 37 p.

Kissinger, M. and Rees, W. E. 2009. Footprints on the prairies: Degradation and sustainability of Canadian agricultural land in a globalizing world. *Ecological Economics,* **68**, 2,309-2,315.

Kite, G. W. 1995. The SLURP model. In: Computer models of watershed hydrology. V.P. Singh (ed.), Water Resources Publications, Colorado, USA, pp. 521-562.

Klaassen, W. and Claussen, M. 1995. Landscape variability and surface flux parameterization in climate models. *Agricultural and Forest Meteorology*, **73**, 181-188.

Kouwen, N. 2001. WATFLOOD/SPL8 Flood Forecasting System, University of Waterloo, Waterloo, 156 p.

Kovacs, G. 1987. Estimation of average areal evapotranspiration - proposal to modify Morton's model based on the complementary character of actual and potential evapotranspiration. *Journal of Hydrology*, **95**, 227-240.

Leavesley, G. H., Lichty, R. W., Troutman, B. M. and Saindon L. G. 1983. Precipitation-runoff modelling system: User's manual. US Geological Survey Water Resources Investigations Report 83-4238, 207 p.

Lee, X., Finnigan, J. and Paw U, K. T. 2004b. Coordinate systems and flux bias error. In Handbook of Micrometeorology: A Guide for Surface Flux Measurement and Analysis, (Eds.) Lee, X., Massman, W. J. and Law, B. Kluwer, Dordrecht, p. 33-66.

Lee, X., Massman, W. J. and Law, B. 2004a. Handbook of Micrometeorology: A Guide for Surface Flux Measurement and Analysis. Kluwer, Dordrecht, 250 p.

Lewis, J. M. 1995. The story behind the Bowen Ratio. *Bulletin of the American Meteorological Society*, **76**, 2,433-2,443.

Lhomme, J. P. 1991. The concept of canopy resistance: historical survey and comparison of different approaches. *Agricultural and Forest Meteorology*, **54**, 227-240.

Lhomme, J. P., Elguero, E., Chehbouni, A. and Boulet, G. 1998. Stomatal control of transpiration: Examination of Monteith's formulation of canopy resistance. *Water Resources Research*, **34**, 2,301-2,308.

Lhomme, J. P. and Guilioni, L. 2006. Comments on some articles about the complementary relationship. *Journal of Hydrology*, **323**, 1-3.

Liang, S. 2000. Narrowband to broadband conversions of land surface albedo: I Algorithms. *Remote Sensing of Environment*, **76**, 213-238.

Liang, S. 2004. Quantitative Remote Sensing of Land Surfaces. John Wiley and Sons, Inc., Hoboken, New Jersey, 534 p.

Liang, S. L., Shuey, C. J., Russ, A. L., Fang, H. L., Chen, M. Z., Walthall, C. L., Daughtry, C. and Hunt, R. 2003. Narrowband to broadband conversions of land surface albedo: II. Validation. *Remote Sensing of Environment*, **84**, 25-41.

List, R. J. 1966. Smithsonian Meteorological Tables, 6th Edition. Smithsonian Institution, Washington, D.C., 525 p.

Lucht, W., Schaaf, C. B. and Strahler, A. H. 2000. An algorithm for the retrieval of albedo from space using semiempirical BRDF models. *IEEE Transactions on Geoscience and Remote Sensing*, **38**, 977-998.

Mahrt, L. 1996. The bulk aerodynamic formulation over heterogeneous surfaces. *Boundary-Layer Meteorol*ogy, **78**, 87-119.

Marshall, I. B., Smith, C. A. and Selby, C. J. 1996. A national framework for monitoring and reporting on environmental sustainability in Canada. *Environmental Monitoring and Assessment*, **39**, 25-38.

Martin, F. R. J. 2002. Gross evaporation for the 30-year period 1971–2000 in the Canadian Prairies. Hydrology Report #143, Agriculture and Agri-Food Canada. Prairie Farm Rehabilitation Administration, Regina, Saskatchewan.

Mattikalli, M, N, and Engman, E. T. 2000. Integration of remotely sensed data into geographical information systems. In: Remote Sensing in Hydrology and Water Management. Schultz, G. A. and Engman, E. T. (Eds.), Springer-Verlag, Berlin, Germany, pp 65-82.

Maybank, J., Bonsai, B., Jones, K., Lawford, R., O'Brien, E. G., Ripley, E. A. and Wheaton, E. 1995. Drought as a Natural Disaster. *Atmospheric-Ocean*, **33,** 195-222.

Medina, J. L., Camaco, E., Reca, J., López, R. and Roldán, J. 1998. Determination and analysis of regional evapotranspiration in Southern Spain based on remote sensing and GIS. *Physics and Chemistry of the Earth*, **23**, 427-432.

Menenti, M. 2000. Evaporation. In: Remote Sensing in Hydrology and Water Management. Schultz, G. A. and Engman, E. T. (Eds.), Springer-Verlag, Berlin, Germany, pp 157-188.

Mesinger, F., DiMego, G., Kalnay, E., Mitchell, K., Shafran, P. C., Ebisuzaki, W., Jovic, D., Woollen, J., Rogers, E., Berbery, E. H., Ek, M. B., Fan, Y., Grumbine, R., Higgins, W., Li,

H., Lin, Y., Manikin, G., Parrish, D. and Shi, W. 2006. North American Regional Reanalysis. *Bulletin of the American Meteorological Society*, **87**, 343-360.

Meyers, T. P. 2001. A comparison of summertime water and CO_2 fluxes over rangeland for well watered and drought conditions. *Agricultural and Forest Meteorology*, **106**, 205-214.

Miller, D. K. 1994. Soil heat flux during spring thaw. M.Sc. Thesis, Department of Agricultural Engineering, University of Saskatchewan, 101 p.

Monteith, J. L. 1965. Evaporation and environment. *Symposia of the Society for Experimental Biology*, **19**, 205-234.

Monteith, J. L. 1981. Evaporation and surface temperature. *Quarterly Journal of the Royal Meteorological Society*, **107**, 1-27.

Monteith, 1986. Howard Latimer Penman. *Biographical Memoirs of Fellows of the Royal Society*, **32**, 379-404.

Morton, F. I. 1983. Operational estimates of areal evapotranspiration and their significance to the science and practice of hydrology. *Journal of Hydrology*, **66**, 1-76.

Mu, Q., Heinsch, F. A., Zhao, M. and Running, S. W. 2007. Development of a global evapotranspiration algorithm based on MODIS and global meteorology data. *Remote Sensing of Environment*, **111**, 519-536.

Munn, R. E. 1961. Energy budget and mass transfer theories of evaporation. *Proceedings of National Research Council of Canada Hydrology Symposium No. 2*, Toronto, Canada, pp. 8-26.

Myneni, R. B., Keeling, C. D., Tucker, C. J., Asrar, G. and Nemani, R. R. 1997. Increased plant growth in the northern high latitudes from 1981-1991. *Nature*, **386**, 698-702.

Nace, R. L. 1974. Pierre Perrault: the man and his contribution to modern hydrology. *Water Resources Bulletin*, **10**, 633-647.

Nagler, P. L., Cleverly, J. R., Glenn, E. P., Lampkin, D., Huete, A. R. and Wan, Z. 2005. Predicting riparian evapotranspiration from MODIS vegetation indices and meteorological data. *Remote Sensing of Environment*, **94**, 17-30.

Nichols, W. E. and Cuenca, R. H. 1993. Evaluation of the evaporative fraction for parameterization of the surface energy balance. *Water Resources Research*, **29**, 3,681-3,690.

Nicodemus, F. E., Richmond, J. C., Hsia, J. J., Ginsberg, I. W. and Limperis, T. 1977. Geometrical considerations and nomenclature for reflectance. Washington, DC, National Bureau of Standards Report, 67 p.

Nie, D., Kanemasu, E. T., Fritschen, L. J., Weaver, H. L., Smith, E. A., Verma, S. B., Field, R. T., Kustas, W. P. and Stewart, J. B. 1992. An intercomparison of surface energy flux measurement systems used during FIFE 1987. *Journal of Geophysical Research*, **97**, 18,715-18,724.

Norman, J. M., Kustas, W. P. and Humes, K. S. 1995. Source approach for estimating soil and vegetation energy fluxes in observations of directional radiometric surface temperature. *Agricultural and Forest Meteorology*, **77**, 263-293.

Oke, T. R. 1992. Boundary Layer Climates. Second Edition. Routledge, New York, 435 p.

Parasuraman, K., Elshorbagy, A. and Si, B. C. 2007. Estimating saturated hydraulic conductivity using genetic programming. *Soil Science Society of America Journal*, **71**, 1,676-1,684.

Parlange, M. B., Eichinger, W. E. and Albertson, J. D. 1995. Regional scale evaporation and the atmospheric boundary layer. *Reviews of Geophysics*, **33**, 99-124.

Penman, H. L. 1947. Evaporation in nature. *Reports on Progress in Physics*, **11**, 366-388.

Penman, H. L. 1948. Natural evaporation from open water, bare soil and grass. *Proceedings of the Royal Society of London Series A Mathematical and Physical Sciences*, **193**, 120-146.

Pomeroy, J. W., Granger, R. J., Pietroniro, A., Elliott, J. E., Toth, B. and Hedstrom, N. 1997. Hydrological Pathways in the Prince Albert Model Forest, *Final Report to the Prince Albert*

Model Forest Association. Environment Canada, NHRI Contribution Series No. CS-97004. 154 p + appendices.

Pomeroy, J. W., Gray, D. M., Brown, T., Hedstrom, N. R., Quinton, W. L., Granger, R. J. and Carey, S. K. 2007. The Cold Regions Hydrological Model, a platform for basing process representation and model structure on physical evidence. *Hydrological Processes*, **21**, 2,650-2,667.

Pomeroy, J., Stewart, R. and Lawford, R. 2010. Drought Research Initiative Special Section on Evapotranspiration. *Canadian Water Resources Journal*, **35**, 155-156.

Raddatz, R. L and Cummine, J. D. 2003. Inter-annual variability of moisture flux from the Prairie agro-ecosystem: Impact of crop phenology on the seasonal pattern of tornado days. *Boundary-Layer Meteorology*, **106**, 2,283-2,295.

Raupach, M. R. and Finnigan, J. J. 1988. Single-layer models of evaporation from plant canopies are incorrect but useful, whereas multilayer models are correct but useless: Discuss. *Australian Journal of Plant Physiology*, **15**, 705-716.

Richardson, A. D., Hollinger, D. Y., Burba, G. B., Davis, K. J., Flanagan, L. B., Katul, G. G., Munger, J. W., Ricciuto, D. M., Stoy, P. C., Suyker, A. E., Verma, S. B. and Wofsy, S. C. 2006. A multi-site analysis of random error in tower-based measurements of carbon and energy fluxes. *Agricultural and Forest Meteorology*, **136**, 1-18.

Roberts, G. 2001. A review of the application of BRDF models to infer land cover parameters at regional and global scales. *Progress in Physical Geography*, **25,** 483-511.

Roberts, E., Stewart, R. E. and Lin, C. A. 2006. A Study of Drought Characteristics over the Canadian Prairies. *Atmosphere-Ocean*, **44**, 331-345.

Robertson, G. W. 1968. A biometeorological time scale for a cereal crop involving day and night temperatures and photoperiod. *International Journal of Biometeorology*, **12**, 191-223.

Robinson, P. J. and Henderson-Sellers, A. 1999. Contemporary Climatology, 2nd edition, Harlow: Longman, 317 p.

Robinson, D. A. and Kukla, G. 1984. Albedo of a dissipating snow cover. *Journal of Climate and Applied Meteorology*, **23**, 1,626-1,634.

Royston, J. P. 1995. A remark on AS R94: A remark on Algorithm AS 181: The W test for normality. *Applied Statistics*, **44**, 547-551

Running, S. W., Baldocchi, D., Turner, D. P., Gower, S. T., Bakwin, P. S. and Hibbard, K. A. 1999. A global terrestrial monitoring network integrating tower fluxes, flask sampling, ecosystem modeling and EOS data. *Remote Sensing of Environment*, **70**, 108-127.

Scherer, T. F., Seelig, B. and Franzen, D. 1996. Soil, water and plant characteristics important to irrigation. North Dakota State University (NDSU) Extension Bulletin EB-66.

Schwartz, M. D. 1999. Advancing to full bloom: planning phenological research for the 21st century. *International Journal of Biometeorology*, **42**, 113-118.

Segal, M., Avissar, R., McCumber, M. C. and Pielke, R. A. 1988. Evaluation of vegetation effects on the generation and modification of mesoscale circulations. *Journal of Atmospheric Science*, **45**, 2,268-2,292.

Seguin, B., Assad, E., Freaud, J. P., Imbernon, J. P., Kerr, Y. and Lagouarde, J. P. 1989. Use of meteorological satellite for rainfall and evaporation monitoring. *International Journal of Remote Sensing*, **10**, 1,001-1,017.

Sellers, P. J., Dickinson, R. E., Randall, D. A., Betts, A. K, Hall, F. G, Berry, J. A, Collatz, G. J., Denning, A. S., Mooney, H. A., Nobre, C. A., Sato, N., Field, C. B. and Henderson-Sellers, A. 1997a. Modeling the Exchanges of Energy, Water, and Carbon between Continents and the Atmosphere. *Science*, **275**, 502-509.

Sellers, P. J., Hall, F., Asrar, G., Strebel, D. and Murphy, R. 1992. An overview of the First International Satellite Land Surface Climatology Project (ISLSCP) Field Experiment (FIFE). *Journal of Geophysical Research*, **97**, 19,091-19,109.

Sellers, P. J., Hall, F. G., Kelly, R. D., Black, A., Baldocchi, D., Berry, J., Ryan, M., Ranson, K. J., Crill, P. M., Lettenmaier, D. P., Margolis, H., Cihlar, J., Newcomer, J., Fitzjarrald, D., Jarvis, P. G., Gower, S. T., Halliwell, D., Williams D., Goodison, B., Wickland, D. E. and Guertin, F. E. 1997b. BOREAS in 1997: Experiment overview, scientific results, and future directions. *Journal of Geophysical Research*, **102**, 28,731-28,768.

Sellers, P. J., Mintz, Y., Sud, Y. C. and Dalcher, A. 1986. A simple biosphere model (SiB) for use within general circulation models. *Journal of the Atmospheric Sciences*, **43**, 505-531.

Shen, Y., Kondoh, A., Changyuan, T., Yongqiang, Z., Jianyao, C., Weiqiang, L, Sakura, Y., Changming, L., Tanaka, T. and Shimada, J. 2002. Measurement and analysis of evapotranspiration and surface conductance of a wheat canopy. *Hydrological Processes*, **16**, 2,173-2,187.

Sherratt, D. J. and Wheater, H. S. 1984. The use of surface resistance-soil moisture relationships in soil water budget models. *Agricultural and Forest Meteorology*, **31**, 143-157.

Shook, K. and Pomeroy, J. 2010. Synthesis of incoming shortwave radiation for hydrological simulation. (In Press).

Shuttleworth, W. J. 1991. Evaporation models in hydrology. In Land Surface Evaporation-Measurement and Parameterization, (Eds.) Schmugge, T. J. and André, J. C., Springer-Verlag, New York, pp. 93-120.

Shuttleworth, J. W. and Gurney, R. J. 1990. The theoretical relationship between foliage temperature and canopy resistance in sparse crops. *Quarterly Journal of the Royal Meteorological Society*, **116**, 497-519.

Shuttleworth, W. J. and Wallace, J. S. 1985. Evaporation from sparse crops – an energy combination theory. *Quarterly Journal of the Royal Meteorological Society*, **111**, 839-855.

Soil Landscapes of Canada Working Group, 2007. Soil Landscapes of Canada v3.1.1 Agriculture and Agri-Food Canada. (digital map and database at 1:1 million scale).

Song, C., Woodcock, C. E., Seto, K. C., Lenney, M. P. and Macomber, S. A. 2001. Classification and change detection using landsat tm data: When and how to correct atmospheric effects? *Remote Sensing of Environment*, **75**, 230-244.

Spano, D., Cesaraccio, C., Duce, P. and Snyder, R. 1999. Phenological stages of natural species and their use as climate indicators. *International Journal of Biometeorology*, **42**, 124-133.

Spry, I. M. 1959. Captain John Palliser and the exploration of Western Canada. *The Geographical Journal*, **125**, 149-184.

Stannard, D. I. 1993. Comparison of Penman-Monteith, Shuttleworth-Wallace, and modified Priestley-Taylor evaporation models for wildland vegetation in semiarid rangeland. *Water Resources Research*, **29**, 1379-1392.

Swinbank, W. C. 1951. The measurement of vertical transfer of heat and water vapour by eddies in the lower atmosphere. *Journal of Meteorology*, **8**, 135-145.

Taylor, R. J. and Dyer, A. J. 1958. An instrument for measuring evaporation from natural surfaces. *Nature*, **181**, 408-409.

Teuling, A. J., Uijlenhoet, R., Hupet, F., van Loon, E. E. and Troch, P. A. 2006. Estimating spatial mean root-zone soil moisture from point-scale observations. *Hydrology and Earth System Science Discussions*, **3**, 1447-1485.

Thornthwaite, C. W. 1948. An approach toward a rational classification of climate. *Geographical Review*, **38**, 55-94.

Tobler, W. R. 1970. A computer movie simulating urban growth in the Detroit region. *Economic Geography*, **46**, 234-240.

Töyrä, J., Pietroniro, A., Craymer, M. and Veronneau, M. 2006. Evaluation of LiDAR-derived ground surface digital elevation model (DEM) in low-relief regions: case study on the

Canadian prairies. In: Hydroscan: Airborne laser mapping of hydrological features and resources. Hopkinson, C., Pietroniro, A. and Pomeroy, J. (Eds.) 2008. Hydroscan: Airborne Laser Mapping of Hydrological Features and Resources. Environment Canada and the Canadian Water Resources Association, pp 301-326.

U. S. Department of Agriculture. 1955. Typical water-holding capacities of different-textured soils. In: Water, 1955 Yearbook of Agriculture, Stefferud, A. (Ed.). U. S. Government Printing Office, Washington, D. C. pp 120.

van der Kamp, G., Hayashi, M. and Gallen, D. 2003. Comparing the hydrology of grassed and cultivated catchments in the semi-arid Canadian prairies. *Hydrological Processes*, **17**, 559-575.

Vercauteren, N., Bou-Zeid, E., Huwald, H., Parlange, M. B. and Brutsaert, W. 2009 The estimation of wet-surface evaporation from sensible heat flux measurements. *Water Resources Research*, **45**, W06424.1-W06424.7.

Verma, S. B., Kim, J. and Clement, R. J. 1992. Momentum, water vapor, and carbon dioxide exchange at a centrally located prairie site during FIFE. *Journal of Geophysical Research*, **97**, 18,629-18,639.

Verseghy, D. 2008. THE CANADIAN LAND SURFACE SCHEME. Technical Documentation – Version 3.4. Climate Research Division, Science And Technology Branch Environment Canada, 180 p.

Verseghy, D. L., McFarlane, N. A. and Lazare, M. 1993. A Canadian land surface scheme for GCMs: II. Vegetation model and coupled runs. *International Journal of Climatology*, **13**, 347-370.

Wagner, W., Naeimi, V., Scipal, K., De Jeu, R. and Martiínez-Fernández, J. 2007. Soil moisture from operational meteorological satellites. *Hydrogeology Journal*, **15**, 121-131.

Ward, A. D. and Trimble, S. W. 2004. Environmental hydrology, 2nd ed. Ward, A. D. and Trimble, S. W. (Eds.), Lewis Publishers, Boca Raton, FL, 475 p.

Weaver, J. E. 1925. Investigations on the root habits of plants. *American Journal of Botany*, **12**, 502-509.

Weaver, J. E. 1926. Root development of field crops. New York, McGraw-Hill Book Company, inc, 291 p.

Weaver J. E. 1968. Prairie Plants and Their Environment: A Fifty- year Study in the Mid-west. University of Nebraska Press, Lincoln, 276 p.

Weaver, J. E. and Clements, F. E. 1938. Plant Ecology. New York, London, McGraw-Hill Book Company, Inc, 601 p.

Webb, E. K., Pearman, G. I. and Leuning, R. 1980.Correction of flux measurements for density effects due to heat and water vapour transfer. *Quarterly Journal of the Royal Meteorological Society*, **106**, 85-100.

Western, A. W., Blöschl, G. and Grayson, R. B. 1998a. How well do indicator variograms capture the spatial connectivity of soil moisture? *Hydrological Processes*, **12**, 1851-1868.

Western, A. W., Blöschl, G. and Grayson, R. B. 1998b. Geostatistical characterisation of soil moisture patterns in the Tarrawarra catchment. *Journal of Hydrology*, **205**, 20-37.

Western, A. W., Blöschl, G. and Grayson, R. B. 2001. Toward capturing hydrologically significant connectivity in spatial patterns, *Water Resources Research*, **37**, 83-97.

Western, A.W., Grayson, R. B. and Blöschl, G. 2002. Scaling of soil moisture: A hydrologic perspective. *Annual Review of Earth Planetary Science*, **30**, 149-80.

Wever, L. A., Flanagan, L. B and Carlson, P. J. 2002. Seasonal and interannual variation in evapotranspiration, energy balance, and surface conductance in a northern temperate grassland. *Agricultural and Forest Meteorology*, **112**, 31-49.

Wieringa, J. 1986. Roughness dependent geographical interpolation of surface wind speed averages. *Quarterly Journal of the Royal Meteorological Society*, **112**, 867-889.

Wilczak, J., Oncley, S. and Stage, S. A. 2001. Sonic anemometer tilt correction algorithms. *Boundary-Layer Meteorology*, **99**, 127-150.

Wisniak J. 2001. Historical development of the vapor pressure equation from Dalton to Antoine. *Journal of Phase Equilibria*, **22**, 622-630.

Wolfe, D. W., Schwartz, M. D., Lakso, A. N., Otsuki, Y., Pool, R. M. and Shaulis, N. J. 2005. Climate change and shifts in spring phenology of three horticultural woody perennials in northeastern USA. *International Journal of Biometeorology*, **49**, 303-309.

Wösten, J. H. M., Pachepsky, Ya. and Rawls, W. J. 2001. Pedotransfer functions: Bridging the gap between available basic soil data and missing soil hydraulic characteristics. *Journal of Hydrology*, **251**, 123-150.

Yang, F., Mitchell, K., Hou Y-T., Dai, Y., Zeng, X., Wang, Z. and Liang X-Z. 2008. Dependence of Land Surface Albedo on Solar Zenith Angle: Observations and Model Parameterization. *Journal of Applied Meteorology and Climatology*, **47**, 2,963-2,982.

Yates, T. T., Si, B. C., Farrell, R. E. and Pennock, D. J. 2006. Probability distribution and spatial dependence of nitrous oxide emission: temporal change in hummocky terrain. *Soil Science Society of America Journal*, **70**, 753-762.

Zahner, R. 1967. Refinement in empirical functions for realistic soil moisture regimes under forest cover. In: Forest Hydrology, (Eds.) Sopper, W .E. and Lull, H. W., Pergamon, Oxford, 261 p.

Zha, T., Barr, A. G., van der Kamp, G., Black, T. A., McCaughey, J. H. and Flanagan, L. B. 2010. Interannual variation of evapotranspiration from forest and grassland ecosystems in western Canada in relation to drought. *Agricultural and Forest Meteorology*, **150**, 1476-1484.

Zhang, C. and Guo, X. 2007. Measuring biological heterogeneity in the northern mixed grassland: A remote sensing approach. *The Canadian Geographer*, **51,** 462-474.

Zoran, M. and Stefan, S. 2006. Atmospheric and spectral corrections for estimating surface albedo from satellite data. *Journal of Optoelectronics and Advanced Materials*, **8**, 247-251.

APPENDIX A

GENERAL OBSERVATIONS AT ST. DENIS DURING 2006

Ratio of Evaporation Measurements between the Portable Mast and Reference Site

The figure below shows the ratio of the measured daily evaporation at the portable mast to that for the reference site. The measurements were within 5% or better during testing in late May. Cultivation did not occur until later in June so the portable mast was moved to various bare soil locations throughout the June period. Expectedly, evaporation from the bare soil was much lower than at the reference grass site and ranged from between 70% to 30% of that measured at the reference site when good observations were available. Early in July, the portable mast was moved to an edge of the cropped area. The measured values obtained over the crop were typically within ± 10% of the evaporation measured at the reference site.

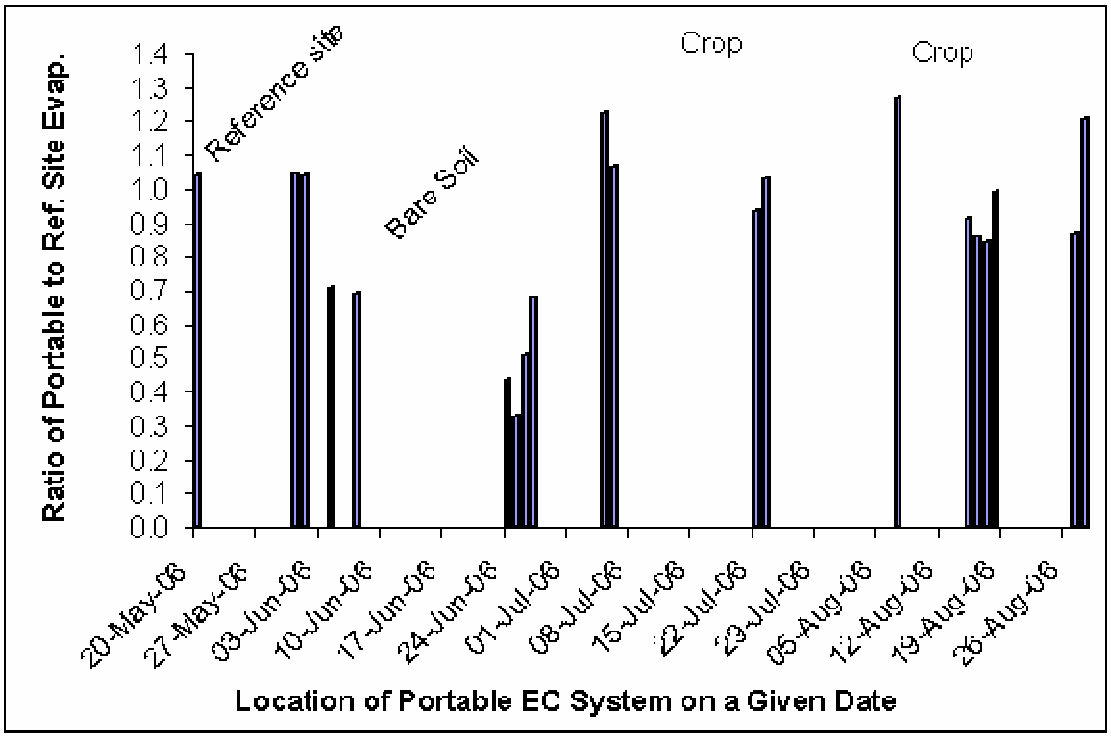

Transect Profiles

The following figures show a profile for transects where measurements were taken of air and surface temperature, relative humidity, and volumetric water content. Transects ranged in length from 100 m to 200 m and samples were taken at a spacing of 5 m apart.

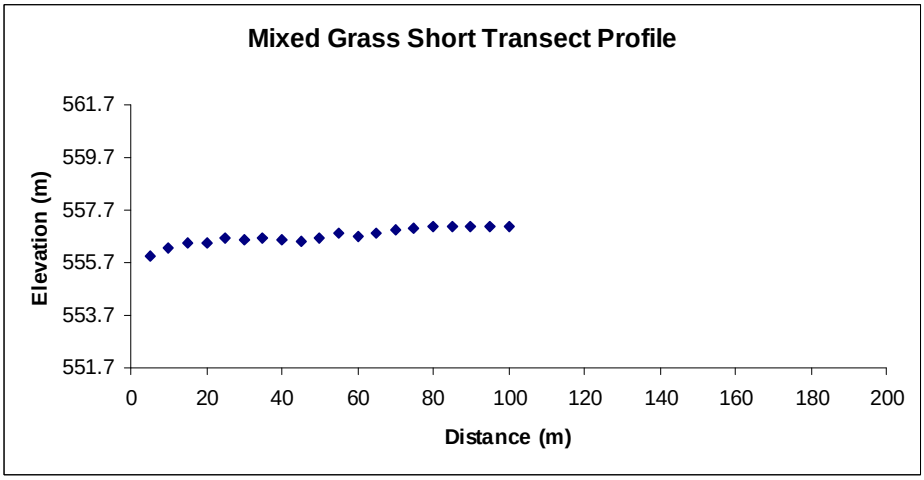

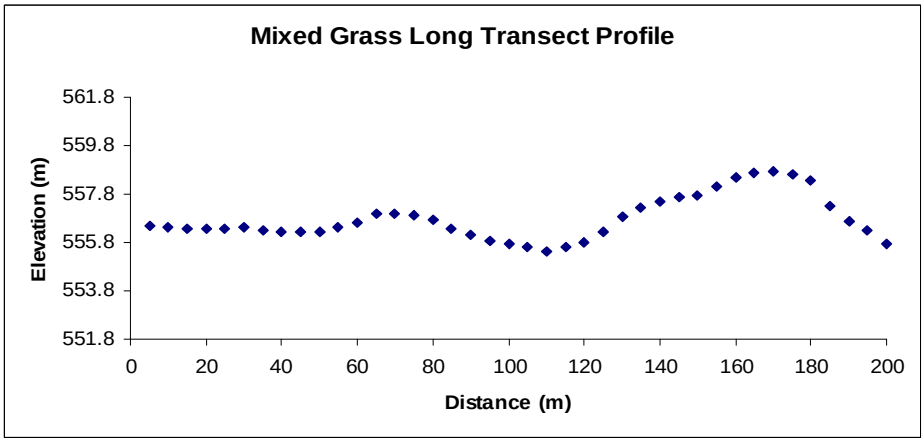

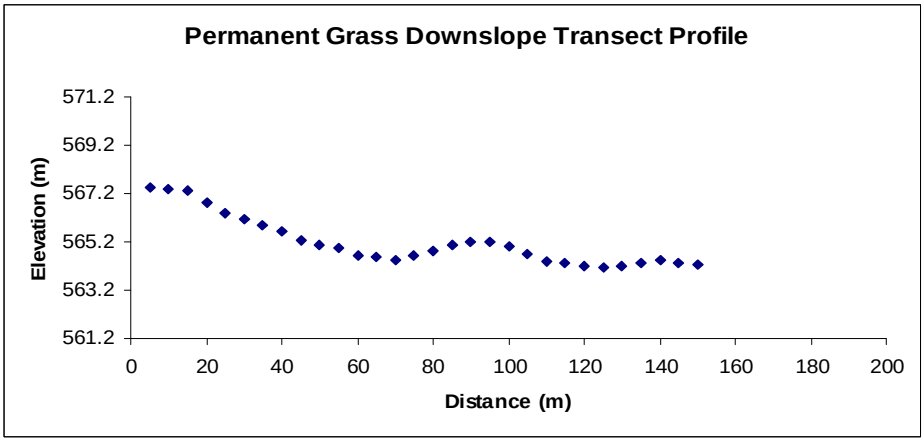

The tables below show the coefficient of variation for measurements taken over the course of the study period and provide an indication of changes in the spatial variability of the variables over time. In general, air temperature and relative humidity were found to be fairly constant along a transect during sampling, and as a result their variability was low. For air temperature the cv ranged from 0.01 to 0.03 and for relative humidity the cv ranged from 0.02 to 0.07. Temperature differences varied by less than ± 1 °C and differences in actual water vapour pressure by only ± 0.1 kPa.

However, the variability of soil moisture and surface temperature was found to be larger than for air temperature and relative humidity depending on the state conditions encountered along the sample points. For example, on June 12 the conditions were relatively wet and the variability of volumetric water content was generally larger than that indicated for air temperature and humidity. The variability of soil moisture during this wet day was lower compared to that observed for the drier conditions on July 10 and July 18 and Aug 3 and Aug 22. Variations in surface temperature tended to be larger as well and depended partly on radiation intensity to the surface which varies temporally in the presence of clouds, cover type and density of the ground coverage, and relative differences in water availability.

		Coefficient of Variation for Volumetric Water Content						
Topography	Vegetation	6-Jun	12-Jun	26-Jun	10-Jul	18-Jul	3-Aug	22-Aug
Flat to depression	Mixed grasses	0.23	0.04	0.10	0.25	0.24	0.21	0.18
Down slope to flat	Brome grass	-	0.17	-	-	0.38	-	0.22
Undulating	Mixed grasses	-	0.13	-	-	-	-	0.20

		Coefficient of Variation for Surface Temperature						
Topography	Vegetation	6-Jun	12-Jun	26-Jun	10-Jul	18-Jul	3-Aug	22-Aug
Flat to depression	Mixed grasses	0.12	0.06	0.07	0.10	0.14	0.06	0.08
Down slope to flat	Brome grass	-	0.08	-	-	0.02	-	0.08
Undulating	Mixed grasses	-	0.09	-	-	-	-	0.12

		Coefficient of Variation for Air Temperature						
Topography	Vegetation	6-Jun	12-Jun	26-Jun	10-Jul	18-Jul	3-Aug	22-Aug
Flat to depression	Mixed grasses	0.02	0.02	0.01	0.01	0.01	0.02	0.02
Down slope to flat	Brome grass	-	0.03	-	-	0.02	-	0.02
Undulating	Mixed grasses	-	0.02	-	-	-	-	0.02

		Coefficient of Variation for Relative Humidity						
Topography	Vegetation	6-Jun	12-Jun	26-Jun	10-Jul	18-Jul	3-Aug	22-Aug
Flat to depression	Mixed grasses	0.07	0.02	0.07	0.03	0.06	0.04	0.04
Down slope to flat	Brome grass	-	0.02	-	-	0.05	-	0.04
Undulating	Mixed grasses	-	0.02	-	-	-	-	0.06

Distribution of Measured Volumetric Water Content during a Wet and Drying Period

In 2006 there were two distinct periods at St. Denis. The first was a relatively wet period where 96 mm of rainfall was received over a period of 30 days extending from June 1 through June 30. There was no rainfall for only 19 out of the 30 days during this period. The second was considered to be a period of drying where 76 mm of rainfall was received over a period of 53 days extending from July 1 through to August 22. There was no rainfall for 22 out the 53 days for this period. Measured values of daily precipitation are shown in the figure below.

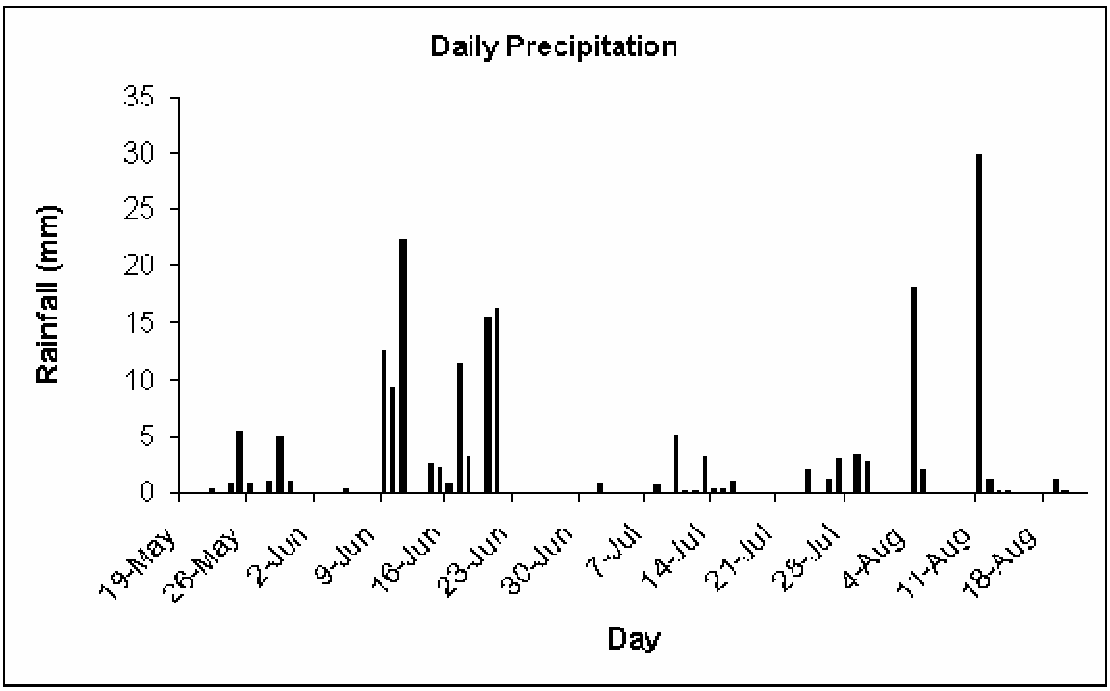

The distributions of measured volumetric water content (VWC) for these respective wet and dry periods are shown in the figure below. In general, the distributions of VWC for these periods very nearly mirror one another. For the wet period the distribution was noticeably left skewed whilst there was a noticeable right skew in the distribution of measurements for the drying period. For these contrasting periods the mean VWC was considerably different; approximately 0.36 or 36% for the wet period and 0.21 or 21% for the drying period. The standard deviation (stdev), however, was essentially the same in both cases.

The coefficient of variation (cv) was also considerably different between the respective periods. In general, the cv gives an indication of the spatial variability of soil moisture. As such, the variability of soil moisture was lower for the wet period than compared to that for the drying period (0.17 vs. 0.28). The increase in variability during the drying period was partly due to the influence of the hummocky terrain characterized by well drained knobs compared with depressions having poor drainage. The fringe areas surrounding wetland depressions were also a major contributing factor where the highest soil moisture contents were typically observed regardless of the antecedent conditions.

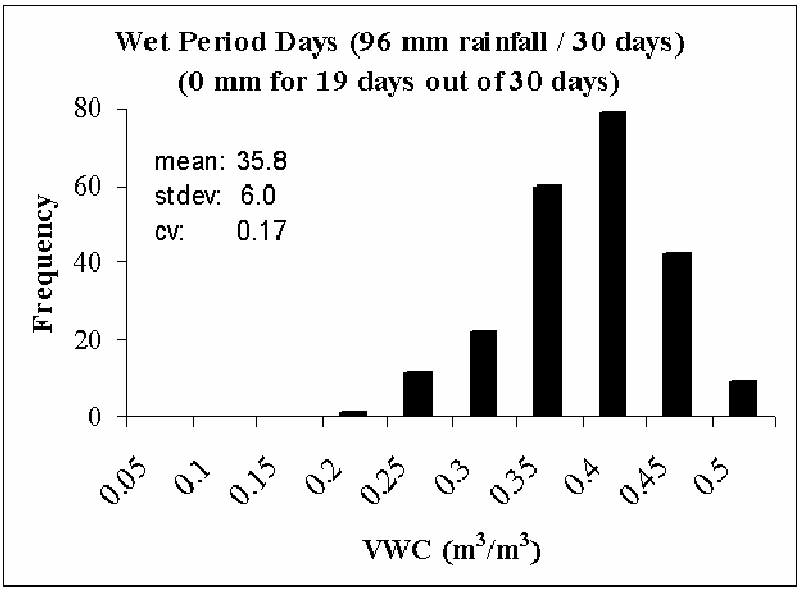

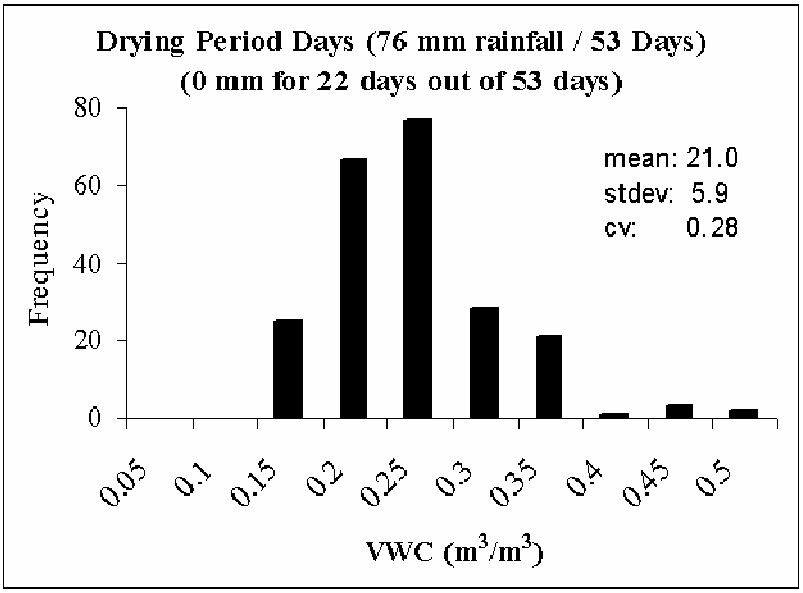

APPENDIX B

VEGETATION MODULE

Vegetation // Sets parameters for vegetation over snow-free period

declreadobs, Ht_obs, NOBS, "vegetation heights", (m)

declparam, Albedo_bare, NHRU, "[0.17]", "0.0", "1.0", "albedo for bare ground", ()

declparam, F_Qg, NHRU, "[0.1]", 0.0, 1.0, "fraction to ground flux, Qg = F_Qg*Rn", ()

declparam, groundcover, NHRU,"[1]", 1, 5, "Vegetation evaporation for HRU: 1 = bare soil , 2 = row crop , 3 = poor pasture, 4 = small grains, 5 = good pasture, 6 = forested", (), Int

declparam, cov_type, NHRU,"[1]", 0, 2, "Vegetation evaporation for HRU: 0 = bare soil (no evaporation), 1 = crops (recharge layer), 2 = grasses & shrubs (all soil moisture)", (), Int

declparam, JCrop_Start, NHRU,"[121]", 1, 366, "start Julian day", ()

declparam, JCrop_Mature, NHRU,"[182]", 1, 366, "maturity Julian day", ()

declparam, JCrop_Harvest, NHRU,"[228]", 1, 366, "harvest Julian day", ()

declparam, rcs, NHRU,"[25]","25.0", "5000.0", "stomatal resistance", ("s/m")

declvar,cov_type_var, NHRU, "recharge/All", ()

declvar,groundcover_var, NHRU, "infiltration", ()

declvar,F_Qg_var, NHRU, " ground heat flux", ()

declvar,rcs_var, NHRU, " canopy resistance", ()

declvar,rechr_saturation, NHRU, "degree of saturation of recharge layer",()

declputvar, *, Albedo, ()

```
declgetvar, *, SWE, ()
declgetvar, *, soil_rechr, ()
declputparam, *, soil_rechr_max, ()
command
  if(FIRSTINT && SWE[hh] <= 0) // check for SWE
  rechr_saturation[hh]=soil_rechr[hh]/soil_rechr_max[hh]
    if(JULIAN >= JCrop_Start[hh] && JULIAN < JCrop_Mature[hh]) // Period 1. during
growing season
      if(Ht_obs[hh] >= 0.02) // cropped or grassed
        if(hh !=3)
// cropped
          groundcover[hh] = 4
          cov_type[hh] = 2
          Albedo_bare[hh] = 0.17
          Albedo[hh] = Albedo_bare[hh]
          rcs[hh] = 50
          F_Qg[hh] = 0.1
        else
// grassed
          groundcover[hh] = 5
          cov_type[hh] = 2
          Albedo_bare[hh] = 0.17
          Albedo[hh] = Albedo_bare[hh]
```

```
          rcs[hh] = 50
          F_Qg[hh] = 0.1
        endif
      else
// fallow
        groundcover[hh] = 1
        cov_type[hh] = 1
        Albedo_bare[hh] = 0.1
        Albedo[hh] = Albedo_bare[hh]
        F_Qg[hh] = 0.2
        if (rechr_saturation[hh] >= 0.933) // i.e. 1 cm in 15 cm
          rcs[hh]=0
        else
          rcs[hh]=50
        endif
       endif
      endif // Period 1
   if(JULIAN >= JCrop_Mature[hh] && JULIAN < JCrop_Harvest[hh]) // Period 2. after
senescence & before harvest
      if(Ht_obs[hh] > 0.02)
        if(hh !=3) // process by HRU type
// cropped
          groundcover[hh] = 4
```

```
          cov_type[hh] = 1
          Albedo_bare[hh] = 0.17
          Albedo[hh] = Albedo_bare[hh]
          rcs[hh] = 50
          F_Qg[hh] = 0.1
        else
// grassed
          groundcover[hh] = 5
          cov_type[hh] = 1
          Albedo_bare[hh] = 0.17
          Albedo[hh] = Albedo_bare[hh]
          rcs[hh] = 5000
          F_Qg[hh] = 0.1
        endif  //cropped/grassed
      else
// fallow
        groundcover[hh] = 1
        cov_type[hh] = 1
        Albedo_bare[hh] = 0.1
        Albedo[hh] = Albedo_bare[hh]
        if (rechr_saturation[hh] >= 0.933) // i.e. 1 cm in 15 cm
          rcs[hh]=0
        else
```

```
          rcs[hh]=50
        endif
        F_Qg[hh] = 0.2
      endif // HRU type test
  endif  // Period 2
 if(JULIAN < JCrop_Start[hh] || JULIAN >= JCrop_Harvest[hh]) //   Period 3. after
harvest & before start of growing season
     if(Ht_obs[hh] >= 0.02)
       if(hh !=3) // process by HRU type
// cropped
          groundcover[hh] = 1
          cov_type[hh] = 1
          Albedo_bare[hh] = 0.17
          Albedo[hh] = Albedo_bare[hh]
          if (rechr_saturation[hh] >= 0.933) // i.e. 1 cm in 15 cm
            rcs[hh]=0
          else
            rcs[hh]=50
          endif
          F_Qg[hh] = 0.2
        else
// grassed
          groundcover[hh] = 5
```

```
          cov_type[hh] = 1
          Albedo_bare[hh] = 0.17
          Albedo[hh] = Albedo_bare[hh]
          rcs[hh] = 5000
          F_Qg[hh] = 0.1
        endif  //cropped/grassed
      else
// fallow
        groundcover[hh] = 1
        cov_type[hh] = 1
        Albedo_bare[hh] = 0.1
        Albedo[hh] = Albedo_bare[hh]
        if (rechr_saturation[hh] >= 0.933) // i.e. 1 cm in 15 cm
          rcs[hh]=0
        else
          rcs[hh]=50
        endif
        F_Qg[hh] = 0.2
      endif // HRU type test
    endif // period test
  endif // SWE check
  cov_type_var[hh] = cov_type[hh]
  groundcover_var[hh] = groundcover[hh]
```

```
  rcs_var[hh]=rcs[hh]

  F_Qg_var[hh] = F_Qg[hh]

end
```